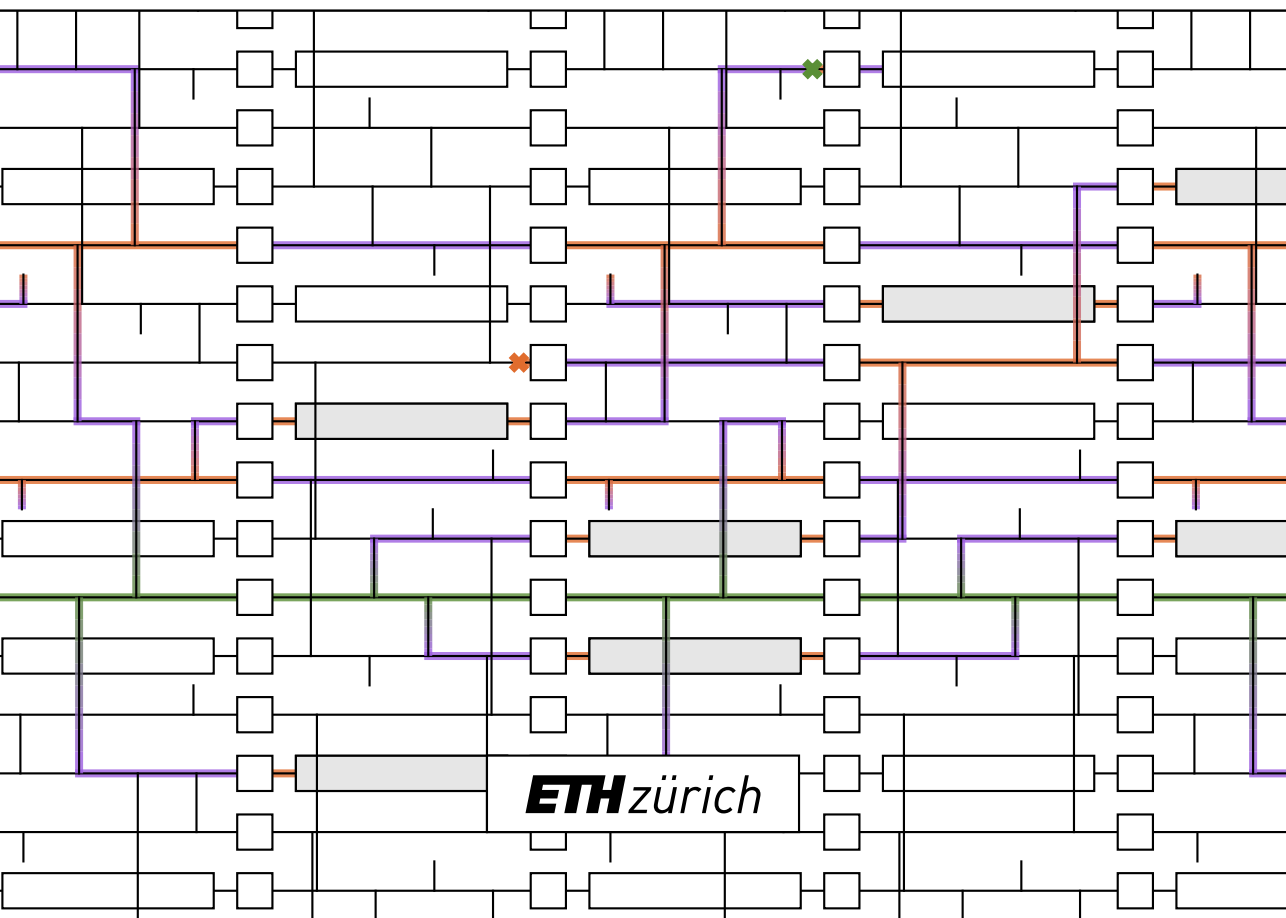


Diss. ETH No. 29740

Implementing Surface Codes with Superconducting Circuits

Ants Remm



DISS. ETH NO. 29740

Implementing Surface Codes with Superconducting Circuits

A thesis submitted to attain the degree of

DOCTOR OF SCIENCES
(Dr. sc. ETH Zurich)

presented by

ANTS REMM

M.Sc. ETH Physics, ETH Zurich

born on 22.05.1992
citizen of Estonia

accepted on the recommendation of
Prof. Dr. Andreas Wallraff, examiner
Dr. Alexander Grimm, co-examiner

2023

Abstract

By utilizing the quantum-mechanical nature of information, quantum computers can execute algorithms that have no equivalent in classical computing. Most known quantum algorithms with useful applications that provide an advantage over classical ones are expected to require billions of quantum operations. Due to a typical error rate of $\sim 10^{-3}$ per operation in current state-of-the-art quantum processors, computations at this scale are currently unattainable. Methods of quantum error correction (QEC) have been developed, which allow to reduce the error probabilities by orders of magnitude by encoding the information in multiple qubits.

In this work, we demonstrate QEC using a surface code implemented as superconducting circuits. First, we present two preliminary experiments, demonstrating the building blocks of the surface code. We stabilize an entangled state of two qubits by repeatedly measuring the $\hat{X}\hat{X}$ and $\hat{Z}\hat{Z}$ operators, called stabilizers, using an auxiliary qubit, and by applying conditional feedforward operations based on the measurement outcomes. In a quantum error detection experiment, we employ similar repeated stabilizer measurements to detect errors in a four-qubit state. We also demonstrate the preparation of protected quantum states by using stabilizer measurements and fault-tolerant measurement of the protected state.

We combine these building blocks in a 17-qubit QEC experiment, where a protected quantum state is preserved over several cycles of stabilizer measurements. While the probability of errors in the protected state is slightly higher than without using the QEC protocol, this experiment constitutes the first demonstration of repeated QEC using a surface code. We discuss in detail some of the technical challenges that we overcame to make the experiment work with high fidelity. This includes the device architecture, pulse shapes for two-qubit gates, drive crosstalk mitigation, interactions with spurious defects in the device, and intermodulation distortion in a traveling-wave parametric amplifier. We also explain how correlations in the stabilizer flips can be used to infer device error probabilities and to compute the parameters of the minimum-weight perfect-matching decoder used to determine the effect of the errors on the protected state.

This work constitutes a milestone in the field of QEC using superconducting circuits, and it paves the way for larger-scale demonstrations of error-corrected qubit operation.

Zusammenfassung

Durch die Nutzung der quantenmechanischen Eigenschaften von Information können Quantencomputer Algorithmen ausführen, die in der klassischen Informatik kein Äquivalent haben. Die meisten solcher anwendungsbezogenen Quantenalgorithmen, die einen Vorteil gegenüber klassischen Algorithmen liefern, erfordern voraussichtlich Milliarden von Quantenoperationen. Aufgrund einer typischen Fehlerrate von $\sim 10^{-3}$ pro Operation in modernsten Quantenprozessoren sind Berechnungen in diesem Maßstab derzeit nicht möglich. Um die Fehlerwahrscheinlichkeiten um Größenordnungen zu reduzieren, wurden Methoden der Quantenfehlerkorrektur (QEC) entwickelt, bei denen die Informationen in mehreren Qubits kodiert werden.

In dieser Arbeit demonstrieren wir QEC in der Form des Surface Codes, implementiert in supraleitenden Schaltkreisen. Zunächst stellen wir zwei vorausgehende Experimente vor, die die Bausteine des Surface Codes darstellen. Wir stabilisieren einen verschränkten Zustand zweier Qubits, indem wir die Operatoren $\hat{X}\hat{X}$ und $\hat{Z}\hat{Z}$, sogenannte Stabilisatoren, wiederholt messen, unter Verwendung eines Hilfs-Qubits und Feedforward-Operationen basierend auf dem Messergebnis. In einem Experiment zur Quantenfehlererkennung verwenden wir ähnliche wiederholte Stabilisatormessungen, um Fehler in einem Vier-Qubit-Zustand zu erkennen. Zudem demonstrieren wir die Initialisierung des geschützten Quantenzustands mithilfe von Stabilisatormessungen und fehlertoleranter Messung des geschützten Zustands.

Diese Bausteine kombinieren wir in einem 17-Qubit-QEC-Experiment, bei dem ein geschützter Quantenzustand über mehrere Zyklen von Stabilisatormessungen erhalten bleibt. Obwohl die Fehlerwahrscheinlichkeit im geschützten Zustand etwas höher ist als ohne Verwendung des QEC-Protokolls, stellt dieses Experiment die erste Realisierung wiederholter Quantenfehlerkorrektur unter Verwendung des Surface Codes dar. Wir erörtern ausführlich einige der technischen Herausforderungen, die wir bewältigt haben, um das Experiment mit hoher Qualität durchzuführen. Dazu gehören die Gerätearchitektur, Pulsformen für Zwei-Qubit-Gatter, die Reduktion von ungewollter Signalkopplungen zwischen Kontrollschaltkreisen auf dem Gerät, Wechselwirkungen mit Stördefekten im Gerät und Intermodulationsverzerrungen in einem parametrischer Wanderwellen-Verstärker. Ebenfalls erklären wir, wie Korrelationen in Veränderungen der Stabilisatoren verwendet werden können, um Gerätefehlerwahrscheinlichkeiten abzuleiten und die Parameter des kostenminimalen, perfekte-Matching Dekodierers zu berechnen, der

zur Bestimmung der Auswirkung der Fehler auf den geschützten Zustand verwendet wird.

Diese Arbeit stellt einen Meilenstein auf dem Gebiet der QEC mit supraleitenden Schaltkreisen dar und ebnet den Weg für Operationen von fehlerkorrigierter Qubits im größeren Maßstab.

Contents

1. Fault-Tolerant Quantum Information Processing	1
1.1. Utility of a Quantum Computer	2
1.2. Quantum Error Correction Protocols	3
1.3. Surface Codes	10
1.4. Overview of the Thesis and Contributions	15
2. Circuit QED with Transmon Qubits	19
2.1. Superconducting Circuit Elements	21
2.2. Transmon Qubit	23
2.3. Readout	26
2.4. Gate Operations	30
2.5. Measurement Setup	40
3. Preliminary Surface Code Experiments	43
3.1. Entanglement Stabilization: Concept	43
3.2. Entanglement Stabilization: Device	45
3.3. Entanglement Stabilization: Results	48
3.4. Quantum Error Detection: Concept	51
3.5. Quantum Error Detection: Device	54
3.6. Quantum Error Detection: Results	57
3.7. Discussion	62
4. Quantum Error Correction Experiment	65
4.1. Concept	65
4.2. Device Architecture	67
4.3. Device Parameters	71
4.4. Results	74
4.5. Technical Challenges	79
4.6. Discussion	85
5. Decoding Error Syndromes	89
5.1. From Errors to the Syndrome	90

5.2. Minimum-Weight Perfect Matching Decoder	94
5.3. Syndrome Correlations to Error Probabilities	98
5.4. Device Diagnostics Using Error Probabilities	103
5.5. Discussion	107
6. Signal Mixing in a Parametric Amplifier	109
6.1. Characterization of Intermodulation Distortion	110
6.2. Implications for Frequency-Multiplexed Readout	115
6.3. Mitigation Strategies	119
6.4. Discussion	123
7. Outlook	125
A. Distance-Three Surface Code as a Stabilizer Code	129
B. Two-Qubit Gate Swap Errors	131
C. Device Design	133
C.1. Extended Readout Circuit Fitting Model	133
C.2. Reference Planes for Lumped Element Modeling	137
C.3. Qubit-Qubit Coupler Design	139
Acknowledgements	143
Bibliography	145
Curriculum Vitae	171
List of Publications	173

Fault-Tolerant Quantum Information Processing

The invention of the semiconductor transistor in 1947, the essential building block of modern classical computers, set off an incredible advancement of human civilization. Ever since then, the number of transistors per integrated device has doubled roughly every two years, known as Moore's law [Moore65]. The resulting digital technologies have affected all aspects of the modern society. However, there exists an even more powerful model for computation than the well-known classical digital computation. At a microscopic level the universe behaves according to the rules of quantum mechanics, which differ fundamentally from the classical physics we experience in our daily lives. By making use of interference between quantum probability amplitudes, certain problems, which are practically unsolvable by classical computers, become tractable using quantum computers [Feynman82].

Quantum information can not, however, be copied, like classical information can, due to the no-cloning theorem [Wootters82]. A significant implication of this is that any interaction with the environment, which could lead to transfer of information, will lead to decoherence of the quantum system. Therefore, any system used for quantum computation needs to be perfectly isolated from its environment. A conflicting requirement is that we need to maintain control over the system to execute the quantum algorithms. For executing algorithms at the scale needed for many practical algorithms, these requirements exclude using individual physical systems as quantum bits, or *qubits*, as they interact too strongly with the environment. Quantum error correction (QEC), however, allows to exponentially reduce the error probabilities in the quantum system at a polynomial overhead in the number of qubits and circuit depth. The surface codes, which are the topic of study of this thesis, are one of the most promising QEC schemes.

1.1. Utility of a Quantum Computer

Why build a quantum computer? There are currently no known classical algorithms that can efficiently simulate the evolution of arbitrary quantum systems. It is, however, unproven that no such classical algorithm can exist [Harrow17]. This means that statements about the advantage of a quantum computer over a classical one can easily change over time, as better classical algorithms are developed [Arute19, Pan22]. On the other hand, more efficient quantum algorithms could also be developed. In this section, we give a brief overview of the currently known problems, where quantum algorithms could be faster compared to classical ones.

The most natural problem for a quantum computer to solve is to simulate the evolution of quantum systems [Feynman82, Georgescu14]. This can be done by either designing the quantum computer to implement the target Hamiltonian directly, called analog quantum simulation, or by executing a sequence of gates to approximate the evolution of the desired quantum system on a general-purpose quantum computer, called digital quantum simulation. For accurate results on system sizes that are intractable to classical algorithms, these algorithms require ~ 100 qubits and circuit depths of $\sim 10^5$ [Kassal08].

A large class of quantum algorithms in which a speedup over classical ones is expected are based on the quantum Fourier transform [Nielsen10]. The applications of the quantum Fourier transform include finding factors of large integers [Shor94], calculating discrete logarithms [Shor97], and finding the eigenvalues of unitary operators using the phase estimation algorithm [Kitaev95]. The first two applications have direct uses in code-breaking, as common cryptography methods assume that integer factorization [Rivest78] and discrete logarithm calculation [Moody23] are exponentially hard problems. However, an estimate of the quantum resources needed for solving a factorization problem that would be infeasible for a classical computer is $\sim 10^3$ qubits and a circuit depth of $\sim 10^9$ [Beauregard03]. Practical application of the discrete logarithm problem has a similar resource requirement [Roetteler17]. The phase estimation algorithm has applications in preparing the ground state of a given Hamiltonian and calculating its energy. However, also in this case, for practical applications around $\sim 10^2$ qubits and a circuit depth of $\sim 10^{11}$ are required [Wecker14, Poulin15].

There also exists an algorithm to invert sparse matrices, but current resource estimates for a quantum computer to provide an advantage over a

classical one are similarly pessimistic [Harrow09, Scherer17].

While the physical qubit counts on the largest existing quantum processors are of the order 100 [Kim23], approaching the number required for the practical applications, the lowest gate errors reported are on the order of $\sim 10^{-3}$ [Kjaergaard20b, Marxer23, Ding23], which are still two-to-eight orders of magnitude higher than what would be required to execute the 10^5 or 10^{11} two-qubit gates of the mentioned practical applications with a reasonable probability of success.

The algorithms mentioned above, where a quantum advantage over a classical algorithm is theoretically expected, are therefore still out of reach, investigations into what can be done on current, noisy intermediate-scale quantum (NISQ) quantum processors [Preskill18, Bharti22] are ongoing. Some of the most prominent algorithms suitable for NISQ devices are hybrid quantum-classical variational quantum algorithms for optimization problems, including variational quantum eigensolver [Peruzzo14, McClean16] and quantum approximate optimization algorithm [Farhi14, Lacroix20]. The resource requirements for those algorithms are attainable, but it is yet to be proven whether any speedup compared to known classical algorithms is to be expected [Barak22]. Another example of an algorithm suitable for NISQ devices is finding the ground state of a Hamiltonian using quantum annealing [Finnila94]. While quantum annealing seems to demonstrate favorable scaling with respect to classical algorithms [King23], the noise in the quantum algorithm still limits it from outperforming the classical counterpart [Perdomo-Ortiz19]. An advantage of a noisy quantum computer over a classical one has been demonstrated for simulating the dynamics of random quantum circuits in cross-entropy benchmarking [Arute19] and Gaussian boson sampling [Zhong20]. However, these algorithms do not currently have known practical applications.

1.2. Quantum Error Correction Protocols

To unlock the proven practical applications of quantum computers, that are, finding the ground state energies of molecules, simulating quantum dynamics, and factoring large numbers, the error rate per operation needs to be reduced by several orders of magnitude. While the physical error rates of quantum operations have been significantly reduced over the years due to improved system design and material engineering [Kjaergaard20a], we

might not reach low enough error rates by optimizing individual qubits only. Fortunately, QEC protocols [Shor95, Knill97] have been developed, which can protect logical quantum information from decoherence by encoding it in a larger protected Hilbert space. Similar error correction ideas are widely used for classical information transmission [IEEE22] and storage [Reed60].

The general necessary and sufficient requirements for a QEC protocol to be successful were derived by Knill and Laflamme [Knill97]. Let $\mathcal{E}(\hat{\rho}) = \sum_i \hat{E}_i \hat{\rho} \hat{E}_i^\dagger$ be a physical error channel that we want to protect against, with \hat{E}_i the Kraus operators, and $\hat{\rho}$ the density matrix, both acting on a large physical Hilbert space [Nielsen10]. The logical information is encoded into a subspace of the larger Hilbert space, and is characterized by the projector $\hat{\Pi}_L$. The Knill-Laflamme condition states, that the effect of the error channel \mathcal{E} can be successfully corrected if and only if the condition

$$\hat{\Pi}_L \hat{E}_i^\dagger \hat{E}_j \hat{\Pi}_L = \lambda_{ij} \hat{\Pi}_L \quad (1.1)$$

is satisfied, where λ_{ij} are scalar coefficients. To understand what the Knill-Laflamme condition implies, we multiply Eq. (1.1) by two states picked from any orthogonal basis of the logical subspace, $\langle \psi_k |$ and $|\psi_l \rangle$, to find that $(\langle \psi_k | \hat{E}_i^\dagger) (\hat{E}_j |\psi_l \rangle) = \lambda_{ij} \delta_{kl}$. For the case $k \neq l$ the right-hand side is zero and we see that the error channel \mathcal{E} takes orthogonal logical states to orthogonal Hilbert spaces. This means that at least the basis states can be uniquely restored by a suitable operation. Furthermore, for $k = l$ we find that the error probability is independent of the logical states, meaning that the error does not involve a partial measurement of the logical state by the environment. The Knill-Laflamme condition provides a useful tool for analyzing, which physical errors a particular logical-qubit encoding can protect against.

Most of the proposed QEC protocols belong to one of two classes, continuous variable QEC codes [Joshi21] or qubit-based *stabilizer codes* [Gottesman97, Terhal15], which we will discuss below.

In continuous variable QEC, also called bosonic QEC, the logical qubit is encoded in the Hilbert space of a harmonic oscillator. Various encoding schemes have been proposed, including cat codes utilizing superpositions of coherent states [Cochrane99, Mirrahimi14, Puri17, Grimm20, Réglade23], binomial codes that make use of only a finite number of photon number states [Michael16, Hu19, Ni23], and Gottesman-Kitaev-Preskill codes, which utilize a superposition of squeezed coherent states on a grid [Gottes-

man01, Flühmann19, Sivak23]. These continuous variable codes have several common properties. First, to protect against a larger number of simultaneous photon loss or dephasing errors or to improve the accuracy of the correction, the logical subspace needs to span more photon states of the harmonic oscillator [Albert18]. And second, the harmonic oscillator needs to be coupled to a nonlinear system, typically a superconducting circuit qubit, for active or passive control, which introduces additional error channels. The fact that error suppression can be increased by utilizing a larger part of the Hilbert space of the harmonic oscillator without adding more hardware to the system is very appealing for scaling to lower error rates. However, accurately controlling the large-photon-number states without introducing additional errors remains a challenge.

Stabilizer codes [Gottesman97], on the other hand, use the Hilbert space of n physical qubits to encode k logical qubits. The logical subspace, or code-space, is specified as the mutual $+1$ eigenspace of $n - k$ independent stabilizer generators \hat{S}_i , or *stabilizers* for short, each of which is a product of Pauli operators of the physical qubits. The stabilizer generators must commute with each other for them to have mutual eigenstates. Because the stabilizers, being products of Pauli operators, have eigenvalues ± 1 , fixing each of the $n - k$ eigenvalues to $+1$ reduces the dimension of the Hilbert space, which is initially 2^n , by a factor of two, down to a dimension of 2^k , which corresponds to k logical qubits. To specify a basis for the logical qubits, k logical Pauli \hat{Z}_L and \hat{X}_L operators should be specified, that commute with all the stabilizers and satisfy the usual commutation relations between each other

$$[\hat{S}_i, \hat{S}_j] = 0, \quad [\hat{Z}_{Lp}, \hat{Z}_{Lq}] = 0, \quad (1.2ad)$$

$$[\hat{S}_i, \hat{Z}_{Lp}] = 0, \quad [\hat{X}_{Lp}, \hat{X}_{Lq}] = 0, \quad (1.2be)$$

$$[\hat{S}_i, \hat{X}_{Lp}] = 0, \quad [\hat{Z}_{Lp}, \hat{X}_{Lq}] = 0 \text{ for } p \neq q, \quad (1.2cf)$$

$$\{\hat{Z}_{Lp}, \hat{X}_{Lp}\} = 0. \quad (1.2g)$$

Here, the indices i and j go over the $n - k$ stabilizers, and p and q over the k logical qubits. Note that, because the stabilizers commute with all the other stabilizers and logical operators, multiplying any stabilizer or logical operator by another stabilizer gives an equivalent specification of the same stabilizer code. Sometimes, it is useful to provide a complete basis for the Pauli operators, which can be done by providing *destabilizers* \hat{D}_i for each

stabilizer, which anti-commutes with its own stabilizer, but commutes with all other stabilizers and logical operators, see for example Appendix A. The effect of applying a destabilizer \hat{D}_i is to flip the value of a single stabilizer \hat{S}_i , leaving the other stabilizers and logical operators unchanged.

The operation of a stabilizer code involves repeatedly measuring the stabilizer operators. Let's say an error \hat{E} , which is a product of Pauli operators, occurs. Because all multi-qubit Pauli operators either commute or anticommute, the error will flip the value of all the stabilizers with which it does not commute. The set of stabilizer value flips σ_i from one cycle of stabilizer measurements is called the syndrome of the error. There are usually many errors that have the same syndrome, some of which also flip logical operators and some do not. Decoding the error syndrome then involves deciding, whether a flip of a logical operator value was more likely than no flip.

How good a given code is against correcting Pauli errors can be characterized in terms of its distance d . The distance is the minimum *Hamming weight*, that is, the number of nonidentity single-qubit Pauli operators of an error that flips one of the logical operators but does not affect any of the stabilizers. In other words, if we consider different equivalent logical operators that can be obtained by multiplying them by the stabilizers, the distance of the code is the minimum weight of those logical operators. This means that any error that has a weight of $d - 1$ or less can be detected by the stabilizer code. To see, which errors can be corrected, not just detected, let's consider some Pauli error \hat{E} with weight w . The error $\hat{L}\hat{E}$, where \hat{L} is any logical operator with weight d , has the same syndrome, but a different effect on the logical subspace. A logical error in the decoding can happen if both $\hat{L}\hat{E}$ and \hat{E} are part of the possible set of errors, or in other words $\hat{L}\hat{E}$ has a lower or equal weight compared to \hat{E} . The weight of $\hat{L}\hat{E}$ must be at least $d - w$, which occurs when \hat{E} cancels w single-qubit Pauli operators of \hat{L} . Therefore, a logical error can happen only if $d - w \leq w$. The lowest-weight physical error that can cause a logical error is therefore of weight $\lceil d/2 \rceil$, and all errors of weight $\lfloor (d - 1)/2 \rfloor$ or lower can be corrected. A quantum code that encodes k logical qubits in n physical qubits with a distance d is denoted as $[[n, k, d]]$.

Let's consider, as an example, the smallest stabilizer code that can correct any single-qubit Pauli error, called the $[[5, 1, 3]]$ five-qubit code [Laflamme96, Gottesman97]. The stabilizers and logical operators of the code are given in Table 1.1. Writing down all the syndromes for possible single-qubit errors,

Table 1.1: Five-qubit code. The stabilizers and logical operators of the five-qubit code.

	Qubit				
	Q1	Q2	Q3	Q4	Q5
Stabilizer					
\hat{S}_1	\hat{X}	\hat{Z}	\hat{Z}	\hat{X}	\hat{I}
\hat{S}_2	\hat{I}	\hat{X}	\hat{Z}	\hat{Z}	\hat{X}
\hat{S}_3	\hat{X}	\hat{I}	\hat{X}	\hat{Z}	\hat{Z}
\hat{S}_4	\hat{Z}	\hat{X}	\hat{I}	\hat{X}	\hat{Z}
Logical op.					
\hat{X}_L	\hat{X}	\hat{X}	\hat{X}	\hat{X}	\hat{X}
\hat{Z}_L	\hat{Z}	\hat{Z}	\hat{Z}	\hat{Z}	\hat{Z}

see Table 1.2, we see that all of them are unique, allowing us to always correct the effect of the error on the logical operators.

We list an overview of various error correction protocols that have been demonstrated using superconducting circuits, which is the platform used in this thesis, in Table 1.3. Some of the listed codes denoted as $[n, k, d]$ protect against errors on only one logical operator, which then corresponds to encoding k classical bits in n qubits with distance d .

While a simple error correction code like the five-qubit code can in theory correct all single-qubit errors, its effective practical application suffers from two main problems. First, if the probability that a single-qubit error occurs between two syndrome measurement rounds is p , then there is still a finite probability $\sim p^2$ that two such errors happen, leading to a logical error. Fortunately, it has been shown that concatenating the same distance d code for r levels by using lower-level encoded logical qubits as the constituent qubits for the higher levels of error correction reduces the logical error rate as $p^{\lfloor (d+1)/2 \rfloor^r}$, as long as the initial error probability p is smaller than some threshold value $p < p_c$ [Aharonov97, Knill98, Preskill98]. Some classes of error correction codes, like the $[[d^2, 1, d]]$ surface code, can be scaled up to arbitrary distance d , which also exponentially suppresses the logical error rate as $p^{\lfloor (d+1)/2 \rfloor}$ [Bravyi98, Fowler12b]. The second challenge is how to implement the stabilizer measurements with a low error probability. Typical

Table 1.2: Five-qubit code syndromes. The syndromes $\sigma_1\sigma_2\sigma_3\sigma_4$ for all possible single-qubit errors in the five-qubit code.

Qubit	Error		
	\hat{X}	\hat{Y}	\hat{Z}
Q1	0001	1011	1010
Q2	1000	1101	0101
Q3	1100	1110	0010
Q4	0110	1111	1001
Q5	0011	0111	0100
Correction	\hat{Z}_L	$\hat{X}_L\hat{Z}_L$	\hat{X}_L

implementations of the stabilizer measurement use an auxiliary qubit onto which the stabilizer is mapped and which is then read out. To make the stabilizer measurement fault-tolerant when scaling to larger code sizes, one needs to either apply QEC techniques also to the auxiliary qubit [Preskill98] or consider syndrome elements over multiple rounds when decoding the logical errors [Dennis02].

With currently known QEC protocols and current physical device error rates, the overhead of QEC is still very large, meaning that it is not realistic to see any advantage over classical algorithms if the quantum algorithm provides only a quadratic speedup [Babbush21]. For the algorithms of quantum dynamics simulation, number factorization, and calculation of the system's energy spectrum, mentioned in Section 1.1, the estimated resource requirements for relevant problem sizes are $\sim 10^7$ physical qubits and a runtime of up to a month [Beverland22]. New QEC codes have been invented, in particular from the quantum low-density parity check (QLDPC) class [Gottesman14, Bravyi23], where the encoding rate r , that is, the ratio of number of encoded logical qubits k to the physical qubits n , can be much higher than for the surface codes $r = 1/d^2$ [Bravyi23]. Recently, $[[n, \Theta(n), \Theta(n)]]$ codes with a constant encoding rate have been proposed [Dinur23]. Here, $\Theta(n)$ indicates that for asymptotically large n , the value is proportional to n . Practical implementations of these codes remain to be demonstrated and many challenges related to scaling remain to be solved. In particular, nonlocal stabilizer measurements are a necessary com-

Table 1.3: QEC experiments with superconducting qubits. Adapted and extended from Ref. [Acharya23].

Reference	Year	Code name	Code size	Qb.	Cycles
[Reed12]	2011	Repetition code	$[3, 1, 3]$	3	1
[Ristè15]	2014	Repetition code	$[3, 1, 3]$	5	1
[Kelly15]	2014	Repetition code	$[3-5, 1, 3-5]$	5-9	1-8
[Córcoles15]	2015	Bell state	$[[2, 0, \cdot]]$	4	1
[Takita17]	2017	Toric code	$[[4, 2, 2]]$	5	1
[Wootton18]	2017	Repetition code	$[3-8, 1, 3-8]$	15	1
[Andersen19] ¹	2019	Bell state	$[[2, 0, \cdot]]$	3	1-12
[Bultink20]	2019	Bell state	$[[2, 0, \cdot]]$	3	1-26
[Gong22]	2019	Five-qubit code	$[[5, 1, 3]]$	5	1
[Andersen20] ¹	2019	Surface code	$[[4, 1, 2]]$	7	1-11
[Wootton20]	2020	Repetition code	$[3-22, 1, 3-22]$	5-43	1
[Chen21]	2021	Repetition code	$[3-11, 1, 3-11]$	5-21	1-50
[Chen21]	2021	Surface code	$[[4, 1, 2]]$	7	1-15
[Marques22]	2021	Surface code	$[[4, 1, 2]]$	7	1-15
[Krinner22] ¹	2021	Surface code	$[[9, 1, 3]]$	17	1-16
[Zhao22b]	2021	Surface code	$[[9, 1, 3]]$	17	1-11
[Sundaresan23]	2022	Subsystem code	$[[9, 1, 3]]$	23	1-10
[Acharya23]	2022	Repetition code	$[3-25, 1, 3-25]$	5-49	50
[Acharya23]	2022	Surface code	$[[9-25, 1, 3-5]]$	17-49	1-25
[Ye23]	2023	Surface code	$[[9, 1, 3]]$	17	1-9
[Gupta23]	2023	Toric code	$[[4, 2, 2]]$	7	1

¹This thesis includes contributions to these works.

ponent of those codes due to the Bravyi-Poulin-Terhal bound, which states that $kd^{2/(D-1)} = O(n)$ for $[[n, k, d]]$ codes that are local in D -dimensional space [Bravyi10]. Here, $O(n)$ indicates that for asymptotically large n , the value is proportional to n or infinitely smaller than it.

1.3. Surface Codes

In this work we implement surface codes. Surface codes are stabilizer codes, but also two-dimensional topological codes [Kitaev03]. The topological nature of the codes means that the stabilizers of the codes are local, involving only nearest neighbors on the two-dimensional lattice. The logical operators, however, span across the entire surface. Furthermore, it is one of the codes that can tolerate the highest amount of per-operation errors, with a threshold of approximately 1% when considering circuit-level uniform depolarizing noise [Raussendorf07, Fowler09].

A surface code consists of a $d \times d$ square lattice of data qubits, see red circles in Fig. 1.1, that encode a protected quantum state. Assuming that the data qubits are at the vertices of a square lattice, stabilizers are then the products of Pauli operators of the data qubits surrounding each face of the lattice. The stabilizers alternate between products of \hat{Z} and \hat{X} , see green and blue circles in Fig. 1.1,

$$\hat{S}_{X_i} = \prod_{Dj \in N(X_i)} \hat{X}_{Dj} \quad \text{and} \quad \hat{S}_{Z_i} = \prod_{Dj \in N(Z_i)} \hat{Z}_{Dj}, \quad (1.3)$$

where $N(A_i)$ denotes the set of four or two qubits surrounding the auxiliary qubit A_i which is used to measure the stabilizer \hat{S}_{A_i} , see the gray lines in Fig. 1.1. In addition to the weight-four stabilizers in the bulk, there are weight-two stabilizers at every second edge on the boundary of the lattice, with two opposing sides having X-type stabilizers and the remaining two sides Z-type. Hence, there are $(d-1)^2$ total stabilizers in the bulk and $2(d-1)$ on the boundaries of the lattice, adding up to $d^2 - 1$ total stabilizers, meaning that the logical subspace corresponds to $k = 1$ qubit. A possible pair of minimal-weight logical operators is

$$\hat{Z}_L = \prod_{Dj \in \text{row}} \hat{Z}_{Dj} \quad \text{and} \quad \hat{X}_L = \prod_{Dj \in \text{column}} \hat{X}_{Dj}, \quad (1.4)$$

where any row and column can be used equivalently, see the black lines in Fig. 1.1. It is easy to verify that all the stabilizers commute with each

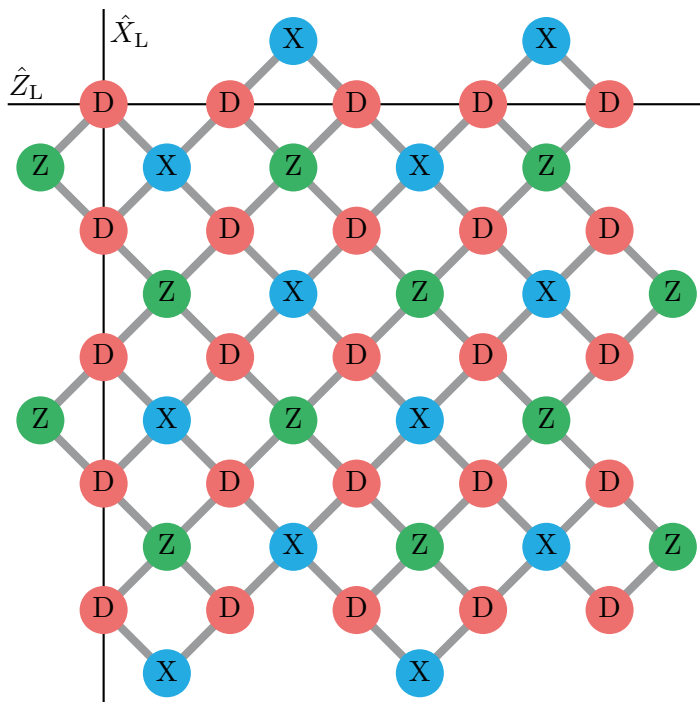


Figure 1.1: Surface code lattice. The lattice of a $d = 5$ surface code with data qubits in red and X- and Z-type auxiliary qubits in blue and green, respectively. The logical operators are indicated as black lines. Gray lines between qubits indicate couplers that allow two-qubit gates to be implemented.

other and with the logical operators by noticing that two multi-qubit Pauli operators anticommute only if they overlap with different Pauli operators on an odd number of qubits.

The surface codes are Calderbank-Shor-Steane [Calderbank96, Steane96] codes, meaning that their stabilizers and logical operators consist of only Pauli \hat{X} or only Pauli \hat{Z} operators. This allows separate decoding of X- and Z-type errors, simplifying the process. Furthermore, the codes are completely symmetrical with respect to swapping the X- and Z-type stabilizers and logical operators and rotating the lattice by $\pi/2$.

If we now consider only \hat{X} errors, which flip the Z-type stabilizers and

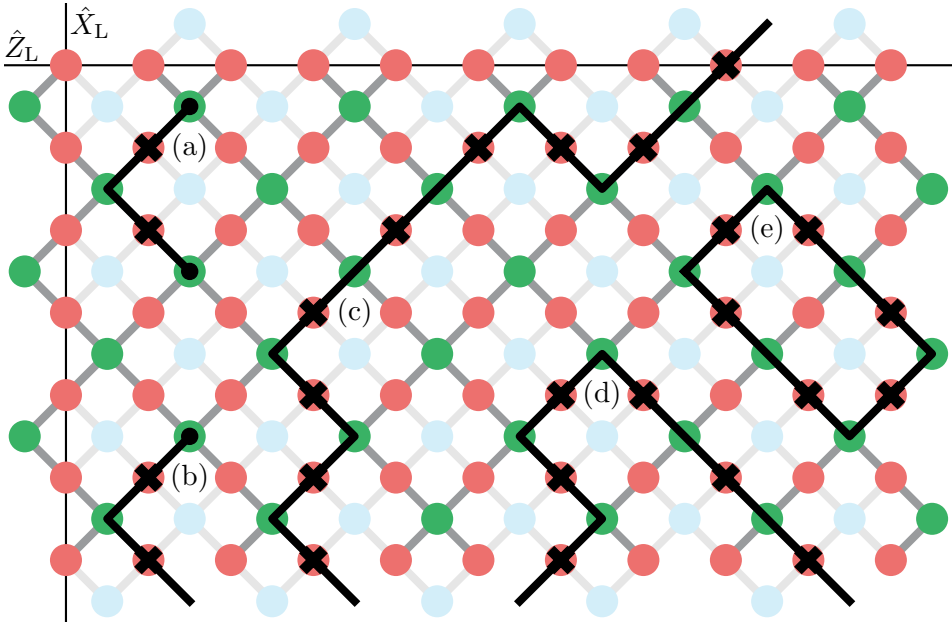


Figure 1.2: Surface code error chains. Examples of bit flip error (black crosses) chains as black lines. Chain (a) has two, (b) one and (c,d,e) zero open ends and correspondingly flip as many stabilizers (black dots). Chain (c) is equivalent to the \hat{X}_L operator, while chains (d) and (e) are equivalent to stabilizers and have no effect on the logical subspace.

the \hat{Z}_L logical operator, we see another manifestation of the surface codes' topological nature, see Fig. 1.2. A chain of errors on neighboring data qubits (connected by a common auxiliary qubit) leads to syndrome element flips only at the endpoints of the chain, as the stabilizers at the middle of the chain are flipped twice and remain in their original state, see examples (a) and (b). Furthermore, the effect of an error chain on the logical state depends only on its endpoints, and not the path. To see that, consider the total effect of applying both the inverse of the original error as well as another error that has the same endpoints. Because Pauli operators are their own inverses, this leads to a circular error chain, see for example (d) and (e). We see that a circular chain \hat{X} of errors is equal to the product of the X-type stabilizers inside the loop, the application of which has no effect on the logical subspace. For an error chain that does not flip any stabilizers

to cause a logical error, it needs to span from one boundary of the surface to the opposite boundary, see example (c).

To use the logical qubits protected by a surface code in an algorithm, one needs to be able to implement a universal set of gates. While the logical \hat{X}_L and \hat{Z}_L gates can be implemented by applying the corresponding single-qubit gates, or by reinterpreting the measurement outcomes, other gates are more difficult to implement. Furthermore, the Eastin-Knill theorem [Eastin09] states that there can not exist a universal gate set for a logically-encoded qubit that can be implemented transversally, that is, by applying a constant-depth sequence of physical operations on the data qubits. So, to implement two-qubit gates between two surface-code logical qubits, two techniques have been proposed. First, by removing one of the stabilizers at the middle of the lattice, a *defect* is created. This defect adds another logical qubit to the code, but also reduces the distance of the code. The defects can be moved around on the surface code lattice, and by braiding one defect around another, a CNOT gate is implemented [Fowler12b]. Another strategy is to merge and split neighboring surface code lattice patches, called lattice surgery [Horsman12]. The lattice surgery architecture is thought to have a smaller resource requirement than the defect braiding architecture [Fowler18]. Merging two logical qubits implements either a $\hat{Z}_L \otimes \hat{Z}_L$ or a $\hat{X}_L \otimes \hat{X}_L$ measurement, depending on the type of boundary that is merged. A split that creates two boundaries with X-type stabilizers, however, implements the $|00\rangle_L \langle 0|_L + |11\rangle_L \langle 1|_L$ operation. Similarly, a split along Z-type boundaries implements the $|++\rangle_L \langle +|_L + |--\rangle_L \langle -|_L$ operation. A CNOT operation between two logical qubits can be implemented using a sequence of split and merge operations and an auxiliary logical qubit. Both the split and the merge are naturally described in the language of ZX-calculus [deBeaudrap20].

However, the logical single-qubit π rotations and CNOT gates are still not sufficient to implement any algorithm that provides a speedup over a classical algorithm, as they belong to the Clifford group. This is apparent from the Gottesman-Knill theorem [Gottesman99a], which states that any Clifford circuit can be efficiently simulated on a classical computer. To make the gate set complete, we also need to be able to execute the \sqrt{X} gate and the $Z^{1/4}$ gate, also known as the T gate. While the Hadamard H gate can be implemented by shifting the surface code by one lattice unit, any single-qubit $Z^{1/2^r}$ gate or $X^{1/2^r}$ gate can be implemented, with the help of special *magic* states and $Z^{1/2^{r-1}}$ or $X^{1/2^{r-1}}$ rotations, using gate

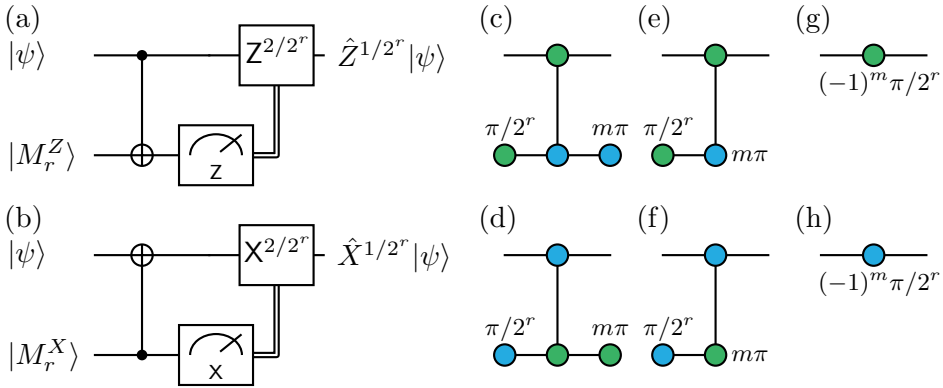


Figure 1.3: Single-qubit gate teleportation. Circuit for (a) $Z^{1/2^r}$ gate and (b) $X^{1/2^r}$ gate implementation using CNOT gates and magic states. (c,d) The ZX-calculus diagrams equivalent to the circuits (a) and (b), without the feedback operation. The measurement outcome is $m = 0$ or 1 . The single-armed green circles with angle α represent preparation of $Z^{\alpha/\pi}|+\rangle$ or projection onto it. The two-armed green circles represent the $Z^{\alpha/\pi}$ rotations, and three-armed green circles represent the projection $|0\rangle\langle 00| + |1\rangle\langle 11|$. The blue circles represent equivalent operations with 0 , 1 , and Z replaced with $+$, $-$, and X , respectively. (e,f) ZX-calculus diagrams that are equivalent to the ones shown in (c) and (d), and also depict merging the qubit with an auxiliary qubit in the magic state using lattice surgery. Here m depicts the outcome of the parity measurement between the two logical qubits. (g,h) The diagrams equivalent to (e) and (f) show that the circuits implement $Z^{\pm 1/2^r}$ and $X^{\pm 1/2^r}$ operations, respectively.

teleportation [Gottesman99b]. To see how to implement the $Z^{1/2^r}$ gate, we prepare the $|M_r^Z\rangle = Z^{1/2^r} |+\rangle$ magic state on an auxiliary logical qubit. This can be done fault-tolerantly by magic state distillation [Knill04, Bravyi05]. We then do a CNOT gate with the logical state $|\psi\rangle$ as a control and the magic state $|M_r^Z\rangle$ as the target, and measure the qubit that was initially in the magic state in the \hat{Z}_L basis. If the measurement outcome is $+1$, then the circuit implements the target unitary $Z^{1/2^r}$, while if the measurement outcome is -1 , then it implements $Z^{-1/2^r}$, which can be corrected by conditionally applying the $Z^{2/2^r}$ gate, see Fig. 1.3(a). The primitive two-qubit gate operations of lattice surgery are the split and merge operations, not the CNOT gate. Using ZX-calculus, it is easy to see that the circuit simplifies to a single merge operation with the magic state, see Fig. 1.3(c,e,g). The $X^{1/2^r}$ is implemented analogously, see Fig. 1.3(b,d,f,h).

1.4. Overview of the Thesis and Contributions

In this thesis, we present the work done toward demonstrating a single distance $d = 3$ surface code logical qubit, its operation, and some of the technical challenges encountered.

The platform we use to implement surface codes is superconducting transmon qubits that are coupled to resonators for readout and two-qubit interactions. In Chapter 2 we review the requirements for implementing a scalable platform for quantum information processing and how these are satisfied in our case. In brief, the requirements are a physical system for storing the qubit, an implementation of single- and two-qubit gate operations, and state preparation and readout. In particular, we focus on the two-qubit gate implementation using novel net-zero flux pulse shapes, which is novel work done by the author of this thesis (A.R.) together with Michael Kershbaum and not based on prior work.

In Chapter 3, we describe two preliminary experiments, that demonstrate the building blocks required for QEC at a smaller scale. In the first experiment, we stabilize an entangled state on two data qubits by repeatedly measuring stabilizers using an auxiliary qubit, thereby demonstrating the essential building block of the surface code [Andersen19]. In the second experiment, we demonstrate logical state preservation using quantum error detection on a distance $d = 2$ surface code, consisting of four data qubits and three auxiliary qubits [Andersen20]. For this work, we prepare highly

entangled logical states and implement logical-qubit readout. For the entanglement stabilization experiment, A.R. conceptualized the experiment together with Christian Kraglund Andersen (C.K.A.), Sebastian Krinner (S.K.), and Johannes Heinsoo (J.H.); A.R. fabricated the quantum device together with S.K., Jean-Claude Besse, and Mihai Gabureac (M.G.); A.R. set up the measurement electronics and wrote the experimental control software together with C.K.A., Stefania Lazăr (S.L.), S.K. and J.H.; and A.R. carried out the experiment, analyzed the data and produced the figures together with C.K.A., and S.L. For the quantum error detection experiment, A.R. fabricated the device together with S.K., G.J.N., and M.G.; A.R. set up the measurement electronics together with C.K.A., S.K., and Nathan Lacroix (N.L.); A.R. wrote the experimental control software together with S.L. and N.L.; and A.R. characterized and calibrated the device and the experimental setup together with C.K.A. and S.L. Andreas Wallraff (A.W.), and Christopher Eichler (C.E.) supervised both projects.

In Chapter 4 we present an experiment that demonstrates QEC in a distance $d = 3$ surface code. The device consists of nine data qubits and eight auxiliary qubits. Numerous technical challenges had to be overcome to demonstrate QEC with a reasonable fidelity. In this thesis, I present some of the topics which I worked more closely on, including the novel architecture of the device, drive crosstalk cancellation, and the characterization of parasitic two-level systems (TLSs) to which the qubits couple strongly. A.R. planned the experiments together with S.K. and N.L.; A.R. designed the device parameters together with C.K.A.; A.R. fabricated the device together with S.K. and G.J.N.; A.R. developed the control and calibration software routines with Christoph Hellings (C.H.), N.L., S.K. and S.L.; A.R. designed, built, and maintained the experimental control electronics and cabling together with C.H., Johannes Herrmann, S.K., C.H., S.L., N.L., and François Swiadek; and A.R. characterized and calibrated the quantum device and the electronics setup together with S.K., N.L., C.H., S.L., and C.K.A. The project was supervised by A.W. and C.E..

In QEC experiments, the syndrome of the code needs to be decoded to find the effect of physical errors on the logical operators, which is not a trivial task. In Chapter 5, I describe, how the decoding of the experimental data that was presented in Chapter 4 was done using a minimum-weight perfect matching (MWPM) decoder. We extract the weights of the MWPM decoder based on the correlations in the syndrome elements. Furthermore, we found a new analytical formula for calculating the per-cycle probabilities

of physical errors based on the syndrome correlations, which we used to analyze the errors in the distance $d = 3$ surface code implementation. A.R. came up with the new analytical formula, took the experimental data, and analyzed the details of the MWPM decoder. The initial decoding script was developed by S.K. and C.K.A. The quantum device, together with its design, fabrication, characterization and calibration are the same as in Chapter 4.

Finally, in Chapter 6, we go into detail with the analysis of one technical issue, intermodulation distortion in the traveling-wave parametric amplifier (TWPA), which was uncovered during the implementation of the work presented in Chapter 4. The intermodulation distortion leads to spurious tones at the output spectrum of the TWPA at integer multiples of the input tones. We characterize the frequencies and the amplitudes of these intermodulation products and show that significant crosstalk can arise when their frequencies coincide with the readout tones. For this investigation, A.R. conceptualized the work, carried out the measurements and analysis. The issue was initially discovered by A.R. together with N.L. and C.H. The quantum device, together with its design, fabrication, characterization and calibration are the same as in Chapter 4.

Circuit QED with Transmon Qubits

To implement any quantum error correction protocol, a physical quantum processor is needed, the creation of which is by itself a very complex technical challenge. For the processor to be useful for any quantum information processing, it needs to satisfy a set of requirements [DiVincenzo00].

First, a well-defined physical platform, in which the quantum information is stored, is needed. The system, called a *qudit*, should have a small set of physical states, in which the quantum state is encoded. For qubits, which we will consider in the following, the number of states is two. Scaling can then be achieved by producing a system with many qubits. Second, it should be possible to prepare the system in a known initial state with high purity, and to measure the state of the system or of a subset of qubits. Furthermore, to be able to implement all possible quantum operations, a *universal* gate set is needed. A gate set is universal, if any unitary operation can be decomposed, up to some arbitrary error, as a sequence of operations from the gate set. Various gate sets have been proven to be universal. For example, the CNOT gate together with arbitrary single-qubit rotations is universal [Nielsen10]. It can be shown, that restricting to the finite the set of $\{\text{CNOT}, \sqrt{X}, Z^{1/4}\}$ is also sufficient [Nielsen10]. Finally, the coherence time of the qubits should be long enough compared to the gate durations, such that there is a significant probability of having no errors after executing the target circuit. In the context of quantum error correction (QEC), the error probabilities of individual operations should be below the threshold p_c , such that increasing the code distance will reduce the logical error probability.

Various architectures that can satisfy all or some of these requirements have been proposed. A natural choice for the physical system to define a qubit would be two energy eigenstates of a single atom. This was pursued in early experiments which utilized rubidium atoms in Rydberg states flying

through microwave cavities [Brune96, Raimond01]. Later experiments have also focused on holding the Rydberg atoms in optical traps [Saffman10, Bluvstein22]. Alternatively, instead of neutral atoms, ions can be trapped in radio frequency traps for manipulation with lasers and microwave signals [Leibfried03]. In addition to the quantum states of matter particles, the states of photons can also be used as qubits. This includes flying qubits encoded in two spatial, polarization, or time-bin modes [Kok07], and stationary qubits encoded in the state of a microwave cavity [Joshi21]. In lieu of using naturally occurring systems like atomic particles and photons, one can also isolate the states of a qubit from a larger solid-state system. For example, individual charge carriers can be confined in a quantum dot, and the spin [Burkard23] or charge [vanderWiel02] degrees of freedom can be used to define a qubit.

A very promising platform for implementing quantum processors, which we utilize in this thesis, is circuit quantum electrodynamics (QED) with superconducting circuits [Blais21]. The circuits to implement the desired Hamiltonians can be flexibly designed using electronic design automation software, and manufactured using optical and electron-beam lithography. Furthermore, the supercurrent provides a lossless medium for the qubit. Many circuits to implement a qubit have been proposed, including the charge qubit, the flux qubit, and many others [Kjaergaard20a]. In this work, we use the *transmon* qubit, which consists of a Josephson junction shunted by a large capacitance [Koch07, Blais21]. The advantages of transmon qubits include insensitivity to both electric field (charge) and magnetic field (flux) noise, and the simplicity with which it can be interfaced with other circuit elements for readout and gates.

We start this chapter by introducing the basic building blocks of circuit QED: the coplanar capacitor, the coplanar waveguide, and the Josephson junction, see Section 2.1. We then show how these elements can be combined in a circuit to define a transmon qubit in Section 2.2. We proceed by explaining the implementation of readout (Section 2.3) and gates (Section 2.4), with extra focus on various pulse shapes that can be used for the two-qubit gates. Finally, we discuss how to interface the quantum device with the classical control electronics to run the experiments in Section 2.5.

2.1. Superconducting Circuit Elements

To facilitate the manufacturing of nano- and micrometer-scale circuits, optical and electron-beam lithography techniques are used to fabricate the quantum devices. These well-developed fabrication techniques have the additional advantage that the material composition, both in bulk and at the interfaces, can be accurately controlled. The fabricated devices consist of a bulk dielectric substrate and thin layers of metals on top. It is crucial to avoid losses in the electrical circuits used to implement the qubits, as loss would lead to energy relaxation and decoherence. Therefore, a low-loss dielectric and a lossless conductor (superconductor) are needed. The lithographic fabrication techniques require that the circuit elements are implemented in a planar geometry. In Fig. 2.1, a capacitor, a transmission line and a Josephson junction, implemented in planar geometry, are shown. All the electrical circuits used in this work can be accurately modeled using these three circuit elements, so we will discuss them in more detail.

In our architecture, capacitors are used for coupling qubits and resonators on the chip to each other, see Fig. 2.1(a). The coupling is mediated by the electric field between the two pads. In addition to the capacitance between the pads, it is also important to consider the capacitance of the pads to the ground, the self-consistent simulation of which we discuss in Section C.2. While an interdigital geometry is often used for coplanar capacitors [Simons01], we use designs without fingers to reduce the sensitivity of the capacitance to fabrication inaccuracies. We routinely fabricate capacitors with pad-to-pad capacitances between 0.1 fF and 100 fF, which enables great flexibility in the design.

We use transmission lines to connect various elements in the circuit to each other and to form resonators. The planar geometry prompts us to use coplanar waveguides (CPWs), consisting of a center conductor separated by a gap from the ground plane on either side, see Fig. 2.1(b). In addition to the CPW mode, for which the two ground planes on either side have equal potential, the CPW geometry also supports the slotline mode, for which there is a potential difference between the two planes [Simons01]. We suppress the undesired slotline modes by placing airbridges across the CPW which connect the two ground planes. Furthermore, we use the airbridges to cross one CPWs over another. To implement a CPW resonator, we terminate each end of the waveguide either by a short or by an open. A waveguide of length ℓ supports modes at frequencies $\omega = n\pi v_p/2\ell$, where

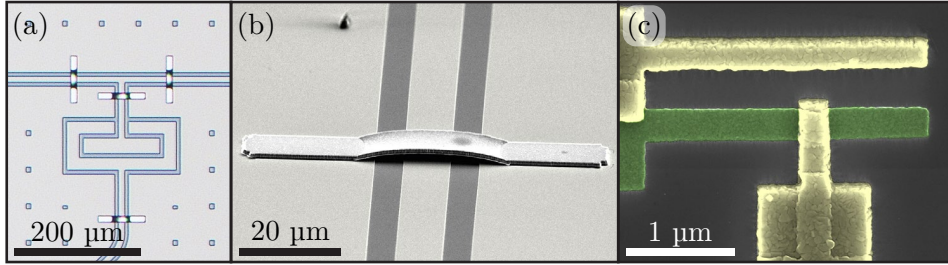


Figure 2.1: Superconducting circuit elements. (a) Optical micrograph of a coplanar capacitor and a T-junction. (b) Tilted-angle scanning electron microscope (SEM) image of a coplanar waveguide and an airbridge. Image by Dante Colao Zanuz. (c) SEM image of an Josephson junction fabricated using the shadow evaporation technique. The first and the second aluminum layers are colored green and yellow, respectively. Image by Sebastian Krinner.

v_p is the phase velocity and n is an even or odd integer, depending on whether the terminations are of the same or different kind, respectively. The wavelength λ of the lowest-frequency modes in open-short-terminated resonators and open-open-terminated resonators is 4ℓ and 2ℓ , respectively, which leads to their names $\lambda/4$ resonator and $\lambda/2$ resonator, respectively. The characteristic impedance of the CPW resonator is set by the ratio of the gap width and center conductor width. Controlling the characteristic impedance allows us to tune the ratio of zero-point fluctuations of the electric and the magnetic fields, thereby tuning the capacitive and inductive coupling strength of the resonator to other elements.

Combining linear capacitors and transmission lines, one can only create circuits that behave as a set of harmonic oscillators in the quantum regime. A quantum harmonic oscillator has a constant difference in energy between neighboring eigenstates, making it hard to isolate a Hilbert space of exactly two states. Therefore, when driving the transition between Fock states $|0\rangle$ and $|1\rangle$, the transitions between $|1\rangle$ and $|2\rangle$, and $|2\rangle$ and $|3\rangle$ are also driven, as the transition frequency is the same. To break the uniform energy spacing of the oscillator, we need a nonlinear circuit element, which also needs to be lossless to avoid decoherence. The most commonly used such element is the Josephson junction. The Josephson junction consists of two pieces of

superconductor, separated by a thin barrier of insulator or normal metal, see Fig. 2.1(c). The dynamics of such a junction are described by the Josephson equations

$$I(t) = I_J \sin\left(2\pi \frac{\Delta\Phi(t)}{\Phi_0}\right), \quad \Phi_i(t) = \int_{-\infty}^t d\tau V_i(\tau), \quad (2.1)$$

where $I(t)$ is the current through the junction, I_J the junction critical current, $\Delta\Phi$ the difference of generalized fluxes Φ_i on either side of the junction, V_i the voltage at either side of the junction, $\Phi_0 = h/2e$ the magnetic flux quantum, h the Planck constant, and e the elementary charge. The energy stored in the junction is given by the integral

$$E = \int dt V(t)I(t) = -E_J \cos\left(2\pi \frac{\Delta\Phi(t)}{\Phi_0}\right), \quad (2.2)$$

where $V = V_1 - V_2$ is the voltage across the junction and $E_J = I_J\Phi_0/2\pi$ is called the Josephson energy of the junction. Expanding Eq. (2.2) up to quadratic terms in the generalized flux difference $\Delta\Phi$, and comparing to the energy of an inductor $E = \Delta\Phi^2/2L$ with inductance L , we see that the Josephson junction behaves like an inductor with inductance $L_J = \Phi_0/2\pi I_J$ in the small current limit. However, due to the cosine term, the effective inductance will depend on the current I , leading to the nonlinearity that we can exploit to implement an oscillator with an unevenly-spaced energy spectrum.

2.2. Transmon Qubit

By replacing the inductor of a parallel LC circuit with a Josephson junction, we obtain the Cooper pair box circuit, which is the basis for a transmon qubit. The circuit consists of an island (yellow) isolated from ground (black) by a capacitor with capacitance C and a junction with critical current I_J , see Fig. 2.2(a,b). In practice, we want to have dynamic control over the system, so we introduce two additional control lines. The charge control line (pink) is capacitively coupled to the island with capacitance C_e and can be used to control the offset charge $Q_e = C_e V_e$ of the island, by applying a voltage V_e to it. To provide control over the Josephson energy of the junction, it is split into two smaller junctions with critical currents I_{J1} and I_{J2} , forming a small loop. The circuit is called the superconducting quantum interference

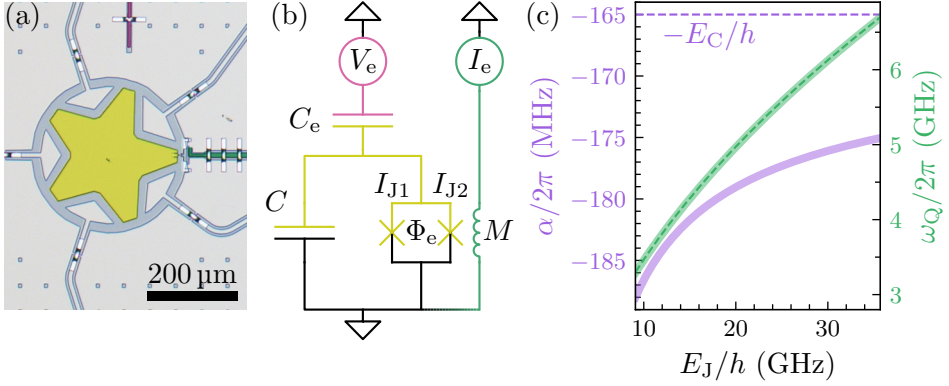


Figure 2.2: Transmon qubit. (a) A false-color optical micrograph of a transmon qubit with the island in yellow, charge control line in pink and flux control line in green. (b) The equivalent electrical circuit of a transmon qubit. (c) Qubit frequency ω_Q and the anharmonicity α as a function of the Josephson energy E_J for a charging energy of $E_C/h = 165$ MHz, calculated analytically according to Eq. (2.6) (dashed thin lines) and numerically by diagonalizing Eq. (2.4c) (solid thick lines).

device (SQUID), because the effective critical current of the split junction is determined by the interference of the currents flowing in two junctions, which depends on the magnetic flux penetrating the loop Φ_e

$$I_J(\Phi_e) = \sqrt{I_{J\Sigma}^2 \cos^2\left(\pi \frac{\Phi_e}{\Phi_0}\right) + I_{J\Delta}^2 \sin^2\left(\pi \frac{\Phi_e}{\Phi_0}\right)}, \quad (2.3)$$

with $I_{J\Sigma} = I_{J1} + I_{J2}$ and $I_{J\Delta} = I_{J1} - I_{J2}$. While a larger asymmetry of the junction sizes I_{J1}/I_{J2} at a fixed maximum critical current $I_{J\Sigma}$ reduces the tunability range of the critical current, it also reduces its sensitivity to external flux noise. When flux-biased to its maximal or minimal value, the critical current becomes first-order insensitive to fluctuations of the external flux. A flux control line (green) is inductively coupled to the SQUID loop with mutual inductance M , allowing to control the external flux $\Phi_e = MI_e$ by applying a current I_e to it.

By doing a canonical quantization of the system [Dirac58], we find that

the Hamiltonian is

$$\hat{H} = \frac{1}{2(C + C_e)}(\hat{Q} - Q_e)^2 - \frac{\Phi_0}{2\pi} I_J(\Phi_e) \cos\left(2\pi \frac{\hat{\Phi}}{\Phi_0}\right), \quad (2.4a)$$

where the island charge \hat{Q} and generalized flux $\hat{\Phi}$ are conjugate variables with the commutator $[\hat{\Phi}, \hat{Q}] = i\hbar$. The Hamiltonian (2.4a) is frequently written in terms of the unitless number of Cooper pairs $\hat{n} = \hat{Q}/2e$, the charging energy $E_C = e^2/2(C + C_e)$, and the reduced generalized flux $\hat{\phi} = 2\pi\hat{\Phi}/\Phi_0$, satisfying the commutation relation $[\hat{\phi}, \hat{n}] = i$,

$$\hat{H} = 4E_C(\hat{n} - n_e)^2 - E_J(\phi_e) \cos(\hat{\phi}) \quad (2.4b)$$

$$= 4E_C(\hat{n} - n_e)^2 - \frac{1}{2}E_J(\phi_e) \sum_{n=-\infty}^{\infty} (|n\rangle\langle n+1| + |n+1\rangle\langle n|). \quad (2.4c)$$

In Eq. (2.4c) we expressed $\hat{\phi}$ in the charge number basis by using the identity $e^{i\hat{\phi}} = \sum_{n=-\infty}^{\infty} |n-1\rangle\langle n|$ [Langford13].

Initial implementations of the Hamiltonian (2.4) [Nakamura99, Wallraff04] had the intrinsic junction capacitance dominate the capacitance C and were in the regime $E_C \sim E_J$, for which the eigenenergies depend strongly on the offset charge number n_e . This dependence of the qubit frequency on the offset charge, called *charge dispersion*, leads to low coherence times of any qubit system due to dephasing by ubiquitous charge noise [Ithier05]. A major improvement to qubit coherence times came by increasing the shunt capacitance of the qubit into the regime $E_C \ll E_J$ [Koch07, Schreier08]. In this so-called transmon regime the eigenstates are spread over many charge states and the eigenenergies become insensitive to static offset charge. In the large E_J/E_C limit, the variation of the transition frequencies of the transmon qubit with the charge offset is suppressed as $e^{-\sqrt{8E_J/E_C}}$ [Koch07].

In the large E_J/E_C limit, the energy spectrum of the transmon qubit is approximately that of a Kerr-nonlinear resonator, corresponding to the Hamiltonian

$$\hat{H} = \hbar\omega_Q \hat{b}^\dagger \hat{b} + \hbar \frac{\alpha}{2} \hat{b}^\dagger \hat{b}^\dagger \hat{b} \hat{b}, \quad (2.5)$$

where $\hat{b} = (E_J/32E_C)^{1/4} \hat{\phi} + i(2E_C/E_J)^{1/4} \hat{n}$ is the excitation annihilation operator [Koch07]. The charge number operator is given as $\hat{n} = -i(E_J/8E_C)^{1/4} (\hat{b} - \hat{b}^\dagger)/\sqrt{2}$. The qubit frequency ω_Q and anharmonicity α determine the frequency of the first transition and the differences of the

frequencies of the subsequent transitions, respectively, and are given by the asymptotic approximations [Koch07]

$$\omega_Q = \left(\sqrt{8E_J E_C} - E_C \right) / \hbar, \quad \alpha = -E_C / \hbar. \quad (2.6)$$

In Fig. 2.2(c), we compare these frequently used asymptotic formulas to exact diagonalization of the Hamiltonian in the charge basis, see Eq. (2.4c). We used 31 charge basis states for the diagonalization, which is well above the maximal charge fluctuation $n_{\text{rms}} = 2.7$ for the states and parameter values shown [Koch07]. For a typical charging energy of $E_C/h = 165$ MHz, targeted for the qubits in the device presented in Chapter 4 and shown in Fig. 2.2(a), we see that the asymptotic formula is very accurate for the qubit frequency ω_Q . However, the absolute value of the anharmonicity is underestimated by the asymptotic formula by up to 20 MHz, amounting to about 10%. Variations at this level are important to account for, when estimating inter-qubit residual couplings and swap errors during two-qubit gates in the low-anharmonicity architectures as we will discuss in Section 4.2 and Appendix B.

2.3. Readout

Having defined the subspace of the two lowest-lying energy states of the transmon qubit as the Hilbert space that we use to encode a physical qubit, we proceed with discussing, how to read out the qubit state. We use the dispersive readout technique [Blais04, Wallraff05], in which we capacitively couple the transmon to a $\lambda/4$ CPW resonator, which is far-detuned from the qubit, see in red in Fig. 2.3(a,b). The Hamiltonian, describing the joint transmon-resonator system is given by

$$\hat{H} = 4E_C \hat{n}^2 - E_J \cos(\hat{\phi}) + \hbar\omega_R \hat{a}^\dagger \hat{a} + \hbar g_n \hat{n} (\hat{a} + \hat{a}^\dagger), \quad (2.7)$$

with ω_R the readout resonator frequency and \hat{a} its annihilation operator [Koch07]. The coupling rate between the transmon charge and resonator field is given by $g_n = 2eC_{\text{QR}}V_{\text{rms}}^0/\hbar C_\Sigma$, where C_{QR} is the capacitance between the transmon and the resonator, C_Σ is the total capacitance of the transmon, and V_{rms}^0 is the zero-point fluctuation of the voltage of the resonator at the coupling point to the qubit. In our case we have a $\lambda/4$ resonator with characteristic impedance Z_0 , coupled at the open end, for

which the zero-point voltage fluctuation is $V_{\text{rms}}^0 = \omega_{\text{R}} \sqrt{\hbar Z_0} / \pi$ [Pechal16], yielding

$$g_n = 4\epsilon\omega_{\text{R}} \frac{C_{\text{QR}}}{C_{\Sigma}} \sqrt{\frac{Z_0}{\hbar}}. \quad (2.8)$$

To see, how the resonator can be used for qubit readout, we again go to the $E_{\text{C}} \ll E_{\text{J}}$ limit, where the transmon is described by a nonlinear oscillator, as in Eq. (2.5). By including the resonator and applying the rotating wave approximation, we obtain the Hamiltonian of a Kerr-nonlinear resonator coupled to a linear resonator

$$\hat{H} = \hbar\omega_{\text{Q}} \hat{b}^\dagger \hat{b} + \hbar \frac{\alpha}{2} \hat{b}^\dagger \hat{b}^\dagger \hat{b} \hat{b} + \hbar\omega_{\text{R}} \hat{a}^\dagger \hat{a} + \hbar g (\hat{a} \hat{b}^\dagger + \hat{a}^\dagger \hat{b}). \quad (2.9)$$

The coupling rate is given by $g = g_n (E_{\text{J}} / 32 E_{\text{C}})^{1/4}$ [Koch07]. By considering the interaction term as a second-order perturbation, we can calculate how much the energy $E_{k,n}$ of the dressed eigenstate with k and n excitations in the transmon and resonator, respectively, is shifted relative to the energy of the bare states of the transmon and the resonator $E_{k,n}^{(0)}$

$$(E_{k,n} - E_{k,n}^{(0)}) / \hbar \approx g^2 \left(\frac{k(n+1)}{\Delta_{\text{QR}} + (k-1)\alpha} - \frac{(k+1)n}{\Delta_{\text{QR}} + k\alpha} \right), \quad (2.10)$$

with $\Delta_{\text{QR}} = \omega_{\text{Q}} - \omega_{\text{R}}$. We see that these eigenenergies correspond to the Hamiltonian

$$\hat{H} / \hbar = \omega_{\text{Q}} \hat{b}^\dagger \hat{b} + \frac{\alpha}{2} \hat{b}^\dagger \hat{b}^\dagger \hat{b} \hat{b} + \omega_{\text{R}} \hat{a}^\dagger \hat{a} + \sum_{k=0}^{\infty} \left(\chi_k + (\chi_k - \chi_{k+1}) \hat{a}^\dagger \hat{a} \right) |k\rangle \langle k|, \quad (2.11)$$

with $\chi_k = kg^2 / (\Delta_{\text{QR}} + (k-1)\alpha)$ being the dispersive shift of the k -th transmon level. In particular, the resonator frequency is shifted by $-\chi_1$ or $\chi_1 - \chi_2$, if the transmon is in the ground state or first excited state, respectively. Furthermore, the transmon first transition frequency is shifted by $\chi_1 + n(2\chi_1 - \chi_2)$ for n photons in the resonator. Therefore, by restricting the Hamiltonian (2.11) to the qubit subspace, we get the effective Hamiltonian

$$\begin{aligned} \hat{H} &= -(\omega_{\text{Q}} + \chi_1) \frac{\hat{Z}}{2} + \left(\omega_{\text{R}} + \chi_1 - \frac{\chi_2}{2} \right) \hat{a}^\dagger \hat{a} - \left(\chi_1 - \frac{\chi_2}{2} \right) \hat{a}^\dagger \hat{a} \hat{Z} \\ &= -\omega'_{\text{Q}} \frac{\hat{Z}}{2} + \omega'_{\text{R}} \hat{a}^\dagger \hat{a} - \chi \hat{a}^\dagger \hat{a} \hat{Z}, \end{aligned} \quad (2.12)$$

with the first transition dispersive shift χ given by

$$\chi = \chi_1 - \frac{\chi_2}{2} = \frac{g^2 \alpha}{\Delta_{\text{QR}}(\Delta_{\text{QR}} + \alpha)} = -\frac{g_n^2}{16} \frac{\sqrt{8E_J E_C}}{\Delta_{\text{QR}}(\hbar\Delta_{\text{QR}} - E_C)}. \quad (2.13)$$

To probe the resonator for qubit readout, we must couple it to the outside environment. Coupling the $\lambda/4$ resonator at its open end via a capacitor with capacitance C_κ to the external environment with an impedance of Z_E gives the resonator a linewidth (inverse decay time) of $\kappa_{\text{R}} = 4\omega_{\text{R}}^3 C_\kappa^2 \omega_{\text{R}}^3 Z_0 Z_E / \pi$ [Göppl08, Pechal16]. This coupling, however, also leads to energy relaxation of the qubit mode at a rate [Blais04, Houck08]

$$\gamma_{\text{R}} = \kappa_{\text{R}} \frac{g^2}{\Delta_{\text{QR}}^2}. \quad (2.14)$$

This interplay between the qubit decay rate and the cavity is called the Purcell effect [Purcell46]. The inverse of the resonator linewidth $1/\kappa_{\text{R}}$ sets a lower bound on the readout duration as the resonator can not be populated more quickly, and the inverse decay rate sets an upper bound to the qubit energy relaxation time $T_1 < 1/\gamma_{\text{R}}$. These constraints make it challenging to achieve fast readout with a high qubit coherence time. Fortunately, the qubit decay rate can be suppressed by filtering the readout circuit to reduce the transmission at the qubit frequency [Reed10, Sete15]. This can be done for example by engineering a band-block filter at the qubit frequency or a band-pass filter at the resonator frequency. We take the approach of using another resonator, which is designed to be resonant with the readout resonator, as a band-pass filter. Using a resonator with a large external coupling κ_{P} and an inter-resonator coupling of J_{PR} as the so-called *Purcell filter*, we get an effective linewidth of the readout resonator of $\kappa_{\text{R}'} = 4J_{\text{PR}}^2/\kappa_{\text{P}}$, and a qubit energy relaxation rate of [Sete15]

$$\gamma_{\text{R}'} = \kappa_{\text{P}} \frac{J_{\text{PR}}^2 g^2}{\Delta_{\text{QR}}^4} = \kappa_{\text{R}'} \frac{g^2 \kappa_{\text{P}}^2}{4\Delta_{\text{QR}}^4}. \quad (2.15)$$

The decay rate is suppressed by a factor of $\kappa_{\text{P}}^2/4\Delta_{\text{QR}}^2$ at a fixed readout resonator effective linewidth. In the actual devices presented in the following chapters, we use the Purcell filters in the regime where $\kappa_{\text{P}} \sim J_{\text{PR}}$, in which case there are two distinct resonator eigenmodes which can be used for readout. The transmission spectra and an expression for the effective

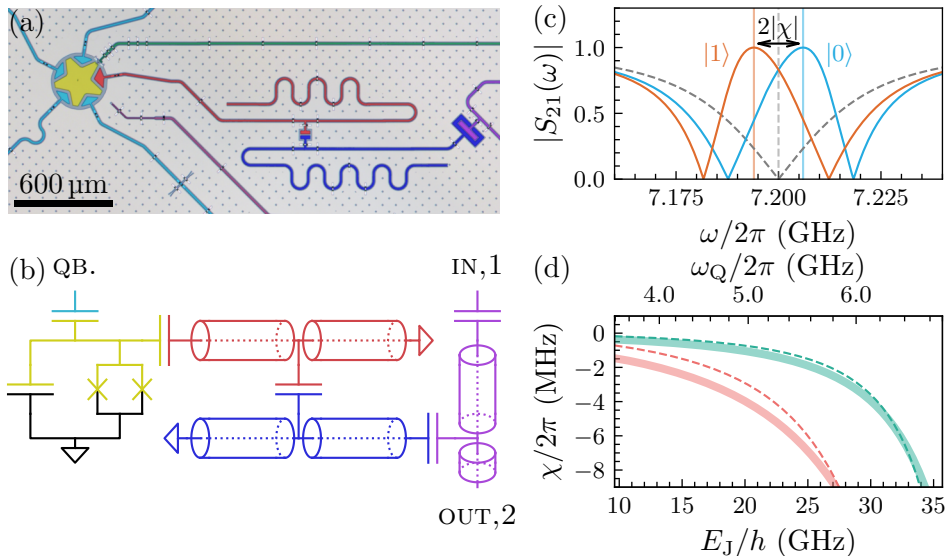


Figure 2.3: Transmon with readout circuit. (a) False-color optical micrograph of a transmon qubit (yellow) that is connected to its readout circuit. The readout resonator is colored red, the Purcell filter blue and the readout feedline purple. The qubit is additionally connected to neighboring qubits using the capacitively coupled CPW sections in cyan. (b) The equivalent circuit corresponding to the micrograph shown in (a). (c) Feedline transmission spectrum for a qubit in the $|0\rangle$ and $|1\rangle$ states in blue and orange, respectively. The dashed transmission spectrum corresponds to a Purcell filter that is not coupled to a readout resonator. The vertical colored and dashed lines indicate the resonance frequencies of the readout resonator and Purcell filter, respectively. (d) The dispersive shift χ , calculated analytically based on Eq. (2.13) (thin dashed lines), and by numerical diagonalization of the Hamiltonian (2.7) (thick solid lines). The green and red data correspond to charge coupling rates of $g_n/2\pi = 110$ MHz and 220 MHz, respectively. The charging energy is $E_C/h = 165$ MHz.

resonator linewidth for this case are derived in Ref. [Heinsoo18] and the readout performance is further analyzed in Ref. [Swiadek23].

We can see this shift of the resonator frequency predicted by Eq. (2.12) when measuring the transmission spectrum $|S_{21}|$ through the feedline of the chip for the two qubit states, see Fig. 2.3(c) for the spectra and (b) for the port labels. For each qubit state, we observe a double-dip structure corresponding to the readout resonator and Purcell filter, which are capacitively coupled to the feedline. We employ a capacitor at the input port of the feedline to direct the radiation emitted from the resonator predominantly toward the output port. However, its presence does not change the spectrum qualitatively, see Section C.1 for a discussion of the analytical model for the transmission spectrum. Therefore, by probing the resonator transmission at a frequency ω_r at which it strongly depends on the qubit state, we can infer the qubit state. The interaction term between the qubit and the resonator $\chi \hat{a}^\dagger \hat{a} \hat{Z}$ commutes with the qubit Hamiltonian, and therefore the measurement is quantum nondemolition and does not introduce additional state transitions beyond projecting on to the state that corresponds to the measurement outcome [Braginsky80]. We typically couple the readout circuits of multiple readout resonators to the same feedline to reduce the number of readout lines needed [Heinsoo18]. We refer the reader to Refs. [Remm17, Heinsoo19] for a more detailed discussion about our readout implementation.

When determining the qubit capacitance to the readout resonator to target a specific dispersive shift χ , one should remember that Eq. (2.13) is only valid in the regime $E_C \ll E_J$ and $g \ll \Delta_{QR}$. Comparing the values of Eq. (2.13) to the dispersive shifts found by the numerical diagonalization of Hamiltonian (2.7), see Fig. 2.3(d), we find a mismatch of up-to a factor two. It is therefore important numerically diagonalize the Hamiltonian in case accurate targeting of the dispersive shift is required.

2.4. Gate Operations

To implement any quantum circuit on the quantum processor, we need to be able to apply single- and two-qubit gate operations. In our architecture, we can implement single-qubit rotations by any angle around a combination of \hat{X} and \hat{Y} operators and arbitrary rotations around the \hat{Z} operator. For two-qubit operations, we implement the conditional phase gate CZ. These

gates, the details of which we discuss in this section, form a universal set, allowing us to implement any quantum operation.

2.4.1. Single-Qubit Operations

We start by introducing notation for the single-qubit gates and the unitaries which they implement. That includes π and $\pi/2$ rotations around the three cardinal axes of the qubit, associated with the \hat{X} , \hat{Y} and \hat{Z} Pauli operators

$$\mathbf{X} = e^{-i\pi\hat{X}/2} = -i \begin{array}{c} \langle 0| \\ |1\rangle \end{array} \begin{array}{c} \langle 1| \\ \left(\begin{array}{cc} 0 & 1 \\ 1 & 0 \end{array} \right) \end{array}, \quad \sqrt{\mathbf{X}} = e^{-i\pi\hat{X}/4} = \frac{1}{\sqrt{2}} \begin{array}{c} \langle 0| \\ |1\rangle \end{array} \begin{array}{c} \langle 1| \\ \left(\begin{array}{cc} 1 & -i \\ -i & 1 \end{array} \right) \end{array}, \quad (2.16ab)$$

$$\mathbf{Y} = e^{-i\pi\hat{Y}/2} = -i \begin{array}{c} \langle 0| \\ |1\rangle \end{array} \begin{array}{c} \langle 1| \\ \left(\begin{array}{cc} 0 & -i \\ i & 0 \end{array} \right) \end{array}, \quad \sqrt{\mathbf{Y}} = e^{-i\pi\hat{Y}/4} = \frac{1}{\sqrt{2}} \begin{array}{c} \langle 0| \\ |1\rangle \end{array} \begin{array}{c} \langle 1| \\ \left(\begin{array}{cc} 1 & -1 \\ 1 & 1 \end{array} \right) \end{array}, \quad (2.16cd)$$

$$\mathbf{Z} = e^{-i\pi\hat{Z}/2} = -i \begin{array}{c} \langle 0| \\ |1\rangle \end{array} \begin{array}{c} \langle 1| \\ \left(\begin{array}{cc} 1 & 0 \\ 0 & -1 \end{array} \right) \end{array}, \quad \sqrt{\mathbf{Z}} = e^{-i\pi\hat{Z}/4} = \frac{1}{\sqrt{2}} \begin{array}{c} \langle 0| \\ |1\rangle \end{array} \begin{array}{c} \langle 1| \\ \left(\begin{array}{ccc} 1 & -i & 0 \\ 0 & 1 & i \end{array} \right) \end{array}, \quad (2.16ef)$$

and arbitrary-angle rotations around the three axes

$$\mathbf{X}^{\theta/\pi} = e^{-i\theta\hat{X}/2}, \quad \mathbf{Y}^{\theta/\pi} = e^{-i\theta\hat{Y}/2}, \quad \mathbf{Z}^{\theta/\pi} = e^{-i\theta\hat{Z}/2}. \quad (2.16ghi)$$

We implement rotations by an arbitrary angle around any axis in the X-Y plane by using physical microwave pulses. To see, how this can be implemented, we look back at the Hamiltonian (2.4). Although in the transmon limit the energy spectrum is independent of the static offset charge number n_e , we can still use it to couple to the qubit by applying microwave pulses resonant with the qubit transition frequency. Expanding the quadratic $4E_C(\hat{n} - n_e)^2$ term, we obtain the interaction term of the Hamiltonian $-8E_C n_e \hat{n} = -2e(C_e/C_\Sigma)V_e \hat{n}$. Considering the transmon limit $E_C \ll E_J$, restricting the Hamiltonian to the qubit subspace, and applying the rotating wave approximation for a voltage pulse $V_e(t) = \text{Re}\{V_0(t) \exp(-i\omega_Q t)\}$ with

a slowly varying envelope $V_0(t)$, we get the driven Hamiltonian

$$\hat{H} = -\hbar\omega_Q \frac{\hat{Z}}{2} + \hbar \left(\Omega(t) e^{-i\omega_Q t} \hat{\sigma}_+ + \Omega^*(t) e^{i\omega_Q t} \hat{\sigma}_- \right) / 2, \quad (2.17)$$

with $\Omega(t) = 2e(C_e/C_\Sigma)(E_J/32E_C)^{1/4}V_0(t)$ being the complex instantaneous Rabi frequency and $\hat{\sigma}_\pm = (\hat{X} \mp i\hat{Y})/2$ the qubit excitation creation and annihilation operators. In the frame rotating with the qubit, this Hamiltonian reduces to $\hbar \operatorname{Re}\{\Omega(t)\}\hat{X}/2 + \hbar \operatorname{Im}\{\Omega(t)\}\hat{Y}/2$, which corresponds exactly to rotations around the X and Y axes.

Because our two-qubit gate of choice, the CZ gate, commutes with the $Z^{\theta/\pi}$ rotations, and we measure the qubit in the \hat{Z} basis, we can implement the $Z^{\theta/\pi}$ rotations virtually, without applying any pulses [McKay17]. We do that by commuting all $Z^{\theta/\pi}$ rotations of the circuit to the subsequent measurement operation. The effect of commuting a $Z^{\theta/\pi}$ through a $X^{\xi/\pi}$ pulse is a change of the rotation axis of the $X^{\xi/\pi}$ gate by θ , as

$$e^{-i\xi\hat{X}/2} e^{-i\theta\hat{Z}/2} = e^{-i\theta\hat{Z}/2} e^{-i\xi(\cos(\theta)\hat{X} - \sin(\theta)\hat{Y})/2}. \quad (2.18)$$

In summary, we can implement any single-qubit unitary rotation with at-most one microwave pulse by decomposing the gate as $Z^{\alpha/\pi} X^{\beta/\pi} Z^{\gamma/\pi}$ and by choosing the angles α , β , and γ accordingly [Nielsen10].

2.4.2. Two-Qubit Operations

We choose the CZ gate as the native gate, the implementation of which we discuss below, into which we decompose the circuits we want to implement. We also encounter the iSWAP interaction in Section 4.5, which comes about systems interact resonantly under a $\hat{\sigma}_- \otimes \hat{\sigma}_+ + \text{c.t.}$ interaction Hamiltonian.

The unitaries for these two operations are given by

$$\text{CZ} = e^{-i\pi(\hat{Z}-\hat{I})\otimes(\hat{Z}-\hat{I})/4} = \begin{array}{c} \langle 00| \langle 01| \langle 10| \langle 11| \\ |00\rangle \\ |01\rangle \\ |10\rangle \\ |11\rangle \end{array} \begin{pmatrix} 1 & 0 & 0 & 0 \\ 0 & 1 & 0 & 0 \\ 0 & 0 & 1 & 0 \\ 0 & 0 & 0 & -1 \end{pmatrix}, \quad (2.19a)$$

$$\text{iSWAP} = e^{i\pi(\hat{X}\otimes\hat{X}+\hat{Y}\otimes\hat{Y})/4} = \begin{array}{c} \langle 00| \langle 01| \langle 10| \langle 11| \\ |00\rangle \\ |01\rangle \\ |10\rangle \\ |11\rangle \end{array} \begin{pmatrix} 1 & 0 & 0 & 0 \\ 0 & 0 & i & 0 \\ 0 & i & 0 & 0 \\ 0 & 0 & 0 & 1 \end{pmatrix}. \quad (2.19b)$$

To mediate interactions between neighboring qubits, we add a capacitively coupled section of CPW between them. This induces a $\hat{n}_1 \otimes \hat{n}_2$ interaction term in the Hamiltonian, which approximates to

$$\hat{V}/\hbar = J_{\text{QQ}}(\hat{b}_1\hat{b}_2^\dagger + \hat{b}_1^\dagger\hat{b}_2) \quad (2.20)$$

in the transmon regime $E_J \gg E_C$ under the rotating wave approximation $|\Delta_{11}| \ll \omega_{Q1}, \omega_{Q2}$. Here, the operator subscripts 1 and 2 correspond to the two transmons qubits, $\Delta_{kl} = \omega_{Q1} + (k-1)\alpha_1 - \omega_{Q2} - (l-1)\alpha_2$ is the detuning between the k -th and l -th transition of the two transmons, and the coupling rate J_{QQ} depends both on the coupling capacitances, the length of the CPW section, and the frequencies of the two qubits, see Section C.3 for more details.

To be able to control the interaction dynamically, we design our chip architecture such that, when not executing two-qubit gates, the neighboring qubits are operated at a large detuning $\Delta_{11} \gg J_{\text{QQ}}$. In this, dispersive regime, using second order perturbation theory, we find that the dominant effect of the interaction is a residual $\hat{Z} \otimes \hat{Z}$ interaction. That is, the k -th transition of the qubit is shifted by $\zeta^{(k,l)}$, when a neighboring qubit is in the l -th state (compared to being in the ground state). The relevant shifts

for our qubits, when considering the first two excited states, are given by

$$\zeta^{(1,1)} = 2J_{\text{QQ}}^2 \left(\frac{1}{\Delta_{12}} - \frac{1}{\Delta_{21}} \right), \quad (2.21a)$$

$$\zeta^{(2,1)} = J_{\text{QQ}}^2 \left(\frac{1}{\Delta_{11}} - \frac{2}{\Delta_{12}} - \frac{3}{\Delta_{31}} + \frac{4}{\Delta_{22}} \right), \quad (2.21b)$$

$$\zeta^{(1,2)} = J_{\text{QQ}}^2 \left(-\frac{1}{\Delta_{11}} + \frac{2}{\Delta_{12}} + \frac{3}{\Delta_{13}} - \frac{4}{\Delta_{22}} \right). \quad (2.21c)$$

On the other hand, if we bring the k -th and l -th transition into resonance under the interaction Hamiltonian (2.20), then the transitions transfer population at a rate $2\sqrt{kl}J_{\text{QQ}}$. We make use of the resonant interaction between the $|11\rangle$ and the $|20\rangle$ states, that is, the second and first transition of the two qubits are resonant, to implement the CZ gate. We bring the two states into resonance by using short sudden flux-bias pulses of duration $\tau = \pi/J_2$, where we denote the relevant coupling rate as $J_2 = \sqrt{2}J_{\text{QQ}}$, to induce a full population swap from the $|11\rangle$ state to the $|20\rangle$ state and back [Strauch03, DiCarlo10]. If we account for the possibility that the population recovered from the $|20\rangle$ state p_{11} can be less than one, we obtain the non-trace-preserving operation

$$\hat{U} = \begin{array}{c} \langle 00| \quad \langle 01| \quad \langle 10| \quad \langle 11| \\ \begin{array}{c} |00\rangle \\ |01\rangle \\ |10\rangle \\ |11\rangle \end{array} \end{array} \begin{pmatrix} 1 & 0 & 0 & 0 \\ 0 & e^{-i\phi_1} & 0 & 0 \\ 0 & 0 & e^{-i\phi_2} & 0 \\ 0 & 0 & 0 & \sqrt{p_{11}}e^{-i(\phi_1+\phi_2+\phi_c)} \end{pmatrix}. \quad (2.22)$$

In addition to inducing a conditional phase ϕ_c , the flux-bias pulse, which can be applied to either or both of the qubits, induces single-qubit phase rotations ϕ_1 and ϕ_2 , which can be easily corrected for with virtual $Z^{\phi/\pi}$ gates.

We qualitatively show the flux-bias pulse shape and the corresponding qubit frequency trajectory in Fig. 2.4(a). This unipolar pulse shape was used for the experiments presented in Sections 3.1 to 3.3. At the bottom of the panel, we show how the conditional phase ϕ_c and population recovery p_{11} depend on the two tuning parameters of such a gate, the detuning $\delta = \omega_{\text{Q1}} + \alpha_1 - \omega_{\text{Q2}}$ during interaction, and the pulse length τ . We observe a chevron landscape, with the target gate parameters being realized at $\delta = 0$ and $\tau = \pi/J_2$. While being simple to implement and fast to execute,

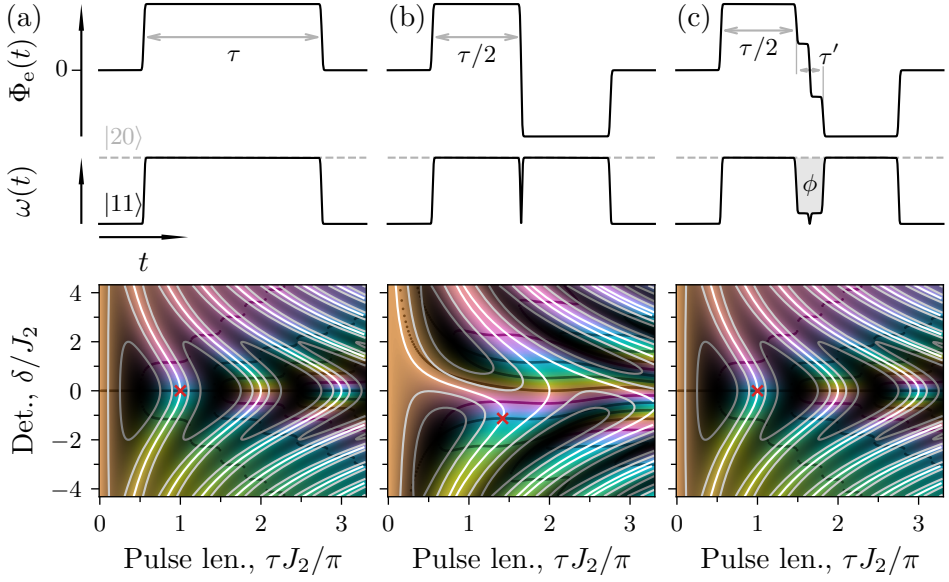


Figure 2.4: Two-qubit gate pulse shapes. (a) Unipolar pulse. (b) Not-phase-kick-controlled net-zero pulse. (c) Phase-kick-controlled net-zero pulse. For each pulse type, the shape of the applied flux pulse $\Phi_e(t)$ is shown in the first row, the trajectories of the qubit energy levels $\omega(t)$ in the second row and a map of conditional phase ϕ_c (as colors) and population recovery p_{11} (as lightness) as a function of pulse length τ and $|20\rangle$ - $|11\rangle$ detuning δ in the third row. $\phi_c = \{0, \pi/2, \pi, 3\pi/2\}$ are marked with dark contour lines in orange, green, blue and pink, respectively. For population recovery, contour lines are drawn at $p_{11} = \{1, 0.9, 0.5\}$. The red crosses mark the target point, where $\phi_c = \pi$ and $p_{11} = 1$.

this pulse shape has a few downsides. In particular, it is sensitive to low-frequency flux noise, which can shift the idling flux-bias point. While the flux noise does not have a detrimental effect when the qubit is biased at its flux-insensitive frequency, a small flux offset $\Delta\Phi$ leads to a proportional conditional phase error. Furthermore, to generate the flux-bias pulse, an arbitrary waveform generator (AWG) needs to be connected to the flux line, which has significantly larger noise compared to a direct current source. To mitigate dephasing of the qubit due to the low-frequency noise of the AWG, we combine a static flux bias, generated by a low-noise current source, with dynamic pulses, generated by the AWG, using a microwave bias tee. The high-pass characteristic of the bias tee, while filtering the low-frequency noise of the AWG, requires us to apply ever-larger outputs from the AWG with every consecutive dc flux pulse.

To overcome these two issues we moved to a net-zero pulse shape for the experiments presented in Sections 3.4 to 3.6, see top rows of Fig. 2.4(b). The pulse consists of two square halves with equal amplitudes but opposite signs. The net-zero pulse shape does not have a dc component, and therefore the pulse distortions due to the bias tee do not accumulate over multiple pulses. We find that the conditional phase ϕ_c and population recovery p_{11} landscape has changed, see the bottom row of Fig. 2.4(b). The landscape is not symmetric with respect to the detuning δ , and the best gate fidelity is achieved at pulse lengths $\tau > J_2/\pi$. The asymmetry is due to a phase kick ϕ of the $|20\rangle$ state with respect to the $|11\rangle$ state due to the finite rise and fall times of the pulse when transitioning from the first half of the pulse to the second.

To take advantage of this phase kick as a control parameter, we introduce a finite length τ' between the two halves of the net-zero pulse, which we use to control the phase kick by tuning either the duration τ' or the pulse amplitude during this time. By setting the phase kick to a suitable value, we can recover the symmetric shape of the conditional phase ϕ_c and population recovery p_{11} landscape, reducing the gate time and facilitating tuneup, see Fig. 2.4(c). Similar pulse shapes were independently developed at the same time in Ref. [Negîrneac21].

We introduce a simple model to analyze how the phase-kick-controlled net-zero gate works. The subspace of the two-qubit Hamiltonian (2.5) with

the interaction term (2.20) relevant for the dynamics is given by

$$\hat{H}(t)/\hbar = \begin{array}{c} \langle 00| \\ \langle 01| \\ \langle 10| \\ \langle 11| \\ \langle 20| \end{array} \begin{pmatrix} \langle 00| & \langle 01| & \langle 10| & \langle 11| & \langle 20| \\ 0 & 0 & 0 & 0 & 0 \\ 0 & \omega_{Q1}(t) & J_{QQ} & 0 & 0 \\ 0 & J_{QQ} & \omega_{Q2}(t) & 0 & 0 \\ 0 & 0 & 0 & \omega_{Q1}(t) + \omega_{Q2}(t) & J_2 \\ 0 & 0 & 0 & J_2 & 2\omega_{Q1}(t) + \alpha_1 \end{pmatrix} \quad (2.23)$$

If the detuning between the qubit frequencies remains large during the interaction $J_{QQ}/|\Delta_{11}(t)| \ll 1$, then we can ignore the coupling in the single-qubit subspace J_{QQ} , which will only lead to additional conditional phase due to the dispersive coupling strength $\zeta^{(1,1)}$, see Eq. (2.21a). We analyze the magnitude of the swap errors due to this coupling in Appendix B. Furthermore, by transforming the Hamiltonian to a reference frame that co-rotates with the single-qubit subspace using the unitary

$$\hat{U} = e^{i \int_{-\infty}^t dt \text{diag}(0, \omega_{Q1}(t), \omega_{Q2}(t), \omega_{Q1}(t) + \omega_{Q2}(t), \omega_{Q1}(t) + \omega_{Q2}(t))}, \quad (2.24)$$

with $\text{diag}(\cdot)$ representing a matrix with the given values on the diagonal, we are left with the effective Hamiltonian

$$\hat{H}' = \hat{U} \hat{H} \hat{U}^\dagger + i\hbar \frac{\partial \hat{U}}{\partial t} \hat{U}^\dagger = \hbar \delta(t) |20\rangle\langle 20| + \hbar J_2 (|20\rangle\langle 11| + |11\rangle\langle 20|), \quad (2.25)$$

with $\delta(t) = \omega_{Q1}(t) + \alpha_1 - \omega_{Q2}(t)$. By expressing the evolution operator for the Hamiltonian (2.25) in the form of Eq. (2.22), we find that ϕ_c and p_{11} can be calculated as the negative of the argument and modulus squared of the complex $|11\rangle$ amplitude

$$c_{11} = \langle 11| e^{-i\hat{H}'t/\hbar} |11\rangle, \quad \phi_c = -\arg(c_{11}), \quad p_{11} = |c_{11}|^2. \quad (2.26)$$

Equations (2.25) and (2.26) provide us with a simple framework to calculate the conditional phase for a given pulse shape. In the simplest case, for a pulse of duration τ and constant detuning δ , the unitary for the evolution is given by

$$\hat{U}(\tau, \delta) = e^{-i\delta\tau/2} \left(\hat{I} \cos(\tilde{J}\tau) + i \left(\frac{\delta}{2\tilde{J}} \hat{Z} - \frac{J_2}{\tilde{J}} \hat{X} \right) \sin(\tilde{J}\tau) \right), \quad (2.27)$$

where we have defined the effective coupling rate $\tilde{J} = \sqrt{J_2^2 + \delta^2/4}$, and the Pauli matrices act on the $|11\rangle$ - $|20\rangle$ subspace, $\hat{Z} = |11\rangle\langle 11| - |20\rangle\langle 20|$ and $\hat{X} = |11\rangle\langle 20| + |20\rangle\langle 11|$. Therefore, for the unipolar pulse shape we have $c_{11} = e^{-i\delta\tau/2}(\cos(\tilde{J}\tau) + i\delta \sin(\tilde{J}\tau)/2\tilde{J})$, the negative argument and modulus squared of which are visualized in Fig. 2.4(a).

For the net-zero pulse shape, we need to account for the phase kick at the middle of the pulse $\phi \approx \int dt \delta(t)$, which can be modeled for sudden pulses as an instantaneous phase change of the $|20\rangle$ state $\hat{U}_\phi = |11\rangle\langle 11| + e^{-i\phi} |20\rangle\langle 20|$. We also consider that the detunings during the two pulse halves can be different by an amount Δ , see Fig. 2.5(a,b). In this case, the probability amplitude is given by

$$\begin{aligned} c_{11} &= \langle 11 | \hat{U}\left(\frac{\tau}{2}, \bar{\delta} - \frac{\Delta}{2}\right) \hat{U}_\phi \hat{U}\left(\frac{\tau}{2}, \bar{\delta} + \frac{\Delta}{2}\right) | 11 \rangle \\ &= \left(\cos\left(\frac{\tilde{J}^+\tau}{2} - i \operatorname{arcsinh}\left(\frac{2\bar{\delta} + \Delta}{4J_2}\right)\right) \cos\left(\frac{\tilde{J}^-\tau}{2} - i \operatorname{arcsinh}\left(\frac{2\bar{\delta} - \Delta}{4J_2}\right)\right) \right. \\ &\quad \left. - e^{-i\phi} \sin\left(\frac{\tilde{J}^+\tau}{2}\right) \sin\left(\frac{\tilde{J}^-\tau}{2}\right) \right) \frac{J_2^2}{\tilde{J}^+ \tilde{J}^-} e^{-i\bar{\delta}\tau/2}, \end{aligned} \quad (2.28)$$

where $\tilde{J}^\pm = \sqrt{J_2^2 + (2\bar{\delta} \pm \Delta)^2/16}$ are the effective couplings during the two halves of the pulse and $\operatorname{arcsinh}(\cdot)$ is the inverse of the hyperbolic sine function. For $\Delta = 0$, $\phi = 0$ this equation reduces to the one for the unipolar pulse, shown also in Fig. 2.4(c).

We show the conditional phase ϕ_c and population recovery p_{11} of the phase-kick-controlled net-zero gate as a function of the phase kick ϕ and pulse duration τ for various detunings in Fig. 2.5(c-e). If the detunings during the two pulse halves are accurately calibrated $\bar{\delta} = \Delta = 0$, then the optimization of the two gate parameters becomes orthogonal in the two control parameters around the optimum, with ϕ controlling only ϕ_c and τ controlling only p_{11} see panel (c). This allows for a fast tuneup of the gate by the means of one-dimensional parameter sweeps. However, even if the mean detuning $\bar{\delta}$, which is determined by the flux pulse amplitude, is miscalibrated, an error-free CZ gate can be implemented, albeit at a slightly longer gate duration, see panel (d). A change in the qubit's flux-bias offset will not lead to a change in the mean detuning $\bar{\delta}$, but in the difference of the detunings Δ , which will lead to population loss, see Fig. 2.5(e). However, population loss, given by $1 - p_{11} \approx \Delta^2/4J_2^2$ for small Δ , is first order

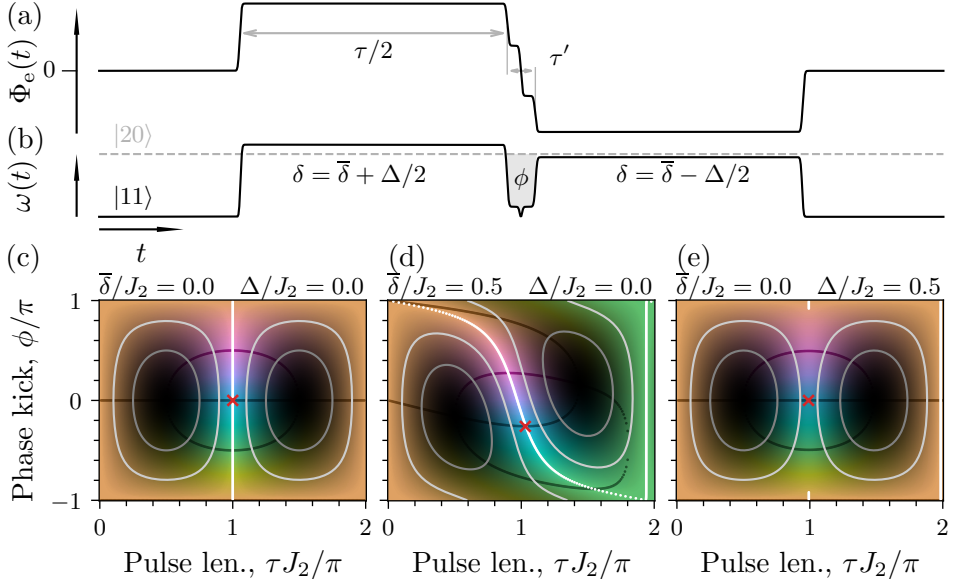


Figure 2.5: Phase-kick-controlled gate. (a) The applied flux pulse shape. (b) Trajectory of the qubit energy levels $\omega(t)$. (c–e) Map of conditional phase ϕ_c (as colors) and population recovery p_{11} (as lightness) as a function of the phase kick ϕ and pulse length τ for various values of mean detuning $\bar{\delta}$ and detuning difference Δ . $\phi_c = \{0, \pi/2, \pi, 3\pi/2\}$ are marked with dark contour lines in orange, green, blue and pink, respectively. For population recovery, contour lines are drawn at $p_{11} = \{1, 0.9, 0.5\}$. The red crosses mark the highest-fidelity point, where $\phi_c = \pi$ and $p_{11} = 1$, 1, and 0.94 in panels (c), (d), and (e), respectively.

insensitive with respect to variations in Δ .

For experimental characterization of the phase-kick-controlled net-zero gate, see Ref. [Kerschbaum20].

2.5. Measurement Setup

Finally, we discuss how we mount the quantum device for measurements and how we send all the control signals to it. The device should be cooled to temperatures low enough that the residual excitations do not lead to excessive energy relaxation and dephasing of the qubit. Furthermore, the temperature should be low enough for the circuit to be superconducting. For example, a readout resonator's thermal population, given by the Bose-Einstein statistics $\bar{n}_{\text{th}} = 1/(e^{\hbar\omega_{\text{R}}/k_{\text{B}}T} - 1)$, leads to dephasing of the qubit at a rate $\gamma_{\phi} = \bar{n}_{\text{th}}\kappa_{\text{R}}\chi^2/(\kappa_{\text{R}}^2/4 + \chi^2)$, where ω_{R} is the resonator frequency, κ_{R} its linewidth, and χ the dispersive shift [Gambetta06]. For typical parameters of $\omega_{\text{R}}/2\pi = 7.5$ GHz, $\kappa_{\text{R}}/2\pi = 10$ MHz, and $\chi/2\pi = 5$ MHz, to achieve dephasing times $1/\gamma_{\phi} > 1$ ms, we need the resonator temperature to be below $T < 38$ mK.

To achieve such low temperatures, we use a closed-cycle $^3\text{He}/^4\text{He}$ dilution refrigerator, pre-cooled to 4 K using a pulse tube cryocooler. We mount the superconducting quantum device at the base temperature stage of the dilution refrigerator, which achieves temperatures around 10 mK, see Fig. 2.6(a). The device is enclosed in a copper package, which is a good thermal conductor, allowing it to thermalize well with the cryostat. Furthermore, it is enclosed in a set of magnetic shields to reduce external magnetic field noise. The electronic control signals are routed to the device through coaxial cables, which are filtered and attenuated at various temperature stages of the cryostat to reduce room-temperature noise [Krinner19]. The output signals are filtered and amplified using a traveling-wave parametric amplifier (TWPA) and a high-electron-mobility transistor (HEMT) amplifier. The detailed cabling diagrams for each of the experiments presented in Chapters 3 to 6 are presented in the corresponding publications [Andersen19, Andersen20, Krinner22, Remm23b, Remm23a]. We use a carrier-circuit-board inside the copper mount to route the signals to and from the coaxial cables to the millimeter-sized superconducting quantum device, see Fig. 2.6(b). The connection between the circuit board and the quantum chip is done using aluminum bond wires, see Fig. 2.6(c).

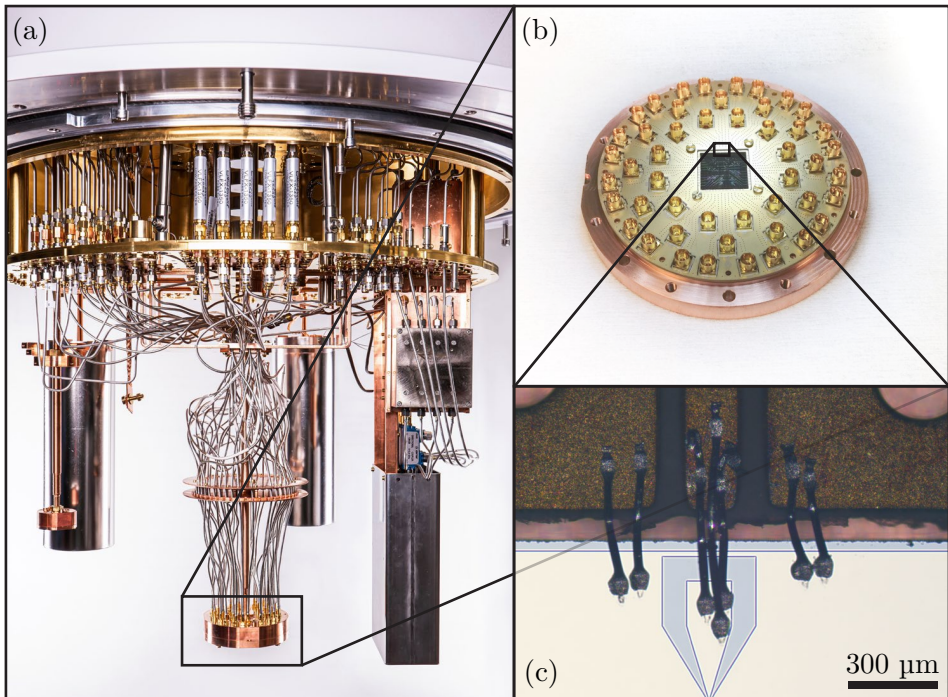


Figure 2.6: Quantum device mounting. (a) The base-temperature stage of a dilution refrigerator. Several sample holders with and without magnetic shielding are attached, as well as the traveling-wave parametric amplifiers with their related circuitry on the right. Photo by Octavian Lazăr. (b) A 17-qubit device is mounted to the copper sample holder. The signals are routed to the chip on a carrier circuit board with SMP connectors. (c) Connections between the chip and the printed circuit board are made using aluminum bond wires.

Preliminary Surface Code Experiments

As discussed in Chapter 1, the central component for the operation of a surface code is the stabilizer measurement. The individual stabilizer measurements of the code, which are usually executed at the same time, can be divided into two parts. First, the parity of neighboring data qubits is mapped onto an auxiliary qubit using single-qubit gates and entangling two-qubit gates. Then, the state of the auxiliary qubit is measured with minimal disturbance to the data qubits. This chapter presents two experiments that demonstrate these building blocks, although they do not yet reach the scale required for quantum error correction. In the first experiment, see Sections 3.1 to 3.3, we repeatedly measure the $\hat{X}_{D1}\hat{X}_{D2}$ and $\hat{Z}_{D1}\hat{Z}_{D2}$ parities of two data qubits D1 and D2 using an auxiliary qubit A, which projects the data qubits into a Bell state [Andersen19]. By applying single-qubit gates conditioned on the measurement outcomes, we stabilize the data qubits in the $|\Phi^+\rangle$ Bell state. In the second experiment, see Sections 3.4 to 3.6, we implement a distance $d = 2$ surface code using four data qubits D1 to D4 and three auxiliary qubits Z1, Z2, and X [Andersen20]. The small code distance only allows for error detection, not for correction by identifying of the effect on the logical operators based on the syndrome. We conclude the chapter with a discussion of the results and an outlook in Section 3.7.

3.1. Entanglement Stabilization: Concept

A pure state of two data qubits D1 and D2 can be written as a superposition of the orthogonal Bell states $|\Phi^+\rangle$, $|\Psi^+\rangle$, $|\Phi^-\rangle$, and $|\Psi^-\rangle$. These states correspond to the mutual $(+1, +1)$, $(+1, -1)$, $(-1, +1)$, and $(-1, -1)$ eigenstates of the $\hat{X}_{D1}\hat{X}_{D2}$ and $\hat{Z}_{D1}\hat{Z}_{D2}$ operators, respectively, see Fig. 3.1(a). In this experiment, we aim to stabilize the $|\Phi^+\rangle$ state by repeatedly measuring

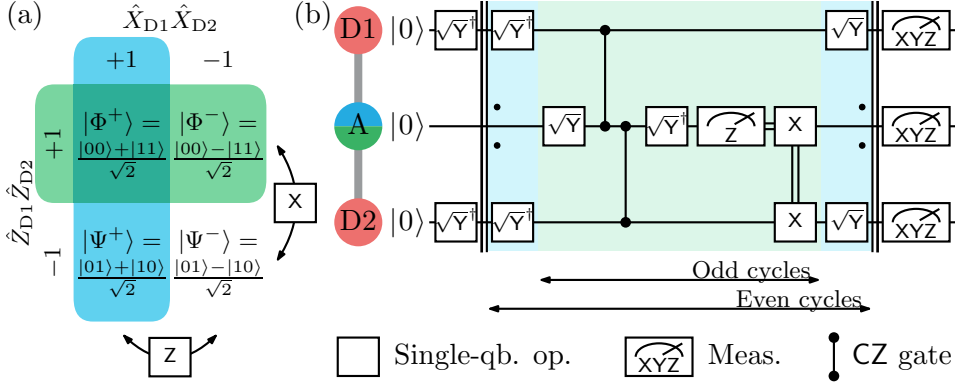


Figure 3.1: Entanglement stabilization concept and circuit. (a) Diagram of the Bell states as the mutual eigenstates of the $\hat{X}_{D1}\hat{X}_{D2}$ and $\hat{Z}_{D1}\hat{Z}_{D2}$ operators. The eigenvalues can be flipped using Z and X gates on either of the data qubits, respectively, as indicated. (b) The circuit diagram for repeated $|\Phi^+\rangle$ state stabilization. The double circuit line indicates classical feedback conditioned on the measurement outcome being $|1\rangle$. The repetition bars indicate that the stabilization circuit can be repeated for multiple cycles, alternating between $\hat{Z}_{D1}\hat{Z}_{D2}$ (green background) and $\hat{X}_{D1}\hat{X}_{D2}$ (blue and green backgrounds) stabilization.

the $\hat{X}_{D1}\hat{X}_{D2}$ and $\hat{Z}_{D1}\hat{Z}_{D2}$ operators using the auxiliary qubit A. If the measurement outcome for $\hat{X}_{D1}\hat{X}_{D2}$ or $\hat{Z}_{D1}\hat{Z}_{D2}$ is -1 , we apply a \hat{Z}_{D2} or \hat{X}_{D2} operation, respectively.

We initiate the experimental sequence, see Fig. 3.1(b), by preparing the data qubits in their thermal ground state and then applying \sqrt{Y}^\dagger gates to create an two-qubit equal superposition state $|--\rangle$. The $|--\rangle$ state is a $+1$ eigenstate of the $\hat{X}_{D1}\hat{X}_{D2}$ operator, but not an eigenstate of the $\hat{Z}_{D1}\hat{Z}_{D2}$ operator. Next, we perform a $\hat{Z}_{D1}\hat{Z}_{D2}$ measurement which projects the qubits into either the $|\Phi^+\rangle$ or the $|\Psi^+\rangle$ state depending on the outcome, $+1$ or -1 , respectively. To implement the $\hat{Z}_{D1}\hat{Z}_{D2}$ measurement, we prepare the auxiliary qubit in the $|+\rangle$ state with a \sqrt{Y} gate and apply CZ gates between A-D1 and A-D2. Each CZ gate flips the phase of the auxiliary qubit if the corresponding data qubit is in the $|1\rangle$ state. Finally, the auxiliary qubit is rotated back to the original basis using a \sqrt{Y}^\dagger gate and measured. If the data qubits were in the $|00\rangle$ or $|11\rangle$ state ($\hat{Z}_{D1}\hat{Z}_{D2} = +1$), the auxiliary

qubit is flipped zero or two times, respectively, leaving it in the $|0\rangle$ state for the readout. For the data qubit states $|01\rangle$ and $|10\rangle$ ($\hat{Z}_{D1}\hat{Z}_{D2} = -1$), the auxiliary qubit phase is flipped once, leaving it in the $|1\rangle$ state for the readout. In case the measurement outcome is $|1\rangle$, indicating an odd parity of the data qubits, we apply feedback X gates on A and D2 to reset the auxiliary qubit back into its ground state and flip the parity of the data qubits.

To measure and stabilize the $\hat{X}_{D1}\hat{X}_{D2}$ operator instead of $\hat{Z}_{D1}\hat{Z}_{D2}$, we apply \sqrt{Y}^\dagger gates on the data qubits before the parity mapping circuit, which converts $\hat{X}_{D1}\hat{X}_{D2}$ to $\hat{Z}_{D1}\hat{Z}_{D2}$. After the feedback operation, we rotate back to the original basis using \sqrt{Y} gates. To stabilize the $|\Phi^+\rangle$ state over multiple cycles, we alternate between stabilizing the $\hat{Z}_{D1}\hat{Z}_{D2}$ operator during odd cycles and the $\hat{X}_{D1}\hat{X}_{D2}$ operator during even cycles.

3.2. Entanglement Stabilization: Device

We implement the protocol on a four-transmon-qubit processor, shown in Fig. 3.2, utilizing three qubits for our purposes. The device is fabricated using a thin niobium film on a silicon substrate, with Josephson junctions made of aluminum and aluminum oxide, as well as aluminum-titanium-aluminum trilayer airbridges, following our standard recipe, see Ref. [Andersen19] for details. Each of the qubits (highlighted in yellow) is connected to its individual microwave drive (pink) and flux control (green) lines, as well as individual readout resonators (red). Additionally, each readout resonator is coupled to the common feedline (purple) through individual Purcell filters (blue), which help suppress qubit decay via the readout resonators and minimize data qubit dephasing due to auxiliary qubit readout [Heinsoo18]. Two-qubit interactions between neighboring qubits are mediated by capacitively coupled resonators (cyan) with an impedance of $80\ \Omega$ at the ends to increase the coupling rate to the qubits, see Section C.3. The rest of the coplanar waveguide elements on the device are designed with an impedance of $50\ \Omega$.

While A has a fixed frequency on this device due to a junction fabrication defect, qubits D1 and D2 are flux-tunable with a junction size asymmetry of 1:8, and are biased to their maximum and minimum frequencies, respectively, see Table 3.1 for the values. The qubits have a charging energy 242 MHz, energy relaxation times between $13.7\ \mu\text{s}$ and $23.4\ \mu\text{s}$, and echo decay times

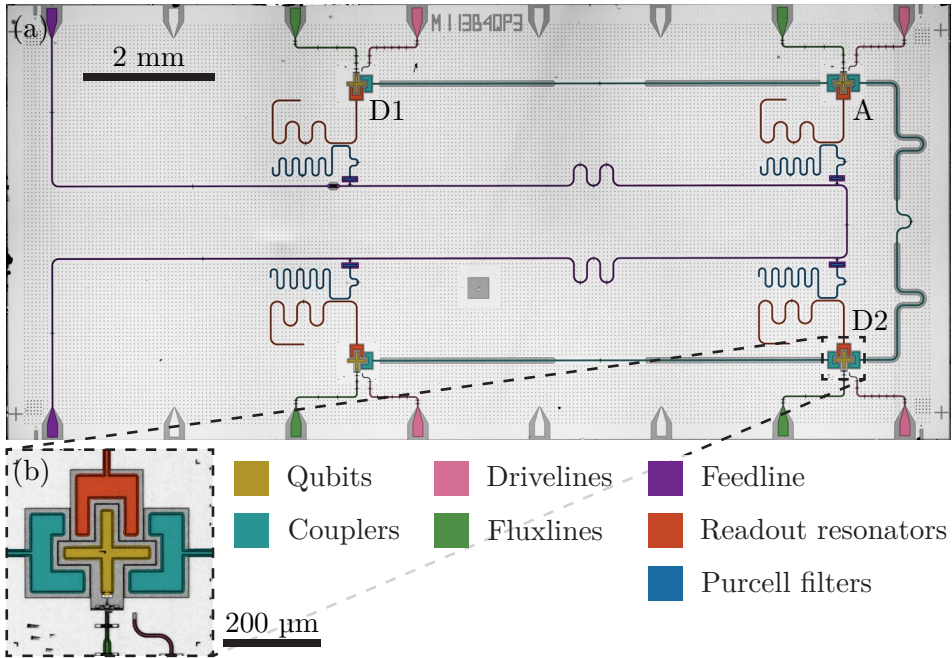


Figure 3.2: Entanglement stabilization device. (a) Full-view false-color micrograph of the 14.3 mm \times 6.6 mm device used for the entanglement stabilization experiment. See main text for a description of the components. (b) Zoom-in of the qubit D2.

between 11.2 μ s and 12.5 μ s. For single-qubit gates, we employ 50-ns-long truncated Gaussian microwave pulses of width $\sigma = 10$ ns. These pulses utilize the derivative removal by adiabatic gate (DRAG) technique [Motzoi09, Gambetta11]. The average single-qubit gate error [Bowdrey02], as characterized by randomized benchmarking, is $\varepsilon_{1i} = 0.31\%$ [Magesan11, Epstein14]. Two-qubit gates are implemented using unipolar flux pulses applied to D1 and D2 to bring the $|11\rangle$ state into resonance with the $|20\rangle$ state of the A-D system [Strauch03, DiCarlo10]. The length of the pulses is approximately 100 ns, with 40-ns-long buffer times before and after the pulse. To compensate for flux pulse distortion caused by the bias tee in the flux line, we pre-distort the generated flux waveforms using the inverse of an in-situ-measured step response. The average gate error [Bowdrey02] for the two CZ gates, characterized by process tomography [Nielsen10], is

Table 3.1: Entanglement stabilization device parameters. Single-qubit parameters and qubit-pair parameters are given in the top and bottom half of the table, respectively.

	D1	A	D2
Qubit frequency, $\omega_Q/2\pi$ (GHz)	5.72	5.21	4.88
Energy relaxation time, T_1 (μs)	19.7	13.7	23.4
Ramsey decay time, T_2^* (μs)	12.5	11.7	11.2
Echo decay time, T_2^e (μs)	22.4	14.5	15.0
Dispersive shift, $\chi/2\pi$ (MHz)	-3.9	-1.6	-1.8
Readout pulse frequency, $\omega_r/2\pi$ (GHz)	6.89	7.09	6.69
Readout mode linewidth, $\kappa_{R'}/2\pi$ (MHz)	3.0	2.1	1.7
Purcell filter linewidth, $\kappa_P/2\pi$ (MHz)	27.2	34.7	10.7
Purcell-readout coupling, $J_{PR}/2\pi$ (MHz)	10.9	8.2	9.5
Purcell-readout detuning, $\Delta_{PR}/2\pi$ (MHz)	29.5	27.5	19.4
Thermal population, p_{th} (%)	0.9	1.4	1.4
Individual readout error, ε_{ri} (%)	0.8	1.3	0.9
Multiplexed readout error, ε_{rm} (%)	1.3	1.1	0.9
Individual single-qubit gate error, ε_{li} (%)	0.30	0.31	0.33
Coupling resonator frequency, ω_C (GHz)	7.45	7.48	
Resonant qb.-qb. coupl., $J_{QQ}/2\pi$ (MHz)	3.8	3.4	
Individual CZ gate error, ε_{2i} (%)	1.0	0.5	
Dispersive qb.-qb. coupling, $\zeta/2\pi$ (MHz)	-0.11	-0.37	

$\varepsilon_{2i} = 0.7\%$.

The qubit state is read out using a 200-ns-long pulse and a 400-ns-long integration time. For both individual and simultaneous readout of all qubits, the average readout error is approximately 1%. Furthermore, we find that the readout of the auxiliary qubit induces a stochastic phase flip in a data qubit with a probability of less than 0.3%. However, we observe deterministic phase shifts of 0.583 rad and 0.579 rad on qubits D1 and D2, respectively, which we correct with virtual $Z^{\theta/\pi}$ gates. We attribute these phase shifts to frequency shifts of the data qubits caused by off-resonant drive by the readout pulse that is mediated by the coupling resonators. The delay from the end of the integration until the feedback pulse is applied is 600 ns, primarily

due to classical signal processing and pulse generation delays. To mitigate dephasing resulting from low-frequency noise, we employ a four-pulse Carr-Purcell-Meiboom-Gill [Carr54, Meiboom58] dynamical decoupling sequence on the data qubits during this waiting time. Considering the durations of the single and two-qubit gates, measurement, and feedback delay, the total cycle duration amounts to $T_{\text{cyc.}} = 1.51 \mu\text{s}$.

3.3. Entanglement Stabilization: Results

We verify the performance of a single stabilizer measurement operation, starting with the parity map only. For this, we perform state tomography on the three-qubit coherent state before the first readout of the auxiliary qubit. The obtained readout-error-compensated state fidelity is $F = 94.2\%$ relative to the target state $(|0\rangle_A |\Phi^+\rangle_{D1,D2} + |1\rangle_A |\Psi^+\rangle_{D1,D2})/\sqrt{2}$. The full three-qubit density matrix $\hat{\rho} = \sum_{\hat{P}} \langle \hat{P} \rangle \hat{P}/d$ is represented in Fig. 3.3(a) in terms of the expectation values of the Pauli operators $\langle \hat{P} \rangle$, with $d = 2^3$ being the dimension of the Hilbert space and the summation being over all products \hat{P} of Pauli matrices (including the identity operator) on three qubits. This high fidelity indicates that the circuit accurately maps the $\hat{Z}_{D1}\hat{Z}_{D2}$ parity of the data qubits to the auxiliary qubit without destroying the $\hat{X}_{D1}\hat{X}_{D2}$ coherence of the initial state. By appending the auxiliary qubit readout to the parity map, we complete the stabilizer measurement circuit. When postselecting for the auxiliary qubit outcome of $|0\rangle_A$, data qubit state tomography yields a high fidelity of $F = 93.8\%$ to the target state $|\Phi^+\rangle$, see Fig. 3.3(b). Here, data qubit tomography was performed in parallel with the auxiliary qubit readout. Similarly, when postselecting on $|1\rangle_A$, the fidelity to the $|\Psi^+\rangle$ state is $F = 92.9\%$, see Fig. 3.3(c). To make the $\hat{Z}_{D1}\hat{Z}_{D2} = +1$ stabilization deterministic, we introduce a feedback pulse on D2 for the $|1\rangle_A$ auxiliary qubit outcome. This reduces the fidelity of the data qubit state to $F = 86.7\%$, primarily due to decoherence during the feedback delay time, see Fig. 3.3(d). Finally, we add a cycle of $\hat{X}_{D1}\hat{X}_{D2} = +1$ stabilization after the $\hat{Z}_{D1}\hat{Z}_{D2} = +1$ stabilization, which can correct for phase flip errors in the stabilized Bell state. Since the data qubits are initially prepared in the $|--\rangle$ state, the $\hat{X}_{D1}\hat{X}_{D2}$ value is already close to $+1$ after one cycle of $\hat{Z}_{D1}\hat{Z}_{D2} = +1$ stabilization. As a result of additional decoherence, the fidelity is reduced to $F = 74.5\%$ after the additional $\hat{X}_{D1}\hat{X}_{D2} = +1$ stabilization cycle.

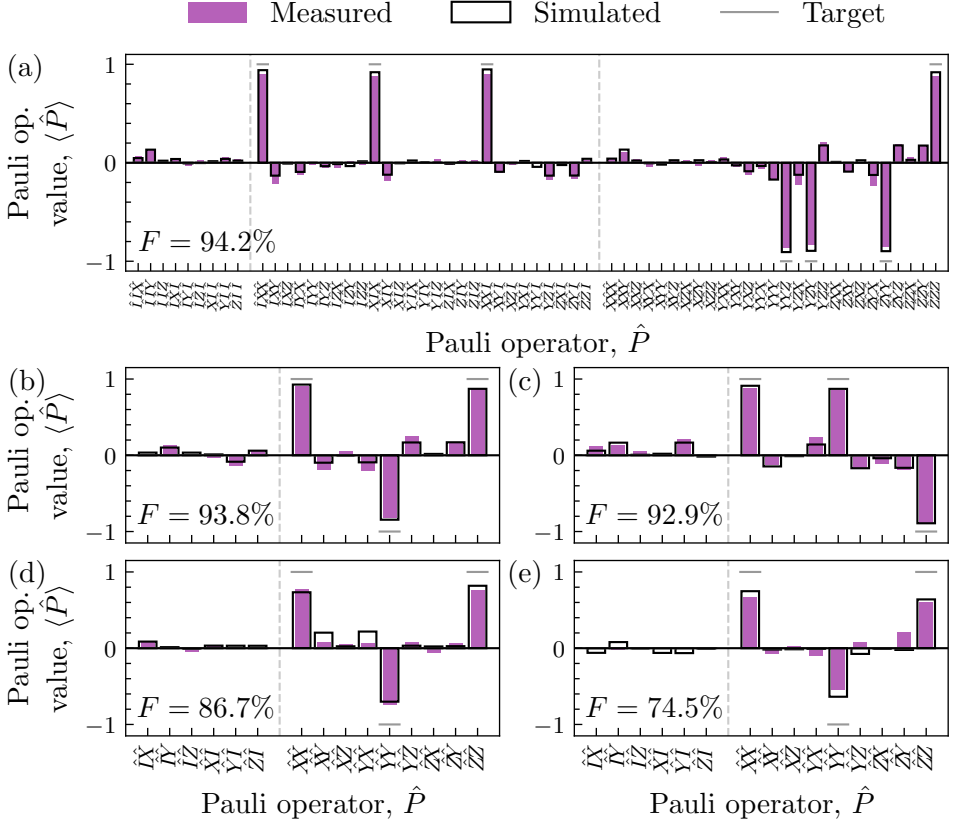


Figure 3.3: Entanglement stabilization initialization. (a) Expectation values of Pauli operators of the three-qubit coherent state before the first auxiliary qubit readout. (b) Expectation values of Pauli operators of the data qubits conditioned on A in $|0\rangle$ and (c) in $|1\rangle$. (d) Deterministic expectation values of Pauli operators of the data qubits after a single round of $\hat{Z}_{D1}\hat{Z}_{D2}$ stabilizer correction and (e) after $\hat{Z}_{D1}\hat{Z}_{D2}$ and $\hat{X}_{D1}\hat{X}_{D2}$ stabilizer correction.

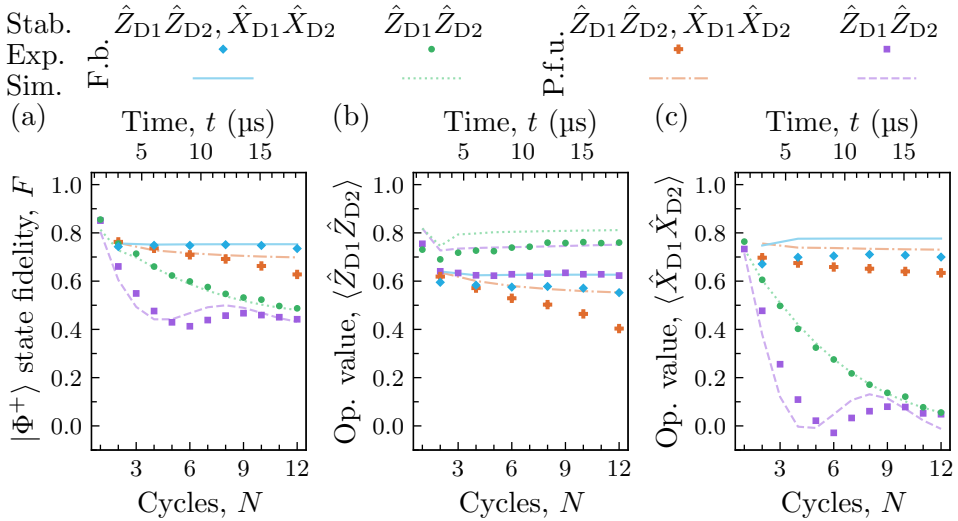


Figure 3.4: Repeated entanglement stabilization. (a) The $|\Phi^+\rangle$ Bell state fidelity, (b) $\hat{Z}_{D1}\hat{Z}_{D2}$ expectation value, and (c) $\hat{X}_{D1}\hat{X}_{D2}$ expectation value after N cycles of entanglement stabilization. The different traces indicate whether only $\hat{Z}_{D1}\hat{Z}_{D2}$ is stabilized or both $\hat{Z}_{D1}\hat{Z}_{D2}$ and $\hat{X}_{D1}\hat{X}_{D2}$ are stabilized, alternating every cycle. Stabilization using active feedback (f.b.) on D2 and Pauli frame updating (P.f.u.) are compared.

To be useful for quantum error correction, the stabilizer measurement needs to maintain a low error rate over many cycles. To demonstrate that in our implementation, we repeat the $\hat{Z}_{D1}\hat{Z}_{D2} = +1$ and $\hat{X}_{D1}\hat{X}_{D2} = +1$ stabilization for N cycles. After completing the stabilization cycles, we conduct data qubit state tomography to determine the fidelity to the $|\Phi^+\rangle$ state and to measure the $\hat{Z}_{D1}\hat{Z}_{D2}$ and $\hat{X}_{D1}\hat{X}_{D2}$ values. We observe that the fidelity and the stabilizer values remain constant for up to $N = 12$ cycles, which is the maximum number of cycles tested, see blue points in Fig. 3.4. The stable and good performance over many cycles indicates that the circuit is performing as intended, without significant accumulation of leakage or errors on the data qubits. In contrast, when only stabilizing $\hat{Z}_{D1}\hat{Z}_{D2} = +1$, then the $\hat{Z}_{D1}\hat{Z}_{D2}$ expectation value remains constant, but the $\hat{X}_{D1}\hat{X}_{D2}$ value decays exponentially toward zero, leading to a decrease in the state fidelity, see the green points.

In large-scale quantum error correction experiments, it is not necessary to correct the detected errors after every cycle. Instead, a strategy called Pauli frame updating can be employed, where errors are tracked and measurement outcomes are reinterpreted accordingly [Knill05]. We implement the Pauli frame updating strategy for both $\hat{Z}_{D1}\hat{Z}_{D2} = +1$ and $\hat{X}_{D1}\hat{X}_{D2} = +1$ stabilization, see orange points in Fig. 3.9, as well as for $\hat{Z}_{D1}\hat{Z}_{D2} = +1$ only stabilization, see purple points, while keeping the reset pulse on A. In both cases the fidelity is reduced compared to the implementation with active feedback, which we attribute to the asymmetry of the qubit relaxation channel and readout errors. With Pauli frame updating, the auxiliary qubit spends more time in the $|1\rangle_A$ state compared to the feedback-based data qubit state correction, and therefore suffers more bit flip errors. Furthermore, when stabilizing only $\hat{Z}_{D1}\hat{Z}_{D2} = +1$, we observe a decaying oscillation in the $\hat{X}_{D1}\hat{X}_{D2}$ value, see Fig. 3.4(c). This behavior is expected due to an accumulation of phase errors on the data qubits due to dispersive qubit-qubit coupling, see Table 3.1. All experimental results are accurately reproduced by master equation simulations that consider independently characterized qubit relaxation and dephasing rates, dispersive qubit-qubit couplings, and readout errors, see the lines in Fig. 3.4. This indicates that the contributions of crosstalk and control errors are insignificant compared to the accounted-for error mechanisms.

3.4. Quantum Error Detection: Concept

Having demonstrated that we can execute high-fidelity weight-two stabilizer measurements over many cycles, we aim to assess the performance of the stabilizer measurements on a larger system. For this, we implement the smallest nontrivial surface code, a distance $d = 2$ code consisting of four data qubits, D1 to D4, and three stabilizers

$$\hat{S}_{Z1} = \hat{Z}_{D1}\hat{Z}_{D3}, \quad \hat{S}_X = \hat{X}_{D1}\hat{X}_{D2}\hat{X}_{D3}\hat{X}_{D4}, \quad \hat{S}_{Z2} = \hat{Z}_{D2}\hat{Z}_{D4}. \quad (3.1)$$

The layout of this code is depicted in Fig. 3.5(a). We define the logical Pauli operators as

$$\hat{X}_L = \hat{X}_{D1}\hat{X}_{D3} \quad \text{and} \quad \hat{Z}_L = \hat{Z}_{D1}\hat{Z}_{D2}, \quad (3.2)$$

which commute with all the stabilizers and anticommute with each other. It is worth noting that equivalent choices of logical operators can be obtained by multiplying the logical operators by any stabilizers, as the commutation and

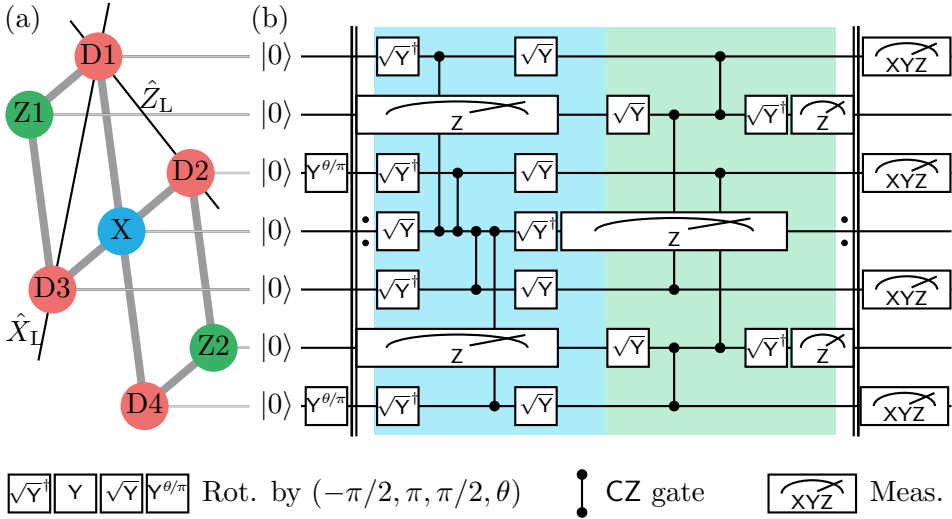


Figure 3.5: Error detection code layout and circuit. (a) Layout of the data qubits (red) and X- (blue) and Z-type (green) auxiliary qubits, and the physical couplings between them as thick gray lines. The support of the logical operators is indicated as black lines. (b) Error detection circuit that is repeated for N cycles. The parts of the circuit with the blue and green background correspond to X-type and Z-type stabilizer parity maps, respectively. The X-type auxiliary qubit readout is done during the Z-type stabilizer parity map and vice versa. The angles θ of the initial $Y^{\theta/\pi}$ gates are chosen according to the target logical state. After N cycles of stabilizer measurements, either state tomography of the data qubits is done or they are measured in \hat{Z} or \hat{X} basis for \hat{Z}_L or \hat{X}_L readout, respectively.

anticommutation relations are maintained. For instance, $\hat{X}_L \hat{S}_X = \hat{X}_{D2} \hat{X}_{D4}$ and $\hat{Z}_L \hat{S}_{Z1} \hat{S}_{Z2} = \hat{Z}_{D3} \hat{Z}_{D4}$ are also valid choices.

The circuit used for the stabilizer measurements, see Fig. 3.5(b), follows a structure similar to the entanglement stabilization experiment. To initialize the $|0\rangle_L$, $|1\rangle_L$, $|+\rangle_L$, or $|-\rangle_L$ logical state, the data qubits D1 to D4 are prepared in the corresponding initial state $|0000\rangle$, $|0101\rangle$, $|0-0-\rangle$, or $|0-0+\rangle$, respectively. This is achieved by applying single-qubit $Y^{\theta/\pi}$ -rotations on D2 and D4. Within the logical subspace, each of the initial separable data qubit states has overlap only with the corresponding target logical state. By measuring all the stabilizers and postselecting on their outcomes being +1, we effectively implement the projection operator to the logical subspace, given by

$$\hat{\Pi}_L = \frac{1}{8} (\hat{I} + \hat{S}_{Z1}) (\hat{I} + \hat{S}_X) (\hat{I} + \hat{S}_{Z2}), \quad (3.3)$$

where \hat{I} is the identity operator on all data qubits. The probability of a state $|\psi\rangle$ being in the logical subspace is given by $\langle \psi | \hat{\Pi}_L | \psi \rangle$, which is ideally 1/2 when preparing $|0\rangle_L$ and $|1\rangle_L$, and 1/4 when preparing $|+\rangle_L$ and $|-\rangle_L$. The stabilizer measurements are then repeated for N cycles. Because each stabilizer of the code has a dedicated auxiliary qubit, we pipeline the Z- and X-type stabilizer measurements. This means that we map the Z-type parities to auxiliary qubits while the X-type auxiliary qubit readout is still ongoing, and vice versa. This pipelined approach helps to reduce the number of simultaneous two-qubit gates that have to be applied [Versluis17]. The circuit can be concluded either by performing data qubit tomography to fully characterize the quantum state or by reading out the data qubits in the \hat{Z} or \hat{X} basis for \hat{Z}_L or \hat{X}_L readout, respectively.

Any single-qubit Pauli error in the circuit that flips a logical operator value will also change at least one of the stabilizer measurement outcomes. By postselecting on all the measured stabilizer outcomes being +1, we therefore discard most events where an error on the logical operator has occurred, significantly reducing the logical error rate. To detect errors that happen during the last stabilizer measurement cycle, the Z-type or X-type stabilizer values can be calculated from the final readout when the data qubits are read out in the \hat{Z} basis or \hat{X} basis, respectively. Multiple single-qubit errors that in total flip all stabilizers an even number of times can still introduce logical errors.

Due to the small distance $d = 2$ of the code, it is not possible to determine whether the logical operator was flipped when we do detect an error. For

example, if \hat{S}_X is found to be -1 , it could be caused by a \hat{Z} error on any of the data qubits, but only errors on D1 and D3 would flip the logical operator, whereas errors on D2 and D4 would not. Because experimental runs where an auxiliary qubit is measured in the $|1\rangle$ state are postselected out, we do not implement any feedback pulses on the data qubits or for resetting auxiliary qubits.

3.5. Quantum Error Detection: Device

The seven-qubit device for the error detection experiment, see Fig. 3.6, was implemented in the same overall architecture and with the same fabrication methods as the one for entanglement stabilization. It consists of seven single-island transmon qubits (yellow) with individual microwave drive (pink) and flux control (green) lines, readout resonators (red), and Purcell filters (blue). The readout circuits are distributed between two feedlines (purple), with D1, D2, X, and Z2 on the top line and D3, D4, and Z1 on the bottom line. The qubit-qubit couplers (cyan), which have an $84\ \Omega$ section at the middle, are now shorter and better modeled as two series capacitances instead of a resonator, see Section C.3 for more details. Regarding the qubit design, see Fig. 3.6(b), there is no longer a ground strip between the qubit island and the large capacitive couplers. Instead, the ground plane is closed around the qubit by crossing under airbridges that are placed in line with the coplanar waveguide of the coupled elements. This modification allows for an increased fraction of the total capacitance of the qubit to come from the coupled elements, leading to higher coupling rates [Koch07]. To reduce the number of ports required on the device, we multiplex the microwave drive lines of Z1 and Z2 with the top and bottom readout feedlines, respectively.

All the seven qubits have a charging energy of 264 MHz and are flux tunable with a junction size asymmetry of 1:3. They are biased to their maximum frequencies, which are designed in three bands. Data qubits D1 and D2 are in the upper band at around 5.6 GHz, the auxiliary qubits in the middle band at 5.0 GHz, and data qubits D3 and D4 are in the lower band at 4.2 GHz, see Table 3.2 for exact values. The energy relaxation times range between $8.4\ \mu\text{s}$ and $20.0\ \mu\text{s}$, while the echo decay times range from $15.7\ \mu\text{s}$ to $27.6\ \mu\text{s}$. The low-frequency band qubits, D3 and D4, have a relatively large charge dispersion of around 200 kHz due to the small E_J/E_C ratio of around 34, which limits their effective Ramsey decay time to about $8.8\ \mu\text{s}$.

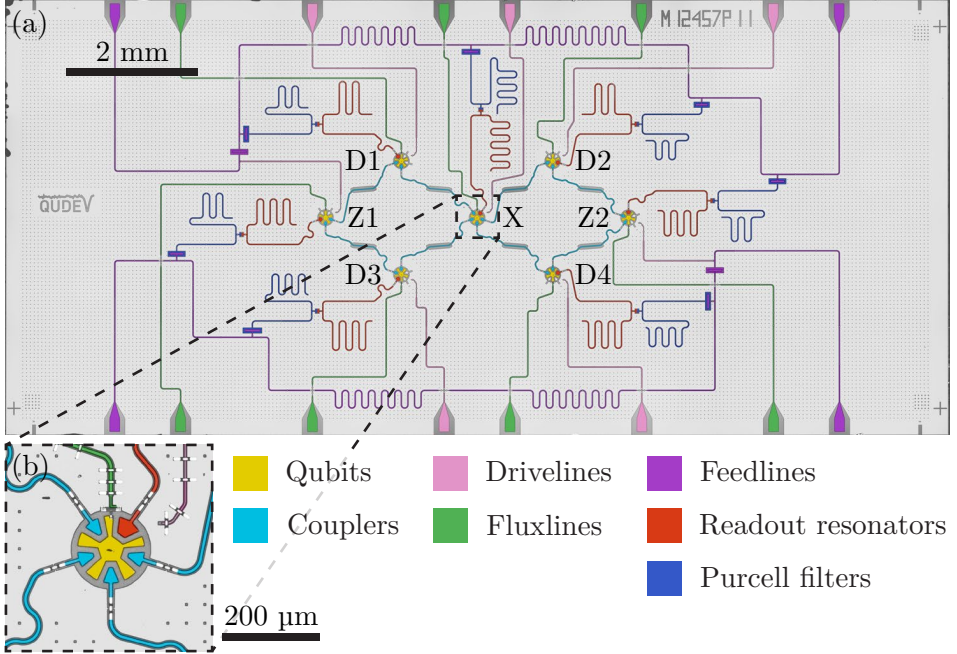


Figure 3.6: Error detection device. (a) Full-view false-color micrograph of the 14.3 mm \times 6.6 mm device used for the error detection experiment. See main text for a description of the components. (b) Zoom-in of the qubit X.

We implement single-qubit gates using 53.3-ns-long Gaussian microwave pulses with a width of $\sigma = 10$ ns, utilizing DRAG. The mean single-qubit gate error, characterized by randomized benchmarking [Magesan11, Epstein14], is $\varepsilon_{1i} = 0.3\%$. For two-qubit CZ gates, we apply a diabatic net-zero pulse to the higher-frequency qubit without explicitly tuning the phase kick between the two halves of the pulse [Rol19], see Section 2.4. The net-zero square flux pulse is smoothed with a 4 ns Gaussian filter and has a total length between 91 ns and 147 ns, with buffer times of 32 ns before and after the pulse. We correct for in-situ-measured flux pulse distortion in the line by pre-distorting the waveforms. The average gate error for the CZ gates is $\varepsilon_{2i} = 2.9\%$ on average, as characterized by interleaved randomized benchmarking [Magesan12, Barends14].

We read out the qubit state using a 200-ns-long pulse and a 300-ns-long integration time. The average readout error is around 1.3% for individual

Table 3.2: Error detection device parameters. Single-qubit parameters and qubit-pair parameters are given in the top and bottom half of the table, respectively.

	D1	D2	D3	D4	Z1	X	Z2
Qubit frequency, $\omega_Q/2\pi$ (GHz)	5.49	5.71	4.11	4.22	4.85	4.96	5.19
Energy relaxation time, T_1 (μs)	10.3	8.4	20.0	16.9	12.9	10.3	17.2
Ramsey decay time, T_2^* (μs)	17.5	14.6	8.5	9.0	14.7	18.5	26.0
Echo decay time, T_2^e (μs)	18.4	15.7	26.0	26.3	27.6	15.9	27.3
Dispersive shift, $\chi/2\pi$ (MHz)	-2.5	-2.5	-0.8	-1.0	-1.2	-2.4	-2.0
Readout pulse frequency, $\omega_r/2\pi$ (GHz)	6.61	6.84	5.83	6.06	6.26	6.04	6.30
Readout mode linewidth, $\kappa_{R'}/2\pi$ (MHz)	7.5	10.6	6.0	7.2	17.3	10.9	11.0
Purcell filter linewidth, $\kappa_P/2\pi$ (MHz)	47.6	46.4	13.6	49.2	56.3	68.1	46.4
Purcell-readout coupl., $J_{PR}/2\pi$ (MHz)	20.0	22.2	17.5	18.4	18.8	18.7	19.0
Purcell-readout det., $\Delta_{PR}/2\pi$ (MHz)	33.8	25.7	19.4	32.3	11.3	25.6	20.6
Thermal population, p_{th} (%)	0.06	0.04	0.8	0.8	0.08	0.4	0.6
Individual readout error, ε_{ri} (%)	0.6	0.8	2.2	1.8	1.3	1.2	1.2
Multiplexed readout error, ε_{rm} (%)	1.1	0.9	1.8	2.6	2.3	1.6	1.4
Measurement efficiency, η (%)	30	24	15	15	20	27	22
Individ. single-qubit gate err., ε_{li} (%)	0.18	0.37	0.25	0.26	0.34	0.20	0.52
Res. coupling to X, $J_{\text{QQ}}/2\pi$ (MHz)	5.4	3.0	3.8	4.0			
Res. coupling to Z, $J_{\text{QQ}}/2\pi$ (MHz)	5.0	5.2	3.7	2.9			
Individual CZ gate to X error, ε_{2i} (%)	2.1	4.3	2.2	3.3			
Individual CZ gate to Z error, ε_{2i} (%)	2.1	2.2	3.4	3.8			
Disp. coupling to X, $\zeta/2\pi$ (MHz)	-0.14	-0.05	-0.03	-0.03			
Disp. coupling to Z, $\zeta/2\pi$ (MHz)	-0.08	-0.15	-0.04	-0.03			

readout and 1.7% for simultaneous readout of all qubits. Additionally, we find that the readout of the auxiliary qubit induces a phase flip of a data qubit with a probability of less than 0.3%. To mitigate dephasing caused by low-frequency noise, we apply Y pulses for dynamical decoupling on auxiliary qubits at the middle of the parity map sequence and on data qubits between each stabilizer cycle. Considering the readouts, single-qubit gates, and two-qubit gates, the total cycle duration amounts to $T_{\text{cyc.}} = 1.92 \mu\text{s}$.

3.6. Quantum Error Detection: Results

In order to assess the performance of each stabilizer measurement separately, we initialize the data qubits neighboring the auxiliary qubit of the corresponding stabilizer in all possible product states that are also eigenstates of the stabilizer operator. By executing the stabilizer measurement circuit and analyzing the average outcome of the auxiliary qubit readout, we calculate the mean stabilizer value $\langle \hat{S} \rangle$ for each input state. For the three stabilizers \hat{S}_{Z1} , \hat{S}_X , and \hat{S}_{Z2} , we find average probabilities of an error in the stabilizer measurement $\varepsilon_S = (1 - S\langle \hat{S} \rangle)/2$, with $S = \pm 1$ denoting the expected stabilizer value, of 4.9%, 16.4%, and 8.2%, respectively, see Fig. 3.7. The results are in good agreement with master equation simulations that consider energy relaxation, dephasing, and readout errors. The main source of errors is data qubit energy relaxation, as evidenced by the higher error probabilities observed for input states with a larger excitation number during the parity map, such as $|11\rangle$ and $|----\rangle$, the last of which is rotated to $|1111\rangle$ by the \sqrt{Y}^\dagger gates at the start of the X-type parity map.

To prepare the logical states, we start by preparing a separable data qubit state that has overlap only with the target logical state within the logical subspace and perform one cycle of stabilizer measurements as described in Section 3.4. We perform state tomography of the data qubits for the runs where all stabilizer measurements yield a +1 result to characterize the resulting states. As an example, let's consider the case of preparing the $|0\rangle_L$ state. The resulting four-qubit density matrix $\hat{\rho}$ is shown in Fig. 3.8(a,b). The probability that all stabilizers measurements yield +1 is 25.1%, compared to the ideal error-free case of 50%. The state has a fidelity $F = \langle 0|_L \hat{\rho} |0\rangle_L = 70.3\%$ with respect to the target state. We observe that a significant portion of the error is due to energy relaxation and dephasing. This is indicated by the reduced amplitude of the $|1111\rangle \langle 1111|$ term and the coherences. In addition,

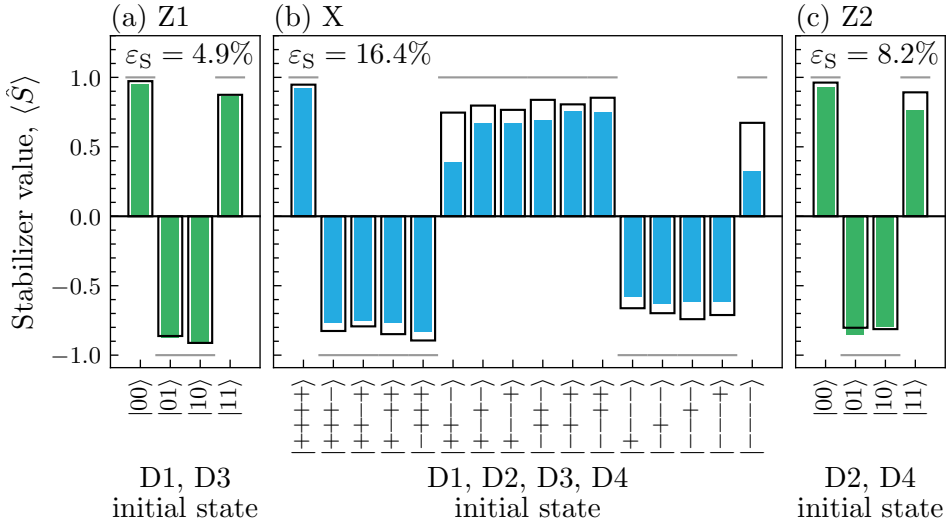


Figure 3.7: Error detection stabilizer fidelity. Average outcomes of stabilizer measurements with (a) Z1, (b) X, and (c) Z2 for various neighboring data qubit states as filled bars. The black boxes and gray lines indicate the master equation simulation and target stabilizer value, respectively. The average measured stabilizer error probability ϵ_S is indicated for each stabilizer.

we observe a small coherent phase error indicated by the nonzero imaginary parts of the coherences, corresponding to a phase error of 0.09 rad on any of the data qubits. We note that the found state $\hat{\rho}$ is not fully in the logical subspace, and many of the errors present in the state would be detected either in consecutive stabilizer measurements or when calculating the stabilizer values from the final readout. The probability of finding the prepared physical state within the logical subspace is $P_L = \text{Tr}(\hat{\Pi}_L \hat{\rho}) = 71.7\%$. Within the logical subspace, the state is characterized by the density matrix $\hat{\rho}_L = \hat{\Pi}_L \hat{\rho} / P_L$, which has a fidelity of $F_L = \langle 0|_L \hat{\rho}_L |0\rangle_L = F / P_L = 98.2\%$ with respect to the target state. When preparing $|+\rangle_L$, $|+\rangle_L$, and $|-\rangle_L$, we find fidelities within the logical subspace of 97.3%, 94.2%, and 94.8%, respectively, see Fig. 3.8(e-j). The lower fidelity observed for the logical superposition states $|+\rangle_L$ and $|-\rangle_L$ compared to $|0\rangle_L$ and $|1\rangle_L$ can be explained by the presence of single-qubit errors during the preparation circuit that flip the logical

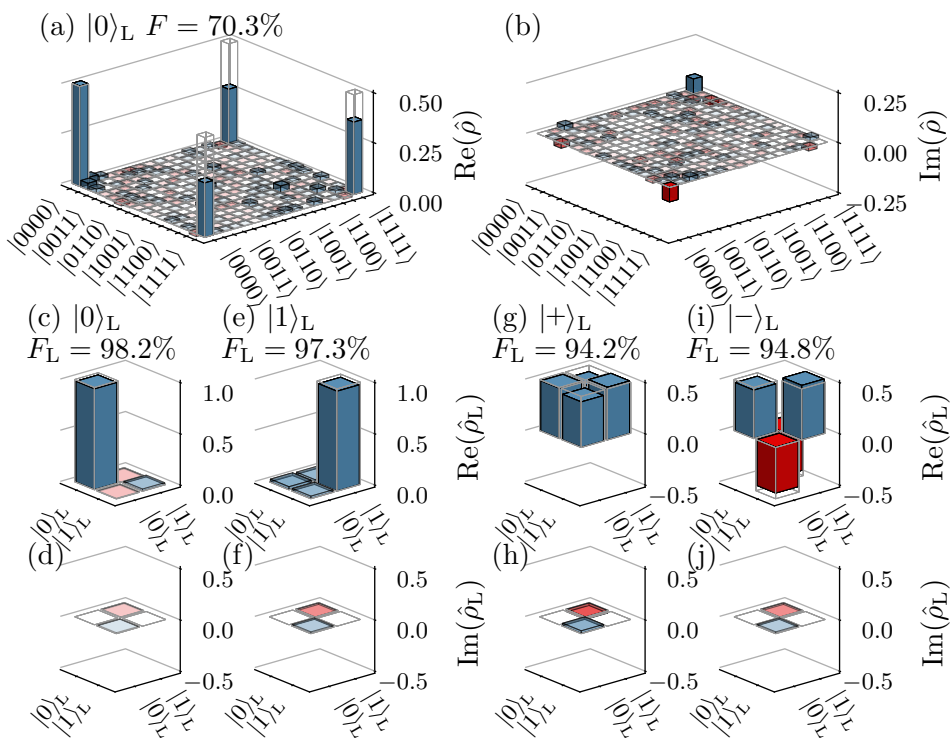


Figure 3.8: Error-detected logical state initialization. (a,b) Real and imaginary part of the four-data-qubit density matrix $\hat{\rho}$ as reconstructed using state tomography after initializing the $|0\rangle_L$ state. (c-j) Real and imaginary parts of $\hat{\rho}_L$, the data qubit density matrix projected onto the logical subspace with $\hat{\Pi}_L$, when preparing $|0\rangle_L$, $|1\rangle_L$, $|+\rangle_L$, and $|-\rangle_L$.

operator but do not affect any of the stabilizers. These errors would be detected by \hat{S}_X when initially preparing the data qubits in $|++++\rangle$ and $|+---\rangle$ instead, making the preparation fault-tolerant [Marques22].

Finally, we assess the performance of the stabilizer measurements when repeating them over multiple cycles, and characterize the logical relaxation and dephasing times. The experiment is started by preparing one of the logical states $|0\rangle_L$, $|1\rangle_L$, $|+\rangle_L$, or $|-\rangle_L$, followed by consecutive stabilizer measurements for up to $N = 10$ cycles. After the stabilizer measurements, all data qubits are read out either in the \hat{X} or \hat{Z} basis. The experiment is repeated for up to $3 \cdot 10^5$ times per preparation at $N = 10$ and progressively fewer times at smaller N . We calculate the logical operator value \hat{X}_L or \hat{Z}_L from the final readout and average over all the experimental runs where all the stabilizer measurements, including from the final data qubit readout, yield +1, see Fig. 3.9(a,b). By fitting an exponential decay model $\langle \hat{Z}_L \rangle = \langle \hat{Z}_L \rangle_{t=0} \exp(-t/T_1^L)$ to the extracted data, we extract the decay time of the \hat{Z}_L operator $T_1^L = 63(9) \mu\text{s}$. The corresponding per-cycle logical bit flip probability is $\varepsilon_z^L = [1 - \exp(-T_{\text{cyc.}}/T_1^L)]/2 = 1.5(2)\%$. Similarly, the decay time of the \hat{X}_L operator is extracted $T_2^L = 72(33) \mu\text{s}$, corresponding to a per-cycle error probability of $\varepsilon_x^L = [1 - \exp(-T_{\text{cyc.}}/T_2^L)]/2 = 1.3(6)\%$. The reduced logical operator value already after the first cycle could be related to the non-fault-tolerant preparation of the $|+\rangle_L$ and $|-\rangle_L$ states. Simulations yield logical error probabilities of $\varepsilon_z^L = 2.1\%$ and $\varepsilon_x^L = 1.6\%$, which align well with the experimentally obtained values within the experimental uncertainty. Notably, both logical decay times (T_1^L and T_2^L) exceed the decoherence times of the individual physical qubits of the device. This is evident from the comparison with the decay of the longest-lived physical operators $T_1^{\text{D3}} = 20.0 \mu\text{s}$ and $T_2^{\text{e,Z1}} = 27.6 \mu\text{s}$, as shown by the dashed lines in Fig. 3.9(a,b).

Postselection on no detected errors is a crucial aspect of quantum error detection codes, and it plays a significant role in improving the coherence of the logical qubit compared to its physical constituents. In our implementation, we retain approximately 40% to 50% of the data in each cycle due to the postselection criterion. This probability is slowly increasing over the cycles, see Fig. 3.9(c). The apparent improvement of performance over the cycles, which we do not observe when not postselecting on no detected errors, could be caused by a change in the physical error probabilities during the data collection. In that case, the relative fraction of runs with a lower error probability increases over the cycles in the postselected dataset. In simulation, we observe a constant probability of no detected errors at

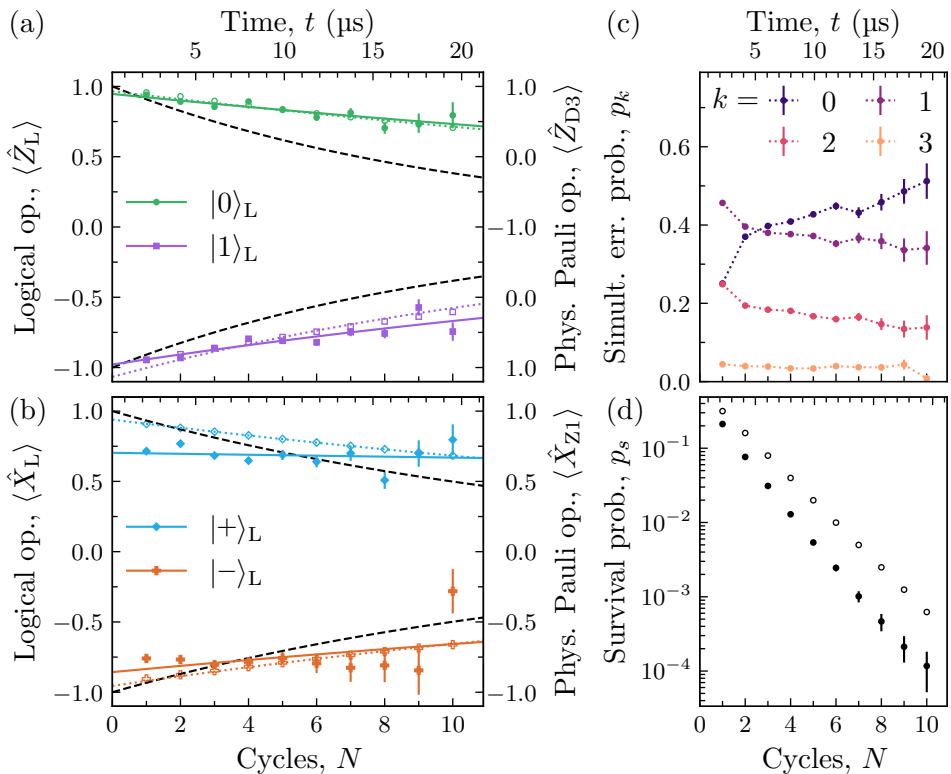


Figure 3.9: Repeated error detection. (a,b) Evolution of the logical operator expectation values $\langle \hat{Z}_L \rangle$ and $\langle \hat{X}_L \rangle$ when postselecting on no detected errors for the initial $|0\rangle_L$, $|1\rangle_L$, $|+\rangle_L$, and $|-\rangle_L$ states. The measured values are indicated as filled markers, master equation simulation as empty markers, and exponential fits as solid and dotted lines, respectively. The decay of the \hat{Z} and \hat{X} operators of the longest lived physical qubits is shown as dashed lines on the right axis. (c) Probability of detecting k simultaneous errors on cycle N conditioned on no detected errors on prior rounds. Markers indicate the data while the dashed lines are guides for the eye. (d) The cumulative survival probability p_s from the experiment (filled dots) and from the simulation (open circles). In all panels, the error bars indicate one standard deviation uncertainty.

50%. The probability p_k of k simultaneous errors is roughly exponentially suppressed as k increases. The constant per-cycle probability of passing the postselection leads to an exponentially decaying cumulative survival probability p_s , see Fig. 3.9(d). After 10 cycles, we observe a cumulative survival probability of about 10^{-4} , which closely matches the simulated value of $6 \cdot 10^{-4}$.

3.7. Discussion

In our milestone experiments, we have successfully demonstrated the use of repeated high-fidelity stabilizer measurements for stabilizing an entangled two-qubit state and for improving the decoherence time of a qubit through quantum error detection and postselection. The dominant source of errors in both experiments was decoherence, emphasizing the importance of minimizing the overall cycle time. Having fast auxiliary qubit readout while maintaining high fidelity and low crosstalk is essential for these demonstrations, as readout constitutes the longest operation in both experiments, apart from the feedback delay which we discuss in the next paragraph. While our achieved readout integration and resonator reset times of 400 ns and 300 ns, respectively, compare favorably to other demonstrations of repeated stabilizer measurements [Bultink20, Chen21, Zhao22b, Marques22, Sundaresan23, Acharya23], they still fall short of the fastest high-fidelity readouts reported in the literature [Walter17, Heinsoo18, Sunada22, Swiadek23]. Future improvements in readout speed and fidelity would contribute significantly to reducing the overall error detection rate. In addition to readout, the speed and fidelity of parity maps, which involve two-qubit CZ gates, are crucial. In the entanglement stabilization experiment, the choice of a unipolar flux pulse shape made the gates sensitive to long-time distortions caused by a high-pass filter in the flux line. We improved on that in the quantum error detection experiment by using a net-zero pulse shape, although it was not specifically optimized for fast gates. Further optimization of the pulse shape, making use of the phase-kick control parameter, can lead to a faster gate, see Section 2.4. Moreover, to achieve faster gates at the expense of increased dispersive couplings between qubits, it would be beneficial to increase the qubit-qubit coupling rates, which range from 2.9 MHz to 5.4 MHz on these devices.

In the long term, the implementation of non-Clifford gates on logical

qubits will require feedback based on decoded error syndromes [Fowler12a]. However, for quantum memories, using Pauli frame updating only can be a viable approach. In our entanglement stabilization experiment, we observed that Pauli frame updating resulted in lower fidelities compared to using active feedback. In this case, we did not fully leverage the potential of the Pauli frame updating for reducing the cycle time because we kept the feedback pulses to reset the auxiliary qubits. A circuit without feedback could have been 40% shorter, likely leading to an increase in the Bell state fidelity. The decrease of fidelity when using Pauli frame updating rather implies that the qubit-qubit dispersive couplings need to be suppressed further. This can be achieved either by increasing the detuning between qubits, reducing anharmonicity, or using better dynamical decoupling schemes.

Leakage of qubits outside the computational subspace to higher excited states of the transmon is an important consideration for quantum error correction, as a single leakage event can lead to many correlated errors. It can occur during two-qubit gates, which involve second excited state of one of the qubits [Strauch03, DiCarlo10], as well as due to readout-induced state transitions [Sank16]. In both of the demonstrated experiments, the auxiliary qubits were predominantly read out in their ground state which is less susceptible to readout-induced leakage. The only exception to that is the entanglement stabilization experiment with Pauli frame updating, in which case the individual auxiliary qubit readout outcomes approach an equal mixture of $|0\rangle$ and $|1\rangle$ after a few cycles. We do observe a reduction of fidelity in the experimental data at larger cycle numbers N , which is not present in the simulation, see the orange points and line in Fig. 3.4(a) This trend suggests that leakage could be occurring in this particular scenario, but further investigation is required to confirm this hypothesis. Further open questions include how detrimental leakage errors would be when repeating the stabilizer measurements for even longer, say hundreds of cycles, and when scaling the code distance.

As the next step, we deploy the general architecture demonstrated in those experiments to a distance $d = 3$ surface code, see Chapter 4. While designing the parameters of the device, we keep in mind the lessons from the small-scale experiments, that is, the necessity of fast and low-crosstalk readout and two-qubit gates, and a low qubit-qubit dispersive coupling rate.

Quantum Error Correction Experiment

Having demonstrated high-fidelity stabilizer measurements in the entanglement stabilization and the distance $d = 2$ error detection experiments, see Chapter 3, our next objective is to demonstrate the operation of a single quantum-error-corrected logical qubit using a distance $d = 3$ surface code. This task poses several challenges that need to be addressed, some of which were discussed in Section 3.7. Crucially, to maintain a low rate of errors per stabilizer measurement cycle, the operations for the stabilizer measurements need to be executed rapidly relative to the coherence times of the qubits, while ensuring high fidelity and low crosstalk.

We start the chapter by presenting the concept of the $d = 3$ surface code and the circuit that we have implemented for its operation, see Section 4.1. Due to the large number of simultaneous two-qubit gates required by the code, careful consideration is given to the frequency configuration of the qubits to enable efficient parallel execution of these gates while minimizing unwanted couplings between qubits. To address these issues, we present a novel frequency configuration scheme in Section 4.2. We present the quantum device and its parameters in Section 4.3, followed by the presentation of the quantum error correction (QEC) experiment results in Section 4.4. Among the many technical challenges that had to be overcome, we discuss the topics of drive crosstalk cancellation and parasitic two-level defects in more detail in Section 4.5.

4.1. Concept

The smallest variant of a distance $d = 3$ surface code comprises nine data qubits, labeled D1 to D9 here, along with eight stabilizers, denoted \hat{S}_{Z1} to \hat{S}_{Z4} and \hat{S}_{X1} to \hat{S}_{X4} , which are the products of the \hat{Z} or \hat{X} operators of

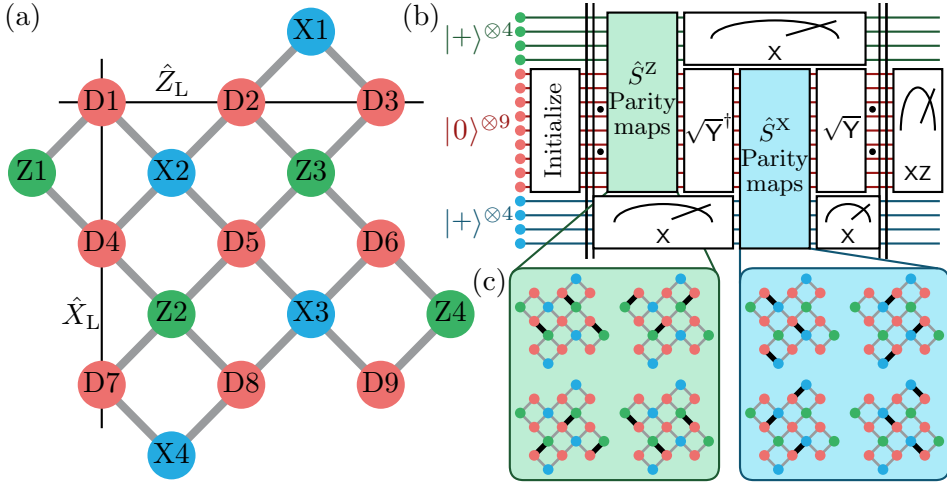


Figure 4.1: Quantum error correction concept. (a) Layout of the data qubits (red) and X- (blue) and Z-type (green) auxiliary qubits, and the physical couplings between them as thick gray lines. The support of the logical operators is indicated as black lines. (b) The conceptual circuit for an error correction measurement including initialization, repeated stabilizer measurement with pipelined parity maps and auxiliary qubit readout, and final data qubit measurement. See main text for more details. (c) The four steps of simultaneous CZ gates for the \hat{S}_Z (green background) and \hat{S}_X (blue background) parity maps are indicated with thick black lines.

the two or four neighboring data qubits [Horsman12]. The layout of such a device, where we label the auxiliary qubits used to measure the stabilizers as Z1 to Z4 and X1 to X4, correspondingly, is shown in Fig. 4.1(a). As described in Section 1.3, we define the logical Pauli operators as products of single-qubit Pauli operators in one row or column

$$\hat{Z}_L = \hat{Z}_{D1}\hat{Z}_{D2}\hat{Z}_{D3} \quad \text{and} \quad \hat{X}_L = \hat{X}_{D1}\hat{X}_{D4}\hat{X}_{D7}. \quad (4.1)$$

These operators commute with all the stabilizers and satisfy the usual anticommutation relation $\hat{Z}_L\hat{X}_L = -\hat{X}_L\hat{Z}_L$. See also Appendix A for a potential set of destabilizers, which flip one stabilizer without disturbing the logical operators, and can be used for efficient simulation of Clifford operations on the code. Equivalent definitions for the logical operators can be obtained by multiplying either operator with any of the stabilizers.

To reduce the number of gates that need to be executed simultaneously, we employ a pipelined circuit where parity maps for the \hat{S}_Z stabilizers are executed while the auxiliary qubits for the \hat{S}_X stabilizers are read out, and vice versa, see Fig. 4.1(b) [Versluis17]. Since our architecture utilizes the CZ gate as the physical two-qubit gate, which maps the \hat{Z} parity of the data qubits to the phase of the auxiliary qubit, we change the basis of the data qubits for the \hat{S}_X measurements using \sqrt{Y}^\dagger and \sqrt{Y} rotations. To implement the parity maps of either \hat{S}_Z or \hat{S}_X stabilizers, twelve CZ gates need to be executed, distributed across at least four steps of gates that are executed in parallel. An example of these four steps, where all gates in the same intercardinal direction (NW, NE, SE, SW) are executed simultaneously, is shown in Fig. 4.1(c). Note that each step involves two gates on neighboring qubits which must be executed in parallel and therefore require careful consideration to avoid unwanted interactions.

To initialize a specific logical state, we prepare the data qubits in a separable state that is an eigenstate of the corresponding logical operator and a +1 eigenstate of as many stabilizers as possible. By starting in an eigenstate of a stabilizer, we can detect errors, signaled by a flip of the stabilizer value, already during the first measurement of that stabilizer. More specifically, we prepare $|000000000\rangle$, $|100100100\rangle$, $|+++++++\rangle$, or $|---+++++\rangle$ on qubits D1 to D9 to prepare the $|0\rangle_L$, $|1\rangle_L$, $|+\rangle_L$, or $|-\rangle_L$, respectively. To measure the logical qubit state, we read out the data qubits in either the \hat{Z} or \hat{X} basis, depending on the logical operator that is measured. We calculate \hat{Z}_L or \hat{X}_L along with a final set of stabilizer values as the product of the corresponding data qubit readout outcomes.

4.2. Device Architecture

An important factor for achieving fast, high-fidelity, and low-crosstalk implementation of single-qubit gates, two-qubit gates, and readout is the choice of qubit frequencies for idling and for two-qubit gate interactions. In this work, we consider architectures with static, as opposed to tunable, couplings, which results in devices that are simpler to fabricate and control due to a smaller number of Josephson-junction-based flux-tunable elements [Collodo20]. A scheme proposed in Ref. [Versluis17] addresses these considerations and is scalable by repeating the same frequency configuration pattern by making use of three distinct idling frequencies. In the proposed scheme, all qubits

idle at their upper flux-insensitive point. For the auxiliary qubits this corresponds to a middle frequency ω_M , while data qubits are distributed between high and low idling frequencies denoted ω_H and ω_L , respectively, see Fig. 4.2(a,b). For the execution of a CZ gate between two qubits Q1 and Q2, the qubit with the higher idling frequency Q1 is tuned down in frequency for the interaction. Additionally, neighboring qubits in the frequency band of Q2 are also tuned down to ensure that they do not participate in the interaction. These additional pulses prevent unwanted crossing of neighboring qubits that should not interact, and allow the qubits to stay at their first-order flux-insensitive positions for most of the QEC cycle. However, the extensive use of flux-bias pulses on qubits that are neighboring, but not directly involved in the CZ gates leads to some disadvantages. Biasing the qubits away from their flux-insensitive frequencies leads to additional dephasing and complicates the execution of single-qubit gates and readout simultaneously with the two-qubit gate, as the qubit frequency will depend on whether the nearby two-qubit gate is executed. Moreover, if a bias tee is employed in the flux line, as is the case for our setup, then unipolar pulses can lead to long-lasting flux distortions that are challenging to correct [Neill18, Rol20].

We propose a novel frequency configuration scheme for surface codes, which facilitates the parallel execution of operations, thereby simplifying the tune-up and operation of the device. In this scheme, all data qubits idle at their lower flux-insensitive frequencies in a frequency band denoted ω_L , and auxiliary qubits idle at their upper flux-insensitive frequencies in a frequency band denoted ω_H , which are at the lower and upper limits of the frequency band used for qubits. To enable CZ gates, the high-frequency qubits are flux-biased down in frequency while the low-frequency qubits are biased up, bringing them together at an intermediate interaction frequency. This configuration eliminates the need for pulses on neighboring qubits that are not involved in the gate, thereby reducing the associated dephasing and easing the parallel execution of operations. During the implementation of the CZ gate, the higher-frequency qubit will occupy the second excited state of the transmon, which might lead to leakage errors. Leakage on the auxiliary qubit is less detrimental than leakage on the data qubits, as the auxiliary qubits are repeatedly read out, which facilitates the detection and correction of the leakage events [Lacroix23]. Furthermore, having the data qubits at lower frequencies can be advantageous for the performance of the QEC code. This is because the logical error rate in a surface code is more sensitive to data qubit errors than auxiliary qubit errors [Fowler12b], and transmon qubits

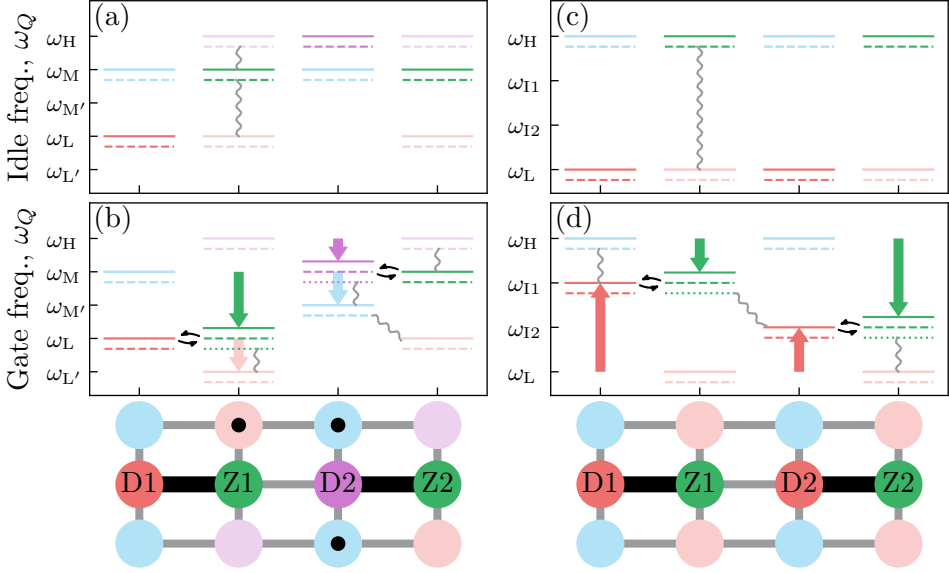


Figure 4.2: Frequency configuration architectures. Frequencies of a subset of qubits from a larger surface code grid (a) during idling and (b) during simultaneous CZ gates between D1-Z1 and D2-Z2 pairs for the three-idling-frequency configuration proposed in Ref. [Versluis17]. (c) Idling and (d) gate frequencies for the newly-proposed two-idling-frequency configuration. In all panels, thick, dashed and dotted lines indicate the first, second and third transmon transition frequency, respectively. The color of the lines matches the color on the qubit in the diagram below. The gray wavy lines indicate undesired dispersive interactions between the transmons. Wide arrows in panels (b) and (d) indicate the change of qubit frequency during gates compared to idling, while the black double arrows indicate the resonant $|20\rangle \leftrightarrow |11\rangle$ interaction used for the CZ gates. The black dots in the diagram below panel (b) indicate qubits that are not involved in the CZ gates, but are biased away from their flux-insensitive point.

typically have longer coherence times at lower frequencies due to weaker coupling to the environment [Martinis05, Koch07]. If the readout resonators have higher frequencies than the qubits, then the proposed frequency scheme has another advantage. In such a setting, the auxiliary qubits, which undergo repeated readouts during the operation of the code, have a small detuning from their corresponding readout resonators. This facilitates the implementation of fast and high-fidelity readout for the auxiliary qubits.

Next, we examine the dispersive qubit-qubit couplings for the two frequency schemes in more detail. According to Eq. (2.21), the dominant terms contributing the dispersive coupling are proportional to $2J_{\text{QQ}}^2/\Delta_{21}$ if the qubits are in the computational subspace and $3J_{\text{QQ}}^2/\Delta_{31}$ if the high-frequency qubit can be in the $|2\rangle$ state. Here, Δ_{ij} represents the detuning between the i -th transition of the high-frequency qubit and j -th transition of the low-frequency qubit. With the three-idling-frequency scheme, to ensure the detunings in the dominant terms are at least Δ_{min} , we need a separation between the highest and lowest frequency band of at least $\omega_{\text{H}} - \omega_{\text{L}'} = 4\Delta_{\text{min}} + 2|\alpha_{\text{H}}| + 2|\alpha_{\text{M}}|$. Here, α_{H} and α_{M} are the anharmonicities of the high- and medium-frequency band qubits, respectively. The detunings that set this limit for Δ_{min} are indicated as gray wavy lines in Fig. 4.2(b). On the other hand, for the two-idling-frequency scheme, the minimum separation is smaller $\omega_{\text{H}} - \omega_{\text{L}} = 3\Delta_{\text{min}} + 3|\alpha_{\text{H}}|$, see Fig. 4.2(d) and the gray wavy lines. This means that the overall error due to dispersive qubit-qubit couplings during gates will be smaller for this scheme. The situation is even more in favor of the two-idling-frequency scheme during idling, see Fig. 4.2(a,c).

While the proposed frequency configuration scheme offers several advantages, it does have some limitations when scaling to larger surface code sizes. One drawback is the lack of a repeating frequency configuration pattern at large scales. As an example, let's consider the case of executing two CZ gates in parallel on neighboring data-auxiliary qubit pairs, labeled D1-Z1 and D2-Z2 as shown in Fig. 4.2(d). To avoid unwanted interactions between the neighboring qubits Z1 and D2, the interaction frequency ω_{11} of D1-Z1 needs to be higher than the interaction frequency ω_{12} of D2-Z2. When extending this requirement for a distance d surface code, where $k = (d + 1)/2$ neighboring gates need to be executed in parallel, we find that k distinct interaction frequencies need to fit between ω_{H} and ω_{L} with a large detuning between them. By executing the parity maps in more than

four steps, the simultaneous gates could be executed without neighboring each other, rendering the frequency configuration scalable at the cost of a longer cycle time. Another downside of the two-frequency-band scheme is that it requires the qubits to maintain good coherence over a wide range of frequencies to implement all the two-qubit gates. This can be particularly complicated if parasitic strongly-coupled two-level systems are present in the system [Simmonds04, Lisenfeld15, Müller19], as even crossing the qubit over one of these defects can lead to significant population loss as we present in Section 4.5.2.

4.3. Device Parameters

We design and fabricate a 17-qubit quantum processor to implement quantum error correction protocol, see the optical micrograph in Fig. 4.3. The device is fabricated using a thin niobium film on a silicon substrate, with Josephson junctions made of aluminum and aluminum oxide, as well as aluminum-titanium-aluminum trilayer airbridges, following our standard recipe, see Ref. [Krinner22] for details. Each qubit (highlighted in yellow) has an individual microwave drive (pink) and flux control (green) line, as well as an individual readout resonator (red). The readout resonators are coupled to one of the four frequency-multiplexed feedlines (purple) through individual Purcell filters (blue), which help suppress qubit decay via the readout resonators and minimize data qubit dephasing due to auxiliary qubit readout [Heinsoo18]. Two-qubit interactions between neighboring qubits are mediated by short capacitively coupled sections of coplanar waveguide (cyan), see Section C.3.

To ensure a low charge dispersion of low-frequency qubits, and to reduce residual inter-qubit dispersive couplings, we target a low charging energy of $E_C/h = 165$ MHz for all the qubits, leading to anharmonicities $\alpha/2\pi = -177(7)$ MHz. At this value, the charge dispersions of the first and second transition of a qubit are low enough that it will not be the limiting mechanism for dephasing [Koch07]. More specifically, in the worst case for a qubit at 3.5 GHz the values are 1 kHz and 33 kHz, respectively. For the qubit frequencies, we employ the two-idling-frequency-band configuration presented in Section 4.2. The data qubit frequencies $\omega_D/2\pi$ are between 3.7 GHz and 4.1 GHz, and auxiliary qubit frequencies $\omega_{X|Z}/2\pi$ between 5.9 GHz and 6.3 GHz, see Fig. 4.4(a). To implement two-qubit gates, we

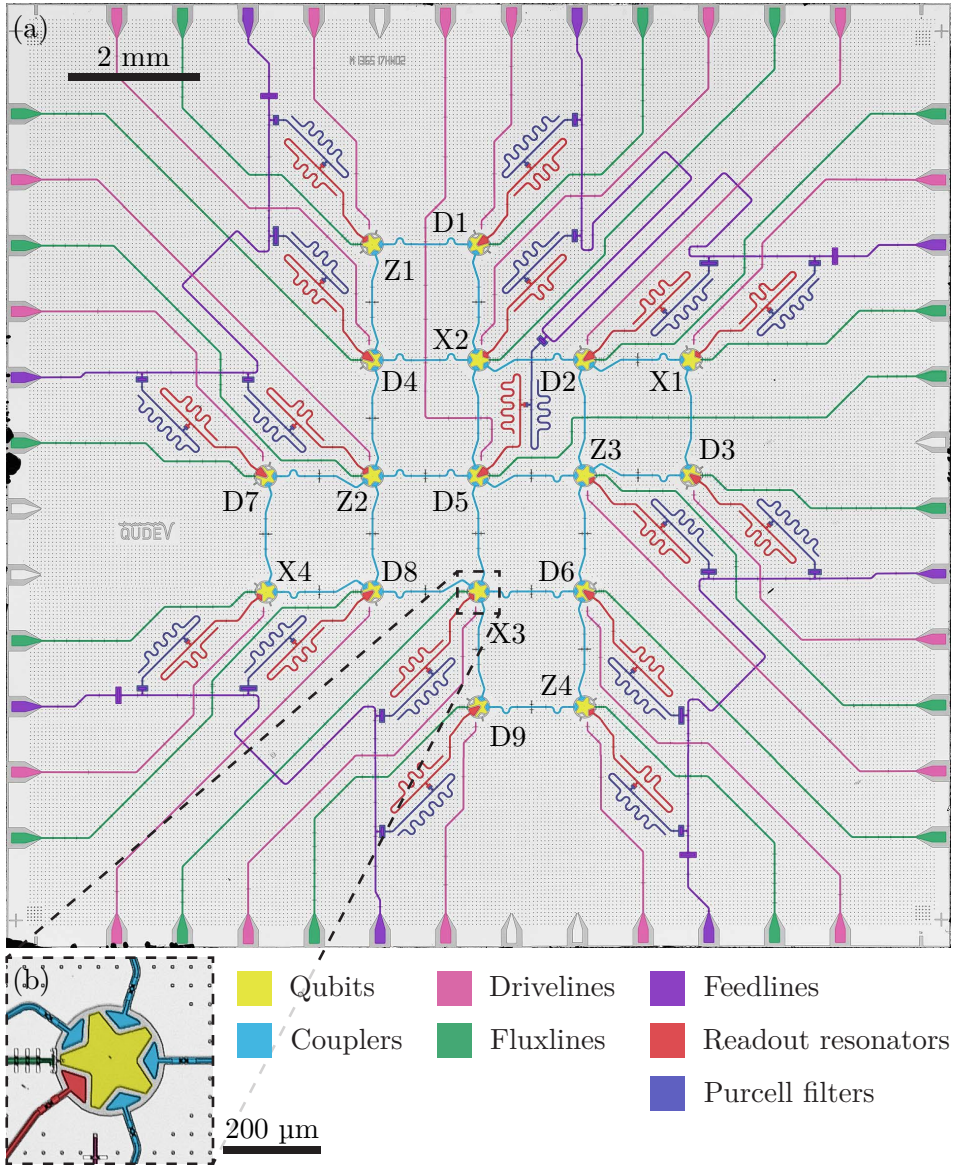


Figure 4.3: Error correction device. (a) Full-view false-color micrograph of the 14.3 mm \times 14.3 mm device. See main text for a description of the components. (b) Zoom-in of the qubit X3.

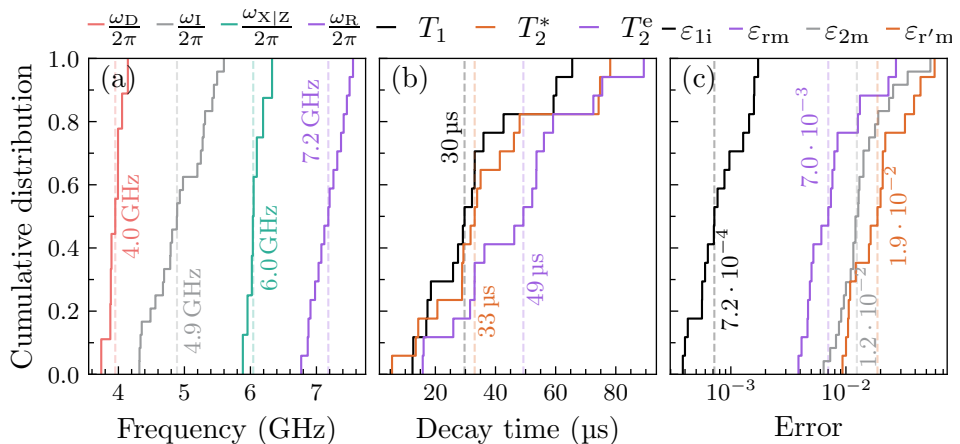


Figure 4.4: Error correction device parameters. Cumulative distributions of (a) data qubit $\omega_D/2\pi$, inter-qubit interaction $\omega_I/2\pi$, auxiliary qubit $\omega_{X|Z}/2\pi$, and readout resonator $\omega_R/2\pi$ frequencies, (b) energy relaxation T_1 , Ramsey dephasing T_2^* and echo dephasing T_2^e times, and (c) average single-qubit gate ε_{1i} , readout with two-state classification ε_{rm} , three-state classification $\varepsilon_{r'm}$, and two-qubit gate ε_{2m} errors. In all panels, the median values are indicated with a dashed line and a number.

apply flux-bias pulses to both qubits such that the first transition of the data qubit and second transition of the auxiliary qubit meet at a frequency $\omega_I/2\pi$ ranging between 4.3 GHz and 5.6 GHz. The readout resonator frequencies $\omega_R/2\pi$ are between 6.8 GHz and 7.6 GHz. To read out the data qubits, we utilize unipolar flux-bias pulses that bring the data qubits to approximately 5 GHz, reducing their detuning from the readout resonators to reduce readout-induced state transitions and increase the dispersive shift [Sank16, Khezri22, Swiadek23]. The combinations of Purcell filter linewidths $\kappa_P/2\pi = 29(5)$ MHz, readout resonator and Purcell filter couplings $J_{PR}/2\pi = 29(2)$ MHz and the detunings between the Purcell filters and the readout resonators $\Delta_{PR}/2\pi = 9(14)$ MHz result in effective linewidths of $\kappa_{R'}/2\pi = 13(5)$ MHz and dispersive shifts of $\chi'/2\pi = -2.2(11)$ MHz for the eigenmode of the readout resonator and Purcell filter system that is used for readout. The energy relaxation times T_1 of the qubits range from 12 μs to 66 μs with a median of 30 μs , whereas the echo-dephasing times T_2^e

range from $16\ \mu\text{s}$ to $89\ \mu\text{s}$ with a median of $49\ \mu\text{s}$, see Fig. 4.4(b) for the distributions.

We read out the qubits with a 200-to-300-ns-long pulse and integrate the response for 400 ns, achieving a median multiplexed qubit readout error of $\varepsilon_{\text{rm}} = 0.7\%$, see Fig. 4.4(c). When classifying also for the second excited transmon state $|2\rangle$, the median error is $\varepsilon_{\text{r'm}} = 1.9\%$. The single-qubit gates, implemented using 40-ns-long truncated Gaussian pulses of width $\sigma = 10\ \text{ns}$ and utilizing derivative removal by adiabatic gate (DRAG) [Motzoi09, Gambetta11], achieve a median gate error of $\varepsilon_{\text{li}} = 0.07\%$ when individually characterized using randomized benchmarking [Magesan11, Epstein14]. For two-qubit gates, we apply distortion-corrected [Rol20] net-zero flux-bias pulses on both interacting qubits, and optimize the conditional phase to π by controlling the phase kick between the $|20\rangle$ and $|11\rangle$ states at the middle of the pulses, see Section 2.4. The coupling rates between neighboring qubits at their interaction points are approximately $J_{\text{QQ}}/2\pi \approx 7\ \text{MHz}$, leading to a worst-case swap angle of $\theta = 4\arctan|2J_{\text{QQ}}/\alpha| = 0.31\ \text{rad}$, which corresponds to a gate error of $\varepsilon_{\text{2i}} = (5 - 4\cos\theta/2 - \cos\theta)/10 = 1.0\%$, see Appendix B. However, we expect that the actual swap errors are smaller due to the finite rise and fall time of the flux-bias pulses of around 1 ns and nonconstructive interference between the four edges of the net-zero pulse. In practice, we find a median two-qubit gate error of $\varepsilon_{\text{2m}} = 1.2\%$ from interleaved randomized benchmarking [Magesan12, Barends14], when simultaneously characterizing the sets of gates that are executed in parallel during the surface code cycle.

4.4. Results

To verify the high-fidelity operation all gates and readouts, we first characterize the eight stabilizers individually. For each stabilizer \hat{S} , we prepare the data qubits in product states that are also eigenstates of the stabilizer, execute the parity map circuit, and read out the auxiliary qubit. The average measurement outcomes, see Fig. 4.5, reveal a mean stabilizer error ranging from $\varepsilon_{\text{S}} = (1 - S\langle\hat{S}\rangle)/2 = 2.5\%$ to 5.7% for weight-two stabilizers, and from 5.9% to 11.8% for weight-four stabilizers, with S denoting the expected stabilizer outcome. To further validate these results, we simulate these experiments using Monte Carlo wave functions [Dalibard92, Dum92]. We find errors that are slightly lower than in experiment, between 2.0% and

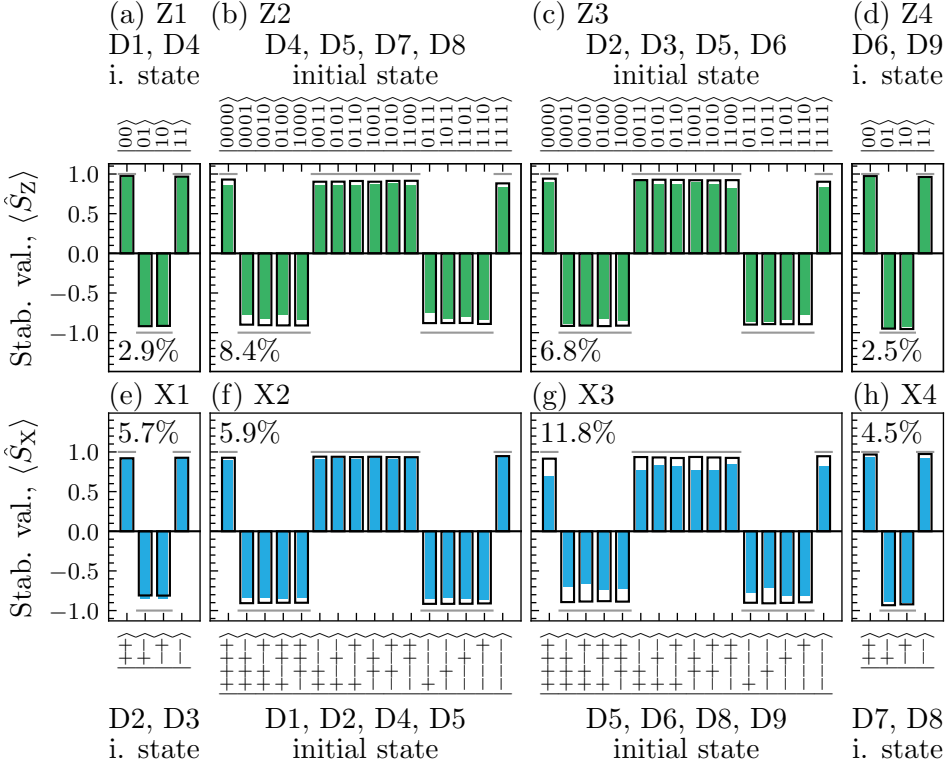


Figure 4.5: Error correction stabilizer fidelity. Average outcomes of stabilizer measurements for (a–d) Z-type and (e–h) X-type stabilizers for various neighboring data qubit states as filled bars. The gray lines and black boxes indicate the target stabilizer value and master equation simulation result, respectively. The average measured stabilizer error probability ε_S is indicated for each stabilizer.

4.4% for weight-two, and between 3.9% and 5.0% for weight-four stabilizers. Additional details of the simulation can be found in Ref. [Krunner22]. Overall, the low error probabilities and good quantitative match between the measured and simulated stabilizer errors indicate that individual stabilizer measurements are working well and the error mechanisms are understood.

To analyze the fidelity of logical state preparation, let's consider the example of preparing the $|0\rangle_L$ state. We prepare the data qubits in the product state $|0\rangle^{\otimes 9}$ and measure one cycle of stabilizers, see Fig. 4.1(b) for the conceptual circuit. The duration of this one cycle of stabilizer measurements is $T_{\text{cyc.}} = 1.1 \mu\text{s}$. Runs where any of the read-out qubits are classified as being in the $|2\rangle$ state are discarded. Because the initially prepared state is a +1 eigenstate of the Z-type stabilizers, their measurement outcomes should ideally be +1. On the other hand, for each of the \hat{S}_{X_i} stabilizers, we expect a random outcome $S_{X_i} = \pm 1$ with equal probability for each value. The measurement projects the state to a mutual eigenstate of all the stabilizers, leaving the value of the logical operator \hat{Z}_L unaffected. The probability of the resulting state $\hat{\rho}$ being in the logical subspace is calculated as $P_L = \text{Tr}(\hat{\Pi}_L \hat{\rho})$, where the projector to the logical subspace is given by

$$\hat{\Pi}_L = \prod_{i=1}^4 \left(\frac{\hat{I} - \hat{S}_{Z_i}}{2} \right) \prod_{i=1}^4 \left(\frac{\hat{I} - S_{X_i} \hat{S}_{X_i}}{2} \right). \quad (4.2)$$

Here, we adjust the sign of the X-type stabilizers to the stabilizer measurement outcomes S_{X_i} in each run of the experiment. Furthermore, the fidelity to the target state is calculated by additionally projecting onto the $\hat{Z}_L = +1$ subspace as $F = \text{Tr}((\hat{I} + \hat{Z}_L) \hat{\Pi}_L \hat{\rho})/2$. Expanding the traces to sums of multi-qubit Pauli operator expectation values, we calculate the values $P_L = 54.2(1)\%$ and $F = 54.0(1)\%$ as the weighted sum of 2^9 experimentally measured terms [Nigg14]. As in Section 3.6, the fidelity of the state within the logical subspace is calculated as $F_L = F/P_L = 99.6(2)\%$. This fidelity corresponds to one minus the probability of an error occurring that is undetectable from the stabilizer measurements in the subsequent cycles.

On the other hand, the overlap of the physical state with any state $\hat{E} |0\rangle_L$, where \hat{E} is a correctable Pauli error, is given by

$$F_{L,C} = \sum_{\hat{E}} \text{Tr}(\hat{E}(\hat{I} + \hat{Z}_L) \hat{\Pi}_L \hat{E}^\dagger \hat{\rho})/2 = 96.0(9)\%. \quad (4.3)$$

Here, we consider an error \hat{E} to be correctable if the class of errors with the same syndrome and same effect on the \hat{Z}_L operator, $\{\hat{P}\hat{E}\}$, where \hat{P} is the product of any subset of stabilizers and \hat{Z}_L , is more probable than the class of errors with the same syndrome but different effect on the \hat{Z}_L operator, $\{\hat{X}_L\hat{P}\hat{E}\}$. We assume that a higher-weight error is always less probable than any set of lower-weight errors. If the weights of two errors are the same, we randomly pick one of them to be more probable. See the supplementary information of Ref. [Krunner22] for more details. The rest of the eigenstates of \hat{Z}_L and \hat{X}_L operators are prepared in a similar fashion, preparing other initial data qubit states, see Section 4.1.

Finally, to assess the performance of our implementation of the code, we repeat the stabilizer measurements for N cycles and extract the logical coherence times and error probabilities per cycle. The logical state is initialized during the first cycle using the sequence described above. Instead of measuring the expectation values of the multi-qubit Pauli operators after the first stabilizer measurement cycle, we now continue measuring the stabilizers for $N - 1$ additional cycles. At the end, we read out the data qubits either in the \hat{Z} or the \hat{X} basis, depending on whether we prepared an eigenstate of \hat{Z}_L or \hat{X}_L , respectively. Again, we discard all runs where we identify any of the read-out qubits as being in the $|2\rangle$ state, which amounts to 7.9(3)% of the runs per stabilizer measurement cycle. We calculate the raw logical operator value and a set of final stabilizer values from the final readout. To decode the errors that occurred during each run of the state preservation experiment and determine whether the logical operator was flipped, we calculate the error syndrome based on all the stabilizer measurement outcomes. We use a minimum-weight perfect matching (MWPM) decoder for the decoding, see Chapter 5 for a detailed description of the decoding process.

The evolution of the expectation values of the logical operators with the decoded correction applied is shown in Fig. 4.6. We find that one minus the error probability for the $|0\rangle_L$ state after $N = 1$ stabilizer measurement cycle, given by $(1 + \langle \hat{Z}_L \rangle)/2 = 95.3\%$, closely matches the fidelity of the prepared state in the correctable subspace as given by Eq. (4.3). By simultaneously fitting the corrected \hat{Z}_L expectation values when preparing $|0\rangle_L$ and $|1\rangle_L$ to an exponential model $\langle \hat{Z}_L \rangle = \langle \hat{Z}_L \rangle_{t=0} \exp(-t/T_1^L)$, we extract a decay time of the \hat{Z}_L operator of $T_1^L = 16.4(5) \mu\text{s}$. Similarly, we extract the decay time of the \hat{X}_L operator of $T_2^L = 18.2(3) \mu\text{s}$ from a fit to the corrected \hat{X}_L expectation value after preparing $|+\rangle_L$ and $|-\rangle_L$. Alternatively, we can express the

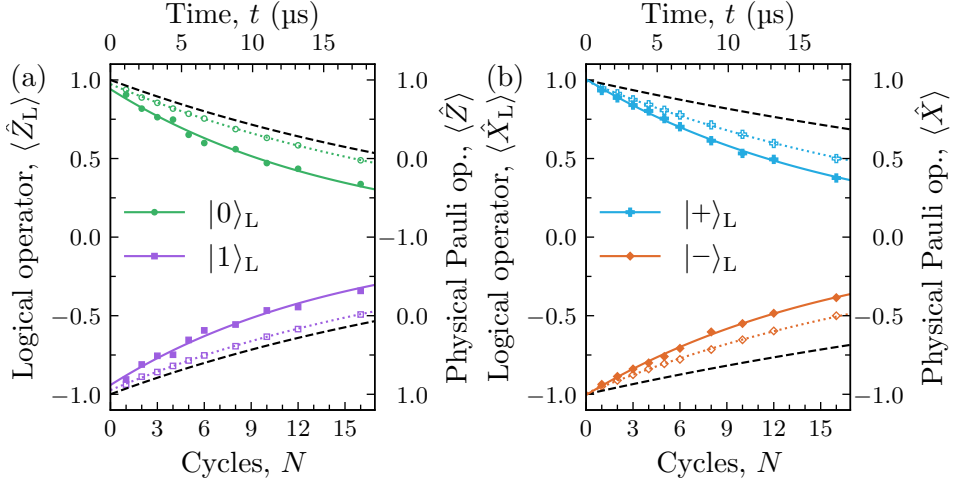


Figure 4.6: Repeated error correction. Evolution of the logical operator expectation values (a) $\langle \hat{Z}_L \rangle$ and (b) $\langle \hat{X}_L \rangle$ for the initial $|0\rangle_L$, $|1\rangle_L$, $|+\rangle_L$, and $|-\rangle_L$ states. The measured and simulated values are indicated as filled and empty markers, respectively. Solid and dotted lines indicate fits to exponential models. The decay of the \hat{Z} and \hat{X} operators with a median time-constant for the physical qubits is shown as dashed lines on the right axis.

performance of the experiment in terms of the probability of logical error happening each cycle, which we find to be $\varepsilon_z^L = [1 - \exp(-T_{\text{cyc.}}/T_1^L)]/2 = 3.23(10)\%$ and $\varepsilon_x^L = [1 - \exp(-T_{\text{cyc.}}/T_2^L)]/2 = 2.93(4)\%$ for errors flipping \hat{Z}_L and \hat{X}_L , respectively. From a simulation using Monte Carlo wave functions, we extract the decay times $T_1^L = 25.7(2) \mu\text{s}$ and $T_2^L = 26.1(2) \mu\text{s}$, corresponding to error probabilities $\varepsilon_z^L = 2.10(1)\%$ and $\varepsilon_x^L = 2.07(1)\%$, in close agreement with the experimental data, see also open markers and dotted lines in Fig. 4.6. Comparing the logical qubit performance to the physical qubits, we find that the \hat{Z}_L and \hat{X}_L decay times are slightly shorter than the median physical qubit energy relaxation time $T_1 = 30 \mu\text{s}$ and echo dephasing time $T_2^e = 49 \mu\text{s}$, see dashed lines in Fig. 4.6. Similarly, the logical error probabilities are only slightly larger than the median physical two-qubit gate error $\varepsilon_{2\text{m}} = 1.2\%$. Assuming a quadratic scaling between the logical and physical error rates [Fowler12b], we expect that only a

modest reduction of the physical error rates could lead to the logical qubit performance surpassing physical qubit performance.

4.5. Technical Challenges

Several technical challenges had to be overcome to achieve the high-fidelity operation of the device required for the logical error rate to approach break-even with the physical error rate. These challenges encompassed drive-, flux- and readout-crosstalk, flux-bias pulse distortion compensation, accurate timing calibration of the pulses, and mitigating interactions with parasitic two-level systems (TLSs) on the device. We discuss one particular readout crosstalk mechanism, that is, intermodulation distortion in the traveling-wave parametric amplifier (TWPA) that is used to amplify the readout signals, in detail in Chapter 6. In this section, we discuss two specific challenges: drive crosstalk and the interactions with parasitic TLSs.

4.5.1. Drive Crosstalk

To characterize the coupling rates between the drive lines and qubits of the device, we use a cross-Rabi measurement. Specifically, we measure the excited state population of a qubit Q_j while sweeping the amplitude of a 400-ns-long drive pulse with a Gaussian envelope ($\sigma = 100$ ns) that is applied to drive line DL_{Q_i} of Q_i at the frequency of qubit Q_j . We extract the pulse amplitude $a_{Q_j}^{DL_{Q_i}}$ corresponding to a π -rotation from a cosine fit. Analysis of the ratios of amplitudes for driving qubits Q_j and Q_i via drive line DL_{Q_i} of Q_i reveals that the cross-talk is mostly effectively suppressed, see Fig. 4.7(a).

A few qubit pairs, however, have larger-than-expected cross-couplings. For example, the qubit and drive line pairs Z1- DL_{D4} , D1- DL_{X2} , X2- DL_{D5} , D9- DL_{X3} , and Z4- DL_{D6} are as strongly coupled as the drive lines to their targeted qubits. This cross-coupling is likely mediated by the strongly-coupled qubit-qubit couplers, see Fig. 4.3. However, since these drive lines address qubits in a different frequency band compared to the cross-coupled qubits, the cross-driving will be far-detuned. Based on simulated evolution under the detuned drive, the frequency shift of the cross-coupled qubit when applying an X gate on the targeted qubit leads to average errors of $\epsilon_{1m} = 0.17\%$ and 0.06% with respect to the identity operation for the two

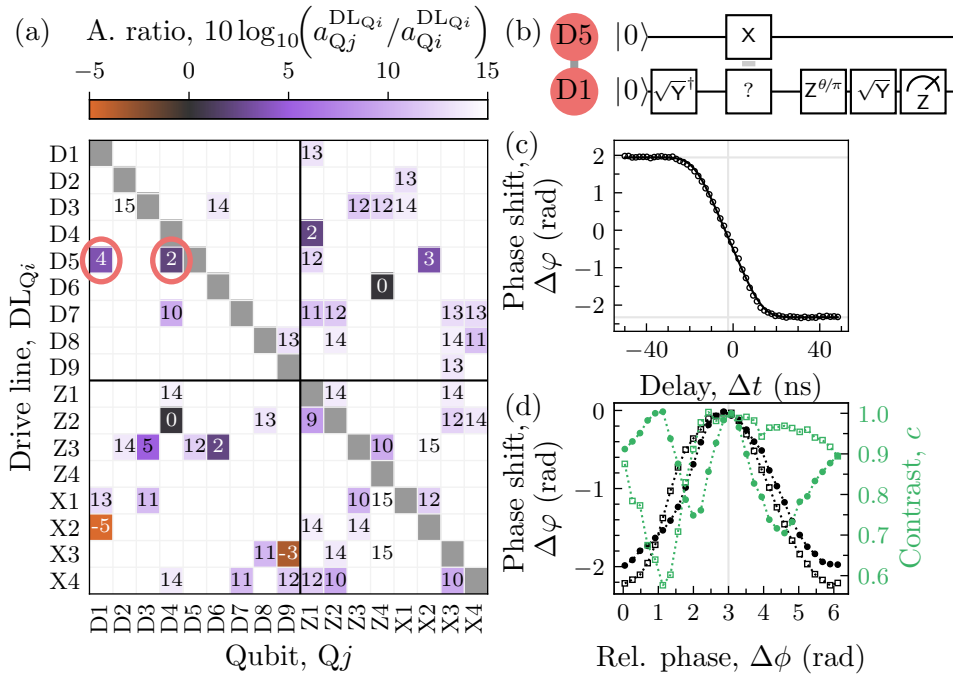


Figure 4.7: Drive crosstalk. (a) Logarithm of the ratio of pulse amplitudes needed to drive a π -rotation on qubits Q_j and Q_i via the drive line DL_{Q_i} of qubit Q_i . The ratios less than $10^{1.5} \approx 32$ are indicated with numbers. The two drive line and qubit pairs for which we interferometrically cancel the crosstalk are circled in red. (b) The circuit for the calibration of crosstalk cancellation. The $?$ denotes the combined effect of the X pulse on D5 and the cancellation pulse applied to drive line of D1. The angle θ of the $Z^{\theta/\pi}$ gate is swept to find the phase shift and contrast loss due to the pulse on D5. (c) Phase shift $\Delta\varphi$ of D1 as a function of cancellation pulse delay Δt (circles) together with a fit (line) to an empirical Gaussian-filtered piecewise linear function. The gray lines indicate the minimum, maximum and symmetry point of the fitted model. (d) Phase shift $\Delta\varphi$ (black) and contrast c (green) of D1 as a function of the relative phase $\Delta\phi$ between the pulses applied to drive lines of D1 and D5. The filled circles and open squares indicate values when an X or Y gate is applied to D5, respectively. The dotted lines connect the points as guides to the eye, and the gray vertical line indicates the optimal relative phase $\Delta\phi$.

worst pairs D1-DL_{X2} and D9-DL_{X3}, respectively. The error is less than 0.01% for any other auxiliary and data qubit pair. For all qubit pairs within the same frequency band, we expect to find average errors due to drive crosstalk below 0.11%, except for errors on D1 and D4 when applying π -rotations on D5, which we calculate to be $\varepsilon_{1m} = 19.2\%$ and 16.5% , respectively. The large cross-coupling rate between the drive line DL_{D5} and qubits D1 and D4 is likely due to a combination of capacitive coupling at points where the drive line crosses over the qubit-qubit couplers between Z1-D1 and X2-D4, see Fig. 4.3. Another cross-coupling mechanism could be inductive coupling between the bond wires connecting the drive lines to the carrier circuit board, see Section 2.5 and Ref. [Haegi23].

We mitigate the crosstalk from drive line DL_{D5} to the cross-coupled qubits D1 and D4 by applying pulses to their respective drive lines which interferometrically cancel with the cross-coupled drive. Achieving high-fidelity cancellation requires an accurate calibration of the delay, phase, and amplitude of the cancellation pulse relative to the effect of the cross-coupled pulse sent to DL_{D5}. To this end, we use a Ramsey sequence on the cross-coupled qubit D1 or D4, where we apply an X or a Y gate on the target qubit D5 at the middle of the circuit, see Fig. 4.7(b). Ideally, we want to implement an X or a Y on the target qubit D5 and an identity on the cross-coupled qubit D1 or D4. Because in our device the bandwidth of the pulse on the target qubit is comparable to its detuning from the cross-coupled qubit, the detuned drive can implement an arbitrary single-qubit rotation of the cross-coupled qubit.

To align the pulses in time, we sweep the relative delay of the cancellation pulse and the cross-coupled pulse Δt and measure the phase shift $\Delta\varphi$ of the cross-coupled qubit using the Ramsey sequence, see Fig. 4.7(c). We see a difference in $\Delta\varphi$ depending on the order of arrival of the cancellation pulse and the cross-coupled pulse because the rotation axes are different and therefore the operations do not commute. Due to the symmetry of the pulse sequence, the cross-coupled pulse and cancellation pulse are aligned at the symmetry point of the response, see the vertical gray line in Fig. 4.7(c).

We calibrate the relative phase $\Delta\phi$ and amplitude of the cancellation pulse with a similar Ramsey sequence, sweeping them and optimizing for a small Ramsey phase shift $\Delta\varphi$ and a high contrast c , see Fig. 4.7(d). Although the optimization landscape is complex due to the off-resonant drive with a time-dependent pulse envelope, we find a set of parameters where $\Delta\varphi \approx 0$ and $c \approx 1$ for both X and Y gates on D5. We note that, for the phase

difference of the cancellation pulse and the cross-coupled pulse to remain stable over long timescales, it is crucial to use the same microwave generator as the local oscillator when up-converting the pulses from baseband to microwave frequencies.

4.5.2. Parasitic Two-Level Systems

A major challenge in scaling superconducting-circuit-based quantum processors to larger scales [Arute19, Klimov20] is the ubiquitous presence of parasitic TLSs [Simmonds04, Müller19]. The exact microscopic nature of the TLSs is not fully understood, but they have been observed in various superconducting qubit architectures [Simmonds04, Barends13, Sun23], giving rise to fluctuations of qubit frequency and decay rates. While thermal fluctuations of low-frequency TLSs can cause dephasing, high-frequency TLSs can interact directly with the qubit, leading to energy relaxation. On our device, we observe many such high-frequency parasitic modes with an average density of 0.83(16)/GHz [Zanuz23] when counting defects with coupling rates $g_{\text{TLS}}/2\pi > 0.5$ MHz. An avoided crossing of the qubit D2 with one such strongly-coupled defect is visible in two-tone spectroscopy, see Fig. 4.8(a), where the readout signal is shown as a function of qubit drive frequency and flux bias. We extract a coupling rate of $g_{\text{TLS}}/2\pi = 31.5$ MHz from a fit to an avoided-crossing model, which is significantly larger than the coupling rate between neighboring qubits $J_{\text{QQ}}/2\pi \approx 7$ MHz.

To verify that the parasitic mode is indeed a two-level system, and not a spurious harmonic mode, we perform the following experiment. First, we excite the defect by driving it via the drive line of D2 with a 400-ns-long Gaussian pulse ($\sigma = 100$ ns) with a variable amplitude Ω_0 . We then tune the qubit into resonance with the defect using a flux-bias pulse for a duration τ , during which the systems undergo resonant population swaps, see Fig. 4.8(b,c) for the resulting qubit populations and the circuit.

To compare the experimental results with simulations, we calculate the state of the defect by evolving the ground state under the effect of the drive Hamiltonian

$$\hat{H}_d = \Omega(t)e^{-i\Delta_d t}\hat{\sigma}_-^{\text{TLS}} + \text{c.t.}, \quad (4.4)$$

with the pulse envelope $\Omega(t) = \Omega_0 e^{-t^2/2\sigma^2}$ and detuning Δ_d . Here, $\hat{\sigma}_-^{\text{TLS}}$ is the annihilation operator of the parasitic TLS. The resonant interaction

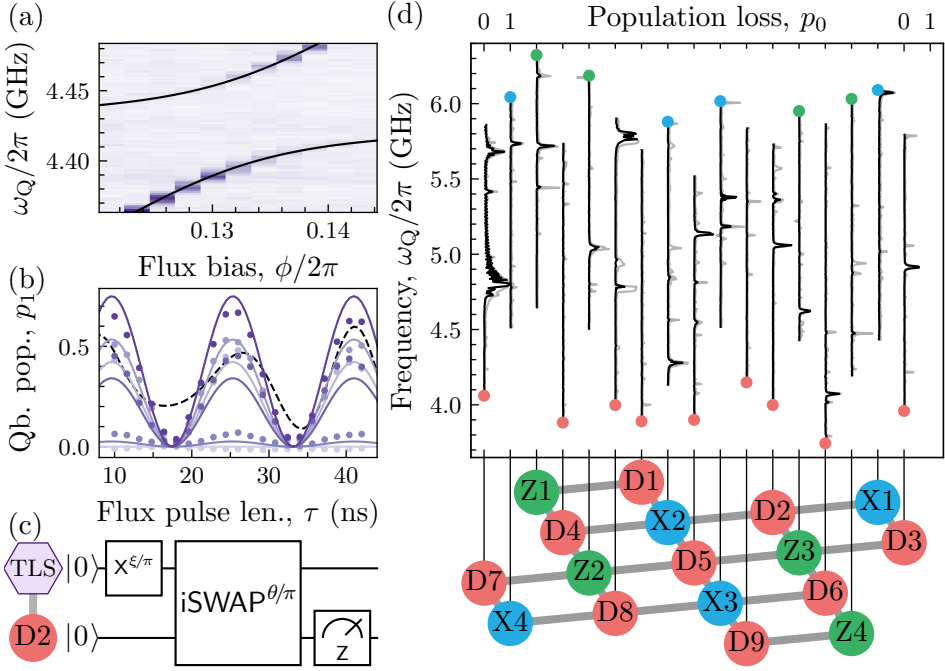


Figure 4.8: Two-level systems. (a) Two-tone spectroscopy of qubit D2 as a function of the flux bias ϕ , with color intensity indicating the principal component of the readout signal. The coupling rate to a parasitic TLS is extracted from a fit to an avoided crossing model shown in black. (b) Qubit population (dots) after exciting the TLS with a Gaussian pulse and resonant interaction between the qubit and TLS for a duration τ . The excitation pulse amplitude is swept uniformly between zero (light purple) and the maximum (dark purple). A fit to a model including a detuned drive is shown as solid lines. The dashed black line indicates the qubit population if the parasitic mode was a harmonic oscillator, with an initial displacement of 1, instead of a two-level system. (c) Circuit diagram for the experiment in (b). Resonant interaction for τ implements the operation $i\text{SWAP}^{\theta/\pi}$ with $\theta = -2\tau g_{\text{TLS}}$. (d) Defect-spectroscopies of the 17 qubits. The black and gray lines indicate excited state population loss after 100 ns and 1 μ s at the indicated frequency, respectively. The small circles indicate the idling flux-bias point. The data in panels (a) and (b) is taken during a different cool-down of the cryostat than the data in panel (d).

between the qubit and the defect is described by the Hamiltonian

$$\hat{H}_{\text{int}} = g_{\text{TLS}} \hat{\sigma}_{-}^{\text{TLS}} \hat{\sigma}_{+}^{\text{D2}} + \text{c.t.}, \quad (4.5)$$

where $\hat{\sigma}_{+}^{\text{D2}} = (\hat{X}_{\text{D2}} - i\hat{Y}_{\text{D2}})/2$ is the creation operator of the qubit. The experimental data shows good agreement with the described model, see the solid lines in Fig. 4.8(b). The remaining differences between the experimental data and simulation might be due to compression of the up-conversion electronics when applying high-amplitude pulses needed to drive the defect mode. In contrast, replacing the two-level defect annihilation operator $\hat{\sigma}_{-}^{\text{TLS}}$ in Eq. (4.5) with a harmonic oscillator annihilation operator \hat{a}^{TLS} yields the time evolution indicated with a dashed line. The model corresponding to the two-level defect matches the data much better than the one corresponding to the spurious harmonic mode, indicating that the defect is indeed a TLS. Employing the direct microwave drive of the TLSs and readout by swapping into the qubit, we characterize the coherence times of five defects in time domain. We find energy relaxation times T_1 between $0.3 \mu\text{s}$ and $1.9 \mu\text{s}$, Ramsey dephasing times T_2^* between $0.08 \mu\text{s}$ and $1.0 \mu\text{s}$, and echo dephasing times T_2^e between $0.2 \mu\text{s}$ and $1.5 \mu\text{s}$, consistent with previously reported values [Lisenfeld16].

To characterize the overall count and frequency-distribution of the two-level systems, we employ the defect spectroscopy method [Shalibo10, Lisenfeld15]. We first excite the qubit to the $|1\rangle$ state, and then tune it to various interaction frequencies ω_Q for either $\tau = 100 \text{ ns}$ or $1 \mu\text{s}$ using a square flux-bias pulse. The final population p_0 of the $|0\rangle$ state indicates the excitation loss at the frequency ω_Q , see Fig. 4.8(d). We see a multitude of peaks in the defect spectra, which we associate with individual TLSs coupled to the qubit with various rates. Most of the observed defects have weak couplings to the qubit and do not significantly affect the execution of the surface code protocol as long as the qubits are not resonant with the defect during idle periods or two-qubit gates. However, we also observe a few very-strongly-coupled defects, for which the population loss is significant $p_0 > 1\%$ even when the qubit only crosses the defect without staying resonant during the flat part of the flux-bias pulse. These very-strongly-coupled defects usually exhibit an oscillating tail in the defect spectrum when measured with a short flux pulse ($\tau = 100 \text{ ns}$) due to interference between the coherent population swaps when crossing in the two directions, see for example the defect at 4.8 GHz coupled to D7 in Fig. 4.8(d). The oscillations are not visible with the longer

flux pulse length of $\tau = 1 \mu\text{s}$ due to dephasing of the defect during that time. We observe one or two of such defects per 17 qubits on average. To prevent errors due to interactions with the very-strongly-coupled TLSs, we choose gate interaction frequencies that avoid crossing these defects. However, this constraint can limit the range of available interaction frequencies, and thereby lead to increased dispersive qubit-qubit couplings during gates. In the experimental results presented in Section 4.4, we reduced the interaction frequency for the gate Z2-D7 to avoid crossing D7 with the strongly coupled defect. Furthermore, we changed the gate order from that indicated in Fig. 4.1(c) by swapping the time slots of gates Z3-D5 and Z3-D6 to avoid interactions between Z2 and D5 when implementing the gates Z2-D7 and Z3-D5 in parallel.

4.6. Discussion

We have presented the first demonstration of a repeated quantum error correction of errors on both \hat{Z}_L and \hat{X}_L operators in a superconducting circuit architecture. The necessary technological components for this result include high-fidelity and low-crosstalk frequency-multiplexed readout, and high-fidelity two-qubit and single-qubit gates, as well as a high-yield fabrication process. We achieve logical error probabilities that are close to, but slightly higher than the native physical error probabilities, indicating that we are approaching the break-even point. However, there are a few technical challenges that were largely unaddressed in this work that need to be overcome for future experiments of larger scale and higher fidelity, which we discuss below.

Physical errors that lead to highly correlated error syndromes are detrimental for the performance of QEC [Aharonov06, Fowler13a]. In particular, in this work, we mitigated the effect of leakage of the transmon qubits outside the computational subspace, mostly caused by two-qubit gates and readout, by discarding any runs where the auxiliary qubit was read out in the $|2\rangle$ state. By extrapolating the current per-cycle leakage probability of 7.9% to a $d = 5$ code, we expect a per-round leakage probability of 21.9%, assuming the leakage probability for each auxiliary qubit stays the same. At this leakage rate, the survival probability after $N = 20$ cycles of stabilizer measurements will be just 0.7%. To overcome the challenge in a scalable fashion, it will be crucial to actively bring the qubits back to the

computational subspace, for which various techniques have been recently demonstrated [Miao22, Marques23, Lacroix23], in addition to reducing the leakage caused by individual operations.

Another major challenge for realizing the experiment were the strong interactions between qubits and spurious TLSs. The few very-strongly-coupled defects that we observed in each of the seven defect configurations on this device severely limited the choice of interaction frequencies such that executing all the gates without substantial population loss into the defects was not possible. Only for the one defect configuration, see Fig. 4.8(d), and by changing the gate order, were we able to implement all the stabilizer measurements with high fidelity. While the defect configurations randomize when warming up the device to room temperature, the probability of a usable defect mode configuration becomes exponentially small with increasing qubit numbers. Therefore, reducing the density of very-strongly-coupled defects will be crucial for implementing a larger-scale surface code. One approach to achieve this would be to reduce the junction size, as there is evidence that the defect density scales with the dimensions of the junction [Mamin21, Bilmes22, Zanuz23]. Alternatively, different junction fabrication techniques and materials could be investigated [Oh06, Kim21]. It will also be useful to employ flux pulse shapes that can cross defects or other qubits without significant population exchange [Orekhov22], but the robustness of such schemes against time-variation of defect properties is yet to be demonstrated. It has also been demonstrated that the defect frequencies can be controlled by changing the mechanical strain in the device, which might allow to avoid collisions with the very-strongly-coupled defects [Lisenfeld16].

Overcoming the technical challenges identified in this study would open up possibilities for the realization of several interesting experiments. To demonstrate that QEC can be useful for exponentially suppressing the logical error probability, experiments where the distance of the code is increased are required. An experiment where a $d = 5$ surface code marginally outperforms a $d = 3$ code has recently been demonstrated in Ref. [Acharya23]. Furthermore, the implementation of two-qubit gates [Horsman12, Fowler12b], and the fault-tolerant preparation of magic states [Fowler12b] required for logical non-Clifford gates are yet to be demonstrated. Because the gate sequences of these operations are conditional on the outcomes of mid-circuit logical measurements [Gottesman99b, Horsman12], real-time decoding of the syndromes will be required to implement them without postselection. In a recent experiment, high-fidelity but non-fault-tolerant preparation of

arbitrary states in a surface code was demonstrated [Ye23].

Decoding Error Syndromes

Typical errors in the quantum error correction (QEC) codes are accompanied by flips of the stabilizer values. These changes in the stabilizer values, called *syndrome elements*, can then be used to infer whether the logical operator was flipped, a process called decoding. While the main challenge in implementing quantum error corrected devices remains the production of large devices with low error rates, a topic of rising relevance is how to efficiently decode large scale devices [Battistel23, iOlius23]. Accurate decoding always relies on a good error model of the device. The topic of this chapter, based on Ref. [Remm23b], is to describe how we implement the minimum-weight perfect matching (MWPM) decoder for the experimental results presented in Chapter 4, and how the correlations in the syndrome data can be used to derive an error model of the device. This error model can then be used to find optimal parameters for the decoder, but also to diagnose issues in device performance such as crosstalk or leakage.

Different physical errors at various locations in the gate sequence lead to specific stabilizers being flipped. We discuss how basic physical errors propagate through the circuit and classify their corresponding signatures in Section 5.1. We then explain how one of the most common decoding algorithms, the MWPM decoder, was implemented for the results presented in Chapter 4 in Section 5.2. In previously published work, the decoding of experimental quantum error correction data has relied on error models either numerically optimized for maximal logical fidelity [Sundaresan23], analytically calculated from correlations between syndrome elements [Chen21, Krinner22], or numerically optimized to match the higher-order correlations between syndrome elements [Chen22, Acharya23]. Here, we present an analytical method to calculate the probability of any error event that can flip an arbitrary number of syndrome elements, based on the higher-order correlations in the

syndrome data, see Section 5.3. The method allows for a characterization of the full error model for any decoding algorithm using the same circuit as for the final QEC experiment. In addition to using the error model for decoding, it is also valuable for characterizing device performance. For example, we find significant presence of errors that correlate with leakage of the data qubits outside the computational subspace and have signatures that span multiple syndrome elements over many cycles, which we discuss in detail in Section 5.4.

5.1. From Errors to the Syndrome

Each stabilizer \hat{S}_{Ai} of the surface code is repeatedly measured during the operation of the code. In our implementation, without resetting the auxiliary qubits, the effect of the stabilizer measurement circuit is to flip the state of the corresponding auxiliary qubit Ai if the stabilizer value is $S_{Ai} = -1$, that is, the parity of data qubits is odd. We can therefore infer the stabilizer value $S_{Ai}^{(m)} = M_{Ai}^{(m-1)} M_{Ai}^{(m)} = \pm 1$ from the change of the measurement outcomes $M_{Ai}^{(m)} = \pm 1$, with m being the index of the error correction cycle.

Because the stabilizers involving \hat{X} and \hat{Z} operators of each data qubit are repeatedly measured, all physical single-qubit errors get projected to bit and phase flips. These bit and phase flips of the physical qubits will cause some stabilizers to flip and might also flip the logical operator values \hat{X}_L and \hat{Z}_L , depending on where the error occurred. Because the physical errors are signaled not by specific stabilizer values, but by the changes in them, we provide the syndrome elements $\sigma_{Ai}^{(m)} = (1 - S_{Ai}^{(m-1)} S_{Ai}^{(m)})/2 = 0, 1$ as inputs to the decoding algorithm. The set of all syndromes elements generated from one run of the QEC experiment is called the *syndrome*. Furthermore, we call the set of syndrome elements that is flipped by an independent physical error the *signature* of that error. Next we will discuss the signatures of the most common errors.

Let's consider a bit flip (\hat{X}) error on one of the data qubits, indicated by the orange cross in Fig. 5.1(a). Note, that this error is equivalent to a phase flip (\hat{Z}) before the preceding \sqrt{Y} gate on that qubit. Because a bit flip error before a CZ gate creates a phase flip after the CZ gate on the other qubit, the error propagates to the two auxiliary qubits that neighbor the data qubit as phase flip errors. These phase flip errors will change the outcomes of the following auxiliary qubit readouts. As the error on the data qubit

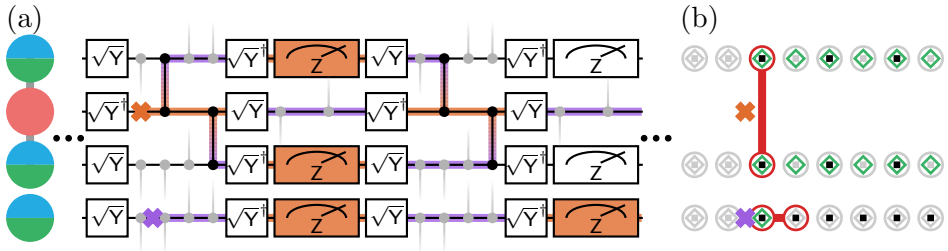


Figure 5.1: Syndrome generation. (a) The circuit for two cycles of syndrome measurement, with a data qubit as a red circle and auxiliary qubits as split blue-green circles. The propagation of a bit flip error (orange cross) and a phase flip error (purple cross) is indicated with orange (as a bit flip) and purple (as a phase flip) lines. The measurement outcomes that are flipped as a result of the bit flip error are marked with an orange background. (b) The corresponding measurement outcome flips are indicated as black ($M = -1$) and gray ($M = +1$) squares, stabilizer value flips as green ($S = -1$) and gray ($S = +1$) diamonds, and syndrome element flips as red ($\sigma = 1$) and gray ($\sigma = 0$) circles. The physical error locations are indicated as orange and purple crosses and the two syndrome elements that are flipped by each error are connected by a red line.

remains, the auxiliary qubits will be flipped again in every consecutive cycle the same way. Converting the measurement outcome flip $M_{A_i}^{(m)}$ to stabilizer flip $S_{A_i}^{(m)}$ and to syndrome elements $\sigma_{A_i}^{(m)}$ as illustrated in Fig. 5.1(b), we see that two syndrome elements are created by this error. The events are detected on neighboring auxiliary qubits during the same cycle. We group all errors with such signatures together and label them $\mathbf{S}^{X|Z}$ for errors with space-separated signatures due to \hat{X} and \hat{Z} errors on data qubits.

Because the data qubits are rotated using \sqrt{Y} or \sqrt{Y}^\dagger gates between each half-cycle of parity maps, all of which are implemented using the same physical CZ gate, see also Fig. 4.1(b), both the X- and Z-type stabilizer measurement circuits are sensitive to the same physical errors. Therefore, these $\mathbf{S}^{X|Z}$ errors appear on neighboring X- and Z-type auxiliary qubits in the same fashion, as also indicated by the split color of the auxiliary qubits in Fig. 5.1, and there is no connection between physical error type and the stabilizer type. This is a general observation, also valid for the other error

classes described below.

Another common error is a phase flip error on an auxiliary qubit, see the purple cross in Fig. 5.1(a), or equivalently a bit flip error just before, during, or after measurement. In this case, the error flips all following measurement outcomes $M_{Ai}^{(m)}$ on that auxiliary qubit, which is then interpreted as two consecutive syndrome element flips on that auxiliary qubit, see Fig. 5.1(b). We label all errors with such signatures as **T** for errors with time-separated signatures.

A few additional error classes are shown in Fig. 5.2. If an \hat{X} error occurs on a data qubit between the two CZ gates of one cycle, then the syndrome elements are flipped on the neighboring auxiliary qubits on consecutive cycles. We label such errors as **ST^X** for errors with a space-time separated signature. If an \hat{X} error occurs on an auxiliary qubit that is used to measure a weight-four Z-type stabilizer at the middle of the parity map, then this error propagates as phase flip errors to two neighboring data qubits that will do a gate with that auxiliary qubit next. Depending on the gate order in the parity map, these phase flip errors will flip two or four neighboring syndrome elements of X-type. We label such errors as **H^X** for \hat{X} -caused hook errors. Bit flip errors on the auxiliary qubit at other times during the parity map lead to a phase flip error on zero, one, three, or four neighboring data qubits. Because the neighboring qubits are part of a Z-type stabilizer, and the application of a stabilizer has no effect on the quantum state, the error propagating to three or four neighboring qubits is equivalent to errors on the complementary one or zero neighboring data qubits. Therefore, these errors are indistinguishable from single phase flip errors on data qubits, which belong to the **S^{X|Z}** class. Again, the situation is the same for \hat{X} errors on X-type auxiliary qubits, in which case Z-type syndrome elements are flipped. Finally, also \hat{Y} errors can occur at the same locations as the **S^{X|Z}**, **ST^X** and **H^X** errors, which have signatures flipping both Z- and X-type syndrome elements. We label the corresponding error classes as **S^Y**, **ST^Y** and **H^Y**. Near the boundary of the surface code lattice, errors can have signatures that include only a single syndrome element, which we will label boundary errors **B**. Finally, we label measurement misclassification errors, for which the auxiliary qubit state is incorrectly classified, but does not get flipped, as **T'** errors. These errors are equivalent to a correlated bit flip just before and after a perfect measurement, and they flip two syndrome elements on a single auxiliary qubit $\Delta m = 2$ cycles apart.

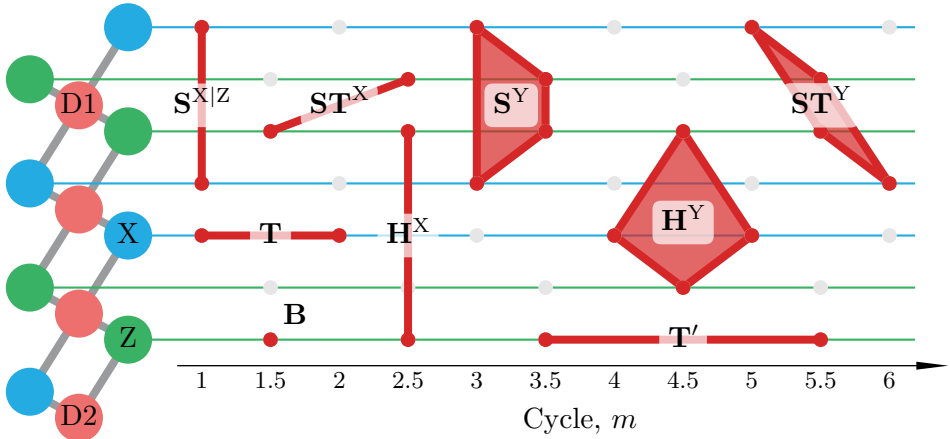


Figure 5.2: Error signature classes. Examples of error signatures caused by single-qubit Pauli errors of various signature classes. Due to the pipelined stabilizer measurement circuit, different types of stabilizer measurements are separated by a half-cycle. Each signature includes the syndrome elements flips (red circles) connected by red lines and polygons. Pauli \hat{X} and \hat{Z} errors on a data qubit D1 have space-like ($\mathbf{S}^{X|Z}$) and space-time-like (\mathbf{ST}^X) signatures, while Pauli \hat{X} and \hat{Z} errors on auxiliary qubit X can have time-like (\mathbf{T}) and hook (\mathbf{H}^X) signatures, all of which flip a pair of syndrome elements. Pauli \hat{Y} errors, however, lead to syndromes that are detected on up-to-four auxiliary qubits and have space-like (\mathbf{S}^Y), space-time-like (\mathbf{ST}^Y), and hook (\mathbf{H}^Y) signatures. Furthermore, errors on the border of the lattice on D2 have a signature on a single auxiliary qubit only (\mathbf{B}) and readout misclassification errors on Z lead to time-like signatures on syndrome elements two cycles apart (\mathbf{T}').

We also consider correlated two-qubit Pauli errors, not shown in Fig. 5.2, which might arise due to the two-qubit gates. We distinguish between the \mathbf{M}^{ZZ} class, corresponding to a correlated phase flip error $\hat{Z} \otimes \hat{Z}$, and the \mathbf{M}^{XY} class, corresponding to a correlated bit flip error $\hat{X} \otimes \hat{X}$, $\hat{X} \otimes \hat{Y}$, $\hat{Y} \otimes \hat{X}$ or $\hat{Y} \otimes \hat{Y}$. Other two-qubit Pauli errors are equivalent to a single-qubit Pauli error on one of the qubits before or after the CZ gate. While we do not expect to observe correlated bit flips, errors of the \mathbf{M}^{ZZ} class could occur due to residual interactions between the qubits [Krinner20] or a miscalibrated conditional phase of the CZ gate.

5.2. Minimum-Weight Perfect Matching Decoder

There are various strategies for decoding the syndrome data. Most accurate results can be achieved by maximum likelihood decoding, in which case all possible combinations of physical errors that are consistent with the observed syndrome data are considered. Each set of physical errors leads to some correction of the logical qubit state, and the decoder picks the correction with the largest total likelihood. Since the number of physical error combinations is exponentially large in code size and number of executed cycles, maximum likelihood decoding is prohibitively expensive for all but the very smallest of codes [Iyer15]. Approximations of the likelihood calculation using tensor networks can reduce the complexity [Bravyi14], but the complexity remains high enough to not be considered scalable for realistic datasets [Acharya23].

When considering one type of stabilizers at a time, the signature of each physical error has at most two syndrome element flips. Furthermore, a chain of neighboring errors leads to flipped syndrome elements only at the ends of the chain, since the syndrome element flips in the middle of the chain cancel with each other, see Section 1.3. This property allows for a much more efficient MWPM decoder to be used. In MWPM decoding, all nonzero elements of the syndrome are matched in pairs. Because the logical correction is independent of the exact path of the chain of physical errors, a matching leads to a unique logical correction operator. By assigning a weight to each potential pair of nonzero elements of the syndrome according to the likelihood of its occurrence, the problem of finding the most likely matching can be converted to finding the minimum-weight matching.

Compared to maximum likelihood decoding, this leads to two approximations. Foremost, by decoding the Z- and X-type stabilizers separately,

we ignore the correlations between the syndrome types, which can contain extra information in the presence of errors that lead to flipping of both types of stabilizers. Second, we find the most likely matching, but ignore that many matchings can lead to the same logical correction, and the most likely logical correction might be different from the logical correction corresponding to the most likely matching. For large surface codes, it might be necessary to set the weights according to the likelihood of the most likely error chain connecting the syndrome elements [Fowler13b, Higgott23b], not the total likelihood of connecting the syndrome elements via any equivalent path [Stace10, O’Brien17], since the former is more efficient to calculate, which could lead to further errors.

Next, we will discuss the detailed steps for minimum-weight perfect matching. The first step, which can be done offline before running the surface code experiment, is to construct an auxiliary qubit graph (also called a matching graph [Higgott22] or ancilla graph [O’Brien17]), where each vertex k corresponds to a syndrome element $\sigma_{A_i}^{(m)}$ and each edge $q = (k, k')$ corresponds to an uncorrelated physical error process, which flips the connected syndrome elements k and k' , see Fig. 5.3(a). In addition, there are two boundary vertices, which are connected to the syndrome elements near the two boundaries of the surface code lattice that can be flipped on their own. Physically, there might be several independent errors that have the same error signature, but in the context of the auxiliary qubit graph, we consider them as a single process, as they can not be distinguished from the syndrome data. In the analysis, we assume that the effect of those errors on the logical operators is identical, which is the case unless correlated physical errors on $\lfloor (d+1)/2 \rfloor$ data qubits exist. An error probability p_q is associated with each edge of the auxiliary qubit graph. The edges and their probabilities amount to the effective error model of the device, which can be constructed either from an independent physical error model, or based on the correlations in the syndrome data [Spitz18], the latter of which is the main topic of this work, see Section 5.3.

As the next step, for each run of the surface code experiment, a fully connected syndrome graph is constructed, where the vertices correspond to nonzero syndrome elements, see Fig. 5.3(b). A weight w_q is associated with each edge q , which is equal to the negative logarithm of the probability that any chain of errors flipped the connected syndrome elements. Up to first

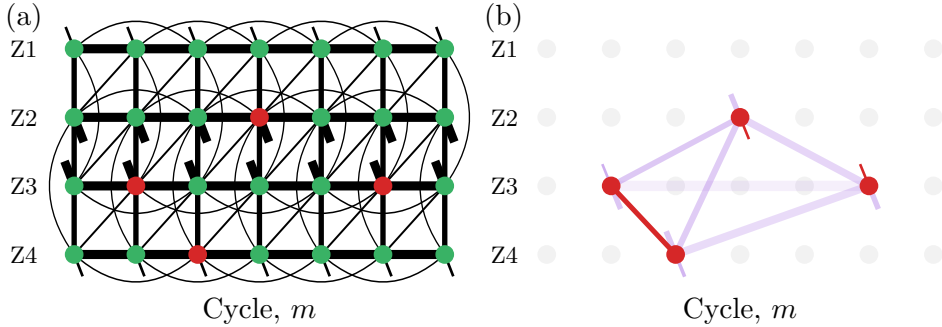


Figure 5.3: Decoding graphs for MWPM. (a) The auxiliary qubit graph for seven cycles of syndrome extraction. Vertices correspond to the measured syndrome elements, while the edge thickness indicates probability of an independent error that flips the connected syndrome elements. The widths of the open edges pointing to top-left and bottom-right indicate boundary error probabilities and their direction to which boundary the syndrome element is connected. (b) The syndrome graph. Vertices are the nonzero syndrome elements of the auxiliary qubit graph, and the thickness and transparency of the edges indicate the weight of the edge for the MWPM decoding. The best matching, which includes the edges between Z3 and Z4, Z2 and the right boundary, and Z3 and the left boundary, is indicated in red. Note that in the auxiliary qubit graph, thick lines indicate probable errors, but in the syndrome graph, thin lines indicate probable error chains.

order in the error probabilities, it can be calculated as [O’Brien17]

$$w_q \approx -\ln \left(\sum_{R \in \mathcal{R}} \prod_{r \in R} p_r \right), \quad (5.1)$$

where \mathcal{R} denotes the set of possible paths between the endpoints of q in the auxiliary qubit graph that does not go through the boundaries, and r are the edges in one of those paths R . For not-too-large code distances, these weights can conveniently be precalculated as [O’Brien17]

$$\mathbf{w} = -\ln \left((\mathbf{1} - \mathbf{A})^{-1} - \mathbf{1} \right), \quad (5.2)$$

where \mathbf{w} is a matrix of weights between all the potential nodes of the syndrome graph, \mathbf{A} is the directed adjacency matrix of the auxiliary qubit

graph with all probabilities going out from the boundary nodes set to zero, $\mathbf{1}$ is the identity matrix, and the logarithm is taken element-wise.

In practice, the error probabilities are not expected to change much from cycle to cycle in the middle of the error correction experiment, and one can calculate the weights as a function of only the cycle difference $\Delta m = m' - m$ instead of cycles m and m'

$$p_{(\sigma_{A_i}^{(m)}, \sigma_{A_j}^{(m')})} = p_{A_i, A_j}^{(\Delta m)}. \quad (5.3)$$

Using this approximation for syndrome elements near logical state preparation and measurement will lead to slightly suboptimal fidelities for those operations, as the error probabilities might be different at the two time-boundaries.

For example, for X-type stabilizers in a $d = 3$ surface code data, see Chapter 4, we can calculate the adjacency matrix for a maximum cycle difference of $\Delta m_{\max} = 2$ as

$$\mathbf{A} = \begin{pmatrix} \mathbf{A}^{(0)} & \mathbf{A}^{(1)} & \mathbf{A}^{(2)} & \mathbf{0} & \mathbf{0} & \mathbf{B} \\ \mathbf{A}^{(-1)} & \mathbf{A}^{(0)} & \mathbf{A}^{(1)} & \mathbf{A}^{(2)} & \mathbf{0} & \mathbf{B} \\ \mathbf{A}^{(-2)} & \mathbf{A}^{(-1)} & \mathbf{A}^{(0)} & \mathbf{A}^{(1)} & \mathbf{A}^{(2)} & \mathbf{B} \\ \mathbf{0} & \mathbf{A}^{(-2)} & \mathbf{A}^{(-1)} & \mathbf{A}^{(0)} & \mathbf{A}^{(1)} & \mathbf{B} \\ \mathbf{0} & \mathbf{0} & \mathbf{A}^{(-2)} & \mathbf{A}^{(-1)} & \mathbf{A}^{(0)} & \mathbf{B} \\ \mathbf{0} & \mathbf{0} & \mathbf{0} & \mathbf{0} & \mathbf{0} & \mathbf{0} \end{pmatrix}, \quad (5.4)$$

with the cycle-shifted adjacency matrix

$$\left(\mathbf{A}^{(0)}\right)_{i,i} = 0 \quad \text{and} \quad \left(\mathbf{A}^{(\Delta m)}\right)_{i,j} = p_{X_i, X_j}^{(\Delta m)}, \quad (5.5)$$

and the boundary adjacency matrix

$$\mathbf{B} = \begin{pmatrix} p_{X1, B1} & 0 \\ 0 & p_{X2, B2} \\ p_{X3, B1} & 0 \\ 0 & p_{X4, B2} \end{pmatrix}. \quad (5.6)$$

The time-span Δm_{\max} determines the maximum time-separation of error chains that are considered in the matching problem. We have set some of the elements of \mathbf{B} to zero, since X1 and X3 connect only to the east boundary (B1 via D3, D6, and D9), and X2 and X4 to the west boundary (B2 via D1, D4, and D7), see Fig. 4.1(a),

As the final step, we run a minimum-weight perfect matching algorithm on the syndrome graph [Edmonds65, O'Brien17, Higgott22]. The space-component of each matched edge corresponds to a set of data qubits, on which an error has occurred, while the time-component, arising from the space-time and auxiliary qubit errors, has no effect on the logical operator value. When decoding the X-type syndrome, each overlap of a data qubit in a matched edge with the logical \hat{X}_L operator corresponds to a \hat{X}_L flip to be corrected. Correspondingly, flips of the \hat{Z}_L operator can be inferred from the Z-type syndrome data.

5.3. Syndrome Correlations to Error Probabilities

Knowing the error model of a device is of high importance for high fidelity decoding independent of the exact decoding algorithm used. While many error processes can be characterized using independent measurements, the effective error rates might differ when running the actual error correction experiment, for example, due to time-drift of parameters or unaccounted-for error mechanisms, like crosstalk. Therefore, we ideally want to construct the error model based on syndrome data produced by running the same circuit as for a QEC experiment. In this section, we explain, based on experimental data, how this can be done.

We acquire 16 cycles of stabilizer measurement data on the device presented in Chapter 4, preparing either the $|0\rangle_L$, $|1\rangle_L$, $|+\rangle_L$ or $|-\rangle_L$ logical state. For each state, we repeat the experiment 500,000 times, and remove the runs where any of the qubits are measured outside the computational subspace, or the initial state is not the ground state, leaving us with about 54,000 runs per state. For calculating the syndrome elements for the first and last cycles, we make use of the known initial state of the auxiliary qubits, the initial parity of the data qubits, and the parity of the data qubits from the final readout.

The average per-cycle probability of detecting a nonzero syndrome element on weight-four and weight-two stabilizers is $\langle\sigma\rangle = 0.165(17)$ and $0.118(6)$, respectively, where the uncertainty indicates the standard deviation among different auxiliary qubits. To visualize the correlations between the syndrome elements, characteristic of the various error classes discussed in Section 5.1, we calculate the covariances $C_{A_i, A_j}^{(\Delta m)}$ between syndrome elements on auxiliary

qubits A_i and A_j , Δm cycles apart as

$$C_{A_i, A_j}^{(\Delta m)} = \langle \sigma_{A_i}^{(m)} \sigma_{A_j}^{(m+\Delta m)} \rangle - \langle \sigma_{A_i}^{(m)} \rangle \langle \sigma_{A_j}^{(m+\Delta m)} \rangle, \quad (5.7)$$

see Fig. 5.4(a). The averaging is done first over the experimental runs, and then over the cycle index m . We omit data from the first and the last cycle when calculating the correlations, since these syndrome elements are measured differently and are not representative of the mean value during the state preservation experiment.

For $\Delta m = 0$, we observe the highest covariance between neighboring auxiliary qubits (first off-diagonal), corresponding to correlated syndrome element flips due to $\mathbf{S}^{X|Z}$ and \mathbf{S}^Y errors. The second off-diagonal, which has significant but lower covariance, corresponds to correlated syndrome element flips on next-nearest neighbors, caused by \mathbf{H}^X and some \mathbf{H}^Y errors. As expected for uncorrelated single-qubit errors, we find negligible covariance between syndrome elements that are separated by more than two data qubits (second off-diagonal). With the pipelined stabilizer measurement circuit that we utilize, the covariance between syndrome elements of different kinds of auxiliary qubits is detected at a cycle separation of $\Delta m = 0.5$. The nonzero covariances occur between neighboring auxiliary qubits and are caused by \mathbf{S}^Y errors. For $\Delta m = 1$, the diagonal elements correspond to \mathbf{T} and \mathbf{H}^Y errors. The high covariance on this diagonal hints at the errors from the \mathbf{T} class having high occurrence probabilities. Some covariances on the first off-diagonal are also nonzero, corresponding to $\mathbf{S}\mathbf{T}^X$ and $\mathbf{S}\mathbf{T}^Y$ errors. There is almost no covariance for $\Delta m = 1.5$, and only diagonal elements for $\Delta m = 2$. An expected source of errors leading to $\Delta m = 2$ correlations is readout overlap errors \mathbf{T}' , where the auxiliary qubit state is misclassified without changing the state of the qubit. However, as we will see in Section 5.4, most of these correlations are likely caused by undetected leakage of the data qubits.

For calculating the weights for minimum-weight perfect matching decoding, we have to convert those covariances into per-cycle error probabilities. An analytical formula for this, assuming that every error flips at most two syndrome elements, is presented in Ref. [Spitz18]. Here, we have generalized those equations for processes flipping an arbitrary number of syndrome elements. In the general case, the probability p_{i_1, \dots, i_n} , that an error that

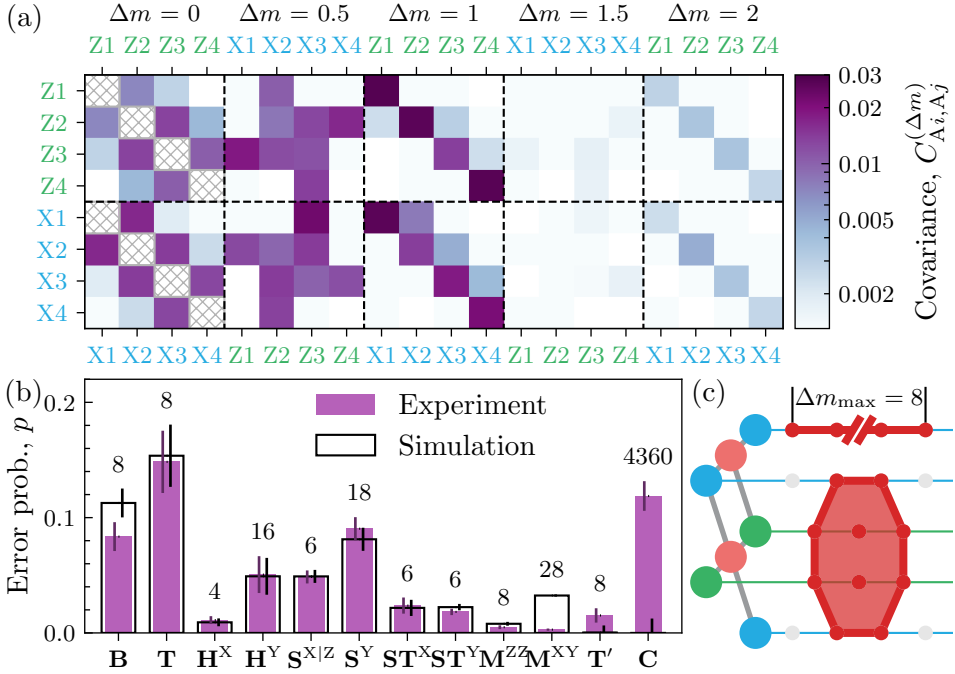


Figure 5.4: Error probabilities by class. (a) Average (over 16 cycles) covariance between pairs of syndrome elements. The syndrome element that is indicated by the column is detected Δm cycles after the syndrome element that is indicated by the row. The covarying qubit is indicated on the top or bottom axis for Z-type and X-type auxiliary qubits, respectively. (b) Total error probability p of the various error classes extracted from the experimental (purple bar) and simulated (black wireframe) syndrome correlations. The number above the bar indicates the number of different signatures that were considered in that class. The error bars indicate the standard deviation of the total error, calculated as the square root of the sum of the squared deviations from the mean within that class. (c) Schematic of the signatures that are considered in the **C** class. That is, any subset of syndrome elements on one auxiliary over nine cycles or on multiple auxiliary qubits neighboring one data qubit up to two cycles apart.

flips n syndrome elements $\sigma_{i_1}, \dots, \sigma_{i_n}$ occurs, can be calculated as

$$p_{i_1, \dots, i_n} = \frac{1}{2} - \frac{1}{2} \frac{\prod_{\substack{\{j_1, \dots, j_q\} \subseteq \\ \{i_1, \dots, i_n\}}} \langle (1 - 2\sigma_{j_1}) \dots (1 - 2\sigma_{j_q}) \rangle^{(-1)^{q-1} 2^{-(n-1)}}}{\prod_{\substack{\{j_1, \dots, j_q\} \supset \\ \{i_1, \dots, i_n\}}} (1 - 2p_{j_1, \dots, j_q})}. \quad (5.8)$$

Here, the indices i and j include both the auxiliary qubit and the cycle number, where and when the syndrome element is measured. The product in the numerator is taken over all the subsets of the set of syndrome elements $\{i_1, \dots, i_n\}$, including the set itself, whereas the product in the denominator is taken over the supersets. For the number of supersets to not grow too large, it is practical to limit the syndrome element sets $\{j_1, \dots, j_q\}$ for which the correlated error probability can be nonzero. For example, if we assume that each independent error flips at most two syndrome elements ($p_{i_1, \dots, i_n} = 0$ for $n > n_{\max} = 2$), then we recover the equations derived in Ref. [Spitz18]

$$p_{ij} = \frac{1}{2} - \sqrt{\frac{1}{4} - \frac{\langle \sigma_i \sigma_j \rangle - \langle \sigma_i \rangle \langle \sigma_j \rangle}{1 - 2\langle \sigma_i \rangle - 2\langle \sigma_j \rangle + 4\langle \sigma_i \sigma_j \rangle}}, \quad p_i = \frac{1}{2} - \frac{1 - 2\langle \sigma_i \rangle}{2 \prod_{j \neq i} (1 - 2p_{ij})}. \quad (5.9)$$

On the other hand, if we consider processes flipping up-to-four syndrome elements $n_{\max} = 4$, then we get the equations

$$p_{ijkl} = \frac{1}{2} - \frac{1}{2} \sqrt[8]{\frac{\langle \tilde{\sigma}_i \tilde{\sigma}_j \tilde{\sigma}_k \rangle \langle \tilde{\sigma}_i \tilde{\sigma}_j \tilde{\sigma}_l \rangle \langle \tilde{\sigma}_i \tilde{\sigma}_k \tilde{\sigma}_l \rangle \langle \tilde{\sigma}_j \tilde{\sigma}_k \tilde{\sigma}_l \rangle \langle \tilde{\sigma}_i \rangle \langle \tilde{\sigma}_j \rangle \langle \tilde{\sigma}_k \rangle \langle \tilde{\sigma}_l \rangle}{\langle \tilde{\sigma}_i \tilde{\sigma}_j \tilde{\sigma}_k \tilde{\sigma}_l \rangle \langle \tilde{\sigma}_i \tilde{\sigma}_j \rangle \langle \tilde{\sigma}_i \tilde{\sigma}_k \rangle \langle \tilde{\sigma}_i \tilde{\sigma}_l \rangle \langle \tilde{\sigma}_j \tilde{\sigma}_k \rangle \langle \tilde{\sigma}_j \tilde{\sigma}_l \rangle \langle \tilde{\sigma}_k \tilde{\sigma}_l \rangle}}, \quad (5.10a)$$

$$p_{ijk} = \frac{1}{2} - \frac{1}{2} \sqrt[4]{\frac{\langle \tilde{\sigma}_i \tilde{\sigma}_j \tilde{\sigma}_k \rangle \langle \tilde{\sigma}_i \rangle \langle \tilde{\sigma}_j \rangle \langle \tilde{\sigma}_k \rangle}{\langle \tilde{\sigma}_i \tilde{\sigma}_j \rangle \langle \tilde{\sigma}_i \tilde{\sigma}_k \rangle \langle \tilde{\sigma}_j \tilde{\sigma}_k \rangle}} \prod_{l \notin \{i, j, k\}} \frac{1}{1 - 2p_{ijkl}}, \quad (5.10b)$$

$$p_{ij} = \frac{1}{2} - \frac{1}{2} \sqrt{\frac{\langle \tilde{\sigma}_i \rangle \langle \tilde{\sigma}_j \rangle}{\langle \tilde{\sigma}_i \tilde{\sigma}_j \rangle}} \prod_{k \notin \{i, j\}} \frac{1}{1 - 2p_{ijk}} \prod_{l \notin \{i, j, k\}} \frac{1}{1 - 2p_{ijkl}}, \quad (5.10c)$$

$$p_i = \frac{1}{2} - \frac{1}{2} \langle \tilde{\sigma}_i \rangle \prod_{j \neq i} \frac{1}{1 - 2p_{ij}} \prod_{k \notin \{i, j\}} \frac{1}{1 - 2p_{ijk}} \prod_{l \notin \{i, j, k\}} \frac{1}{1 - 2p_{ijkl}}, \quad (5.10d)$$

where we have denoted $\tilde{\sigma}_i = 1 - 2\sigma_i$ for brevity. We derived Eq. (5.8) for $n_{\max} = 6$ analytically, and numerically verified its validity for correlated errors on up-to $n_{\max} = 12$ syndrome elements.

Next, using Eq. (5.8), we calculate the probabilities of errors triggering various error signatures in the same dataset as was used to calculate the correlations shown in Fig. 5.4(a). Because each run of the $N = 16$ -cycle-long experiment produces $(d^2 - 1)(2N - 1)/2 = 124$ syndrome elements, it is unfeasible to calculate the error probability for all the 2^{124} signatures. We therefore only consider error signatures that are caused by a single-qubit Pauli error at any position in the circuit or a two-qubit Pauli error during a two-qubit gate, as presented in Section 5.1. To not introduce a bias into the extracted error probabilities by omitting the renormalization by p_{j_1, \dots, j_q} in the denominator in Eq. (5.8), we need to make sure that we include all processes with highly correlated signatures that are present in the system. To that end, we include two additional kinds of error signatures in the analysis, which we label **C**, see Fig. 5.4(c). First, we consider any subset of flipped syndrome elements on up to nine consecutive cycles on a single auxiliary qubit, and second, we consider any subset of syndrome elements on auxiliary qubits neighboring one data qubit, separated by up to two cycles. The maximum cycle separation for both of these signature classes is limited by the computational power, as the number of signatures grows exponentially with the maximum cycle separation. The **C** error class could be associated with undetected leakage of the data qubits to higher transmon states, as we will discuss in Section 5.4. We average the probabilities of errors with the same relative signature over the cycles to obtain the average probabilities for the 116 error signatures that are associated with different Pauli errors in the circuit and 4360 error signatures belonging to the **C** class.

The total probability of an error from each of the twelve signature classes is shown in Fig. 5.4(b). We observe, that **T** errors are most common, amounting to a per-cycle probability of 15% over all the auxiliary qubits. The high error probability might be due to the high readout error probability compared to other errors, see Fig. 4.4(c), and the long time that the auxiliary qubits spend in the superposition state for the parity maps, during which phase flip errors lead to **T** signatures. The probability of errors from most other error classes correlates with the number of different signatures in that class. We analyze this correlation in more detail in Section 5.4. We find a relatively low probability of two-qubit gate errors of the classes \mathbf{M}^{ZZ} and \mathbf{M}^{XY} , indicating that most two-qubit errors can be explained by single-qubit energy relaxation and dephasing, and control and crosstalk errors are small. The second-largest error source is the **C** error class, which we analyze in

more detail in Section 5.4.

We compare the experimental results to a circuit-level Pauli-error simulation, shown as black wireframes in Fig. 5.4(b). The simulation assumes uniform error probabilities across the device, with the probability values based on independent calibration measurements, see Ref. [Remm23b] for details. We find a good match between the simulation and the experiment in most error classes. The most notable difference is in the correlated bit flips due to CZ gates, indicated by the \mathbf{M}^{XY} error class, which are included in the depolarizing error model of the simulation, but are not significantly present in the experimental data. In simulations with a depolarizing Pauli noise model, two-qubit gate errors have been found to contribute the most to the logical error probability [Fowler12b]. However, if correlated bit flip errors are rare for a real implementation of the gate, as we observe in our data, the effect of two-qubit gate errors on the logical error probability in real systems might be more akin to single-qubit errors. Another difference between the simulated and the experimental dataset is the absence of leakage and readout overlap errors, which are not part of the simulation.

The in-situ error characterization method presented here is especially useful for the stabilizer codes, since it yields the occurrence probabilities of errors with a given signature, which is exactly the information needed for decoding, without resorting to gate-based simulation of the circuit. Furthermore, the method allows us to analyze spurious correlations between the syndrome elements not caused by known Pauli errors, and to identify whether they lead to highly correlated errors that are known to be especially harmful quantum error correction [Aharonov06, Jouzdani14].

5.4. Device Diagnostics Using Error Probabilities

The error analysis method allows us to study the per-cycle probabilities of specific errors with various signatures. First, we group the error signatures according to the number ν of circuit location and an error operator combinations that can trigger it. For the location-operator combinations, we consider 15 two-qubit Pauli errors at 24 two-qubit gates of a single stabilizer measurement cycle for a total of 360 combinations. If uniform depolarizing noise at every two-qubit gate was the only error source, then we would expect the error probability to be directly proportional to the number of location-operator combinations that can trigger that signature.

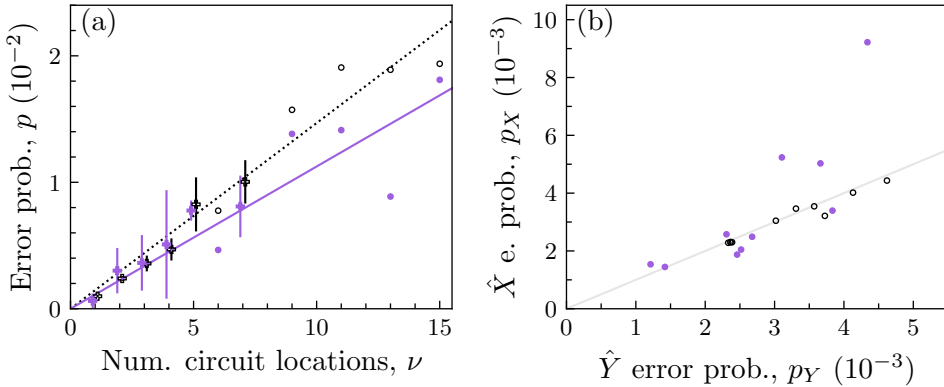


Figure 5.5: Standard error diagnostics. (a) The probability p of triggering an error signature as a function of the number of circuit location and error operator combinations ν that can cause the signature, extracted from experimental (purple) and simulation (black) data. One two-qubit Pauli error at one two-qubit gate constitutes a circuit location and error operator combination, adding up to a total of $15 \times 24 = 360$ combinations. The error bars indicate standard deviation over signatures with the same ν , while circles indicate data points for values of ν which have a single signature. (b) Comparison of error probabilities for signature pairs which can only be caused by an \hat{X} and a \hat{Y} error at a specific circuit location. Purple filled circles correspond to experimental data and black open circles to simulation. Due to the symmetry of our physical operations with respect to \hat{Z} rotations, we expect the two error probabilities to be identical, which is indicated by the diagonal gray line.

We omit signatures from the **T** class in this analysis, since their probability is significantly increased by measurement errors. Overall, we find a strong correlation between the probability of an error syndrome and the number of location-operator combinations, see Fig. 5.5(a). Because, in terms of duration, the circuit consists mostly of two-qubit gates and readouts, this circuit-location correlation explains most of the differences between the probabilities of various signatures. The correlation is also reproduced by the simulation with independently characterized parameters, see black markers and line in Fig. 5.5(a).

Another useful application of the generalized error probability extraction

method is the identification of crosstalk and control errors. For some circuit locations, there are unique signatures for both \hat{X} and \hat{Y} errors. Since the physical energy relaxation of transmon qubits is described by a channel symmetric with respect to changing \hat{X} and \hat{Y} , we expect the corresponding extracted error probabilities p_x and p_y to be equal. We find $p_x \approx p_y$ for all error pairs in simulation and in experiment, see Fig. 5.5(b), except for errors on D2 during the X-type parity map, for which $p_x \approx 2p_y$. Such discrepancy could be caused by control errors or crosstalk of microwave drive signals.

Next, we analyze the potential origins of the **C** signature class errors. First, we consider the covariance between syndrome elements on a single auxiliary qubit Δm cycles apart, which we find decays exponentially as $0.89^{\Delta m}$, see Fig. 5.6(a). Ideally, we would expect the correlations for $\Delta m > 2$ to be zero. The slow decay could be an indication of leakage of the data qubits [McEwen21b] that is not removed by the data qubit leakage rejection scheme based on the final readout of the data qubits. This is supported by the observation that without including the **C** class error signatures in the analysis, the error probability for **T'** signatures is higher at the beginning of the experiment when the data qubits have several cycles to seep [Wood18] back to the computational subspace before the final readout at the end of the experiment, remaining undetected by data qubit leakage rejection, see blue filled dots in Fig. 5.6(b). If we do not reject any runs based on the final data qubit readout, however, the error probability does not depend on the cycle number and is comparable to the error probability with leakage rejection close to the first cycle, see open blue circles in Fig. 5.6(b).

An alternative explanation could be a change of the underlying error probabilities, either during one experimental run, or equivalently during the collection of the full dataset where the correlations are analyzed. These error probability drifts would be interpreted as correlated errors, as the additional error events that are created during a period of increased error probability appear correlated to each other. One source of error probability drift could be related to quasiparticle generation and tunneling, the rate of which can vary, for example, due to impacts with cosmic rays [McEwen21a]. Since quasiparticle tunneling can also cause leakage [Serniak18], it would be consistent with the suppression of errors when data qubit leakage rejection is used. We suspect, however, that error probability drifts on their own could not explain the large total probability of the **C** error class.

With the goal of taking into account the highly correlated errors in our analysis, we include the **C** class signatures. Due to the renormalization term

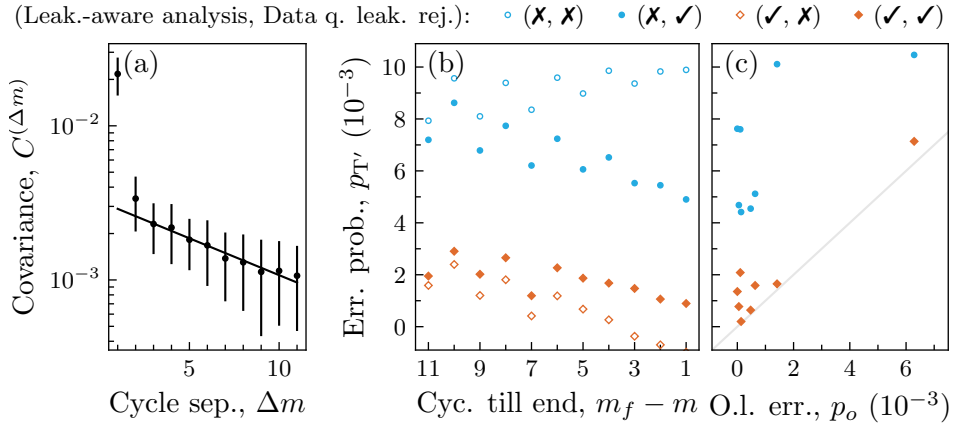


Figure 5.6: Correlated error diagnostics. (a) Covariance between syndrome elements on a single auxiliary qubit Δm cycles apart, averaged over the eight auxiliary qubits. The error bars indicate one standard deviation over the different auxiliary qubits. A fit to an exponential decay model for $\Delta m > 2$ is shown as a line. (b) Probability of an error triggering a \mathbf{T}' syndrome ($\Delta m = 2$) as a function of the number of cycles until the final data qubit readout. The four data series correspond to using data qubit leakage rejection or not and including leakage-related signatures in the analysis or not. The data is averaged over the auxiliary qubits. (c) Average (over cycles) \mathbf{T}' error probability of the eight auxiliary qubits as a function of the independently characterized readout overlap error. The gray line indicates the expected identity relation.

in the denominator of Eq. (5.8), accounting for these additional processes gives us a more accurate value for the probability of a \mathbf{T}' error. With this analysis, we find that the \mathbf{T}' error probability only weakly depends on the cycle number and whether data qubit leakage rejection is used or not, see filled and open orange diamonds in Fig. 5.6(b), respectively. Furthermore, the error probabilities extracted using the improved analysis are consistent with the separately characterized overlap error of auxiliary qubit readout, which is the expected mechanism for \mathbf{T}' errors, see Fig. 5.6(c).

5.5. Discussion

An accurate error model of the QEC circuit is a crucial component for any high-accuracy decoder. In this work, we explained, how the syndrome is generated under a Pauli noise model. Furthermore, we presented a novel analytical method for calculating the error probabilities of errors with a given signature from the correlations between the syndrome elements. These error probabilities are used to calculate the weights of a MWPM decoder, the nuances of which we also explained. The error model can also be used to analyze the crosstalk, control, and leakage errors, measured in the same circuit as is used for executing the QEC experiment. Here, we identified control errors on D2, leading to an imbalance of \hat{X} and \hat{Y} errors, and we identified errors with signatures spanning multiple syndrome extraction cycles, which are consistent with undetected leakage on the data qubits.

While the in-situ error characterization based on syndrome data can be a powerful tool, one needs to be aware of its limitations. First, since the analytical formula allows to easily calculate the probability of error with arbitrarily large signature, it might be tempting to fully characterize the errors by calculating the probabilities for triggering all possible signatures. However, because the number of signatures is exponential in the number of syndrome elements, this is not feasible and one needs to choose the subset of errors to consider. Therefore, some errors with nonstandard signatures might be excluded from the model. Second, many samples need to be taken to accurately estimate the syndrome element correlations used to calculate the error probabilities. Because of the renormalization terms in the denominator of Eq. (5.8), the more high-weight signatures are included in the model, the more the uncertainties of errors with lower-weight signatures increase. Furthermore, if the error model parameters drift during the time it takes to gather the large amount of statistics, then phantom correlations can appear in the data.

The main advantage of the error characterization method presented here is that the error model is extracted using the same circuit as is used for the QEC experiment. This means that error sources not present in individual characterization, like crosstalk, can be identified. Furthermore, the fact that the probability of errors with signatures of arbitrary weight can be calculated is beneficial for deriving error models that include \hat{Y} errors, used for decoders that account for correlations between X- and Z-type stabilizers. This includes correlated MWPM [Fowler13b], belief matching [Higgott23a]

or tensor-network-based decoders [Bravyi14]. As we have shown, the method can also be used to characterize non-Pauli errors with high-weight signatures, that could introduce a bias to the extracted standard error probabilities if unaccounted for.

Signal Mixing in a Parametric Amplifier

Amplification of weak microwave signals is essential for many applications, including readout of superconducting qubits [Blais21, Kjaergaard20a, Wallraff05, Mallet09] and quantum dot devices [Pettersson12, Zheng19, deJong21], as well as for radio astronomy [Day03, Zobrist19]. State-of-the-art low-noise amplifiers in the microwave domain [Yurke96, Castellanos-Beltran07, Castellanos-Beltran08, Eichler14a, Macklin15, Ho Eom12] approach the quantum limit in noise performance [Caves82] by operating at millikelvin temperatures and using parametric pumping of a nonlinear circuit made of Josephson junctions or high kinetic inductance elements. While parametric amplifiers based on nonlinear resonators have typical bandwidths on the order of tens of MHz limited by the gain and the resonator linewidth [Eichler14b, Planat19], traveling-wave parametric amplifiers (TWPAs) [Yurke96, O'Brien14, Macklin15, White15, Planat20, Esposito21, Ranadive22] can have much higher bandwidths of up to several GHz. The high bandwidth enables a high degree of frequency-multiplexing, for example for qubit readout [Heinsoo18, deJong21] and single-photon detectors [Zobrist19]. Multiplexed use of hardware resources [Chen12, Jerger12, Barends14, Schmitt14, Heinsoo18, Arute19, Krinner22] is essential for the operation of large quantum devices.

So far material losses and the generation of signal sidebands have been identified as the main sources of excess noise in TWPAs above the quantum limit [Macklin15, Esposito21, Peng22], characterized by the intrinsic quantum efficiency. In addition to adding as little noise as possible at the signal frequency, broadband amplifiers should not generate spurious tones due to intermodulation of the inputs [Frattini18, Sivak19], in particular when they are used in frequency-multiplexed applications. However, due to amplifier nonlinearities, intermodulation distortion is unavoidable and constitutes a

well-known phenomenon in classical amplifiers [Walker12]. Intermodulation products can lead to crosstalk between the amplified signals if any of their frequencies overlap with one of the signals. The probability of such collisions increases with increasing degree of frequency multiplexing because the number of intermodulation products increases.

In this chapter, which follows closely Ref. [Remm23a], we characterize the intermodulation distortion of a resonantly phase-matched traveling wave parametric amplifier (Section 6.1), produced by MIT Lincoln Laboratory [Macklin15], that is used for qubit readout in the work presented in Chapter 4. We identify intermodulation products of order up to five in the output spectrum and characterize their power and frequency dependence on the input signals. We then show that the frequency collision of an intermodulation product with a readout signal can lead to significant crosstalk and reduction of readout fidelity (Section 6.2). Finally, we discuss strategies to mitigate these errors by the choice of pump and signal frequency and of power levels (Section 6.3).

6.1. Characterization of Intermodulation Distortion

The **TWPA** investigated in this study is a nonlinear transmission line, formed by a series of Josephson junctions and capacitors to ground, which is shunted to ground by capacitively coupled *LC*-resonators at 8.1 GHz to achieve phase matching [Macklin15], see Fig. 6.1(a). The nonlinearity of the Josephson junctions allows for four-and-higher-wave mixing processes between the tones traversing the **TWPA**. In the presence of a strong pump tone, the mixing processes lead to the desired phase-insensitive amplification of weak tones [ω_1, ω_2 in Fig. 6.1(b)] and the generation of corresponding idler tones [$2\omega_p - \omega_1$ in Fig. 6.1(b) for ω_1], but also to sideband generation by absorbing or emitting pump photons [Peng22] and to the mixing of multiple signals [Frattini18], known as intermodulation distortion. An example of intermodulation distortion is the creation of a tone (intermodulation product) at frequency $\omega_2 + \omega_p - \omega_1$ at the output of the **TWPA**, as shown in Fig. 6.1(b). We expect that such intermodulation processes are not unique to traveling wave amplifiers but also present in resonant amplifiers if frequency multiplexing is used.

In our experimental setup the **TWPA** is mounted at the base temperature stage of a dilution cryostat operated at 10 mK, see also Fig. 2.6(a). The

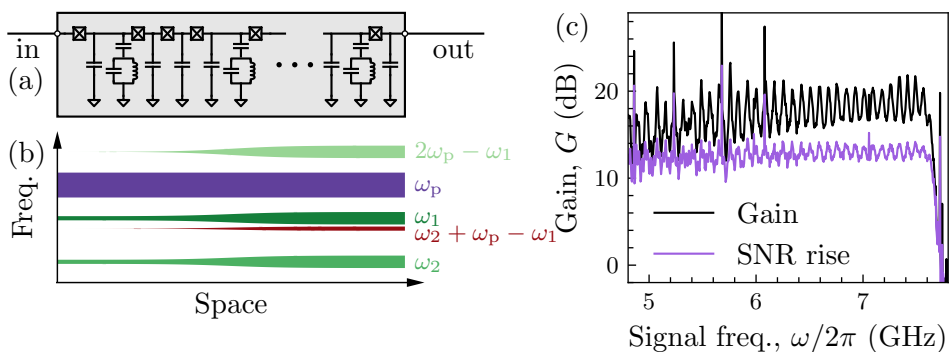


Figure 6.1: Signal mixing in a TWPA. (a) The circuit of a resonantly phase-matched TWPA. (b) Examples of tones propagating along the length of the TWPA and their amplitudes (thickness of the lines, not to scale) in the case of frequency-multiplexed readout at ω_1 and ω_2 with the pump tone at ω_p . In particular, a tone at $\omega_2 + \omega_p - \omega_1$ is created, which is an example of an intermodulation product. (c) The measured gain G (black) and signal-to-noise ratio improvement (purple) spectra of the device under study. The pump frequency is $\omega_p/2\pi = 7.92$ GHz.

signals, generated at room temperature, are up-converted to microwave frequencies using an in-phase and quadrature (IQ) mixer. The output of the TWPA is amplified by a cryogenic high-electron-mobility transistor (HEMT) amplifier and by room-temperature amplifiers. Finally, the signals are down-converted using an IQ-mixer with a local oscillator at 6.9 GHz and digitized, see Ref. [Remm23a] for a detailed setup diagram. The power -62 dBm and frequency $\omega_p/2\pi = 7.92$ GHz of the pump tone are chosen to maximize the signal-to-noise ratio of signals applied between 6.7 GHz and 7.6 GHz, used for qubit readout. The power levels at the input of the TWPA are calculated based on room-temperature measurements and the attenuation of the components within the cryostat. The TWPA achieves a mean gain of $G = 18.4$ dB and a signal-to-noise ratio rise of 13.0 dB relative to not pumping the TWPA, in which case the noise performance is determined by the HEMT amplifier and the losses in cabling before it and the insertion loss in the TWPA, see Fig. 6.1(c).

To observe the intermodulation products that we want to characterize, we apply signal tones at frequencies ω_1 and ω_2 to the input of the TWPA

through a directional coupler which is also used for applying the pump tone. The signal power level at the input of the TWPA is approximately -102 dBm. We acquire 2.275 - μ s-long time traces and multiply them with a Blackman-Harris window [Harris78], before taking the Fourier transform, to avoid windowing effects. By fixing $\omega_2/2\pi = 7.1924$ GHz and sweeping $\omega_1/2\pi$ from 6.9 GHz to 7.8 GHz, we record the spectra shown in Fig. 6.2(a). In addition to the signals at ω_1 and ω_2 (green lines), we observe intermodulation products at frequencies $\omega = n_p\omega_p + \sum_{i=1,2} n_i\omega_i$ with integer n_p and n_i . We can classify the intermodulation products according to their total order $O_t = |n_p| + \sum_i |n_i|$. Four-wave mixing processes lead to products of total order $O_t = 3$ while cascaded four-wave mixing processes and higher-order mixing processes can lead to products with odd order $O_t = 5$ and higher. Of the intermodulation products that lie within the acquisition band, we observe all 17 products with total order $O_t = 3$ or 5 and several products with $O_t = 7$ above the noise floor of -160 dBm (at the output of the TWPA). Potential intermodulation products of even total order, which might arise due to spurious asymmetry in phase potential of the Josephson junctions, fall outside the acquisition bandwidth in our setup. The presence of all the odd O_t intermodulation products implies that there are no selection rules determining which intermodulation products can be created, other than the parity of O_t . While the allowed total orders are determined by the order of the mixing process, the power level of the intermodulation product is mostly determined by the signal order $O_s = \sum_i |n_i|$, as we will see below. The intermodulation products of $O_s = 1, 2, 3$, and 4 and higher are highlighted in Fig. 6.2(a) in green, red, blue, and yellow, respectively. Each intermodulation product also appears mirrored around the local oscillator frequency due to imperfections of the frequency down-conversion process. While in conventional amplifiers the second order intermodulation products are usually of little concern as they are created at twice the signal frequency, in a four-wave mixing parametric amplifier, mixing with the pump tone can up- or downconvert $O_s = 2$ terms into the signal band.

Next, we investigate the power of the intermodulation products P . We fix the frequency $\omega_1/2\pi = 7.5551$ GHz, as indicated by the linecut in Fig. 6.2(b), and vary the input powers p_1 and $p_2 = 0.5p_1$ of the two signals, chosen such that the output powers are similar despite the frequency-dependence of gain and attenuation. We record the power P of the intermodulation products of $O_s \leq 3$, see Fig. 6.2(c), and find that they follow power laws with the signal order O_s as the exponent as long as the amplifier is not

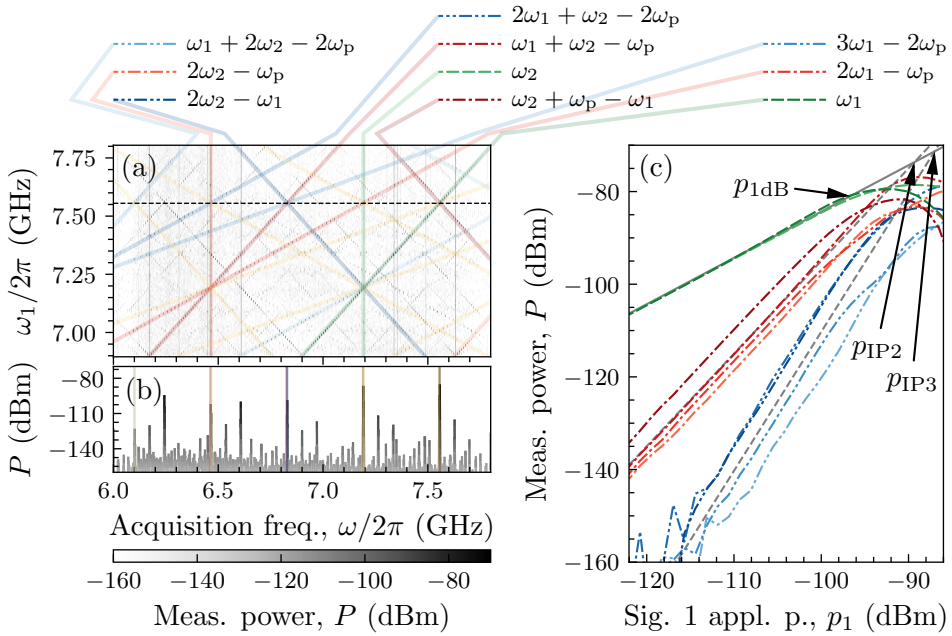


Figure 6.2: Intermodulation distortion. (a) Measured output power spectra when sweeping the frequency of a single tone ω_1 in the presence of a second signal tone ω_2 . Various intermodulation products are highlighted in color according to their signal order, see text for details. (b) Line cut of the data in (a) at ω_1 indicated by the dashed line. (c) Dependence of the power of the intermodulation products P on the applied signal power p_1 . The power of the two signal tones is swept together. The gray lines indicate the mean power level for products of signal order $O_s = 1, 2$, and 3 according to Eq. (6.1), and the arrows indicate the 1 dB compression power p_{1dB} and the intermodulation intercept points p_{IP} for $O_s = 2$ and 3 tones.

saturated. Comparing the powers of different $O_s = 3$ products, we find that they can be of similar magnitude even for different O_t values. The observed power-laws together with the data from independent power sweeps of the two tones [Remm23a] motivate an empirical model of the output power

$$P = G p_{\text{IP}} \prod_i \left(\frac{p_i}{p_{\text{IP}}} \right)^{|n_i|}. \quad (6.1)$$

The model is parametrized by the mean gain G and the intermodulation distortion intercept point p_{IP} [Walker12], that is, the input power level at which the extrapolated intermodulation product power equals the signal power. By sweeping the phases of the input signals ϕ_i , we have also determined that the phase of the intermodulation product is given by $\Phi = \theta + \sum_i n_i \phi_i$ [Remm23a]. Using the average gain of the two signals $G = 17.2(13)$ dB, we calculate p_{IP} for each intermodulation product according to Eq. (6.1). We find a mean second order intercept point $p_{\text{IP}2} = -91(3)$ dBm (for $O_s = 2$) and a mean third order intercept point $p_{\text{IP}3} = -88(3)$ dBm (for $O_s = 3$), see dashed gray lines in Fig. 6.2(c) calculated according to Eq. (6.1) and the mean p_{IP} values. The uncertainties indicate one standard deviation of the spread over different intermodulation products. The p_{IP} values, visualized as the intercepts of the gray dashed lines with the solid gray line (mean signal power) in Fig. 6.2(c), are close to the 1 dB compression power $p_{1\text{dB}} = -96.7(23)$ dBm. The power differences between intermodulation products of the same signal order might be due to differences in the conversion rates or due to the frequency-dependence of the gain.

In nonparametric amplifiers, a simple model can be used to describe the relation between the 1 dB compression power $p_{1\text{dB}}$ and the third order intermodulation intercept power $p_{\text{IP}3}$. In the lowest-order series expansion that can explain four-wave mixing, we write the output voltage of the amplifier as $V_{\text{out}} = \sqrt{G} V_{\text{in}} (1 - k V_{\text{in}}^2)$, for input voltage V_{in} and a coefficient k which determines both saturation and intermodulation properties of the amplifier. From such model, we find $p_{\text{IP}3}/p_{1\text{dB}} \approx 9.6$ dB [Walker12], similar to the observed $p_{\text{IP}3}/p_{1\text{dB}} = 9(4)$ dB. If a similar relation holds for parametric amplifiers, as is hinted by our data, then the intermodulation distortion intercept powers might increase if the 1 dB compression power of the amplifier is increased, providing a strategy for improving the intermodulation distortion performance of the amplifiers.

In this section, we studied the classical properties of the intermodulation products, that is, frequency and power. Because TWPAs can operate with

efficiencies close to the quantum limit, the intermodulation products are expected to have nonclassical properties, for example, multi-mode squeezing, which would be interesting to investigate in the future.

6.2. Implications for Frequency-Multiplexed Readout

We assess the impact of intermodulation distortion on the performance of frequency-multiplexed qutrit readout using the device presented Chapter 4. Specifically, we study how frequency multiplexing affects the readout signal-to-noise ratio, and how frequency collisions with intermodulation products can lead to crosstalk and increased readout errors.

To investigate the noise performance of the TWPA in the presence of multiple input tones, we use input frequencies from the set $\Omega = \{\omega_i\}$, where $\omega_i/(2\pi \text{ GHz}) \in \{7.5551, 7.1924, 7.3725, 6.9790, 6.7608\}$, which could be used for frequency-multiplexed readout of five qubits. We apply tones at the frequencies of each of the 31 different nonempty subsets $B = \{b|b \subset \Omega, b \neq \emptyset\}$ of Ω . We set the power of each of the applied tones to p and record individual time traces. The gain of the signal for a subset b_j at frequency ω_i is calculated as $G_{i,j} = |\langle A_{i,j} \rangle|^2/p$ and noise as $S_{i,j} = \langle |A_{i,j}|^2 \rangle - |\langle A_{i,j} \rangle|^2$, where $A_{i,j}$ is the integrated amplitude of the timetrace, down-converted from frequency ω_i , and the averaging is done over the $2^{10} = 1024$ acquired time traces. To find the average normalized signal gain G/G_{ref} and noise S/S_{ref} for a given degree of multiplexing N , we normalize each value with a low-power single-tone reference value and average over all the frequency components ω_i and subsets b_j , which contain N frequency components. That is,

$$\frac{X}{X_{\text{ref}}} = \frac{1}{|\Omega|} \sum_{\omega_i \in \Omega} \frac{1}{|B_{N,i}|} \sum_{b_j \in B_{N,i}} \frac{X_{i,j}}{X_{\text{ref},i}}, \quad (6.2)$$

with X denoting either the gain G or noise S , $B_{N,i}$ the set of subsets of Ω that include ω_i and have $|B_{N,i}| = N$ components. The reference value $X_{\text{ref},i}$ is measured with a single tone at the lowest used power $p = -126 \text{ dBm}$.

Both the gain and the noise mainly depend on the total applied power p_Σ , and only weakly on the number of tones N , as seen in Fig. 6.3(a) by the collapse of all curves for different N on a single one. This means that the creation of the additional intermodulation products does not significantly reduce the gain nor increase the noise at the signal frequencies as long as the products do not overlap with the signals. The lack of dependence on N could

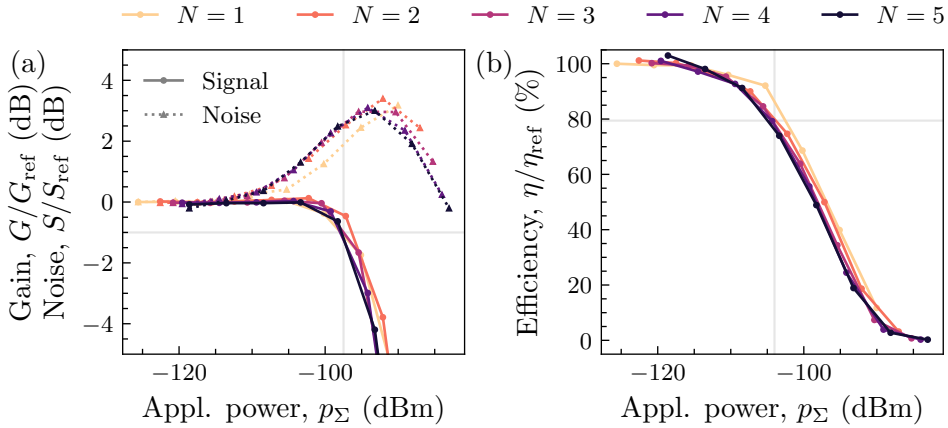


Figure 6.3: Multi-tone noise characterization. (a) Change in the signal gain G and noise power S as a function of the total applied power p_Σ and number of signal tones N , compared to the single-signal ($N = 1$), low-power ($p_\Sigma = -126$ dBm) values G_{ref} and S_{ref} . (b) Change in measurement efficiency η relative to the single-signal, low-power value η_{ref} . The intersection points of the gray lines indicate the 1 dB gain loss in panel (a) and 1 dB efficiency loss in panel (b).

be explained by the balance of the two following tendencies. When increasing the number of input tones N , the number of distinct intermodulation products, which have a frequency that is a linear combination of the input frequencies, also increases. On the other hand, each input signal and therefore also each intermodulation product has a lower power for fixed p_Σ . The total output power from the TWPA might therefore remain unchanged. This hypothesis is supported by a calculation of the total output power in a 6 GHz bandwidth around the pump tone according to Eq. (6.1), which we find to be approximately constant when varying the number of input tones N for a fixed total input power p_Σ .

We also analyze the saturation performance in terms of the amplifier efficiency $\eta = \eta_{\text{ref}}(G/G_{\text{ref}})/(S/S_{\text{ref}})$, that is, the signal-to-noise ratio at its output, relative to the standard quantum limit [Caves82], see Fig. 6.3(b). From a separate characterization measurement [Bultink18], we find a single-signal, low-power measurement efficiency of the total detection line of $\eta_{\text{ref}} = 24(5)\%$ (on a scale where an ideal phase-preserving amplifier would

have $\eta = 1$). When operating the amplifier close to its saturation power, we observe that the noise begins to rise at input powers about 10 dB lower than the value at which the gain is significantly reduced. This is reflected by a 1 dB reduction of efficiency already 6.5 dB before the 1 dB gain compression point is reached. While the origin of the noise rise needs further investigation, we conclude that it is not sufficient to consider only the gain and the 1 dB compression power, but also the noise rise when operating a TWPA close to saturation.

Beyond reducing efficiency, an intermodulation product can overlap with a signal tone used for frequency-multiplexed readout of a transmon qubit. To investigate this effect, we use qubits X2 and D5 from the device presented in Section 4.3. The qubit frequencies during readout are 5.89 GHz and 5.15 GHz, and the readout frequencies are $\omega_1/2\pi = 7.5551$ GHz and $\omega_2/2\pi = 7.1924$ GHz, as before, see Fig. 6.4(b) for the transmission spectrum of the readout feedline.

First, we prepare Q1 in one of its three lowest-lying energy eigenstates, labeled $|0\rangle$, $|1\rangle$, and $|2\rangle$, and then read it out using a 200-ns-long Gaussian-filtered ($\sigma = 10$ ns) square pulse, with mean power at the input of the TWPA of $p_1 = -123$ dBm. We integrate each acquired time trace with two orthogonal weight vectors, leading to the values Q_{01} and $Q_{0\bar{1}}$. The weight vectors are chosen to maximize the distinguishability of the three qutrit states on the Q_{01} - $Q_{0\bar{1}}$ plane [Krinner22]. We use a Gaussian-mixture model to classify the outcome as one of the qutrit states, see Fig. 6.4(a).

We then read out Q2 simultaneously with Q1, preparing it in one of the three qutrit states, in which case the intermodulation product $\omega_2 + \omega_p - \omega_1$ is created at $\omega_1 + 2\pi \times 2.2$ MHz. The average power of the Q2 readout tone at the input of the TWPA is $p_2 = -120$ dBm. We observe that the centers of the Gaussian distributions are shifted depending on the state of Q2, as indicated in Fig. 6.4(a). Because the 2.2 MHz detuning of the intermodulation product from the readout frequency is small compared to the acquisition bandwidth of the 200 ns readout, the intermodulation product will shift the integrated quadratures depending on its phase and amplitude. Furthermore, the amplitude and phase of the intermodulation product depend on the amplitudes and phases of both readout tones, and thereby the state of both qutrits. A different shift of the integrated readout response for each pair of qutrit states is therefore expected, which cannot be corrected by a linear correction operation, and the crosstalk leads to a reduction of readout fidelity.

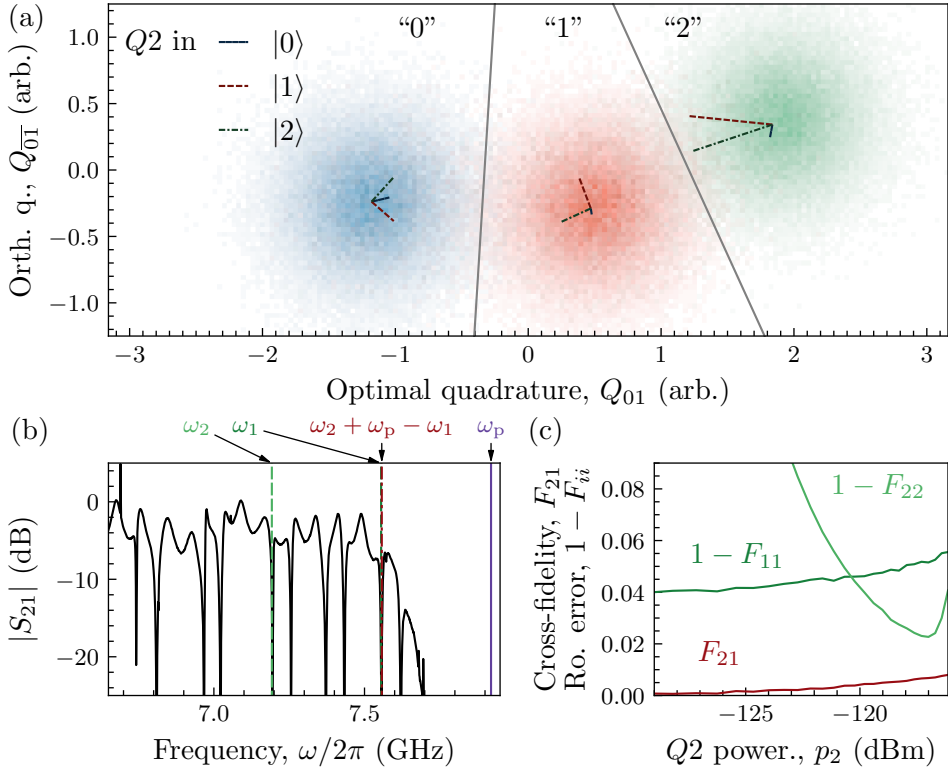


Figure 6.4: Intermodulation-induced readout errors. (a) Readout histograms of Q1 when prepared in each of the three first transmon states $|0\rangle$, $|1\rangle$, and $|2\rangle$. The dash-dotted lines indicate the shift ($\times 4$ for improved visibility) of the mean of the Gaussian distribution of measurement outcomes, when Q2 is prepared in one of the qutrit states and read out in parallel. The gray solid lines indicate classification thresholds. (b) Resonator spectrum of the feedline under inspection. The intermodulation product $\omega_2 + \omega_p - \omega_1$ is 2.2 MHz detuned from the readout tone of Q1 at ω_1 . (c) Readout errors of the two qutrits, $1 - F_{11}$ and $1 - F_{22}$, and the readout cross-fidelity F_{21} , as a function of the average readout power of Q2 at the TWPA input p_2 . The shifts in panel (a) correspond to $p_2 = -120$ dBm.

We sweep the readout power of Q2 while reading out the two qutrits in parallel, and measure the readout cross-fidelity matrix. The readout cross-fidelity F_{ij} , is the readout fidelity of qutrit Q_i when only looking at the classified outcome of Q_j , normalized such that $F_{ij} = 0$ for random assignment [Heinsoo18]. It can be calculated as

$$F_{ij} = \frac{1}{d-1} \left(\sum_{\xi \in \Xi_j} \max_{\zeta \in Z_i} \Pr(\xi|\zeta) - 1 \right), \quad (6.3)$$

where $d = 3$ is the dimensionality of the qutrit, $\Xi_j = \{“0”, “1”, “2”\}$ are the classification outcomes of Q_j , $Z_i = \{|0\rangle, |1\rangle, |2\rangle\}$ are the prepared states of Q_i , and \Pr is the probability distribution of classification results, conditioned on the prepared state of the qutrit. This corresponds to the strategy of labeling each shot as the most likely state ζ of Q_i , given the observed classification outcome ξ of Q_j . For perfect readout, the off-diagonal terms of the cross-fidelity matrix would be zero, while the diagonal terms would be one. A nonzero off-diagonal term F_{21} means that we can get some information about the state of Q2 from the readout of Q1, a clear indication of crosstalk. We see in Fig. 6.4(c), that the readout error of Q2, $1 - F_{22}$, decreases as we increase the readout power p_2 , but at the same time the readout error of Q1, $1 - F_{11}$, increases as does the cross-fidelity F_{21} . This highlights the trade-off between high-fidelity and low-crosstalk readout.

The probability and impact of such frequency-collisions increases with the speed of the readout, as the acquisition bandwidth needs to be wider and the signal power levels higher, implying that the relative amplitude of the intermodulation products is also higher according to Eq. (6.1).

6.3. Mitigation Strategies

We can categorize the methods to reduce the crosstalk and readout errors from intermodulation in the TWPA into two broad classes. First, one can accept that there will be frequency-collisions with the intermodulation products and try to reduce the relative amplitudes of the spurs compared to the signal. Second, one can try to avoid frequency-collisions with the intermodulation products.

The most practical way to reduce amplitudes of intermodulation products is to increase the intercept powers p_{IP} by increasing the saturation

power [Eichler14b], as we discussed in Section 6.1. For example, similar TWPAAs are available with a nominal 1 dB compression power of $p_{1\text{dB}} = -85$ dBm [O'Brien14, Oliver18]. Alternatively, the power applied to the amplifier could be reduced. This could be done for example by optimizing the ratio of the dispersive shift and the resonator linewidth, or by interferometrically canceling the mean response of the system by displacing the input field via the directional coupler that is used to add the pump tone to the TWPA input [Remm23a].

Alternatively, many of the intermodulation products can be avoided by choosing the frequencies of the signals and the pump carefully. To identify at which frequencies the intermodulation products occur, we divide the intermodulation products arising from amplification of N frequency-multiplexed signals into classes with bounded bandwidth according to how many signal photons and which signs are involved in the process, see Fig. 6.5(a). The width of the frequency band of each intermodulation product class is proportional to its signal order O_s . If all signal frequencies ω_i are chosen between ω_{\min} and ω_{\max} (the signal band), and the pump is detuned by more than the width of the signal band

$$\omega_p > 2\omega_{\max} - \omega_{\min}, \quad (6.4)$$

then none of the intermodulation frequency components of the form $\omega_i \pm (\omega_p - \omega_j)$, where $i, j \in \{1..N\}$, can collide with the signals. This corresponds to the pump frequency in Fig. 6.5(a) where the diagonal red bands do not overlap with the green horizontal signal band. The main intermodulation products that can cause significant crosstalk fall into these two classes as they have signal order $O_s = 2$ and have therefore the highest amplitudes according to our measurements and Eq. (6.1). For typical widths of the signal band of about 1 GHz, this implies signal-pump detunings of up to 2 GHz. In Fig. 6.1(c) we see that, while the gain of the TWPA is slightly reduced at large detunings from the pump, it is still sufficient to overcome the HEMT amplifier noise, as the signal-to-noise ratio remains constant over several gigahertz. Using three-wave mixing amplifiers, for which the pump frequency is about twice the signal frequency, could be beneficial for avoiding frequency collisions, as all the $O_s = 2$ intermodulation products are far detuned from the signals in this case, see right side of Fig. 6.5(a). We also see that overlap of the signal band with the $O_s = 3$ band of intermodulation products of the class $\omega_i + \omega_j - \omega_k$ (blue horizontal band in Fig. 6.5(a))

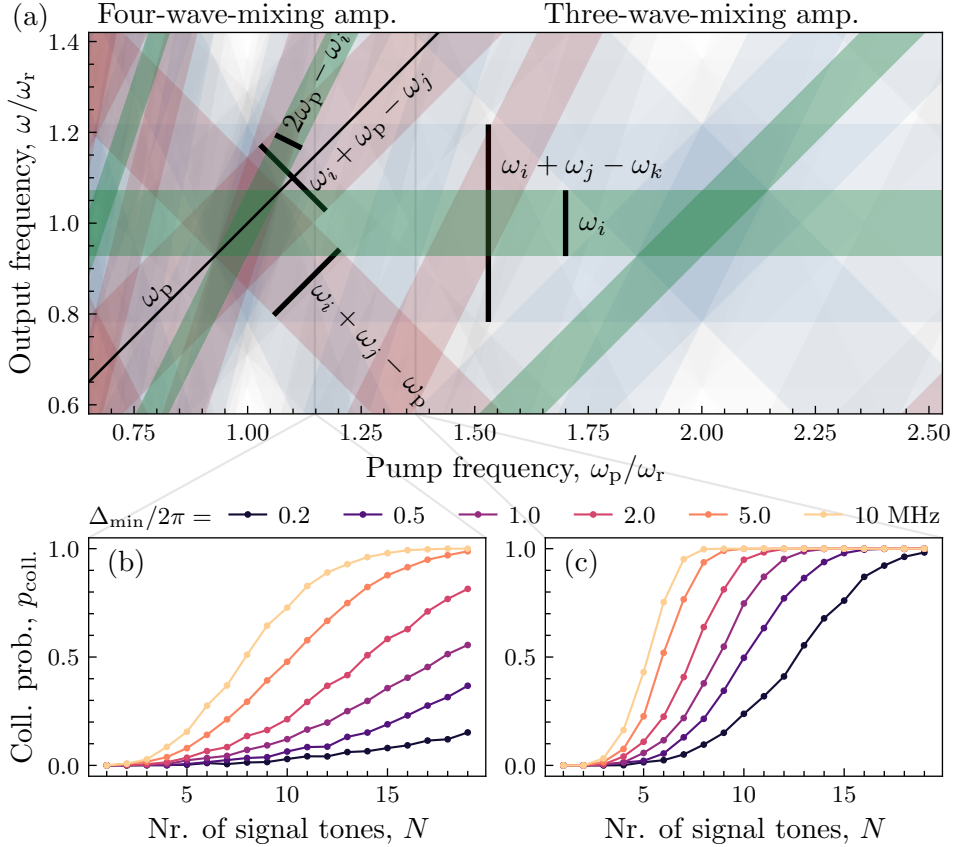


Figure 6.5: Intermodulation product avoidance. (a) Frequencies ω of intermodulation product classes as a function of pump frequency ω_p . Applied readout tones ω_i, ω_j , and ω_k have any frequency in the readout band (green horizontal band) with center frequency ω_r and width $0.145\omega_r$. Green, red, and blue colors of the bands indicate $O_s = 1, 2$, and 3 , respectively, while higher order bands are light gray. The pump tone, signals, idlers, and dominant mixing processes are labeled. (b) Probability $p_{\text{coll.}}$ of an intermodulation product with $O_s = 2$ colliding with a readout tone within a detuning Δ_{min} as a function of the degree of multiplexing N . Readout frequencies are sampled uniformly within a 1 GHz band. The pump is detuned by 0.52 GHz from the edge of the signal band. (c) Same as (b), but for $O_s = 3$ and a pump detuning of 2.05 GHz.

cannot be avoided and frequency collisions are likely for a high degree of multiplexing.

To assess the difficulty of avoiding frequency collisions with intermodulation products, we determine the probability of a collision for various degrees of readout multiplexing N using numerical simulations. We sample 2000 signal frequency configurations from a uniform distribution between 6.4 GHz and 7.4 GHz with a minimal detuning of 20 MHz between any signals. If any intermodulation product has a smaller detuning from a signal than $\Delta_{\min}/2\pi = \{0.2, 0.5, 1.0, 2.0, 5.0, 10\}$ MHz, we consider it as a collision. These detunings correspond to the full-width half-maximum bandwidths of square pulses of lengths $\{3, 1.2, 0.6, 0.3, 0.12, 0.06\}$ μ s. First, we consider a pump frequency of $\omega_p/2\pi = 7.92$ GHz, in which case condition (6.4) is not satisfied, and we calculate the probability of collision with $O_s = 2$ intermodulation products, see Fig. 6.5(b). Second, we consider a pump frequency of $\omega_p/2\pi = 9.45$ GHz, for which there are no collisions with $O_s = 2$ intermodulation products and we calculate the collision probability with $O_s = 3$ terms, see Fig. 6.5(c).

By carefully choosing the readout frequencies, it is possible to avoid all $O_s = 2$ intermodulation products when multiplexing even a 120-ns-short readout of up to $N = 10$ qubits even when the condition given by Eq. (6.4) is not satisfied, as the collision probability is around 50% for random sampling of readout frequencies [see $\Delta_{\min}/2\pi = 5$ MHz line in Fig. 6.5(b)]. However, if the difference of readout frequencies from their design values is on the order of 10 MHz, for example, because of variations in the resonator fabrication, avoiding collisions becomes almost impossible, independent of the readout duration [see $\Delta_{\min}/2\pi = 10$ MHz line in Fig. 6.5(b)]. On the other hand, avoiding $O_s = 3$ intermodulation products becomes practically impossible for more than $N = 6$ qubits with $\Delta_{\min}/2\pi = 10$ MHz. This means that for fast high-fidelity readout with a large degree of multiplexing, it is critical to make sure that the third order intercept power of the amplifier p_{IP3} is well above the used signal power.

In practice, a combination of frequency avoidance and suppression of intermodulation distortion will likely be required to achieve a high degree of multiplexing for fast readout with low crosstalk.

6.4. Discussion

In this chapter we characterized the intermodulation distortion of a traveling wave parametric amplifier. We identified intermodulation products at frequencies of all integer prefactor combinations of two signal tone frequencies up to signal order $O_s = 3$ and characterized their dependence on the input power, which we found to be a power law with O_s as the exponent if signal powers are swept together. An interesting topic for future investigation would be the dependence of the intermodulation products on the pump power.

When operating the amplifier close to its saturation point with multiple input signals, we found that neither the gain nor the signal-to-noise ratio are much reduced compared to when using a single tone at the same total input power. Intermodulation distortion can nonetheless lead to significant readout errors and crosstalk for multiplexed readout if an intermodulation product comes close to one of the signal frequencies.

Frequency collisions with intermodulation products of highest signal order $O_s = 2$ can be completely avoided if the pump frequency is designed to be detuned from the signals by more than the total width of the signal band. The relative amplitude of higher-order intermodulation products can be suppressed by increasing the saturation power of the amplifier and by increasing the power-efficiency of readout.

A high degree of frequency multiplexing for readout is very desirable for scaling up general-purpose quantum processors to hundreds of qubits, for example, for quantum error correction, which heavily relies on fast low-crosstalk mid-circuit measurements. We found that careful consideration of the intermodulation distortion and amplifier saturation is needed to achieve the desired amplifier performance.

As the known quantum algorithms with practical applications, which have a proven speedup over known classical algorithms, require millions if not billions of operations, quantum error correction will be needed to achieve error rates low enough for their implementation. In this work, we have demonstrated, for the first time using superconducting circuits, repeated quantum error correction of a single logical qubit. However, the physical error rates were too high to observe a reduced logical error probability. In this chapter we discuss some of the next steps that need to be taken toward the goal of a useful error-corrected quantum processor.

Reducing Error Rates

Because we did not observe a significant advantage in using the error correction scheme over just operating the physical qubit, the first crucial step is to reduce the physical error rates before increasing the code distance or scaling to more logical qubits. There are three main directions toward reducing the physical error rate.

First, one can reduce the decoherence rate of the qubits. The main factor limiting the coherence of current superconducting qubits is material losses. By using tantalum instead of niobium as the base metalization layer, and by increasing the qubit size to ~ 1 mm, qubit coherence times above 200 μ s have been reproducibly demonstrated [Place21], which is almost an order of magnitude improvement over the average lifetime presented in Chapter 4. Furthermore, the density of spurious two-level system (TLS) defects that couple strongly to the qubits needs to be reduced, for example by reducing junction dimensions [Zanuz23], as they were the main limiting factor for improving the fidelity of two-qubit gates so far. As the decoherence due

to material losses is reduced, the requirements on couplings to external control lines, such as the readout resonators, flux lines, and the charge drive line, become also more stringent [Kono20]. To improve the coherence even further, quantum circuits different from the transmon can be utilized. For example, coherence times above 1 ms have been demonstrated with *fluxonium* qubits, which have a very weak electrical coupling to the surrounding lossy environment [Somoroff23]. A device with more than two coupled fluxonium qubits, however, remains to be demonstrated.

Another option is to implement gates faster by increasing the relevant coupling rates. By improving the tuneup procedure of our single-qubit gates, we could reduce the gate duration from current 40 ns down to 20 ns, at which duration the fidelity starts to be limited by leakage into the higher excited states [Lazăr23]. For faster two-qubit gates, the inter-qubit coupling J_{QQ} could be increased, see Section C.3, at the cost of larger dispersive qubit-qubit couplings. Most of the crosstalk due to the increased dispersive couplings could be suppressed by a careful dynamical decoupling scheme, but effects such as the shift of the second excited level of a qubit involved in a gate might still lead to reduced gate fidelities and leakage [Krunner20]. The readout speed can also be increased by at least a factor of two with known techniques by increasing the relevant coupling rates [Heinsoo18, Walter17, Swiadek23].

Finally, reducing control errors will be needed, in particular those that lead to qubit leakage outside the computational subspace. In our demonstration of quantum error correction, we used postselection to remove the detrimental effects of leakage, which caused the loss of about 8% of data for each stabilizer measurement cycle. For a scalable solution against the residual leakage, the leaked population should be actively driven back to the computational subspace, as discussed in Section 4.6.

With sufficiently reduced error rates, an exponential suppression of logical error rates with the distance of the code can be demonstrated. To reach a per-cycle logical error rate of $\sim 10^{-12}$ with a physical error rate of 10^{-3} , a surface code of distance at least $d = 11$, consisting of $n = 241$ qubits, would be needed [Fowler12b]. There are many cryogenic-, electrical-, and fabrication-engineering challenges that need to be resolved to reliably produce and operate such large devices.

Demonstrating Logical Circuit Building Blocks

Demonstrations of quantum error correction (QEC) using surface codes have so far implemented a single logical qubit and used offline decoding. The building blocks of a logical error-corrected circuit remain to be demonstrated in future experiments. These include moving logical qubits across the surface, splitting and merging multiple logical qubits, and fault-tolerant preparation of magic states for single-qubit $\pi/2$ and $\pi/4$ rotations.

While applying the logical corrections arising from the moving, splitting, and merging operations can be deferred using Pauli frame updating [de-Beaudrap20], the $\pi/4$ rotations are probabilistic in their nature and require decoding in real time to be able to apply the correct feedback operation, see also Section 1.3. Real-time decoding has been demonstrated for the distance $d = 3$ color code in an ion-trap quantum processor with a cycle-time of 200 ms, which is a factor 10^5 slower than in our implementation [Ryan-Anderson21]. Decoders alternative to the minimum-weight perfect matching (MWPM) decoder that we used here have been developed for surface codes which are more easily parallelized and can keep up with the rate of syndrome generation at the short stabilizer measurement cycle time of $\sim 1 \mu\text{s}$ [Delfosse21, Liyanage23]

Preparation of magic states is considered to be one of the most resource-intensive requirements of large-scale logical circuits. Initial proposals for preparing magic states for $\pi/4$ rotations involved preparing faulty copies of the magic state and encoding them in a tailored error correcting code, such that the original errors can be detected [Bravyi05, Meier13]. Doing the encoding-fault tolerantly can, however, lead to a large overhead [Fowler18]. Recently, an efficient protocol to prepare magic states on surface code using appropriately-sized surface code patches has been proposed [Litinski19]. But even with the new technique, the resource cost is rather high for near-term demonstration. For example, demonstrating fault-tolerant magic state preparation for a distance $d = 3$ logical qubit using the method from Ref. [Litinski19] requires around 153 physical qubits. For an output error probability corresponding to a distance $d = 11$ code, the number of required physical qubits is 1609.

Using Alternative Codes

As discussed in Section 1.3, surface codes have a large overhead, requiring $\sim 10^7$ qubits and runtimes of up-to a month for many practical applications. Quantum low-density parity check (QLDPC) codes have been proposed, for which the number of encoded logical qubits per physical qubit can be much higher than for surface codes [Bravyi23, Dinur23].

However, these codes require long-distance nonlocal connectivity between qubits. Gates using fixed-frequency couplers over 12 mm distance [Majer07] and tunable couplers over 2 mm distance [Marxer23] have been demonstrated, and over 20 mm distance proposed [Zhao22a]. For a typical qubit lattice spacing of 0.8 mm, these lengths are sufficient to connect 25th nearest neighbors, which is sufficient to connect any two qubits in the 24×12 qubit lattice of the $[[144, 12, 12]]$ code proposed in [Bravyi23]. Couplings over even larger distances could be achieved by emitting and absorbing shaped microwave photons [Campagne-Ibarcq18, Kurpiers18] and doing gates between the photons and qubits [Besse20].

How to implement logical gates in these novel highly efficient codes is, however, currently an open question. Because the good QLDPC codes are so recently invented, efficient gate schemes might still be developed. Even without logical gates, these codes might function as a resource-efficient logical memory, while gates are still implemented on surface codes. In any case, demonstrating small-scale QLDPC codes remains an interesting next step.

Distance-Three Surface Code as a Stabilizer Code

In general, any Pauli operator \hat{E} on the data qubits of a surface code can be decomposed as $\hat{E} = \hat{L}\hat{S}\hat{D}$, where \hat{L} is any product of logical operators, \hat{S} is any product of stabilizers and \hat{D} is any product of the so-called destabilizer generators, or destabilizers for short [Aaronson04]. The logical operator part \hat{L} can flip the logical operators of the code, the stabilizer part \hat{S} has no effect, and the destabilizer part \hat{D} determines, which stabilizer values are flipped by the operator \hat{E} . The destabilizers, which come paired with the stabilizers, should commute with all the logical operators, destabilizers, and stabilizers, except the stabilizer corresponding to it, with which it anticommutes. We present a possible set of minimal-weight destabilizers for the $d = 3$ surface code in Table A.1. We can consider the stabilizers and \hat{Z}_L operator as virtual Pauli \tilde{Z} operators, and the corresponding destabilizers and the \hat{X}_L operator as the corresponding virtual Pauli \tilde{X} operators, as they satisfy the standard Pauli operator commutation relations

$$[\tilde{X}_i, \tilde{X}_j] = 0, \quad [\tilde{Z}_i, \tilde{Z}_j] = 0, \quad (\text{A.1ab})$$

$$[\tilde{X}_i, \tilde{Z}_j] = 0 \text{ for } i \neq j, \quad \{\tilde{X}_i, \tilde{Z}_i\} = 0. \quad (\text{A.1cd})$$

Such a decomposition of the Pauli group is also useful for efficient simulation of Clifford circuits, which convert Pauli operators to other Pauli operators [Gottesman99a, Aaronson04].

Table A.1: Distance-three surface code. The stabilizers, destabilizers and logical operators of the $d = 3$ surface code.

Label	Stabilizer, \hat{S}	Destabilizer, \hat{D}
Z1	$\hat{Z}_{D1}\hat{Z}_{D4}$	$\hat{X}_{D4}\hat{X}_{D7}$
Z2	$\hat{Z}_{D4}\hat{Z}_{D5}\hat{Z}_{D7}\hat{Z}_{D8}$	\hat{X}_{D7}
Z3	$\hat{Z}_{D2}\hat{Z}_{D3}\hat{Z}_{D5}\hat{Z}_{D6}$	$\hat{X}_{D5}\hat{X}_{D7}$
Z4	$\hat{Z}_{D6}\hat{Z}_{D9}$	\hat{X}_{D9}
X1	$\hat{X}_{D2}\hat{X}_{D3}$	\hat{Z}_{D3}
X2	$\hat{X}_{D1}\hat{X}_{D2}\hat{X}_{D4}\hat{X}_{D5}$	$\hat{Z}_{D2}\hat{Z}_{D3}$
X3	$\hat{X}_{D5}\hat{X}_{D6}\hat{X}_{D8}\hat{X}_{D9}$	\hat{Z}_{D6}
X4	$\hat{X}_{D7}\hat{X}_{D8}$	$\hat{Z}_{D6}\hat{Z}_{D8}$
	Logical op., \hat{Z}_L	Logical op., \hat{X}_L
	$\hat{Z}_{D1}\hat{Z}_{D2}\hat{Z}_{D3}$	$\hat{X}_{D1}\hat{X}_{D4}\hat{X}_{D7}$

Two-Qubit Gate Swap Errors

The combination of small anharmonicity α , large qubit-qubit coupling J_{QQ} , and diabatic dynamic flux pulse based two-qubit gates can lead to significant swap errors for the gate. To see that, let's first consider the case of a CZ gate implemented with a diabatic unipolar pulse that brings the $|20\rangle$ state into resonance with the $|11\rangle$ state. During the interaction, the detuning between the $|10\rangle$ and $|01\rangle$ states is the anharmonicity of the high-frequency qubit α . The interaction within the single-excitation subspace can therefore be described by the Hamiltonian

$$\hat{H} = \hbar \frac{\alpha}{2} \hat{Z} + \hbar J_{\text{QQ}} \hat{X}, \quad (\text{B.1})$$

with $\hat{Z} = |01\rangle\langle 01| - |10\rangle\langle 10|$ and $\hat{X} = |01\rangle\langle 10| + |10\rangle\langle 01|$. Turning this interaction on for a pulse duration of τ implements the unitary $\hat{U} = \hat{I} \cos \tilde{J}\tau - i\hat{H}/(\hbar\tilde{J}) \sin \tilde{J}\tau$, where $\tilde{J} = \sqrt{J_{\text{QQ}}^2 + \alpha^2/4}$ is the effective coupling rate for a detuning of α . The unitary implements a swap rotation by an angle

$$\begin{aligned} \theta &= 2 \arcsin |\langle 10|\hat{U}|01\rangle| = 2 \arcsin \left| \frac{J_{\text{QQ}}}{\tilde{J}} \sin \Omega\tau \right| \leq \\ &2 \arcsin \left| \frac{2J_{\text{QQ}}}{\sqrt{\alpha^2 + 4J_{\text{QQ}}^2}} \right| = 2 \arctan \left| \frac{2J_{\text{QQ}}}{\alpha} \right|. \end{aligned} \quad (\text{B.2})$$

For a gate implemented with a net-zero pulse, two such swap operations happen consecutively, leading to a worst-case rotation angle of $\theta = 4 \arctan |2J_{\text{QQ}}/\alpha|$. On the other hand, by controlling the phase gathered between the two parts of the net-zero pulse, the two swap rotations can also be made to cancel one-another.

Ignoring the single-qubit phase errors, which are corrected by virtual $Z^{\phi/\pi}$ gates, we can write the unitary corresponding to a CZ gate with a swap error by an angle θ as

$$\hat{U}_\theta = \begin{array}{c} \langle 00| \quad \langle 01| \quad \langle 10| \quad \langle 11| \\ |00\rangle \\ |01\rangle \\ |10\rangle \\ |11\rangle \end{array} \begin{pmatrix} 1 & 0 & 0 & 0 \\ 0 & \cos \theta/2 & \sin \theta/2 & 0 \\ 0 & \sin \theta/2 & \cos \theta/2 & 0 \\ 0 & 0 & 0 & -1 \end{pmatrix}. \quad (\text{B.3})$$

The average gate error for this process is given by

$$\varepsilon_{2i} = \frac{d^2 - |\text{Tr}(\hat{U}_0^\dagger \hat{U}_\theta)|^2}{d(d+1)} = \frac{1}{10} \left(5 - 4 \cos \frac{\theta}{2} - \cos \theta \right), \quad (\text{B.4})$$

with $d = 4$ the dimension of the Hilbert space and \hat{U}_0 the target CZ gate unitary with $\theta = 0$.

In this appendix, we present three topics related to device design: modeling the frequency-multiplexed readout circuits of our devices in Section C.1, self-consistent simulation of coplanar capacitors in Section C.2, and finally the design of a static two-qubit coupling element in Section C.3.

C.1. Extended Readout Circuit Fitting Model

In this section, we derive the transmission spectrum of a Purcell filter and a readout resonator coupled to a feedline with an input capacitor, following the general procedure outlined in Ref. [Heinsoo18]. There are two differences in our derivation compared to the one in the Ref. [Heinsoo18]. First, we use a sign convention that is standard in electrical engineering, where the time-derivative of a monochromatic field a is given by $\dot{a} = i\omega a$. Second, we consider a piece of transmission line of length ℓ between the input capacitor and the Purcell filter, which affects the interference between the wave directly emitted to the output port the one reflected from the input capacitor, see also Fig. C.1.

The steady-state fields of the two resonators are described by the input-output relations [Gardiner85]

$$i\omega a_{\text{R}} = i\omega_{\text{R}} a_{\text{R}} - \frac{\gamma_{\text{R}}}{2} a_{\text{R}} - iJ_{\text{PR}} a_{\text{P}}, \quad (\text{C.1a})$$

$$i\omega a_{\text{P}} = i\omega_{\text{P}'} a_{\text{P}} - \frac{\gamma_{\text{P}} + \kappa_{\text{P}'}}{2} a_{\text{P}} - iJ_{\text{PR}} a_{\text{R}} - \sqrt{\kappa_{\text{P}'}} b_{\rightarrow}, \quad (\text{C.1b})$$

$$b_{\leftarrow} = b_{\rightarrow} + \sqrt{\kappa_{\text{P}'}} a_{\text{P}}, \quad (\text{C.1c})$$

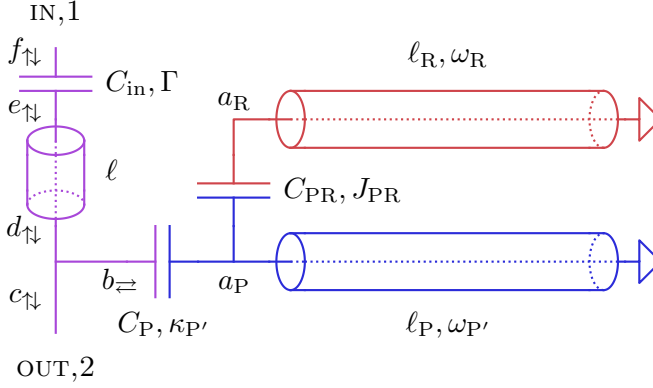


Figure C.1: Readout circuit. The circuit of a Purcell filter and readout resonator coupled to the readout feedline with an input capacitor for directionality.

the T-junction by the equations

$$b_{\rightarrow} = -\frac{1}{3}b_{\leftarrow} + \frac{2}{3}c_{\uparrow} + \frac{2}{3}d_{\downarrow}, \quad (\text{C.1d})$$

$$c_{\downarrow} = \frac{2}{3}b_{\leftarrow} - \frac{1}{3}c_{\uparrow} + \frac{2}{3}d_{\downarrow}, \quad (\text{C.1e})$$

$$d_{\uparrow} = \frac{2}{3}b_{\leftarrow} + \frac{2}{3}c_{\uparrow} - \frac{1}{3}d_{\downarrow}, \quad (\text{C.1f})$$

the transmission line by the equations

$$e_{\uparrow} = e^{-i\omega\ell/v_P}d_{\uparrow}, \quad (\text{C.1g})$$

$$d_{\downarrow} = e^{-i\omega\ell/v_P}e_{\downarrow}, \quad (\text{C.1h})$$

and the input capacitor by the equations

$$f_{\uparrow} = (1 - \Gamma)e_{\uparrow} + \Gamma f_{\downarrow}, \quad (\text{C.1i})$$

$$e_{\downarrow} = (1 - \Gamma)f_{\downarrow} + \Gamma e_{\uparrow}. \quad (\text{C.1j})$$

Here, a_R and a_P are the intra-resonator fields, b_{\rightleftharpoons} , $c_{\uparrow\downarrow}$, $d_{\uparrow\downarrow}$, $e_{\uparrow\downarrow}$, and $f_{\uparrow\downarrow}$ the traveling fields at different points in the circuit, see Fig. C.1, ω_R and $\omega_{P'}$ the frequencies of the resonators, J_{PR} the coupling rate between them, γ_P and γ_R the intrinsic decay rates of the resonators, $\kappa_{P'}$ the external coupling

rate of the Purcell filter, v_p the phase velocity of the transmission line, and $\Gamma = 1/(1 + 2i\omega Z_0 C_{\text{in}})$ the reflection coefficient of the input capacitor with capacitance C_{in} and transmission line characteristic impedance Z_0 .

Solving Eqs. (C.1) for $S_{21} = c_{\downarrow}/f_{\downarrow}$ with no input from the output side $c_{\uparrow} = 0$, we obtain the equation

$$S_{21} = (1 - \Gamma)e^{-i\omega\ell/v_p} \left(1 - \frac{ie^{-i\phi}}{2 \cos \phi} \frac{\kappa_P \Delta_R}{J_{\text{PR}}^2 - \Delta_R \Delta_P} \right), \quad (\text{C.2})$$

where we have written

$$1 + e^{-2i\omega\ell/v_p} \Gamma = re^{-i\phi} \quad (\text{C.3})$$

in a polar form. The effective Purcell filter linewidth is given by $\kappa_P = \kappa_{P'} r \cos(\phi)/2$, its frequency by $\omega_P = \omega_{P'} + \kappa_{P'} r \sin(\phi)/4$, and the complex detunings by $\Delta_R = \omega - \omega_R - i\gamma_R/2$ and $\Delta_P = \omega - \omega_P - i(\gamma_P + \kappa_P)/2$. Note, that the Purcell filter frequency shift has an opposite sign compared to the derivation in Ref. [Heinsoo18]. We have verified the validity of our result by comparing to equivalent microwave circuit simulation.

For fitting the model Eq. (C.2) to experimental data, the quantities r and ϕ can be considered independent of frequency, as they change very little over the linewidth of the resonator for realistic parameters. It is also useful to make the amplitude and electrical delay of the transmission line fitting parameters, yielding the model

$$S_{21} = (A_0 + A_{\omega}\omega)e^{-i(\phi_0 + \tau\omega)} \left(1 - \frac{ie^{-i\phi}}{2 \cos \phi} \frac{\kappa_P \Delta_R}{J_{\text{PR}}^2 - \Delta_P \Delta_R} \right), \quad (\text{C.4})$$

with electrical delay τ and linear overall gain $A_0 + A_{\omega}\omega$.

To provide some intuition about the phase parameter ϕ , we point out that in the small transmission limit $\Gamma \approx 1$, we have $\phi \approx \omega\ell/v_p$, clipped between $\pm\pi/2$, see Fig. C.2(a). We see that $\phi \approx 0$ if we couple at integer multiples of $\lambda_P/2 = \pi v_p/\omega_{P'}$. To understand, how a nonzero ϕ modifies the transmission spectrum, and to verify the fitting model (C.4), we simulate the transmission spectra using the transmission matrix formalism, also known as ABCD-matrix formalism, for the circuit show in Fig. C.1 [Pozar12]. We target $|1 - \Gamma| = 0.16$, $\omega_{P'}/2\pi = \omega_R/2\pi = 7$ GHz, $J_{\text{PR}}/2\pi = 10$ MHz, and

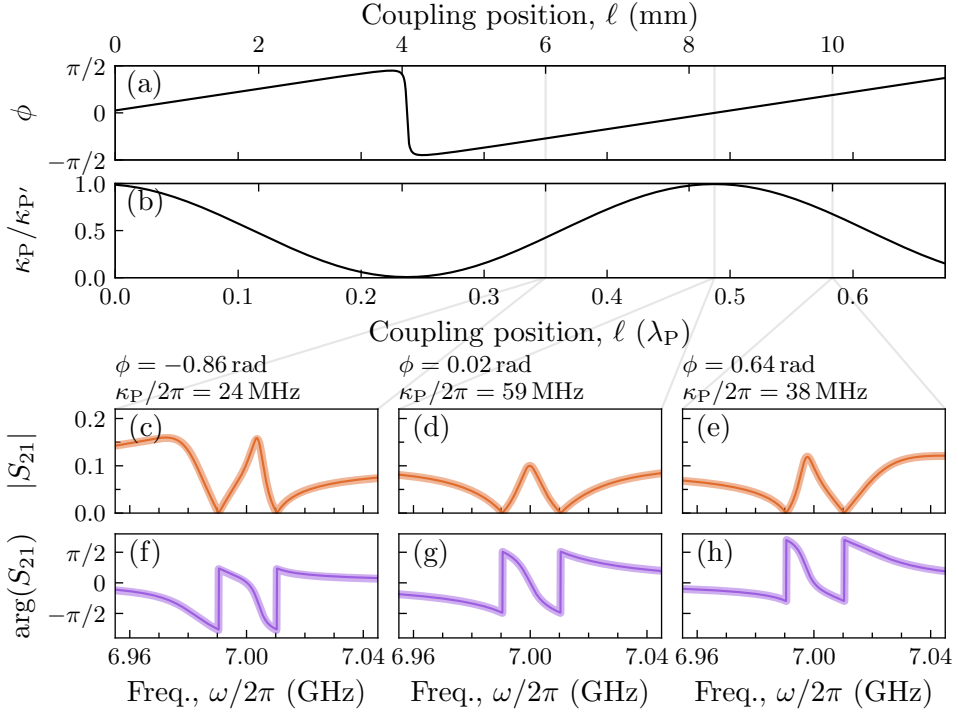


Figure C.2: Readout spectra. (a) The phase ϕ as a function of the coupling position ℓ according to Eq. (C.3) for $|1 - \Gamma| = 0.16$, corresponding to -16 dB power transmission. The bottom axis is given in the units of wavelengths of the Purcell filter and the top axis corresponds to distance from the input capacitor assuming $\omega_{P'}/2\pi = 7$ GHz and $v_p = 120$ mm/ns. (b) The reduction factor $r \cos \phi/2$ of the Purcell filter linewidth. (c,d,e) Modulus of the transmission spectrum $|S_{21}|$. Thin lines are simulated using transmission matrix formalism with Purcell filter coupled to the feedline at $\ell = 6$ mm, 8.4 mm, and 10 mm, respectively. See main text for other simulation details. Lighter thick lines are fits to the model (C.4). The fitted values for ϕ and κ_P are indicated above the panels. (f,g,h) The simulated and fitted phase of the transmission corresponding to panels (c,d,e) with the electrical delay subtracted.

$\kappa_{P'}/2\pi = 60$ MHz, by setting the circuit parameters as

$$C_{\text{in}} = \frac{|1 - \Gamma|}{2\omega_{P'} Z_0 \sqrt{1 - |\Gamma|^2}} = 23 \text{ fF}, \quad (\text{C.5a})$$

$$C_{\text{P}} = \sqrt{\frac{\pi \kappa_{P'}}{4\omega_{P'}^3 Z_0^2}} = 37 \text{ fF}, \quad (\text{C.5b})$$

$$C_{\text{PR}} = \frac{\pi J_{\text{PR}}}{2Z_0 \omega_{P'} \omega_{\text{R}}} = 1.0 \text{ fF}, \quad (\text{C.5c})$$

$$\ell_{\text{P}} = v_{\text{p}} \left(\frac{\pi}{2\omega_{P'}} - Z_0 (C_{\text{P}} + C_{\text{PR}}) \right) = 4.1 \text{ mm}, \quad (\text{C.5d})$$

$$\ell_{\text{R}} = v_{\text{p}} \left(\frac{\pi}{2\omega_{\text{R}}} - Z_0 C_{\text{PR}} \right) = 4.3 \text{ mm}, \quad (\text{C.5e})$$

where we have taken $Z_0 = 50 \Omega$ and $v_{\text{p}} = 120$ mm/ns. The approximate analytical formulas are derived using methods presented in Ref. [Pechal16]. The simulated spectra and the fits with coupling points $\ell = 6$ mm, 8.4 mm, and 10 mm are shown in Fig. C.2(c-h). The excellent match between the simulation and the fit, together with the match between the fitted parameter and target values, verifies the validity of the fitting model.

A distinct feature of nonzero ϕ is the asymmetric shape of the Purcell filter resonance. If the transmission is higher at frequencies below the resonance, compared to the transmission at frequencies above the resonance, then $\phi < 0$, and the coupling length ℓ should be increased to achieve $\phi = 0$, see Fig. C.2(c,f). On the other hand, for $\phi > 0$, the transmission is higher at frequencies above the resonance, and the coupling distance should be reduced, see Fig. C.2(e,h). We emphasize, that the phase parameter ϕ should be minimized by adjusting the coupling points of the readout circuits when designing a frequency-multiplexed readout feedline. This helps avoid excessively large Purcell filter capacitors C_{P} , which could lead to systematic frequency shifts and additional reflections in the readout feedline.

C.2. Reference Planes for Lumped Element Modeling

When simulating a layout of a microwave circuit as a network of connected lumped elements and transmission lines, it is important that the lengths and capacitances of the lumped elements are consistent with the actual laid out design. Usually, the capacitance of a given design is simulated

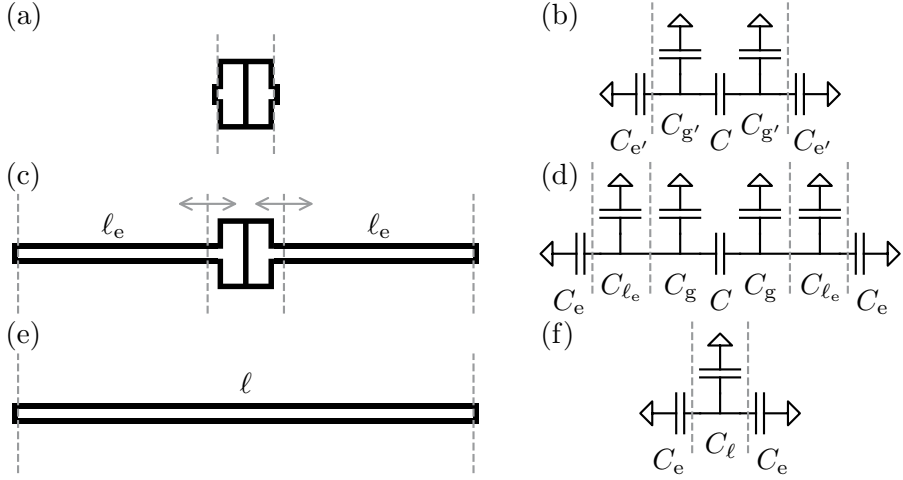


Figure C.3: Layout reference planes. (a) Naive layout for simulating capacitor capacitances without correctly accounting for boundary effects. Black features indicate areas where the thin superconducting film has been removed. (b) Equivalent circuit for the layout (a), where only the sum of the capacitances $C_{g'} + C_{e'}$ can be extracted. (c) Simulation layout of the capacitor with extended CPW sections. The vertical dashed lines indicate reference planes, up-to-which the length of the CPW should be measured. (d) Circuit equivalent to the layout (c), where the capacitance C_{l_e} is proportional to the length l_e . (e) Simulation layout for determining the per-length capacitance C_l/l and the end capacitance C_e .

by solving the electrostatics problem using the finite element method with software such as *ANSYS Maxwell* or *Comsol Multiphysics*. In this section, we describe a self-consistent way, how to simulate these capacitances and set the reference planes of the two-dimensional designs, up-to-which the lengths of the transmission lines should be measured.

Naively, one can simulate the pad-to-pad capacitance C of the capacitor using the layout and equivalent circuit shown in Fig. C.3(a,b). The simulation tool can not, however distinguish between capacitance-to-ground of the pads $C_{g'}$ and the extra capacitance due to the termination the short CPW section $C_{e'}$. Furthermore, the capacitances, as well as their sum, will depend on the

length of the termination in a nontrivial way due to boundary effects.

To correctly account for the boundary effects of the CPW termination, a section of CPW of length ℓ_e , which is much larger than the feature sizes of the capacitor and the CPW, should be included in the simulation, see Fig. C.3(c,d). This way, the extra capacitance due to the CPW termination C_e is independent of the capacitor geometry, and can be self-consistently subtracted. Also, the capacitance due to the CPW section C_{ℓ_e} needs to be subtracted from the total simulated capacitance to ground of the pad $C_g + C_{\ell_e} + C_e$ to obtain the capacitance to ground of the capacitor pad C_g .

The values of the CPW termination capacitance C_e and the capacitance C_ℓ per length ℓ can be found by simulating CPW sections of various lengths ℓ and fitting the total capacitance to a linear model, see Fig. C.3(e,f).

We note, that, as long as the capacitor dimensions are significantly smaller than the wavelength of the field, any self-inductance of the capacitor that is not accounted-for by such modeling should have a negligible effect, as there is no current flowing in the open end of the circuit. This means, that the reference plane, up-to which the transmission line length is measured, can be chosen arbitrarily, as indicated by the double-headed arrows in Fig. C.3(c), as long as it is consistently kept the same in the simulations and when using the element in a later layout. For layout convenience, to decouple the size parameters of the capacitor from the length parameter of the connected CPW, we suggest placing the reference planes at the coordinate origin of the capacitor.

C.3. Qubit-Qubit Coupler Design

In this work we employed sections of capacitively coupled transmission lines between the qubits to mediate the interactions needed to implement two-qubit gates, If the transmission line section is short, then this coupling can be modeled as a direct lumped capacitor between the two qubits [Barends14]. On the other hand, if the frequency of the $\lambda/2$ resonator, formed by the coupling transmission line, is close to the qubit frequencies, then the system can be modeled as three coupled oscillators [Majer07]. The device for the entanglement stabilization experiment, see Section 3.2, was in this latter regime, with the coupler frequencies at about 7.5 GHz. For quantum error detection and correction experiments, however, we increased the resonator frequency to avoid strong coupling of the readout tone of auxiliary qubits

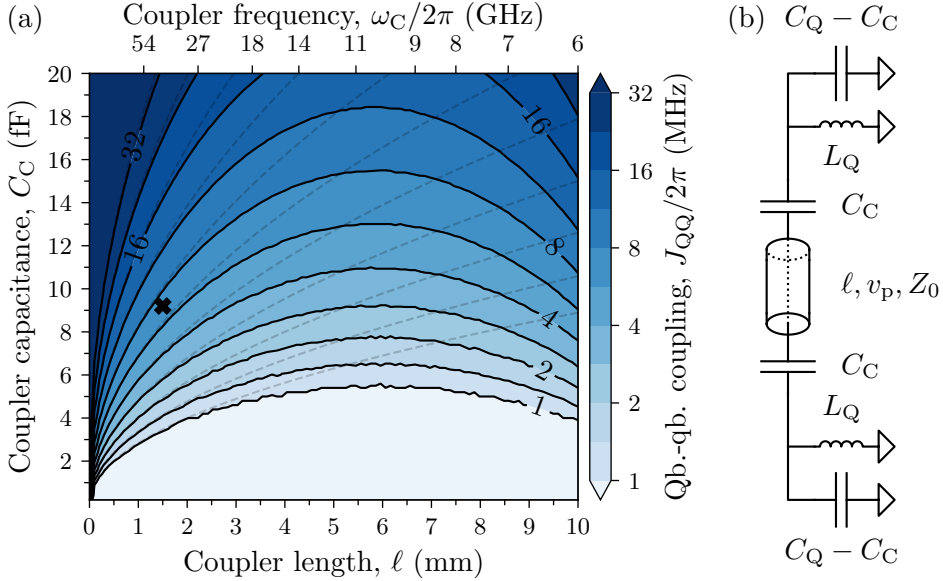


Figure C.4: Qubit-qubit coupling. (a) Coupling J_{QQ} between qubits at 5 GHz when connected using a CPW transmission line of length ℓ and capacitance C_C at each end. Analytical approximation for short lengths according to Eq. (C.6) indicated as dashed contour lines. The phase velocity is 120 nm/ns, the characteristic impedance of the CPW is $50\ \Omega$, and the charging energy of the qubits is $E_C/h = 165$ MHz. The resonance frequency of the $\lambda/2$ coupler ω_C is indicated on the top axis. The parameters targeted for the 17-qubit device presented in Chapter 4 are indicated with a black cross. (b) The simulated equivalent circuit.

to their neighboring data qubits.

Here, we present the dependence of the inter-qubit coupling rate J_{QQ} on the length ℓ of the CPW coupler and its capacitance C_C to the qubits. To determine the coupling rate, we simulate the transmission spectrum through a circuit of two identical LC-resonators connected via a capacitively coupled transmission line using the transmission matrix formalism [Pozar12]. The total capacitance of the qubits is $C_Q = 117$ fF, corresponding to $E_C/h = 165$ MHz, and their frequency is $\omega_Q = 1/\sqrt{C_Q L_Q} = 2\pi \times 5$ GHz. We determine the coupling rate from the frequencies of two resonant peaks that appear in the transmission spectrum and are separated by $2J_{\text{QQ}}$, see

Fig. C.4 for the results.

In the short coupler limit, the coupling transmission line is well-modeled as a shunt capacitance to ground with capacitance $C_{\text{CPW}} = \ell/(v_p Z_0)$, where v_p is the transmission line phase velocity and Z_0 its characteristic impedance. In this case, the coupling rate is given by

$$J_{\text{QQ}} = \frac{C_C \omega_Q}{C_Q} \left(1 + \frac{C_{\text{CPW}}}{2C_C} \right)^{-1}, \quad (\text{C.6})$$

see the dashed lines in Fig. C.4. For the intermediate lengths $\ell \approx \pi v_p / 2\omega_Q$, the short coupler approximation breaks down and the coupling rate starts increasing as the coupler length is increased. Finally, as $\ell \approx \pi v_p / \omega_Q$ the qubits and the resonator are strongly hybridized and the coupling is of a similar magnitude as for $\ell = 0$.

Acknowledgements

This thesis stands on the work of many years by a large team of brilliant people, which I am grateful to be a part of. The work presented here would not have been possible without you.

First, I thank Andreas for setting up a research group where such state-of-the-art experiments can be done. You have taught me the value of polishing the presentation of my work, be it figures, writing, or slides. I will take the high bar of quality with me in my future endeavors. I also appreciate your guidance on how to be successful in science by keeping the experiments simple where possible and thoroughly understanding all aspects of the experimental setup.

I am very grateful to all my direct mentors over the years: Johannes Heinsoo, Christian, Christopher, and Sebi. You have guided me in the process of learning how to work with microwave electronics, cryogenics, and how to analyze quantum circuits. In addition to lab skills, you have as importantly helped me to improve my scientific writing skills. I thank Sebi, Johannes Herrmann and Nathan for reading my thesis and giving detailed feedback. Furthermore, I thank Johannes Herrmann for always happily explaining to me all aspects of electronics design and operation. All my clean-room skills I learned from Mihai, Alex and Mohsen.

I enjoyed all the time spent with the group-room lunch crew: Steph, James, Josua, Kieran, Sasha, Graham, Nicolas, Jakob. I was always looking forward to the lunchtime games. Special thanks goes to Steph for all the philosophical discussions we had over the years. Though often our world-views did not align, the chats always provided interesting food for thought. I also thank Johannes Herrmann, Luca, François, Dante, Josua, Nathan, for all the tennis matches, disc-golf and hiking. Furthermore, I had an excellent time and many insightful scientific discussions with the rest of the current and former team, including Simon, Michael, Colin, Katya, Jean-Claude, Christoph, Marek, Ilya, Anatoly, Andrés, Kevin, Michele, Paul, Yongxin, and many others.

Acknowledgements

I thank my parents for supporting my move to Switzerland and continuing to support me throughout my studies, even though I was physically far away. Finally, I am ever grateful to my wife Sille and my children, who have supported me on this path. You bring me joy every day!

Bibliography

- [Aaronson04] S. Aaronson and D. Gottesman. “Improved simulation of stabilizer circuits.” *Physical Review A* **70**, 052328 (2004). Cited on page 129.
- [Acharya23] R. Acharya, I. Aleiner, R. Allen, T. I. Andersen, M. Ansmann, F. Arute, K. Arya, A. Asfaw, J. Atalaya, R. Babbush, D. Bacon, J. C. Bardin, J. Basso, A. Bengtsson, S. Boixo, G. Bortoli, A. Bourassa, J. Bovaird, L. Brill, M. Broughton, B. B. Buckley, D. A. Buell, T. Burger, B. Burkett, N. Bushnell, Y. Chen, Z. Chen, B. Chiaro, J. Cogan, R. Collins, P. Conner, W. Courtney, A. L. Crook, B. Curtin, D. M. Debroy, A. D. T. Barba, S. Demura, A. Dunsworth, D. Eppens, C. Erickson, L. Faoro, E. Farhi, R. Fatemi, L. F. Burgos, E. Forati, A. G. Fowler, B. Foxen, W. Giang, C. Gidney, D. Gilboa, M. Giustina, A. G. Dau, J. A. Gross, S. Habegger, M. C. Hamilton, M. P. Harrigan, S. D. Harrington, O. Higgott, J. Hilton, M. Hoffmann, S. Hong, T. Huang, A. Huff, W. J. Huggins, L. B. Ioffe, S. V. Isakov, J. Iveland, E. Jeffrey, Z. Jiang, C. Jones, P. Juhas, D. Kafri, K. Kechedzhi, J. Kelly, T. Khattar, M. Khezri, M. Kieferová, S. Kim, A. Kitaev, P. V. Klimov, A. R. Klots, A. N. Korotkov, F. Kostritsa, J. M. Kreikebaum, D. Landhuis, P. Laptev, K.-M. Lau, L. Laws, J. Lee, K. Lee, B. J. Lester, A. Lill, W. Liu, A. Locharla, E. Lucero, F. D. Malone, J. Marshall, O. Martin, J. R. McClean, T. McCourt, M. McEwen, A. Megrant, B. M. Costa, X. Mi, K. C. Miao, M. Mohseni, S. Montazeri, A. Morvan, E. Mount, W. Mruczkiewicz, O. Naaman, M. Neeley, C. Neill, A. Nersisyan, H. Neven, M. Newman, J. H. Ng, A. Nguyen, M. Nguyen, M. Y. Niu, T. E. O’Brien, A. Opremcak, J. Platt, A. Petukhov, R. Potter, L. P. Pryadko, C. Quintana, P. Roushan, N. C. Rubin, N. Saei, D. Sank, K. Sankaragomathi, K. J. Satzinger, H. F. Schurkus, C. Schuster, M. J. Shearn, A. Shorter, V. Shvarts, J. Skrzuzny, V. Smelyanskiy, W. C. Smith, G. Sterling, D. Strain, M. Szalay, A. Torres, G. Vidal, B. Villalonga, C. V. Heidweiller, T. White, C. Xing, Z. J. Yao, P. Yeh, J. Yoo, G. Young, A. Zalcman, Y. Zhang, and N. Zhu. “Suppressing quantum errors by scaling a surface code logical qubit.” *Nature* **614**, 676–681 (2023). Cited on pages 9, 62, 86, 89 and 94.
- [Aharonov97] D. Aharonov and M. Ben-Or. “Fault-tolerant quantum computation with constant error.” In J. L. B. Walker (Ed.), *Proceedings*

- of the 29th Annual ACM Symposium on Theory of Computing*, 176–188. ACM Press (1997). Cited on page 7.
- [Aharonov06] D. Aharonov, A. Kitaev, and J. Preskill. “Fault-tolerant quantum computation with long-range correlated noise.” *Physical Review Letters* **96**, 050504 (2006). Cited on pages 85 and 103.
- [Albert18] V. V. Albert, K. Noh, K. Duivenvoorden, D. J. Young, R. T. Brierley, P. Reinhold, C. Vuillot, L. Li, C. Shen, S. M. Girvin, B. M. Terhal, and L. Jiang. “Performance and structure of single-mode bosonic codes.” *Physical Review A* **97**, 032346 (2018). Cited on page 5.
- [Andersen19] C. K. Andersen, A. Remm, S. Lazar, S. Krinner, J. Heinsoo, J.-C. Besse, M. Gabureac, A. Wallraff, and C. Eichler. “Entanglement stabilization using ancilla-based parity detection and real-time feedback in superconducting circuits.” *npj Quantum Information* **5**, 69 (2019). Cited on pages 9, 15, 40, 43 and 45.
- [Andersen20] C. K. Andersen, A. Remm, S. Lazar, S. Krinner, N. Lacroix, G. J. Norris, M. Gabureac, C. Eichler, and A. Wallraff. “Repeated quantum error detection in a surface code.” *Nature Physics* **16**, 875–880 (2020). Cited on pages 9, 15, 40 and 43.
- [Arute19] F. Arute, K. Arya, R. Babbush, D. Bacon, J. C. Bardin, R. Barends, R. Biswas, S. Boixo, F. G. S. L. Brandao, D. A. Buell, B. Burkett, Y. Chen, Z. Chen, B. Chiaro, R. Collins, W. Courtney, A. Dunsworth, E. Farhi, B. Foxen, A. Fowler, C. Gidney, M. Giustina, R. Graff, K. Guerin, S. Habegger, M. P. Harrigan, M. J. Hartmann, A. Ho, M. Hoffmann, T. Huang, T. S. Humble, S. V. Isakov, E. Jeffrey, Z. Jiang, D. Kafri, K. Kechedzhi, J. Kelly, P. V. Klimov, S. Knysh, A. Korotkov, F. Kostritsa, D. Landhuis, M. Lindmark, E. Lucero, D. Lyakh, S. Mandrà, J. R. McClean, M. McEwen, A. Megrant, X. Mi, K. Michielsen, M. Mohseni, J. Mutus, O. Naaman, M. Neeley, C. Neill, M. Y. Niu, E. Ostby, A. Petukhov, J. C. Platt, C. Quintana, E. G. Rieffel, P. Roushan, N. C. Rubin, D. Sank, K. J. Satzinger, V. Smelyanskiy, K. J. Sung, M. D. Trevithick, A. Vainsencher, B. Villalonga, T. White, Z. J. Yao, P. Yeh, A. Zalcman, H. Neven, and J. M. Martinis. “Quantum supremacy using a programmable superconducting processor.” *Nature* **574**, 505–510 (2019). Cited on pages 2, 3, 82 and 109.
- [Babbush21] R. Babbush, J. R. McClean, M. Newman, C. Gidney, S. Boixo, and H. Neven. “Focus beyond quadratic speedups for error-corrected quantum advantage.” *PRX Quantum* **2**, 010103 (2021). Cited on page 8.
- [Barak22] B. Barak and K. Marwaha. “Classical algorithms and quantum limitations for maximum cut on high-girth graphs.” In M. Braverman (Ed.), *Proceedings of the 13th Innovations in Theoretical*

-
- Computer Science Conference, 14. Schloss Dagstuhl – Leibniz-Zentrum für Informatik (2022)*. Cited on page 3.
- [Barends13] R. Barends, J. Kelly, A. Megrant, D. Sank, E. Jeffrey, Y. Chen, Y. Yin, B. Chiaro, J. Mutus, C. Neill, P. O’Malley, P. Roushan, J. Wenner, T. C. White, A. N. Cleland, and J. M. Martinis. “Coherent Josephson qubit suitable for scalable quantum integrated circuits.” *Physical Review Letters* **111**, 080502 (2013). Cited on page 82.
- [Barends14] R. Barends, J. Kelly, A. Megrant, A. Veitia, D. Sank, E. Jeffrey, T. C. White, J. Mutus, A. G. Fowler, B. Campbell, Y. Chen, Z. Chen, B. Chiaro, A. Dunsworth, C. Neill, P. O’Malley, P. Roushan, A. Vainsencher, J. Wenner, A. N. Korotkov, A. N. Cleland, and J. M. Martinis. “Superconducting quantum circuits at the surface code threshold for fault tolerance.” *Nature* **508**, 500–503 (2014). Cited on pages 55, 74, 109 and 139.
- [Battistel23] F. Battistel, C. Chamberland, K. Johar, R. W. J. Overwater, F. Sebastiano, L. Skoric, Y. Ueno, and M. Usman. “Real-time decoding for fault-tolerant quantum computing: progress, challenges and outlook.” *Nano Futures* **7**, 032003 (2023). Cited on page 89.
- [Beauregard03] S. Beauregard. “Circuit for Shor’s algorithm using $2n + 3$ qubits.” *Quantum Information & Computation* **3**, 175–185 (2003). Cited on page 2.
- [Besse20] J.-C. Besse, S. Gasparinetti, M. C. Collodo, T. Walter, A. Remm, J. Krause, C. Eichler, and A. Wallraff. “Parity detection of propagating microwave fields.” *Physical Review X* **10**, 011046 (2020). Cited on page 128.
- [Beverland22] M. E. Beverland, P. Murali, M. Troyer, K. M. Svore, T. Hoefler, V. Kliuchnikov, G. H. Low, M. Soeken, A. Sundaram, and A. Vashillo. “Assessing requirements to scale to practical quantum advantage.” *arXiv:2211.07629* (2022). Cited on page 8.
- [Bharti22] K. Bharti, A. Cervera-Lierta, T. H. Kyaw, T. Haug, S. Alperin-Lea, A. Anand, M. Degroote, H. Heimonen, J. S. Kottmann, T. Menke, W.-K. Mok, S. Sim, L.-C. Kwek, and A. Aspuru-Guzik. “Noisy intermediate-scale quantum algorithms.” *Reviews of Modern Physics* **94**, 015004 (2022). Cited on page 3.
- [Bilmes22] A. Bilmes, S. Volosheniuk, A. V. Ustinov, and J. Lisenfeld. “Probing defect densities at the edges and inside Josephson junctions of superconducting qubits.” *npj Quantum Information* **8**, 24 (2022). Cited on page 86.
- [Blais04] A. Blais, R.-S. Huang, A. Wallraff, S. M. Girvin, and R. J. Schoelkopf. “Cavity quantum electrodynamics for superconducting electrical circuits: an architecture for quantum computation.” *Physical Review A* **69**, 062320 (2004). Cited on pages 26 and 28.

- [Blais21] A. Blais, A. L. Grimsmo, S. M. Girvin, and A. Wallraff. “Circuit quantum electrodynamics.” *Reviews of Modern Physics* **93**, 025005 (2021). Cited on pages 20 and 109.
- [Bluvstein22] D. Bluvstein, H. Levine, G. Semeghini, T. T. Wang, S. Ebadi, M. Kalinowski, A. Keesling, N. Maskara, H. Pichler, M. Greiner, V. Vuletić, and M. D. Lukin. “A quantum processor based on coherent transport of entangled atom arrays.” *Nature* **604**, 451–456 (2022). Cited on page 20.
- [Bowdrey02] M. D. Bowdrey, D. K. L. Oi, A. J. Short, K. Banaszek, and J. A. Jones. “Fidelity of single qubit maps.” *Physics Letters A* **294**, 258–260 (2002). Cited on page 46.
- [Braginsky80] V. B. Braginsky, Y. I. Vorontsov, and K. S. Thorne. “Quantum nondemolition measurements.” *Science* **209**, 547–557 (1980). Cited on page 30.
- [Bravyi98] S. B. Bravyi and A. Y. Kitaev. “Quantum codes on a lattice with boundary.” *arXiv:quant-ph/9811052* (1998). Cited on page 7.
- [Bravyi05] S. Bravyi and A. Kitaev. “Universal quantum computation with ideal Clifford gates and noisy ancillas.” *Physical Review A* **71**, 022316 (2005). Cited on pages 15 and 127.
- [Bravyi10] S. Bravyi, D. Poulin, and B. Terhal. “Tradeoffs for reliable quantum information storage in 2D systems.” *Physical Review Letters* **104**, 050503 (2010). Cited on page 10.
- [Bravyi14] S. Bravyi, M. Suchara, and A. Vargo. “Efficient algorithms for maximum likelihood decoding in the surface code.” *Physical Review A* **90**, 032326 (2014). Cited on pages 94 and 108.
- [Bravyi23] S. Bravyi, A. W. Cross, J. M. Gambetta, D. Maslov, P. Rall, and T. J. Yoder. “High-threshold and low-overhead fault-tolerant quantum memory.” *arXiv:2308.07915* (2023). Cited on pages 8 and 128.
- [Brune96] M. Brune, F. Schmidt-Kaler, A. Maali, J. Dreyer, E. Hagley, J. M. Raimond, and S. Haroche. “Quantum Rabi oscillation: a direct test of field quantization in a cavity.” *Physical Review Letters* **76**, 1800 (1996). Cited on page 20.
- [Bultink18] C. C. Bultink, B. Tarasinski, N. Haandbæk, S. Poletto, N. Haider, D. J. Michalak, A. Bruno, and L. DiCarlo. “General method for extracting the quantum efficiency of dispersive qubit readout in circuit QED.” *Applied Physics Letters* **112**, 092601 (2018). Cited on page 116.
- [Bultink20] C. C. Bultink, T. E. O’Brien, R. Vollmer, N. Muthusubramanian, M. W. Beekman, M. A. Rol, X. Fu, B. Tarasinski, V. Ostroukh, B. Varbanov, A. Bruno, and L. DiCarlo. “Protecting quantum entanglement from leakage and qubit errors via repetitive parity measurements.” *Science Advances* **6**, eaay3050 (2020). Cited on pages 9 and 62.

-
- [Burkard23] G. Burkard, T. D. Ladd, A. Pan, J. M. Nichol, and J. R. Petta. “Semiconductor spin qubits.” *Reviews of Modern Physics* **95**, 025003 (2023). Cited on page 20.
- [Calderbank96] A. R. Calderbank and P. W. Shor. “Good quantum error-correcting codes exist.” *Physical Review A* **54**, 1098 (1996). Cited on page 11.
- [Campagne-Ibarcq18] P. Campagne-Ibarcq, E. Zayls-Geller, A. Narla, S. Shankar, P. Reinhold, L. Burkhardt, C. Axline, W. Pfaff, L. Frunzio, R. J. Schoelkopf, and M. H. Devoret. “Deterministic remote entanglement of superconducting circuits through microwave two-photon transitions.” *Physical Review Letters* **120**, 200501 (2018). Cited on page 128.
- [Carr54] H. Y. Carr and E. M. Purcell. “Effects of diffusion on free precession in nuclear magnetic resonance experiments.” *Physical Review* **94**, 630–638 (1954). Cited on page 48.
- [Castellanos-Beltran07] M. A. Castellanos-Beltran and K. W. Lehnert. “Widely tunable parametric amplifier based on a superconducting quantum interference device array resonator.” *Applied Physics Letters* **91**, 083509 (2007). Cited on page 109.
- [Castellanos-Beltran08] M. A. Castellanos-Beltran, K. D. Irwin, G. C. Hilton, L. R. Vale, and K. W. Lehnert. “Amplification and squeezing of quantum noise with a tunable Josephson metamaterial.” *Nature Physics* **4**, 929–931 (2008). Cited on page 109.
- [Caves82] C. M. Caves. “Quantum limits on noise in linear amplifiers.” *Physical Review D* **26**, 1817 (1982). Cited on pages 109 and 116.
- [Chen12] Y. Chen, D. Sank, P. O’Malley, T. White, R. Barends, B. Chiaro, J. Kelly, E. Lucero, M. Mariantoni, A. Megrant, C. Neill, A. Vainsencher, J. Wenner, Y. Yin, A. N. Cleland, and J. M. Martinis. “Multiplexed dispersive readout of superconducting phase qubits.” *Applied Physics Letters* **101**, 182601 (2012). Cited on page 109.
- [Chen21] Z. Chen, K. J. Satzinger, J. Atalaya, A. N. Korotkov, A. Duns-
worth, D. Sank, C. Quintana, M. McEwen, R. Barends, P. V.
Klimov, S. Hong, C. Jones, A. Petukhov, D. Kafri, S. Demura,
B. Burkett, C. Gidney, A. G. Fowler, A. Paler, H. Putter-
man, I. Aleiner, F. Arute, K. Arya, R. Babbush, J. C. Bardin,
A. Bengtsson, A. Bourassa, M. Broughton, B. B. Buckley, D. A.
Buell, N. Bushnell, B. Chiaro, R. Collins, W. Courtney, A. R.
Derk, D. Eppens, C. Erickson, E. Farhi, B. Foxen, M. Giustina,
A. Greene, J. A. Gross, M. P. Harrigan, S. D. Harrington,
J. Hilton, A. Ho, T. Huang, W. J. Huggins, L. B. Ioffe, S. V.
Isakov, E. Jeffrey, Z. Jiang, K. Kechedzhi, S. Kim, A. Kitaev,
F. Kostritsa, D. Landhuis, P. Laptev, E. Lucero, O. Martin,
J. R. McClean, T. McCourt, X. Mi, K. C. Miao, M. Mohseni,

- S. Montazeri, W. Mruczkiewicz, J. Mutus, O. Naaman, M. Neeley, C. Neill, M. Newman, M. Y. Niu, T. E. O'Brien, A. Opremcak, E. Ostby, B. Pató, N. Redd, P. Roushan, N. C. Rubin, V. Shvarts, D. Strain, M. Szalay, M. D. Trevithick, B. Villalonga, T. White, Z. J. Yao, P. Yeh, J. Yoo, A. Zalcman, H. Neven, S. Boixo, V. Smelyanskiy, Y. Chen, A. Megrant, and J. Kelly. “Exponential suppression of bit or phase errors with cyclic error correction.” *Nature* **595**, 383–387 (2021). Cited on pages 9, 62 and 89.
- [Chen22] E. H. Chen, T. J. Yoder, Y. Kim, N. Sundaresan, S. Srinivasan, M. Li, A. D. Córcoles, A. W. Cross, and M. Takita. “Calibrated decoders for experimental quantum error correction.” *Physical Review Letters* **128**, 110504 (2022). Cited on page 89.
- [Cochrane99] P. T. Cochrane, G. J. Milburn, and W. J. Munro. “Macroscopically distinct quantum-superposition states as a bosonic code for amplitude damping.” *Physical Review A* **59**, 2631–2634 (1999). Cited on page 4.
- [Collodo20] M. C. Collodo, J. Herrmann, N. Lacroix, C. K. Andersen, A. Remm, S. Lazar, J.-C. Besse, T. Walter, A. Wallraff, and C. Eichler. “Implementation of conditional phase gates based on tunable ZZ interactions.” *Physical Review Letters* **125**, 240502 (2020). Cited on page 67.
- [Córcoles15] A. D. Córcoles, E. Magesan, S. J. Srinivasan, A. W. Cross, M. Steffen, J. M. Gambetta, and J. M. Chow. “Demonstration of a quantum error detection code using a square lattice of four superconducting qubits.” *Nature Communications* **6**, 6979 (2015). Cited on page 9.
- [Dalibard92] J. Dalibard, Y. Castin, and K. Mølmer. “Wave-function approach to dissipative processes in quantum optics.” *Physical Review Letters* **68**, 580–583 (1992). Cited on page 74.
- [Day03] P. K. Day, H. G. LeDuc, B. A. Mazin, A. Vayonakis, and J. Zmuidzinas. “A broadband superconducting detector suitable for use in large arrays.” *Nature* **425**, 817–821 (2003). Cited on page 109.
- [deBeaudrap20] N. de Beaudrap and D. Horsman. “The ZX calculus is a language for surface code lattice surgery.” *Quantum* **4**, 218 (2020). Cited on pages 13 and 127.
- [deJong21] D. de Jong, C. G. Prosko, D. M. A. Waardenburg, L. Han, F. K. Malinowski, P. Krogstrup, L. P. Kouwenhoven, J. V. Koski, and W. Pfaff. “Rapid microwave-only characterization and readout of quantum dots using multiplexed gigahertz-frequency resonators.” *Physical Review Applied* **16**, 014007 (2021). Cited on page 109.
- [Delfosse21] N. Delfosse and N. H. Nickerson. “Almost-linear time decoding algorithm for topological codes.” *Quantum* **5**, 595 (2021). Cited on page 127.

-
- [Dennis02] E. Dennis, A. Kitaev, A. Landahl, and J. Preskill. “Topological quantum memory.” *Journal of Mathematical Physics* **43**, 4452–4505 (2002). Cited on page 8.
- [DiCarlo10] L. DiCarlo, M. D. Reed, L. Sun, B. R. Johnson, J. M. Chow, J. M. Gambetta, L. Frunzio, S. M. Girvin, M. H. Devoret, and R. J. Schoelkopf. “Preparation and measurement of three-qubit entanglement in a superconducting circuit.” *Nature* **467**, 574–578 (2010). Cited on pages 34, 46 and 63.
- [Ding23] L. Ding, M. Hays, Y. Sung, B. Kannan, J. An, A. D. Paolo, A. H. Karamlou, T. M. Hazard, K. Azar, D. K. Kim, B. M. Niedzielski, A. Melville, M. E. Schwartz, J. L. Yoder, T. P. Orlando, S. Gustavsson, J. A. Grover, K. Serniak, and W. D. Oliver. “High-fidelity, frequency-flexible two-qubit fluxonium gates with a transmon coupler.” *Physical Review X* **13**, 031035 (2023). Cited on page 3.
- [Dinur23] I. Dinur, M.-H. Hsieh, T.-C. Lin, and T. Vidick. “Good quantum LDPC codes with linear time decoders.” In *Proceedings of the 55th Annual ACM Symposium on Theory of Computing*, 905–918. ACM Press (2023). Cited on pages 8 and 128.
- [Dirac58] P. A. M. Dirac. *The Principles of Quantum Mechanics*. Oxford at the Clarendon press, London, United Kingdom, 4th edition (1958). Cited on page 24.
- [DiVincenzo00] D. P. DiVincenzo. “The physical implementation of quantum computation.” *Fortschritte der Physik* **48**, 771–783 (2000). Cited on page 19.
- [Dum92] R. Dum, P. Zoller, and H. Ritsch. “Monte Carlo simulation of the atomic master equation for spontaneous emission.” *Physical Review A* **45**, 4879 (1992). Cited on page 74.
- [Eastin09] B. Eastin and E. Knill. “Restrictions on transversal encoded quantum gate sets.” *Physical Review Letters* **102**, 110502 (2009). Cited on page 13.
- [Edmonds65] J. Edmonds. “Paths, trees, and flowers.” *Canadian Journal of Mathematics* **17**, 449–467 (1965). Cited on page 98.
- [Eichler14a] C. Eichler, Y. Salathe, J. Mlynek, S. Schmidt, and A. Wallraff. “Quantum-limited amplification and entanglement in coupled non-linear resonators.” *Physical Review Letters* **113**, 110502 (2014). Cited on page 109.
- [Eichler14b] C. Eichler and A. Wallraff. “Controlling the dynamic range of a Josephson parametric amplifier.” *EPJ Quantum Technology* **1**, 2 (2014). Cited on pages 109 and 120.
- [Epstein14] J. M. Epstein, A. W. Cross, E. Magesan, and J. M. Gambetta. “Investigating the limits of randomized benchmarking protocols.” *Physical Review A* **89**, 062321 (2014). Cited on pages 46, 55 and 74.

- [Esposito21] M. Esposito, A. Ranadive, L. Planat, and N. Roch. “Perspective on traveling wave microwave parametric amplifiers.” *Applied Physics Letters* **119**, 120501 (2021). Cited on page 109.
- [Farhi14] E. Farhi, J. Goldstone, and S. Gutmann. “A quantum approximate optimization algorithm.” *arXiv:1411.4028* (2014). Cited on page 3.
- [Feynman82] R. P. Feynman. “Simulating physics with computers.” *International Journal of Theoretical Physics* **21**, 467–488 (1982). Cited on pages 1 and 2.
- [Finnila94] A. Finnila, M. Gomez, C. Sebenik, C. Stenson, and J. Doll. “Quantum annealing: a new method for minimizing multidimensional functions.” *Chemical Physics Letters* **219**, 343–348 (1994). Cited on page 3.
- [Flühmann19] C. Flühmann, T. L. Nguyen, M. Marinelli, V. Negnevitsky, K. Mehta, and J. P. Home. “Encoding a qubit in a trapped-ion mechanical oscillator.” *Nature* **566**, 513–517 (2019). Cited on page 5.
- [Fowler09] A. G. Fowler, A. M. Stephens, and P. Groszkowski. “High-threshold universal quantum computation on the surface code.” *Physical Review A* **80**, 052312 (2009). Cited on page 10.
- [Fowler12a] A. G. Fowler. “Time-optimal quantum computation.” *arXiv:1210.4626* (2012). Cited on page 63.
- [Fowler12b] A. G. Fowler, M. Mariantoni, J. M. Martinis, and A. N. Cleland. “Surface codes: towards practical large-scale quantum computation.” *Physical Review A* **86**, 032324 (2012). Cited on pages 7, 13, 68, 78, 86, 103 and 126.
- [Fowler13a] A. G. Fowler. “Coping with qubit leakage in topological codes.” *Physical Review A* **88**, 042308 (2013). Cited on page 85.
- [Fowler13b] A. G. Fowler. “Optimal complexity correction of correlated errors in the surface code.” *arXiv:1310.0863* (2013). Cited on pages 95 and 107.
- [Fowler18] A. G. Fowler and C. Gidney. “Low overhead quantum computation using lattice surgery.” *arXiv:1808.06709* (2018). Cited on pages 13 and 127.
- [Frattini18] N. E. Frattini, V. V. Sivak, A. Lingenfelter, S. Shankar, and M. H. Devoret. “Optimizing the nonlinearity and dissipation of a SNAIL parametric amplifier for dynamic range.” *Physical Review Applied* **10**, 054020 (2018). Cited on pages 109 and 110.
- [Gambetta06] J. Gambetta, A. Blais, D. I. Schuster, A. Wallraff, L. Frunzio, J. Majer, M. H. Devoret, S. M. Girvin, and R. J. Schoelkopf. “Qubit-photon interactions in a cavity: measurement-induced dephasing and number splitting.” *Physical Review A* **74**, 042318 (2006). Cited on page 40.

-
- [Gambetta11] J. M. Gambetta, F. Motzoi, S. T. Merkel, and F. K. Wilhelm. “Analytic control methods for high-fidelity unitary operations in a weakly nonlinear oscillator.” *Physical Review A* **83**, 012308 (2011). Cited on pages 46 and 74.
- [Gardiner85] C. W. Gardiner and M. J. Collett. “Input and output in damped quantum systems: quantum stochastic differential equations and the master equation.” *Physical Review A* **31**, 3761 (1985). Cited on page 133.
- [Georgescu14] I. M. Georgescu, S. Ashhab, and F. Nori. “Quantum simulation.” *Reviews of Modern Physics* **86**, 153–185 (2014). Cited on page 2.
- [Gong22] M. Gong, X. Yuan, S. Wang, Y. Wu, Y. Zhao, C. Zha, S. Li, Z. Zhang, Q. Zhao, Y. Liu, F. Liang, J. Lin, Y. Xu, H. Deng, H. Rong, H. Lu, S. C. Benjamin, C.-Z. Peng, X. Ma, Y.-A. Chen, X. Zhu, and J.-W. Pan. “Experimental exploration of five-qubit quantum error-correcting code with superconducting qubits.” *National Science Review* **9**, nwab011 (2022). Cited on page 9.
- [Göppl08] M. Göppl, A. Fragner, M. Baur, R. Bianchetti, S. Filipp, J. M. Fink, P. J. Leek, G. Puebla, L. Steffen, and A. Wallraff. “Coplanar waveguide resonators for circuit quantum electrodynamics.” *Journal of Applied Physics* **104**, 113904 (2008). Cited on page 28.
- [Gottesman97] D. Gottesman. *Stabilizer Codes and Quantum Error Correction*. Ph.D. thesis, California Institute of Technology (1997). Cited on pages 4, 5 and 6.
- [Gottesman99a] D. Gottesman. “The Heisenberg representation of quantum computers.” In *Proceedings of the 22nd International Colloquium on Group Theoretical Methods in Physics*, 32–43. International Press of Boston, Inc. (1999). Cited on pages 13 and 129.
- [Gottesman99b] D. Gottesman and I. L. Chuang. “Demonstrating the viability of universal quantum computation using teleportation and single-qubit operations.” *Nature* **402**, 390–393 (1999). Cited on pages 15 and 86.
- [Gottesman01] D. Gottesman, A. Kitaev, and J. Preskill. “Encoding a qubit in an oscillator.” *Physical Review A* **64**, 012310 (2001). Cited on page 5.
- [Gottesman14] D. Gottesman. “Fault-tolerant quantum computation with constant overhead.” *Quantum Information & Computation* **14**, 1338 (2014). Cited on page 8.
- [Grimm20] A. Grimm, N. E. Frattini, S. Puri, S. O. Mundhada, S. Touzard, M. Mirrahimi, S. M. Girvin, S. Shankar, and M. H. Devoret. “Stabilization and operation of a Kerr-cat qubit.” *Nature* **584**, 205–209 (2020). Cited on page 4.

- [Gupta23] R. S. Gupta, N. Sundaresan, T. Alexander, C. J. Wood, S. T. Merkel, M. B. Healy, M. Hillenbrand, T. Jochym-O'Connor, J. R. Wootton, T. J. Yoder, A. W. Cross, M. Takita, and B. J. Brown. "Encoding a magic state with beyond break-even fidelity." *arXiv:2305.13581* (2023). Cited on page 9.
- [Haegi23] D. Haegi. *Microwave Crosstalk in Quantum Processors and its Treatment in a New Design Software Framework*. Master's thesis, ETH Zurich (2023). Cited on page 81.
- [Harris78] F. Harris. "On the use of windows for harmonic analysis with the discrete Fourier transform." *Proceedings of the IEEE* **66**, 51–83 (1978). Cited on page 112.
- [Harrow09] A. W. Harrow, A. Hassidim, and S. Lloyd. "Quantum algorithm for linear systems of equations." *Physical Review Letters* **103**, 150502 (2009). Cited on page 3.
- [Harrow17] A. W. Harrow and A. Montanaro. "Quantum computational supremacy." *Nature* **549**, 203–209 (2017). Cited on page 2.
- [Heinsoo18] J. Heinsoo, C. K. Andersen, A. Remm, S. Krinner, T. Walter, Y. Salathé, S. Gasparinetti, J.-C. Besse, A. Potočník, A. Wallraff, and C. Eichler. "Rapid high-fidelity multiplexed readout of superconducting qubits." *Physical Review Applied* **10**, 034040 (2018). Cited on pages 30, 45, 62, 71, 109, 119, 126, 133 and 135.
- [Heinsoo19] J. Heinsoo. *Digital Quantum Computing With Superconducting Qubits*. Ph.D. thesis, ETH Zurich (2019). Cited on page 30.
- [Higgott22] O. Higgott. "PyMatching: a Python package for decoding quantum codes with minimum-weight perfect matching." *ACM Transactions on Quantum Computing* **3**, 16 (2022). Cited on pages 95 and 98.
- [Higgott23a] O. Higgott, T. C. Bohdanowicz, A. Kubica, S. T. Flammia, and E. T. Campbell. "Improved decoding of circuit noise and fragile boundaries of tailored surface codes." *Physical Review X* **13**, 031007 (2023). Cited on page 107.
- [Higgott23b] O. Higgott and C. Gidney. "Sparse Blossom: correcting a million errors per core second with minimum-weight matching." *arXiv:2303.15933* (2023). Cited on page 95.
- [Ho Eom12] B. Ho Eom, P. K. Day, H. G. LeDuc, and J. Zmuidzinas. "A wideband, low-noise superconducting amplifier with high dynamic range." *Nature Physics* **8**, 623–627 (2012). Cited on page 109.
- [Horsman12] C. Horsman, A. G. Fowler, S. Devitt, and R. V. Meter. "Surface code quantum computing by lattice surgery." *New Journal of Physics* **14**, 123011 (2012). Cited on pages 13, 66 and 86.
- [Houck08] A. A. Houck, J. A. Schreier, B. R. Johnson, J. M. Chow, J. Koch, J. M. Gambetta, D. I. Schuster, L. Frunzio, M. H. Devoret,

-
- S. M. Girvin, and R. J. Schoelkopf. “Controlling the spontaneous emission of a superconducting transmon qubit.” *Physical Review Letters* **101**, 080502 (2008). Cited on page 28.
- [Hu19] L. Hu, Y. Ma, W. Cai, X. Mu, Y. Xu, W. Wang, Y. Wu, H. Wang, Y. P. Song, C.-L. Zou, S. M. Girvin, L.-M. Duan, and L. Sun. “Quantum error correction and universal gate set operation on a binomial bosonic logical qubit.” *Nature Physics* **15**, 503–508 (2019). Cited on page 4.
- [IEEE22] IEEE Computer Society. “802.3-2022 – IEEE standard for Ethernet.” Technical report, IEEE (2022). Cited on page 4.
- [iOlius23] A. d. iOlius, P. Fuentes, R. Orús, P. M. Crespo, and J. E. Martinez. “Decoding algorithms for surface codes.” *arXiv:2307.14989* (2023). Cited on page 89.
- [Ithier05] G. Ithier, E. Collin, P. Joyez, P. J. Meeson, D. Vion, D. Esteve, F. Chiarello, A. Shnirman, Y. Makhlin, J. Schrieffer, and G. Schön. “Decoherence in a superconducting quantum bit circuit.” *Physical Review B* **72**, 134519 (2005). Cited on page 25.
- [Iyer15] P. Iyer and D. Poulin. “Hardness of decoding quantum stabilizer codes.” *IEEE Transactions on Information Theory* **61**, 5209 (2015). Cited on page 94.
- [Jerger12] M. Jerger, S. Poletto, P. Macha, U. Hübner, E. Il’ichev, and A. V. Ustinov. “Frequency division multiplexing readout and simultaneous manipulation of an array of flux qubits.” *Applied Physics Letters* **101**, 042604 (2012). Cited on page 109.
- [Joshi21] A. Joshi, K. Noh, and Y. Y. Gao. “Quantum information processing with bosonic qubits in circuit QED.” *Quantum Science and Technology* **6**, 033001 (2021). Cited on pages 4 and 20.
- [Jouzani14] P. Jouzdani, E. Novais, I. S. Tupitsyn, and E. R. Mucciolo. “Fidelity threshold of the surface code beyond single-qubit error models.” *Physical Review A* **90**, 042315 (2014). Cited on page 103.
- [Kassal08] I. Kassal, S. P. Jordan, P. J. Love, M. Mohseni, and A. Aspuru-Guzik. “Polynomial-time quantum algorithm for the simulation of chemical dynamics.” *Proceedings of the National Academy of Sciences* **105**, 18681 (2008). Cited on page 2.
- [Kelly15] J. Kelly, R. Barends, A. G. Fowler, A. Megrant, E. Jeffrey, T. C. White, D. Sank, J. Y. Mutus, B. Campbell, Y. Chen, Z. Chen, B. Chiaro, A. Dunsworth, I.-C. Hoi, C. Neill, P. J. J. O’Malley, C. Quintana, P. Roushan, A. Vainsencher, J. Wenner, A. N. Cleland, and J. M. Martinis. “State preservation by repetitive error detection in a superconducting quantum circuit.” *Nature* **519**, 66–69 (2015). Cited on page 9.
- [Kerschbaum20] M. Kerschbaum. *Implementation of a Controlled-Phase Gate with Flexible Interaction Frequency*. Master’s thesis, ETH Zurich (2020). Cited on page 40.

- [Khezri22] M. Khezri, A. Opremcak, Z. Chen, A. Bengtsson, T. White, O. Naaman, R. Acharya, K. Anderson, M. Ansmann, F. Arute, K. Arya, A. Asfaw, J. C. Bardin, A. Bourassa, J. Bovaird, L. Brill, B. B. Buckley, D. A. Buell, T. Burger, B. Burkett, N. Bushnell, J. Campero, B. Chiaro, R. Collins, A. L. Crook, B. Curtin, S. Demura, A. Dunsworth, C. Erickson, R. Fatemi, V. S. Ferreira, L. F. Burgos, E. Forati, B. Foxen, G. Garcia, W. Giang, M. Giustina, R. Gosula, A. G. Dau, M. C. Hamilton, S. D. Harrington, P. Heu, J. Hilton, M. R. Hoffmann, S. Hong, T. Huang, A. Huff, J. Iveland, E. Jeffrey, J. Kelly, S. Kim, P. V. Klimov, F. Kostritsa, J. M. Kreikebaum, D. Landhuis, P. Laptev, L. Laws, K. Lee, B. J. Lester, A. T. Lill, W. Liu, A. Locharla, E. Lucero, S. Martin, M. McEwen, A. Megrant, X. Mi, K. C. Miao, S. Montazeri, A. Morvan, M. Neeley, C. Neill, A. Nersisyan, J. H. Ng, A. Nguyen, M. Nguyen, R. Potter, C. Quintana, C. Rocque, P. Roushan, K. Sankaragomathi, K. J. Satzinger, C. Schuster, M. J. Shearn, A. Shorter, V. Shvarts, J. Skrzynny, W. C. Smith, G. Sterling, M. Szalay, D. Thor, A. Torres, B. W. K. Woo, Z. J. Yao, P. Yeh, J. Yoo, G. Young, N. Zhu, N. Zobrist, D. Sank, A. Korotkov, Y. Chen, and V. Smelyanskiy. “Measurement-induced state transitions in a superconducting qubit: within the rotating wave approximation.” *arXiv:2212.05097* (2022). Cited on page 73.
- [Kim21] S. Kim, H. Terai, T. Yamashita, W. Qiu, T. Fuse, F. Yoshihara, S. Ashhab, K. Inomata, and K. Semba. “Enhanced coherence of all-nitride superconducting qubits epitaxially grown on silicon substrate.” *Communications Materials* **2**, 98 (2021). Cited on page 86.
- [Kim23] Y. Kim, A. Eddins, S. Anand, K. X. Wei, E. van den Berg, S. Rosenblatt, H. Nayfeh, Y. Wu, M. Zaletel, K. Temme, and A. Kandala. “Evidence for the utility of quantum computing before fault tolerance.” *Nature* **618**, 500–505 (2023). Cited on page 3.
- [King23] A. D. King, J. Raymond, T. Lanting, R. Harris, A. Zucca, F. Altomare, A. J. Berkley, K. Boothby, S. Ejtemaee, C. Enderud, E. Hoskinson, S. Huang, E. Ladizinsky, A. J. R. MacDonald, G. Marsden, R. Molavi, T. Oh, G. Poulin-Lamarre, M. Reis, C. Rich, Y. Sato, N. Tsai, M. Volkmann, J. D. Whittaker, J. Yao, A. W. Sandvik, and M. H. Amin. “Quantum critical dynamics in a 5,000-qubit programmable spin glass.” *Nature* **617**, 61–66 (2023). Cited on page 3.
- [Kitaev95] A. Y. Kitaev. “Quantum measurements and the Abelian stabilizer problem.” *arXiv:quant-ph/9511026* (1995). Cited on page 2.
- [Kitaev03] A. Y. Kitaev. “Fault-tolerant quantum computation by anyons.” *Annals of Physics* **303**, 2–30 (2003). Cited on page 10.

-
- [Kjaergaard20a] M. Kjaergaard, M. E. Schwartz, J. Braumüller, P. Krantz, J. I.-J. Wang, S. Gustavsson, and W. D. Oliver. “Superconducting qubits: current state of play.” *Annual Review of Condensed Matter Physics* **11**, 369–395 (2020). Cited on pages 3, 20 and 109.
- [Kjaergaard20b] M. Kjaergaard, M. E. Schwartz, A. Greene, G. O. Samach, A. Bengtsson, M. O’Keeffe, C. M. McNally, J. Braumüller, D. K. Kim, P. Krantz, M. Marvian, A. Melville, B. M. Niedzielski, Y. Sung, R. Winik, J. Yoder, D. Rosenberg, K. Obenland, S. Lloyd, T. P. Orlando, I. Marvian, S. Gustavsson, and W. Oliver. “Programming a quantum computer with quantum instructions.” *arXiv:2001.08838* (2020). Cited on page 3.
- [Klimov20] P. V. Klimov, J. Kelly, J. M. Martinis, and H. Neven. “The Snake Optimizer for learning quantum processor control parameters.” *arXiv:2006.04594* (2020). Cited on page 82.
- [Knill97] E. Knill and R. Laflamme. “Theory of quantum error-correcting codes.” *Physical Review A* **55**, 900–911 (1997). Cited on page 4.
- [Knill98] E. Knill, R. Laflamme, and W. H. Zurek. “Resilient quantum computation.” *Science* **279**, 342–345 (1998). Cited on page 7.
- [Knill04] E. Knill. “Fault-tolerant postselected quantum computation: schemes.” *arXiv:quant-ph/0402171* (2004). Cited on page 15.
- [Knill05] E. Knill. “Quantum computing with realistically noisy devices.” *Nature* **434**, 39–44 (2005). Cited on page 51.
- [Koch07] J. Koch, T. M. Yu, J. Gambetta, A. A. Houck, D. I. Schuster, J. Majer, A. Blais, M. H. Devoret, S. M. Girvin, and R. J. Schoelkopf. “Charge-insensitive qubit design derived from the Cooper pair box.” *Physical Review A* **76**, 042319 (2007). Cited on pages 20, 25, 26, 27, 54, 70 and 71.
- [Kok07] P. Kok, W. J. Munro, K. Nemoto, T. C. Ralph, J. P. Dowling, and G. J. Milburn. “Linear optical quantum computing with photonic qubits.” *Reviews of Modern Physics* **79**, 135–174 (2007). Cited on page 20.
- [Kono20] S. Kono, K. Koshino, D. Lachance-Quirion, A. F. van Loo, Y. Tabuchi, A. Noguchi, and Y. Nakamura. “Breaking the trade-off between fast control and long lifetime of a superconducting qubit.” *Nature Communications* **11**, 3683 (2020). Cited on page 126.
- [Krinner19] S. Krinner, S. Storz, P. Kurpiers, P. Magnard, J. Heinsoo, R. Keller, J. Lütolf, C. Eichler, and A. Wallraff. “Engineering cryogenic setups for 100-qubit scale superconducting circuit systems.” *EPJ Quantum Technology* **6**, 2 (2019). Cited on page 40.
- [Krinner20] S. Krinner, S. Lazar, A. Remm, C. Andersen, N. Lacroix, G. Norris, C. Hellings, M. Gabureac, C. Eichler, and A. Wallraff. “Benchmarking coherent errors in controlled-phase gates due to spectator

- qubits.” *Physical Review Applied* **14**, 024042 (2020). Cited on pages 94 and 126.
- [Krinner22] S. Krinner, N. Lacroix, A. Remm, A. D. Paolo, E. Genois, C. Leroux, C. Hellings, S. Lazar, F. Swiadek, J. Herrmann, G. J. Norris, C. K. Andersen, M. Müller, A. Blais, C. Eichler, and A. Wallraff. “Realizing repeated quantum error correction in a distance-three surface code.” *Nature* **605**, 669–674 (2022). Cited on pages 9, 40, 71, 76, 77, 89, 109 and 117.
- [Kurpiers18] P. Kurpiers, P. Magnard, T. Walter, B. Royer, M. Pechal, J. Heinsoo, Y. Salathé, A. Akin, S. Storz, J.-C. Besse, S. Gasparinetti, A. Blais, and A. Wallraff. “Deterministic quantum state transfer and remote entanglement using microwave photons.” *Nature* **558**, 264–267 (2018). Cited on page 128.
- [Lacroix20] N. Lacroix, C. Hellings, C. K. Andersen, A. Di Paolo, A. Remm, S. Lazar, S. Krinner, G. J. Norris, M. Gabureac, J. Heinsoo, A. Blais, C. Eichler, and A. Wallraff. “Improving the performance of deep quantum optimization algorithms with continuous gate sets.” *PRX Quantum* **1**, 020304 (2020). Cited on page 3.
- [Lacroix23] N. Lacroix, L. Hofele, A. Remm, O. Benhayoune-Khadraoui, A. McDonald, R. Shillito, D. C. Zanuz, A. Flasby, M. B. Panah, M. Kerschbaum, G. J. Norris, F. Swiadek, S. Lazar, C. Hellings, A. Blais, A. Wallraff, and S. Krinner. “Fast flux-activated leakage reduction for superconducting quantum circuits.” *arXiv:2309.07060* (2023). Cited on pages 68 and 86.
- [Laflamme96] R. Laflamme, C. Miquel, J. P. Paz, and W. H. Zurek. “Perfect quantum error correcting code.” *Physical Review Letters* **77**, 198–201 (1996). Cited on page 6.
- [Langford13] N. K. Langford. “Circuit QED - lecture notes.” *arXiv:1310.1897* (2013). Cited on page 25.
- [Lazăr23] S. Lazăr, Q. Ficheux, J. Herrmann, A. Remm, N. Lacroix, C. Hellings, F. Swiadek, D. C. Zanuz, G. J. Norris, M. B. Panah, A. Flasby, M. Kerschbaum, J. Besse, C. Eichler, and A. Wallraff. “Calibration of drive nonlinearity for arbitrary-angle single-qubit gates using error amplification.” *Physical Review Applied* **20**, 024036 (2023). Cited on page 126.
- [Leibfried03] D. Leibfried, R. Blatt, C. Monroe, and D. Wineland. “Quantum dynamics of single trapped ions.” *Reviews of Modern Physics* **75**, 281–324 (2003). Cited on page 20.
- [Lisenfeld15] J. Lisenfeld, G. J. Grabovskij, C. Müller, J. H. Cole, G. Weiss, and A. V. Ustinov. “Observation of directly interacting coherent two-level systems in an amorphous material.” *Nature Communications* **6**, 6182 (2015). Cited on pages 71 and 84.
- [Lisenfeld16] J. Lisenfeld, A. Bilmes, S. Matityahu, S. Zanker, M. Marthaler, M. Schechter, G. Schön, A. Shnirman, G. Weiss, and A. V.

-
- Ustinov. “Decoherence spectroscopy with individual two-level tunneling defects.” *Scientific Reports* **6**, 23786 (2016). Cited on pages 84 and 86.
- [Litinski19] D. Litinski. “Magic state distillation: not as costly as you think.” *Quantum* **3**, 205 (2019). Cited on page 127.
- [Liyanage23] N. Liyanage, Y. Wu, A. Deters, and L. Zhong. “Scalable quantum error correction for surface codes using FPGA.” In *Proceedings of the 31st Annual IEEE International Symposium on Field-Programmable Custom Computing Machines*, 217. IEEE Press (2023). Cited on page 127.
- [Macklin15] C. Macklin, K. O’Brien, D. Hover, M. E. Schwartz, V. Bolkhovskiy, X. Zhang, W. D. Oliver, and I. Siddiqi. “A near-quantum-limited Josephson traveling-wave parametric amplifier.” *Science* **350**, 307–310 (2015). Cited on pages 109 and 110.
- [Magesan11] E. Magesan, J. M. Gambetta, and J. Emerson. “Scalable and robust randomized benchmarking of quantum processes.” *Physical Review Letters* **106**, 180504 (2011). Cited on pages 46, 55 and 74.
- [Magesan12] E. Magesan, J. M. Gambetta, B. R. Johnson, C. A. Ryan, J. M. Chow, S. T. Merkel, M. P. da Silva, G. A. Keefe, M. B. Rothwell, T. A. Ohki, M. B. Ketchen, and M. Steffen. “Efficient measurement of quantum gate error by interleaved randomized benchmarking.” *Physical Review Letters* **109**, 080505 (2012). Cited on pages 55 and 74.
- [Majer07] J. Majer, J. M. Chow, J. M. Gambetta, J. Koch, B. R. Johnson, J. A. Schreier, L. Frunzio, D. I. Schuster, A. A. Houck, A. Wallraff, A. Blais, M. H. Devoret, S. M. Girvin, and R. J. Schoelkopf. “Coupling superconducting qubits via a cavity bus.” *Nature* **449**, 443–447 (2007). Cited on pages 128 and 139.
- [Mallet09] F. Mallet, F. R. Ong, A. Palacios-Laloy, F. Nguyen, P. Bertet, D. Vion, and D. Esteve. “Single-shot qubit readout in circuit quantum electrodynamics.” *Nature Physics* **5**, 791–795 (2009). Cited on page 109.
- [Mamin21] H. Mamin, E. Huang, S. Carnevale, C. Rettner, N. Arellano, M. Sherwood, C. Kurter, B. Trimm, M. Sandberg, R. Shelby, M. Mueed, B. Madon, A. Pushp, M. Steffen, and D. Rugar. “Merged-element transmons: design and qubit performance.” *Physical Review Applied* **16**, 024023 (2021). Cited on page 86.
- [Marques22] J. F. Marques, B. M. Varbanov, M. S. Moreira, H. Ali, N. Muthusubramanian, C. Zachariadis, F. Battistel, M. Beekman, N. Haider, W. Vlothuizen, A. Bruno, B. M. Terhal, and L. Di-Carlo. “Logical-qubit operations in an error-detecting surface code.” *Nature Physics* **18**, 80–86 (2022). Cited on pages 9, 60 and 62.

- [Marques23] J. F. Marques, H. Ali, B. M. Varbanov, M. Finkel, H. M. Veen, S. L. M. van der Meer, S. Valles-Sanclemente, N. Muthusubramanian, M. Beekman, N. Haider, B. M. Terhal, and L. DiCarlo. “All-microwave leakage reduction units for quantum error correction with superconducting transmon qubits.” *Physical Review Letters* **130**, 250602 (2023). Cited on page 86.
- [Martinis05] J. M. Martinis, K. B. Cooper, R. McDermott, M. Steffen, M. Ansmann, K. D. Osborn, K. Cicak, S. Oh, D. P. Pappas, R. W. Simmonds, and C. C. Yu. “Decoherence in Josephson qubits from dielectric loss.” *Physical Review Letters* **95**, 210503 (2005). Cited on page 70.
- [Marxer23] F. Marxer, A. Vepsäläinen, S. W. Jolin, J. Tuorila, A. Landra, C. Ockeloen-Korppi, W. Liu, O. Ahonen, A. Auer, L. Belzane, V. Bergholm, C. F. Chan, K. W. Chan, T. Hiltunen, J. Hotari, E. Hyypä, J. Ikonen, D. Janzso, M. Koistinen, J. Kotilahti, T. Li, J. Luus, M. Papic, M. Partanen, J. Rabinä, J. Rosti, M. Savitskiy, M. Seppälä, V. Sevriuk, E. Takala, B. Tarasinski, M. J. Thapa, F. Tosto, N. Vorobeva, L. Yu, K. Y. Tan, J. Hassel, M. Möttönen, and J. Heinsoo. “Long-distance transmon coupler with CZ-gate fidelity above 99.8%.” *PRX Quantum* **4**, 010314 (2023). Cited on pages 3 and 128.
- [McCleane16] J. R. McClean, J. Romero, R. Babbush, and A. Aspuru-Guzik. “The theory of variational hybrid quantum-classical algorithms.” *New Journal of Physics* **18**, 023023 (2016). Cited on page 3.
- [McEwen21a] M. McEwen, L. Faoro, K. Arya, A. Dunsworth, T. Huang, S. Kim, B. Burkett, A. Fowler, F. Arute, J. C. Bardin, A. Bengtsson, A. Bिल्mes, B. B. Buckley, N. Bushnell, Z. Chen, R. Collins, S. Demura, A. R. Derk, C. Erickson, M. Giustina, S. D. Harrington, S. Hong, E. Jeffrey, J. Kelly, P. V. Klimov, F. Kostritsa, P. Laptev, A. Locharla, X. Mi, K. C. Miao, S. Montazeri, J. Mutus, O. Naaman, M. Neeley, C. Neill, A. Opremcak, C. Quintana, N. Redd, P. Roushan, D. Sank, K. J. Satzinger, V. Shvarts, T. White, Z. J. Yao, P. Yeh, J. Yoo, Y. Chen, V. Smelyanskiy, J. M. Martinis, H. Neven, A. Megrant, L. Ioffe, and R. Barends. “Resolving catastrophic error bursts from cosmic rays in large arrays of superconducting qubits.” *Nature Physics* **18**, 107–111 (2021). Cited on page 105.
- [McEwen21b] M. McEwen, D. Kafri, Z. Chen, J. Atalaya, K. J. Satzinger, C. Quintana, P. V. Klimov, D. Sank, C. Gidney, A. G. Fowler, F. Arute, K. Arya, B. Buckley, B. Burkett, N. Bushnell, B. Chiaro, R. Collins, S. Demura, A. Dunsworth, C. Erickson, B. Foxen, M. Giustina, T. Huang, S. Hong, E. Jeffrey, S. Kim, K. Kechedzhi, F. Kostritsa, P. Laptev, A. Megrant, X. Mi, J. Mutus, O. Naaman, M. Neeley, C. Neill, M. Niu, A. Paler, N. Redd, P. Roushan, T. C. White, J. Yao, P. Yeh, A. Zalcman, Y. Chen, V. N. Smelyan-

-
- skiy, J. M. Martinis, H. Neven, J. Kelly, A. N. Korotkov, A. G. Petukhov, and R. Barends. “Removing leakage-induced correlated errors in superconducting quantum error correction.” *Nature Communications* **12**, 1761 (2021). Cited on page 105.
- [McKay17] D. C. McKay, C. J. Wood, S. Sheldon, J. M. Chow, and J. M. Gambetta. “Efficient Z gates for quantum computing.” *Physical Review A* **96**, 022330 (2017). Cited on page 32.
- [Meiboom58] S. Meiboom and D. Gill. “Modified spin-echo method for measuring nuclear relaxation times.” *Review of Scientific Instruments* **29**, 688–691 (1958). Cited on page 48.
- [Meier13] A. M. Meier, B. Eastin, and E. Knill. “Magic-state distillation with the four-qubit code.” *Quantum Information & Computation* **13**, 195–209 (2013). Cited on page 127.
- [Miao22] K. C. Miao, M. McEwen, J. Atalaya, D. Kafri, L. P. Pryadko, A. Bengtsson, A. Opremcak, K. J. Satzinger, Z. Chen, P. V. Klimov, C. Quintana, R. Acharya, K. Anderson, M. Ansmann, F. Arute, K. Arya, A. Asfaw, J. C. Bardin, A. Bourassa, J. Bo-vaird, L. Brill, B. B. Buckley, D. A. Buell, T. Burger, B. Burkett, N. Bushnell, J. Campero, B. Chiaro, R. Collins, P. Conner, A. L. Crook, B. Curtin, D. M. Debroy, S. Demura, A. Dunsworth, C. Erickson, R. Fatemi, V. S. Ferreira, L. F. Burgos, E. Forati, A. G. Fowler, B. Foxen, G. Garcia, W. Giang, C. Gidney, M. Giustina, R. Gosula, A. G. Dau, J. A. Gross, M. C. Hamilton, S. D. Harrington, P. Heu, J. Hilton, M. R. Hoffmann, S. Hong, T. Huang, A. Huff, J. Iveland, E. Jeffrey, Z. Jiang, C. Jones, J. Kelly, S. Kim, F. Kostritsa, J. M. Kreikebaum, D. Landhuis, P. Laptev, L. Laws, K. Lee, B. J. Lester, A. T. Lill, W. Liu, A. Locharla, E. Lucero, S. Martin, A. Megrant, X. Mi, S. Montazeri, A. Morvan, O. Naaman, M. Neeley, C. Neill, A. Nersisyan, M. Newman, J. H. Ng, A. Nguyen, M. Nguyen, R. Potter, C. Rocque, P. Roushan, K. Sankaragomathi, C. Schuster, M. J. Shearn, A. Shorter, N. Shutty, V. Shvarts, J. Skrzynny, W. C. Smith, G. Sterling, M. Szalay, D. Thor, A. Torres, T. White, B. W. K. Woo, Z. J. Yao, P. Yeh, J. Yoo, G. Young, A. Zalcman, N. Zhu, N. Zobrist, H. Neven, V. Smelyanskiy, A. Petukhov, A. N. Korotkov, D. Sank, and Y. Chen. “Overcoming leakage in scalable quantum error correction.” *arXiv:2211.04728* (2022). Cited on page 86.
- [Michael16] M. H. Michael, M. Silveri, R. T. Brierley, V. V. Albert, J. Salmilehto, L. Jiang, and S. M. Girvin. “New class of quantum error-correcting codes for a bosonic mode.” *Physical Review X* **6**, 031006 (2016). Cited on page 4.
- [Mirrahimi14] M. Mirrahimi, Z. Leghtas, V. V. Albert, S. Touzard, R. J. Schoelkopf, L. Jiang, and M. H. Devoret. “Dynamically protected

- cat-qubits: a new paradigm for universal quantum computation.” *New Journal of Physics* **16**, 045014 (2014). Cited on page 4.
- [Moody23] D. Moody. “Digital signature standard (DSS).” Technical report, National Institute of Standards and Technology (2023). Cited on page 2.
- [Moore65] Moore. “Cramming more components onto integrated circuits.” *Electronics* **38**, 114–117 (1965). Cited on page 1.
- [Motzoi09] F. Motzoi, J. M. Gambetta, P. Rebentrost, and F. K. Wilhelm. “Simple pulses for elimination of leakage in weakly nonlinear qubits.” *Physical Review Letters* **103**, 110501 (2009). Cited on pages 46 and 74.
- [Müller19] C. Müller, J. H. Cole, and J. Lisenfeld. “Towards understanding two-level-systems in amorphous solids: insights from quantum circuits.” *Reports on Progress in Physics* **82**, 124501 (2019). Cited on pages 71 and 82.
- [Nakamura99] Y. Nakamura, Y. A. Pashkin, and J. S. Tsai. “Coherent control of macroscopic quantum states in a single-Cooper-pair box.” *Nature* **398**, 786–788 (1999). Cited on page 25.
- [Negîrneac21] V. Negîrneac, H. Ali, N. Muthusubramanian, F. Battistel, R. Sagastizabal, M. S. Moreira, J. F. Marques, W. J. Vlothuizen, M. Beekman, C. Zachariadis, N. Haider, A. Bruno, and L. DiCarlo. “High-fidelity controlled- Z gate with maximal intermediate leakage operating at the speed limit in a superconducting quantum processor.” *Physical Review Letters* **126**, 220502 (2021). Cited on page 36.
- [Neill18] C. Neill, P. Roushan, K. Kechedzhi, S. Boixo, S. V. Isakov, V. Smelyanskiy, A. Megrant, B. Chiaro, A. Dunsworth, K. Arya, R. Barends, B. Burkett, Y. Chen, Z. Chen, A. Fowler, B. Foxen, M. Giustina, R. Graff, E. Jeffrey, T. Huang, J. Kelly, P. Klimov, E. Lucero, J. Mutus, M. Neeley, C. Quintana, D. Sank, A. Vainsencher, J. Wenner, T. C. White, H. Neven, and J. M. Martinis. “A blueprint for demonstrating quantum supremacy with superconducting qubits.” *Science* **360**, 195–199 (2018). Cited on page 68.
- [Ni23] Z. Ni, S. Li, X. Deng, Y. Cai, L. Zhang, W. Wang, Z.-B. Yang, H. Yu, F. Yan, S. Liu, C.-L. Zou, L. Sun, S.-B. Zheng, Y. Xu, and D. Yu. “Beating the break-even point with a discrete-variable-encoded logical qubit.” *Nature* **616**, 56–60 (2023). Cited on page 4.
- [Nielsen10] M. A. Nielsen and I. L. Chuang. *Quantum Computation and Quantum Information*. Cambridge University Press, New York, USA, 10th anniversary edition (2010). Cited on pages 2, 4, 19, 32 and 46.

-
- [Nigg14] D. Nigg, M. Müller, E. A. Martinez, P. Schindler, M. Hennrich, T. Monz, M. A. Martin-Delgado, and R. Blatt. “Quantum computations on a topologically encoded qubit.” *Science* **345**, 302–305 (2014). Cited on page 76.
- [O’Brien14] K. O’Brien, C. Macklin, I. Siddiqi, and X. Zhang. “Resonant phase matching of Josephson junction traveling wave parametric amplifiers.” *Physical Review Letters* **113**, 157001 (2014). Cited on pages 109 and 120.
- [O’Brien17] T. E. O’Brien, B. Tarasinski, and L. DiCarlo. “Density-matrix simulation of small surface codes under current and projected experimental noise.” *npj Quantum Information* **3**, 39 (2017). Cited on pages 95, 96 and 98.
- [Oh06] S. Oh, K. Cicak, J. S. Kline, M. A. Sillanpää, K. D. Osborn, J. D. Whittaker, R. W. Simmonds, and D. P. Pappas. “Elimination of two level fluctuators in superconducting quantum bits by an epitaxial tunnel barrier.” *Physical Review B* **74**, 100502 (2006). Cited on page 86.
- [Oliver18] W. D. Oliver. “IARPA LogiQ program review.” (2018). Unpublished. Cited on page 120.
- [Orekhov22] A. Orekhov. *Two-Level System Defect Mitigation in Superconducting Quantum Processors*. Master’s thesis, ETH Zurich (2022). Cited on page 86.
- [Pan22] F. Pan, K. Chen, and P. Zhang. “Solving the sampling problem of the Sycamore quantum supremacy circuits.” *Physical Review Letters* **129**, 090502 (2022). Cited on page 2.
- [Pechal16] M. Pechal. *Microwave Photonics in Superconducting Circuits*. Ph.D. thesis, ETH Zurich (2016). Cited on pages 27, 28 and 137.
- [Peng22] K. Peng, M. Naghiloo, J. Wang, G. D. Cunningham, Y. Ye, and K. P. O’Brien. “Floquet-mode traveling-wave parametric amplifiers.” *PRX Quantum* **3**, 020306 (2022). Cited on pages 109 and 110.
- [Perdomo-Ortiz19] A. Perdomo-Ortiz, A. Feldman, A. Ozaeta, S. V. Isakov, Z. Zhu, B. O’Gorman, H. G. Katzgraber, A. Diedrich, H. Neven, J. de Kleer, B. Lackey, and R. Biswas. “Readiness of quantum optimization machines for industrial applications.” *Physical Review Applied* **12**, 014004 (2019). Cited on page 3.
- [Peruzzo14] A. Peruzzo, J. McClean, P. Shadbolt, M.-H. Yung, X.-Q. Zhou, P. J. Love, A. Aspuru-Guzik, and J. L. O’Brien. “A variational eigenvalue solver on a photonic quantum processor.” *Nature Communications* **5**, 4213 (2014). Cited on page 3.
- [Pettersson12] K. D. Pettersson, L. W. McFaul, M. D. Schroer, M. Jung, J. M. Taylor, A. A. Houck, and J. R. Petta. “Circuit quantum electrodynamics with a spin qubit.” *Nature* **490**, 380–383 (2012). Cited on page 109.

- [Place21] A. P. M. Place, L. V. H. Rodgers, P. Mundada, B. M. Smitham, M. Fitzpatrick, Z. Leng, A. Premkumar, J. Bryon, S. Sussman, G. Cheng, T. Madhavan, H. K. Babla, B. Jaeck, A. Gyenis, N. Yao, R. J. Cava, N. P. de Leon, and A. A. Houck. “New material platform for superconducting transmon qubits with coherence times exceeding 0.3 milliseconds.” *Nature Communications* **12**, 1779 (2021). Cited on page 125.
- [Planat19] L. Planat, R. Dassonneville, J. P. Martínez, F. Foroughi, O. Buisson, W. Hasch-Guichard, C. Naud, R. Vijay, K. Murch, and N. Roch. “Understanding the saturation power of Josephson parametric amplifiers made from SQUID arrays.” *Physical Review Applied* **11**, 034014 (2019). Cited on page 109.
- [Planat20] L. Planat, A. Ranadive, R. Dassonneville, J. Puertas Martínez, S. Léger, C. Naud, O. Buisson, W. Hasch-Guichard, D. M. Basko, and N. Roch. “Photonic-crystal Josephson traveling-wave parametric amplifier.” *Physical Review X* **10**, 021021 (2020). Cited on page 109.
- [Poulin15] D. Poulin, M. B. Hastings, D. Wecker, N. Wiebe, A. C. Doherty, and M. Troyer. “The Trotter step size required for accurate quantum simulation of quantum chemistry.” *Quantum Information & Computation* **15**, 361–384 (2015). Cited on page 2.
- [Poazar12] D. M. Pozar. *Microwave Engineering*. Wiley & Sons, Inc., New Jersey, USA, 4th edition (2012). Cited on pages 135 and 140.
- [Preskill98] J. Preskill. “Reliable quantum computers.” *Proceedings of the Royal Society A* **454**, 385–410 (1998). Cited on pages 7 and 8.
- [Preskill18] J. Preskill. “Quantum computing in the NISQ era and beyond.” *Quantum* **2**, 79 (2018). Cited on page 3.
- [Purcell46] E. M. Purcell. “Spontaneous emission probabilities at radio frequencies.” *Physical Review* **69**, 681 (1946). Cited on page 28.
- [Puri17] S. Puri, S. Boutin, and A. Blais. “Engineering the quantum states of light in a Kerr-nonlinear resonator by two-photon driving.” *npj Quantum Information* **3**, 18 (2017). Cited on page 4.
- [Raimond01] J. M. Raimond, M. Brune, and S. Haroche. “Manipulating quantum entanglement with atoms and photons in a cavity.” *Reviews of Modern Physics* **73**, 565–582 (2001). Cited on page 20.
- [Ranadive22] A. Ranadive, M. Esposito, L. Planat, E. Bonet, C. Naud, O. Buisson, W. Guichard, and N. Roch. “Kerr reversal in Josephson meta-material and traveling wave parametric amplification.” *Nature Communications* **13**, 1737 (2022). Cited on page 109.
- [Raussendorf07] R. Raussendorf and J. Harrington. “Fault-tolerant quantum computation with high threshold in two dimensions.” *Physical Review Letters* **98**, 190504 (2007). Cited on page 10.

-
- [Reed60] I. S. Reed and G. Solomon. “Polynomial codes over certain finite fields.” *Journal of the Society for Industrial and Applied Mathematics* **8**, 300–304 (1960). Cited on page 4.
- [Reed10] M. D. Reed, B. R. Johnson, A. A. Houck, L. DiCarlo, J. M. Chow, D. I. Schuster, L. Frunzio, and R. J. Schoelkopf. “Fast reset and suppressing spontaneous emission of a superconducting qubit.” *Applied Physics Letters* **96**, 203110 (2010). Cited on page 28.
- [Reed12] M. D. Reed, L. DiCarlo, S. E. Nigg, L. Sun, L. Frunzio, S. M. Girvin, and R. J. Schoelkopf. “Realization of three-qubit quantum error correction with superconducting circuits.” *Nature* **482**, 382–385 (2012). Cited on page 9.
- [Réglade23] U. Réglade, A. Bocquet, R. Gautier, A. Marquet, E. Albertinale, N. Pankratova, M. Hallén, F. Rautschke, L. Sellem, P. Rouchon, A. Sarlette, M. Mirrahimi, P. Campagne-Ibarcq, R. Lescanne, S. Jezouin, and Z. Leghtas. “Quantum control of a cat-qubit with bit-flip times exceeding ten seconds.” *arXiv:2307.06617* (2023). Cited on page 4.
- [Remm17] A. Remm. *Implementation and Characterization of Multiplexed Readout of Superconducting Qubits*. Master’s thesis, ETH Zurich (2017). Cited on page 30.
- [Remm23a] A. Remm, S. Krinner, N. Lacroix, C. Hellings, F. Swiadek, G. J. Norris, C. Eichler, and A. Wallraff. “Intermodulation distortion in a Josephson traveling-wave parametric amplifier.” *Physical Review Applied* **20**, 034027 (2023). Cited on pages 40, 110, 111, 114 and 120.
- [Remm23b] A. Remm, S. Krinner, *al.*, E. Genois, N. Lacroix, C. Hellings, G. Norris, C. Eichler, A. Blais, and A. Wallraff. “Experimental characterization of stabilizer code error probabilities based on syndrome data.” (2023). In preparation. Cited on pages 40, 89 and 103.
- [Ristè15] D. Ristè, S. Poletto, M.-Z. Huang, A. Bruno, V. Vesterinen, O.-P. Saira, and L. DiCarlo. “Detecting bit-flip errors in a logical qubit using stabilizer measurements.” *Nature Communications* **6**, 6983 (2015). Cited on page 9.
- [Rivest78] R. L. Rivest, A. Shamir, and L. Adleman. “A method for obtaining digital signatures and public-key cryptosystems.” *Communications of the ACM* **21**, 120–126 (1978). Cited on page 2.
- [Roetteler17] M. Roetteler, M. Naehrig, K. M. Svore, and K. Lauter. “Quantum resource estimates for computing elliptic curve discrete logarithms.” In *Proceedings of ASIACRYPT 2017, the 23rd Annual International Conference on the Theory and Application of Cryptology and Information Security*, 241–270. Springer International Publishing (2017). Cited on page 2.

- [Rol19] M. A. Rol, F. Battistel, F. K. Malinowski, C. C. Bultink, B. M. Tarasinski, R. Vollmer, N. Haider, N. Muthusubramanian, A. Bruno, B. M. Terhal, and L. DiCarlo. “Fast, high-fidelity conditional-phase gate exploiting leakage interference in weakly anharmonic superconducting qubits.” *Physical Review Letters* **123**, 120502 (2019). Cited on page 55.
- [Rol20] M. A. Rol, L. Ciorciaro, F. K. Malinowski, B. M. Tarasinski, R. E. Sagastizabal, C. C. Bultink, Y. Salathe, N. Haandbaek, J. Sedivy, and L. DiCarlo. “Time-domain characterization and correction of on-chip distortion of control pulses in a quantum processor.” *Applied Physics Letters* **116**, 054001 (2020). Cited on pages 68 and 74.
- [Ryan-Anderson21] C. Ryan-Anderson, J. G. Bohnet, K. Lee, D. Gresh, A. Hankin, J. P. Gaebler, D. Francois, A. Chernoguzov, D. Lucchetti, N. C. Brown, T. M. Gatterman, S. K. Halit, K. Gilmore, J. A. Gerber, B. Neyenhuis, D. Hayes, and R. P. Stutz. “Realization of real-time fault-tolerant quantum error correction.” *Physical Review X* **11**, 041058 (2021). Cited on page 127.
- [Saffman10] M. Saffman, T. G. Walker, and K. Mølmer. “Quantum information with Rydberg atoms.” *Reviews of Modern Physics* **82**, 2313 (2010). Cited on page 20.
- [Sank16] D. Sank, Z. Chen, M. Khezri, J. Kelly, R. Barends, B. Campbell, Y. Chen, B. Chiaro, A. Dunsworth, A. Fowler, and et al. “Measurement-induced state transitions in a superconducting qubit: beyond the rotating wave approximation.” *Physical Review Letters* **117**, 190503 (2016). Cited on pages 63 and 73.
- [Scherer17] A. Scherer, B. Valiron, S.-C. Mau, S. Alexander, E. van den Berg, and T. E. Chapuran. “Concrete resource analysis of the quantum linear-system algorithm used to compute the electromagnetic scattering cross section of a 2D target.” *Quantum Information Processing* **16**, 60 (2017). Cited on page 3.
- [Schmitt14] V. Schmitt, X. Zhou, K. Juliusson, B. Royer, A. Blais, P. Bertet, D. Vion, and D. Esteve. “Multiplexed readout of transmon qubits with Josephson bifurcation amplifiers.” *Physical Review A* **90**, 062333 (2014). Cited on page 109.
- [Schreier08] J. A. Schreier, A. A. Houck, J. Koch, D. I. Schuster, B. R. Johnson, J. M. Chow, J. M. Gambetta, J. Majer, L. Frunzio, M. H. Devoret, S. M. Girvin, and R. J. Schoelkopf. “Suppressing charge noise decoherence in superconducting charge qubits.” *Physical Review B* **77**, 180502 (2008). Cited on page 25.
- [Serniak18] K. Serniak, M. Hays, G. de Lange, S. Diamond, S. Shankar, L. D. Burkhardt, L. Frunzio, M. Houzet, and M. H. Devoret. “Hot nonequilibrium quasiparticles in transmon qubits.” *Physical Review Letters* **121**, 157701 (2018). Cited on page 105.

-
- [Sete15] E. A. Sete, J. M. Martinis, and A. N. Korotkov. “Quantum theory of a bandpass Purcell filter for qubit readout.” *Physical Review A* **92**, 012325 (2015). Cited on page 28.
- [Shalibo10] Y. Shalibo, Y. Rofe, D. Shwa, F. Zeides, M. Neeley, J. M. Martinis, and N. Katz. “Lifetime and coherence of two-level defects in a Josephson junction.” *Physical Review Letters* **105**, 177001 (2010). Cited on page 84.
- [Shor94] P. W. Shor. “Algorithms for quantum computation: discrete logarithms and factoring.” In *Proceedings of the 35th Annual Symposium on Foundations of Computer Science*, 124–134. IEEE Computer Society Press (1994). Cited on page 2.
- [Shor95] P. W. Shor. “Scheme for reducing decoherence in quantum computer memory.” *Physical Review A* **52**, R2493 (1995). Cited on page 4.
- [Shor97] P. W. Shor. “Polynomial-time algorithms for prime factorization and discrete logarithms on a quantum computer.” *SIAM Journal on Computing* **26**, 1484 (1997). Cited on page 2.
- [Simmonds04] R. Simmonds, K. Lang, D. Hite, S. Nam, D. Pappas, and J. Martinis. “Decoherence in Josephson phase qubits from junction resonators.” *Physical Review Letters* **93**, 077003 (2004). Cited on pages 71 and 82.
- [Simons01] R. N. Simons. *Coplanar Waveguide Circuits, Components and Systems*. John Wiley & Sons, Inc., New York, USA (2001). Cited on page 21.
- [Sivak19] V. V. Sivak, N. E. Frattini, V. R. Joshi, A. Lingenfelter, S. Shankar, and M. H. Devoret. “Kerr-free three-wave mixing in superconducting quantum circuits.” *Physical Review Applied* **11**, 054060 (2019). Cited on page 109.
- [Sivak23] V. V. Sivak, A. Eickbusch, B. Royer, S. Singh, I. Tsioutsios, S. Ganjam, A. Miano, B. L. Brock, A. Z. Ding, L. Frunzio, S. M. Girvin, R. J. Schoelkopf, and M. H. Devoret. “Real-time quantum error correction beyond break-even.” *Nature* **616**, 50–55 (2023). Cited on page 5.
- [Somoroff23] A. Somoroff, Q. Ficheux, R. A. Mencia, H. Xiong, R. Kuzmin, and V. E. Manucharyan. “Millisecond coherence in a superconducting qubit.” *Physical Review Letters* **130**, 267001 (2023). Cited on page 126.
- [Spitz18] S. T. Spitz, B. Tarasinski, C. W. J. Beenakker, and T. E. O’Brien. “Adaptive weight estimator for quantum error correction in a time-dependent environment.” *Advanced Quantum Technologies* **1**, 1800012 (2018). Cited on pages 95, 99 and 101.
- [Stace10] T. M. Stace and S. D. Barrett. “Error correction and degeneracy in surface codes suffering loss.” *Physical Review A* **81**, 022317 (2010). Cited on page 95.

- [Steane96] A. Steane. “Multiple-particle interference and quantum error correction.” *Proceedings of the Royal Society A* **452**, 2551 (1996). Cited on page 11.
- [Strauch03] F. W. Strauch, P. R. Johnson, A. J. Dragt, C. J. Lobb, J. R. Anderson, and F. C. Wellstood. “Quantum logic gates for coupled superconducting phase qubits.” *Physical Review Letters* **91**, 167005 (2003). Cited on pages 34, 46 and 63.
- [Sun23] H. Sun, F. Wu, H.-S. Ku, X. Ma, J. Qin, Z. Song, T. Wang, G. Zhang, J. Zhou, Y. Shi, H.-H. Zhao, and C. Deng. “Characterization of loss mechanisms in a fluxonium qubit.” *Physical Review Applied* **20**, 034016 (2023). Cited on page 82.
- [Sunada22] Y. Sunada, S. Kono, J. Ilves, S. Tamate, T. Sugiyama, Y. Tabuchi, and Y. Nakamura. “Fast readout and reset of a superconducting qubit coupled to a resonator with an intrinsic Purcell filter.” *Physical Review Applied* **17**, 044016 (2022). Cited on page 62.
- [Sundaresan23] N. Sundaresan, T. J. Yoder, Y. Kim, M. Li, E. H. Chen, G. Harper, T. Thorbeck, A. W. Cross, A. D. Córcoles, and M. Takita. “Demonstrating multi-round subsystem quantum error correction using matching and maximum likelihood decoders.” *Nature Communications* **14**, 2852 (2023). Cited on pages 9, 62 and 89.
- [Swiadek23] F. Swiadek, R. Shillito, P. Magnard, A. Remm, C. Hellings, N. Lacroix, Q. Ficheux, D. C. Zanuz, G. J. Norris, A. Blais, S. Krinner, and A. Wallraff. “Enhancing dispersive readout of superconducting qubits through dynamic control of the dispersive shift: experiment and theory.” *arXiv:2307.07765* (2023). Cited on pages 30, 62, 73 and 126.
- [Takita17] M. Takita, A. W. Cross, A. D. Córcoles, J. M. Chow, and J. M. Gambetta. “Experimental demonstration of fault-tolerant state preparation with superconducting qubits.” *Physical Review Letters* **119**, 180501 (2017). Cited on page 9.
- [Terhal15] B. M. Terhal. “Quantum error correction for quantum memories.” *Reviews of Modern Physics* **87**, 307–346 (2015). Cited on page 4.
- [vanderWiel02] W. G. van der Wiel, S. De Franceschi, J. M. Elzerman, T. Fujisawa, S. Tarucha, and L. P. Kouwenhoven. “Electron transport through double quantum dots.” *Reviews of Modern Physics* **75**, 1–22 (2002). Cited on page 20.
- [Versluis17] R. Versluis, S. Poletto, N. Khammassi, B. Tarasinski, N. Haider, D. J. Michalak, A. Bruno, K. Bertels, and L. DiCarlo. “Scalable quantum circuit and control for a superconducting surface code.” *Physical Review Applied* **8**, 034021 (2017). Cited on pages 53, 67 and 69.
- [Walker12] J. L. B. Walker, (Ed.). *Handbook of RF and Microwave Power Amplifiers*. Cambridge University Press, New York, USA (2012). Cited on pages 110 and 114.

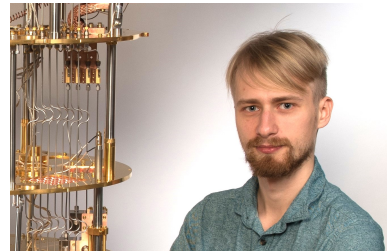
-
- [Wallraff04] A. Wallraff, D. I. Schuster, A. Blais, L. Frunzio, R.-S. Huang, J. Majer, S. Kumar, S. M. Girvin, and R. J. Schoelkopf. “Strong coupling of a single photon to a superconducting qubit using circuit quantum electrodynamics.” *Nature* **431**, 162–167 (2004). Cited on page 25.
- [Wallraff05] A. Wallraff, D. I. Schuster, A. Blais, L. Frunzio, J. Majer, M. H. Devoret, S. M. Girvin, and R. J. Schoelkopf. “Approaching unit visibility for control of a superconducting qubit with dispersive readout.” *Physical Review Letters* **95**, 060501 (2005). Cited on pages 26 and 109.
- [Walter17] T. Walter, P. Kurpiers, S. Gasparinetti, P. Magnard, A. Potočnik, Y. Salathé, M. Pechal, M. Mondal, M. Oppliger, C. Eichler, and A. Wallraff. “Rapid high-fidelity single-shot dispersive readout of superconducting qubits.” *Physical Review Applied* **7**, 054020 (2017). Cited on pages 62 and 126.
- [Wecker14] D. Wecker, B. Bauer, B. K. Clark, M. B. Hastings, and M. Troyer. “Gate-count estimates for performing quantum chemistry on small quantum computers.” *Physical Review A* **90**, 022305 (2014). Cited on page 2.
- [White15] T. C. White, J. Y. Mutus, I.-C. Hoi, R. Barends, B. Campbell, Y. Chen, Z. Chen, B. Chiaro, A. Dunsworth, E. Jeffrey, J. Kelly, A. Megrant, C. Neill, P. J. J. O’Malley, P. Roushan, D. Sank, A. Vainsencher, J. Wenner, S. Chaudhuri, J. Gao, and J. M. Martinis. “Traveling wave parametric amplifier with Josephson junctions using minimal resonator phase matching.” *Applied Physics Letters* **106**, 242601 (2015). Cited on page 109.
- [Wood18] C. J. Wood and J. M. Gambetta. “Quantification and characterization of leakage errors.” *Physical Review A* **97**, 032306 (2018). Cited on page 105.
- [Wootters82] W. K. Wootters and W. H. Zurek. “A single quantum cannot be cloned.” *Nature* **299**, 802–803 (1982). Cited on page 1.
- [Wootton18] J. R. Wootton and D. Loss. “Repetition code of 15 qubits.” *Physical Review A* **97**, 052313 (2018). Cited on page 9.
- [Wootton20] J. R. Wootton. “Benchmarking near-term devices with quantum error correction.” *Quantum Science and Technology* **5**, 044004 (2020). Cited on page 9.
- [Ye23] Y. Ye, T. He, H.-L. Huang, Z. Wei, Y. Zhang, Y. Zhao, D. Wu, Q. Zhu, H. Guan, S. Cao, F. Chen, T.-H. Chung, H. Deng, D. Fan, M. Gong, C. Guo, S. Guo, L. Han, N. Li, S. Li, Y. Li, F. Liang, J. Lin, H. Qian, H. Rong, H. Su, S. Wang, Y. Wu, Y. Xu, C. Ying, J. Yu, C. Zha, K. Zhang, Y.-H. Huo, C.-Y. Lu, C.-Z. Peng, X. Zhu, and J.-W. Pan. “Logical magic state preparation with fidelity beyond the distillation threshold on a superconducting quantum processor.” *arXiv:2305.15972* (2023). Cited on pages 9 and 87.

- [Yurke96] B. Yurke, M. L. Roukes, R. Movshovich, and A. N. Pargellis. “A low-noise series-array Josephson junction parametric amplifier.” *Applied Physics Letters* **69**, 3078 (1996). Cited on page 109.
- [Zanuz23] D. C. Zanuz, J.-C. Besse, Q. Ficheux, A. Orekhov, L. Michaud, K. Hanke, A. Remm, A. Flasby, C. Hellings, M. Kerschbaum, N. Lacroix, S. Lažar, G. J. Norris, M. B. Panah, F. Swiadek, S. Krinner, C. Eichler, and A. Wallraff. “Mitigating losses of superconducting qubits coupled strongly to defect modes.” (2023). In preparation. Cited on pages 82, 86 and 125.
- [Zhao22a] P. Zhao, Y. Zhang, G. Xue, Y. Jin, and H. Yu. “Tunable coupling of widely separated superconducting qubits: a possible application toward a modular quantum device.” *Applied Physics Letters* **121**, 032601 (2022). Cited on page 128.
- [Zhao22b] Y. Zhao, Y. Ye, H.-L. Huang, Y. Zhang, D. Wu, H. Guan, Q. Zhu, Z. Wei, T. He, S. Cao, F. Chen, T.-H. Chung, H. Deng, D. Fan, M. Gong, C. Guo, S. Guo, L. Han, N. Li, S. Li, Y. Li, F. Liang, J. Lin, H. Qian, H. Rong, H. Su, L. Sun, S. Wang, Y. Wu, Y. Xu, C. Ying, J. Yu, C. Zha, K. Zhang, Y.-H. Huo, C.-Y. Lu, C.-Z. Peng, X. Zhu, and J.-W. Pan. “Realization of an error-correcting surface code with superconducting qubits.” *Physical Review Letters* **129**, 030501 (2022). Cited on pages 9 and 62.
- [Zheng19] G. Zheng, N. Samkharadze, M. L. Noordam, N. Kalhor, D. Brousse, A. Sammak, G. Scappucci, and L. M. K. Vandersypen. “Rapid gate-based spin read-out in silicon using an on-chip resonator.” *Nature Nanotechnology* **14**, 742–746 (2019). Cited on page 109.
- [Zhong20] H.-S. Zhong, H. Wang, Y.-H. Deng, M.-C. Chen, L.-C. Peng, Y.-H. Luo, J. Qin, D. Wu, X. Ding, Y. Hu, P. Hu, X.-Y. Yang, W.-J. Zhang, H. Li, Y. Li, X. Jiang, L. Gan, G. Yang, L. You, Z. Wang, L. Li, N.-L. Liu, C.-Y. Lu, and J.-W. Pan. “Quantum computational advantage using photons.” *Science* **370**, 1460 (2020). Cited on page 3.
- [Zobrist19] N. Zobrist, B. H. Eom, P. Day, B. A. Mazin, S. R. Meeker, B. Bumble, H. G. LeDuc, G. Coiffard, P. Szypryt, N. Fruitwala, I. Lipartito, C. Bockstiegel, N. Zobrist, B. H. Eom, P. Day, B. A. Mazin, S. R. Meeker, B. Bumble, H. G. LeDuc, G. Coiffard, P. Szypryt, N. Fruitwala, I. Lipartito, C. Bockstiegel, N. Zobrist, B. H. Eom, P. Day, B. A. Mazin, S. R. Meeker, B. Bumble, H. G. LeDuc, G. Coiffard, P. Szypryt, N. Fruitwala, I. Lipartito, and C. Bockstiegel. “Wide-band parametric amplifier readout and resolution of optical microwave kinetic inductance detectors.” *Applied Physics Letters* **115**, 042601 (2019). Cited on page 109.

Curriculum Vitae

Personal Data

Name	Ants Remm
Date of birth	22.05.1992
Citizenship	Estonian



Professional Experience

2017–2018	ETH Zurich, research assistant
2011–2016	Estonian physics olympiad, committee member
2013	PerkinElmer Cellular Technologies, Estonian branch, research software developer

Education

2018–2023	Ph.D. Physics, ETH Zurich
2015–2017	M.Sc. Physics, ETH Zurich
2011–2014	B.Sc. Physics, University of Tartu

List of Publications

This thesis is mainly based on the following publications:

1. C. K. Andersen¹, **A. Remm**¹, S. Lazăr, S. Krinner, J. Heinsoo, J.-C. Besse, M. Gabureac, A. Wallraff, and C. Eichler, “Entanglement stabilization using ancilla-based parity detection and real-time feedback in superconducting circuits,” *npj Quantum Information* **5**, 69 (2019)
2. C. K. Andersen, **A. Remm**, S. Lazăr, S. Krinner, N. Lacroix, G. J. Norris, M. Gabureac, C. Eichler, and A. Wallraff, “Repeated quantum error detection in a surface code,” *Nature Physics* **16**, 875–880 (2020)
3. S. Krinner¹, N. Lacroix¹, **A. Remm**, A. Di Paolo, E. Genois, C. Leroux, C. Hellings, S. Lazăr, F. Swiadek, J. Herrmann, G. J. Norris, C. K. Andersen, M. Müller, A. Blais, C. Eichler, and A. Wallraff, “Realizing repeated quantum error correction in a distance-three surface code,” *Nature* **605**, 669–674 (2022)
4. **A. Remm**, S. Krinner, N. Lacroix, C. Hellings, F. Swiadek, G. J. Norris, C. Eichler, and A. Wallraff, “Intermodulation distortion in a Josephson traveling-wave parametric amplifier,” *Physical Review Applied* **20**, 034027 (2023)
5. **A. Remm**, S. Krinner, E. Genois, N. Lacroix, C. Hellings, F. Swiadek, G. J. Norris, C. Eichler, A. Blais, A. Wallraff, “Experimental characterization of stabilizer code error probabilities based on syndrome correlations,” in preparation (2023)

In addition, the author made contributions for the following publications:

6. J. Heinsoo, C. K. Andersen, **A. Remm**, S. Krinner, T. Walter, Y. Salathé, S. Gasparinetti, J.-C. Besse, A. Potočník, C. Eichler, and A. Wallraff, “Rapid high-fidelity multiplexed readout of superconducting qubits,” *Physical Review Applied* **10**, 034040 (2018)

¹These authors contributed equally.

7. J.-C. Besse, S. Gasparinetti, M. C. Collodo, T. Walter, **A. Remm**, J. Krause, C. Eichler, and A. Wallraff, “Parity detection of propagating microwave fields,” *Physical Review X* **10**, 011046 (2020)
8. S. Krinner, S. Lazăr, **A. Remm**, C. K. Andersen, N. Lacroix, G. J. Norris, C. Hellings, M. Gabureac, C. Eichler, and A. Wallraff, “Benchmarking coherent errors in controlled-phase gates due to spectator qubits,” *Physical Review Applied* **14**, 024042 (2020)
9. N. Lacroix, C. Hellings, C. K. Andersen, A. Di Paolo, **A. Remm**, S. Lazăr, S. Krinner, G. J. Norris, M. Gabureac, A. Blais, C. Eichler, and A. Wallraff, “Improving the performance of deep quantum optimization algorithms with continuous gate sets,” *PRX Quantum* **1**, 020304 (2020)
10. S. Krinner¹, P. Kurpiers¹, B. Royer, P. Magnard, I. Tsitsilin, J.-C. Besse, **A. Remm**, A. Blais, and A. Wallraff, “Demonstration of an all-microwave controlled-phase gate between far-detuned qubits,” *Physical Review Applied* **14**, 044039 (2020)
11. M. C. Collodo¹, J. Herrmann¹, N. Lacroix, C. K. Andersen, **A. Remm**, S. Lazăr, J.-C. Besse, T. Walter, A. Wallraff, and C. Eichler, “Implementation of conditional phase gates based on tunable ZZ interactions,” *Physical Review Letters* **125**, 240502 (2020)
12. J. Herrmann, S. M. Llima, **A. Remm**, P. Zapletal, N. A. McMahon, C. Scarato, F. Swiadek, C. K. Andersen, C. Hellings, S. Krinner, N. Lacroix, S. Lazăr, M. Kerschbaum, D. Colao Zanuz, G. J. Norris, M. J. Hartmann, A. Wallraff, and C. Eichler, “Realizing quantum convolutional neural networks on a superconducting quantum processor to recognize quantum phases,” *Nature Communications* **13**, 4144 (2022)
13. S. Lazăr¹, Q. Ficheux¹, J. Herrmann, **A. Remm**, N. Lacroix, C. Hellings, F. Swiadek, D. Colao Zanuz, G. J. Norris, M. Bahrami Panah, A. Flasby, M. Kerschbaum, J.-C. Besse, C. Eichler, and A. Wallraff, “Calibration of drive nonlinearity for arbitrary-angle single-qubit gates using error amplification,” *Physical Review Applied* **20**, 024036 (2023)

¹These authors contributed equally.

-
14. K. Reuer, J. Landgraf, T. Fösel, J. O’Sullivan, L. Beltrán, A. Akin, G. J. Norris, **A. Remm**, M. Kerschbaum, J.-C. Besse, F. Marquardt, A. Wallraff, and C. Eichler, “Realizing a deep reinforcement learning agent for real-time quantum feedback,” *Nature Communications* **14**, 7138 (2023)
 15. F. Swiadek, R. Shillito, P. Magnard, **A. Remm**, C. Hellings, N. Lacroix, Q. Ficheux, D. Colao Zanuz, G. J. Norris, A. Blais, S. Krinner, and A. Wallraff, “Enhancing dispersive readout of superconducting qubits through dynamic control of the dispersive shift: experiment and theory,” *arXiv:2307.07765* (2023)
 16. N. Lacroix, L. Hofele, **A. Remm**, O. Benhayoune-Khadraoui, A. McDonald, R. Shillito, S. Lazăr, C. Hellings, F. Swiadek, D. Colao Zanuz, A. Flasby, M. Bahrami Panah, M. Kerschbaum, G. J. Norris, A. Blais, A. Wallraff, and S. Krinner, “Fast flux-activated leakage reduction for superconducting quantum circuits,” *arXiv:2309.07060* (2023)
 17. D. Colao Zanuz, J.-C. Besse, Q. Ficheux, A. Orekhov, L. Michaud, K. Hanke, **A. Remm**, A. Flasby, C. Hellings, M. Kerschbaum, N. Lacroix, S. Lazăr, G. J. Norris, M. Bahrami Panah, F. Swiadek, S. Krinner, C. Eichler, and A. Wallraff, “Mitigating Losses of Superconducting Qubits Coupled Strongly to Defect Modes,” in preparation (2023)

